CAVITATION EROSION OF ENGINEERING MATERIALS

BY

ASOUMU EMMANUEL EWUNKEM

THESIS PRESENTED FOR THE DEGREE OF DOCTOR OF PHILOSOPHY

DEPARTMENT OF MECHANICAL ENGINEERING AND AERONAUTICS
THE CITY UNIVERSITY
LONDON

AUGUST 1993

TABLE OF CONTENT

CHAPTER		PAGE
	TITLE PAGE	i
	LIST OF TABLES	ii
	LIST OF FIGURES	iii
	ACKNOWLEDGEMENTS	xi
	DECLARATION	xii
	ABSTRACT	xiii
	NOMENCLATURE	xiv
1.0	**INTRODUCTION**	**1**
2.0	**LITERATURE REVIEW**	**10**
2.1	INTRODUCTION	10
2.2	COMMON AGREED BASIC PRINCIPLE RELATED TO DAMAGE	12
2.3	TESTING TECHNIQUES	15
2.4	TIME DEPENDENCE OF EROSION RATES	22
2.5	INFLUENCE OF TEST PARAMETERS	26
2.6	FLOW CAVITATION AND CAVITY DYNAMICS	31

2.7 CORRELATION WITH MECHANICAL PROPERTY 37

2.8 CONCLUSION 41

3.0 —— TEST FACILITY 43

3.1 GENERAL DESCRIPTION 43

3.2 WORKING SECTION 44

3.3 RIG PRESSURIZATION 45

3.4 TEMPERATURE REGULATION 46

3.5 AIR CONTENT 47

3.6 FLOW VELOCITY AND CAVITATION NUMBER 48

APPENDIX 3.7 52

APPENDIX 3.8 54

FIGURES

4.0 —— EXPERIMENTAL PROCEDURE 57

4.1 RIG OPERATION 57

4.2 TEST MATERIALS 58

4.2.1 CERAMIC 59

4.2.2 PLASTIC 62

4.2.3 COMPOSITE 63

4.2.4 METAL ALLOYS 65

4.3 TESTING PROCEDURE 66

5.0 —— EXPERIMENTAL RESULT 68

5.1 EROSION RATE TIME PATTERN 69

5.2 RESULT ANALYSIS 73

5.2.1 PLASTICS 77

5.2.2 CERAMICS 79

5.2.3 COMPOSITES 82

5.2.4 METAL ALLOYS 84

5.3 GENERAL OBSERVATION OF EROSION PATTERN 85

5.3.1 PLASTICS 85

5.3.2 CERAMICS 88

5.3.3 COMPOSITES 93

5.3.4 METAL ALLOYS 96

FIGURES

TABLES

6.0 —— DISCUSSION 104

6.1 PLASTICS 105

6.2 CERAMICS 114

6.3 COMPOSITES 124

6.4 METAL ALLOYS 130

APPENDIX 6.1

7.0 ——— CONCLUSIONS AND FURTHER RECOMMENDATIONS 144

REFERENCES 149

LIST OF TABLES

1 RESULT FROM HUTTON AND SELIM

2 CORRELATION WITH MECHANICAL PROPERTIES

3 CERAMIC GENERAL CONDITION

4 PLASTIC GENERAL CONDITION

5 COMPOSITE GENERAL CONDITION

6a METAL ALLOYS NOMINAL COMPOSITION

6b METAL ALLOYS TESTING CONDITIONS

7 MECHANICAL PROPERTIES OF PLASTIC

8 RESULT FOR PLASTICS AS MACHINED

9 RESULT FOR PLASTICS AS CAST

10 VELOCITY EXPONENT FOR PLASTICS

11 MECHANICAL PROPERTIES OF CERAMICS

12 SURFACE ROUGHNESS OF CERAMICS

13 RESULT FOR SILICON CARBIDE

14 RESULT FOR SILICON NITRIDE

15 COMPARISON BETWEEN CARBIDE AND NITRIDE

16 RESULT FOR COMPOSITE

17 RESULT FOR METAL ALLOYS

LIST OF FIGURES

1 BUBBLE'S COLLAPSE MECHANISM, "RE-BOUND"

2 BUBBLE'S COLLAPSE MECHANISM, "NON SYMMETRICAL COLLAPSE"

3a ROTATING DISC DEVICE

3b LOCATION OF SPECIMEN

4a CROSS SECTION

4b LOCATION OF SPECIMEN

5 VENTURI DESIGN

6 VENTURI RIG AT MICHIGAN UNIVERSITY

7 MOUSSON'S VENTURI RIG

8 RAO'S VENTURI RIG

9 VIBRATION DEVICE

10 EROSION RATE TIME DEPENDENCE CURVES

10A EROSION RATE CURVE FROM THIRUVENGADAM

10B EROSION RATE CURVE FROM DEVINE

10C EROSION RATE CURE FROM TICHLER

11 VARIATION OF EROSION RATE WITH VELOCITY

12 VARIATION OF VELOCITY EXPONENT WITH DIFFERENT SHAPE CAVITATION INDUCERS

13 VARIATION OF EROSION RATE WITH PRESSURE

14 VARIATION OF EROSION RATE WITH PRESSURE

15 CAVITY DYNAMICS FROM CON-DIV WEDGE

16 CAVITY DYNAMICS FROM SYMETRICAL WEDGE

17 EROSION VARIATION WITH 1" CAVITY LENGTH

18 EROSION VARIATION WITH 2" CAVITY LENGTH

19 VARIATION OF EROSION RATE WITH MECHANICAL PROPERTIES

20a CAVITATION RIG AT CITY UNIVERSITY

20b CAVITATION EROSION TEST SPECIMEN

20c TEST SECTION

20d TEST SECTION

20e INDUCER

21 PRESSURE TAPPING ARRANGEMENT

22 RIG PRESSURIZATION SYSTEM

23 TEMPERATURE REGULATOR

24 AIR CONTENT OF TEST WATER

25 PRESSURE PLOT ACROSS CONTRACTION

26a S-SHAPE OF EROSION CURVE

26b EROSION STAGES

27-36 GRAPH OF CUMULATIVE VOLUME LOSS AGAINST TIME FOR EPOXY RESINS

37-47 COMPARISON GRAPHS FOR EPOXY RESINS

48-62 GRAPH OF CUMULATIVE VOLUME LOSS AGAINST TIME FOR CERAMICS

63-70 COMPARISON GRAPHS FOR CERAMICS

71-76 GRAPHS OF EROSION RATE AGAINST TIME FOR CERAMICS

77-80 GRAPH CUMULATIVE VOLUME LOSS AGAINST TIME FOR GRP

81 GRAPH OF VOLUME LOSS AGAINST VELOCITY

82 GRAPH OF EROSION RATE AGAINST TIME FOR GRP

83-84 GRAPH OF CUMULATIVE VOLUME LOSS AGAINST TIME FOR FYBROC

85 GRAPH OF EROSION RATE AGAINST TIME FOR FYBROC

86-87 COMPARISON GRAPHS FOR GRP AND FYBROC

88-98 GRAPHS OF CUMULATIVE VOLUME LOSS AGAINST TIME FOR METAL ALLOYS

99 COMPARISON GRAPH FOR VARIOUS ENGINEERING MATERIALS

100a CAST SURFACE OF EPOXY RESIN PRIOR TO TESTING

100b MACHINED SURFACE OF EPOXY RESIN PRIOR TO TESTING

101 DAMAGE PROGRESSION SEQUENCE OF EPOXY RESIN

101a INITIAL DAMAGE FROM AN OPTICAL MICROSCOPE

101b LOCALIZED DAMAGE

101c LARGE CREVICE

102a MATERIAL REMOVAL FROM PERPENDICULAR/PARALLEL PROPAGATION

102b RESIN DISINTEGRATION

102c MACROSCOPIC VIEW OF GROSS DAMAGE ON ONE ERODED AREA

103 PHOTOMICROGRAPH OF SILICON CARBIDE SURFACE PRIOR TO TESTING

103a GROUND SURFACE OF SILICON CARBIDE

103b LAPPED SURFACE OF SILICON CARBIDE

103c FIRED SURFACE OF SILICON CARBIDE

103d MICROSTRUCTURE REVEALING "FREE" SILICON

104 DAMAGE PROGRESSION SEQUENCE FOR SILICON CARBIDE

104a INITIAL PITTING FORMATION

104b DEEPER PITS

104c MAGNIFIED VIEW OF FIG 104b

104d FRAGMENT REMOVAL AS A RESULT OF INTERSECTING CRACKS

104e S.E.M OF SUB-SURFACE CRACK

105a CHIPPING EFFECT

105b S.E.M OF FIG 105a

105c LOCALISED CRACK IN CENTRAL ZONE

105d TOPOGRAPHY OF CHIPPED SURFACE

105e GROSS DAMAGE ON SILICON CARBIDE

106 PHOTOMICROGRAPH OF SILICON NITRIDE SURFACE PRIOR TO TESTING

106a GROUND SURFACE OF SILICON NITRIDE

106b LAPPED SURFACE OF SILICON NITRIDE

106c FIRED SURFACE OF SILICON NITRIDE

107 DAMAGE PROGRESSION IN SILICON NITRIDE

107a PLAIN SURFACE

107b INITIAL DAMAGE

107c PITS FORMATION

107d PITS FORMATION

107e MATERIAL REMOVAL AFTER "NECKING"

107f INTERGRANULAR FRACTURE

107g GROSS DAMAGE SUSTAINED AFTER TEST COMPLETION

108 PORES ON SURFACE OF GRP BEFORE TESTING

108a EXPOSED FIBRE

108b FIBRE DEVOID OF RESIN

108c DELAMINATION

108d FRACTURED FIBRE

108e TUNNELLING EFFECT ON GRP

109 PLAIN SURFACE OF FYBROC BEFORE TESTING

110a INITIAL DAMAGE EXPOSING FIBRE

110b CRUSHED MATRIX

110c BROKEN STRAND

110d GROSS DAMAGE ON ONE ERODED AREA

111 DAMAGE PROGRESSION SEQUENCE FOR ALUMINIUM

111a INITIAL DAMAGE

111b INITIAL MATERIAL REMOVAL

111c S.E.M DAMAGE IN CENTRAL ZONE

111d GROSS DAMAGE AT TEST COMPLETION

112 DAMAGE PROGRESSION IN CUPRO-NICKEL

112a PLAIN SURFACE PRIOR TO TESTING

112b PLASTIC DEFORMATION

112c INCREASE PIT DENSITY

112d MATERIAL REMOVAL AFTER NECKING

112e S.E.M DAMAGE OF CENTRAL ZONE

112f GROSS DAMAGE AFTER TEST COMPLETION

113a INITIAL DAMAGE ON BRASS

113b S.E.M DAMAGE IN CENTRAL ZONE

114 DAMAGE PROGRESSION IN ARMCO IRON

114a INITIAL DAMAGE

114b EFFECT ON REFLECTIVITY OF SURFACE

114c INITIAL MATERIAL REMOVAL

114d S.E.M. DAMAGE OF CENTRAL ZONE

114e S.E.M. DAMAGE SHOWING DUCTILE TEARING

114f GROSS DAMAGE ON COMPLETION OF TEST

115a DUCTILE TEARING IN CARBON STEEL

115b INTERGRANULAR FRACTURE IN CARBON STEEL

115c S.E.M. DAMAGE OF AISI1020 SHOWING DIMPLES

116 DAMAGE PROGRESSION IN STAINLESS STEEL

116a SURFACE PRIOR TO TESTING

116b DIMINISH REFLECTIVITY

116c INITIAL PITTING

116d INITIAL MATERIAL REMOVAL

116e SURFACE TOPOGRAPHY

116f BIGGER CRATERS

116g INTERGRANULAR FRACTURE FROM S.E.M

116h DUCTILE TEARING FROM S.E.M

117 DAMAGE PROGRESSION FOR TOOL STEEL

117a INITIAL PITTING FROM S.E.M

117b INITIAL PITTING FROM OPTICAL MICROSCOPE

117c MICRO-CRACKS LINKING UP

117d DEFORMED SURFACE

117e CRATER FORMATION

117f CENTRAL ZONE DAMAGE FROM S.E.M

117g MACROSCOPIC VIEW OF GROSS DAMAGE

118 DAMAGE PROGRESSION SEQUENCE FOR NITRIDED STEEL

118a INITIAL PITTING FROM OPTICAL MICROSCOPE

118b INITIAL PITTING FROM S.E.M

118c MICRO-CRACKS INTERSECTION

118d PIN HOLE PIT

118e DEFORMED SURFACE

118f SPALLED SURFACE

118g CENTAL ZONE DAMAGE FROM S.E.M

118h MACROSCOPIC VIEW OF GROSS DAMAGE

ACKNOWLEDGMENTS

The work presented here was performed under the supervision of Dr. P.A. Lush to whom I am indebted for his valuable support, guidance and advice.

Special thanks to my sister, Margarritta Ewunkem for her relentless support.

D E D I C A T E D

TO

M U M AND D A D

DECLARATION

I grant powers of discretion to the University librarian to allow this thesis to be copied in whole or in part without further reference to me. This permission covers only single copies made for study purposes, subject to normal conditions of acknowledgement.

ABSTRACT

The work presented in this thesis is concerned with evaluating the erosion resistance or behaviour of various engineering materials to cavitation erosion in a through flow device. A wide range of engineering materials have been utilized, from metal alloys, plastics, ceramics to composites.

These were procured from various industrial and research establishments. The metal alloys which were supplied in various condition of heat treatments, ranged from aluminium alloy to nitrided and tool steels. The plastic employed were epoxy resins. These were supplied in two different formulations the "Novalac" and the "Bisphenol" systems. They were produced in as cast and machined conditions. Thus the influence of both the formulation and the production processes on their cavitation erosion behaviour have been analysed.

Silicon carbide and silicon nitride were the ceramic materials employed in this project. Both were produced under three surface finish conditions. These were fired or sintered, ground and lapped respectively. The performances of all three surface finishes have been elucidated and the cavitation erosion resistance of both silicon carbide and silicon nitride have been ascertained.

Glass reinforced plastic (GRP) and Fybroc were the composites utilized. They both employed glass fibre as the reinforcing element. Their cavitation erosion behaviour and resistance have been evaluated.

Detailed observation of damage progression in the above three classes of materials have been made. A comprehensive cavitation erosion test data base has been obtained. An appraisal on a comparative basis of the different erosion rates of the various material tested is presented.

NOMENCLATURE

A	THROAT AREA (m^2)
A_o	UPSTREAM/DOWNSTREAM WORKING SECTION AREA (m^2)
CLA	CENTRAL LINE AVERAGE (μm)
GRP	GLASS REINFORCED PLASTIC
Hv	VICKER'S HARDNESS
μHv	MICRO-HARDNESS
MDPR	MEAN DEPTH PENETRATION RATE (mm/hr)
ML	MASS LOSS (mg)
MLR	MASS LOSS RATE (mg\hr)
NIP	NOMINAL INCUBATION PERIOD (min)
n	CAVITATION INDEX
$\tilde{n}$	CYCLIC STRAIN HARDENING EXPONENT
P_o	UPSTREAM OR AMBIENT PRESSURE (Pa)
P_2	DOWN STREAM PRESSURE (Pa)
P_C	PRESSURE DIFFERENCE ACROSS CONTRACTION (Pa)
P_{op}	PRESSURE DIFFERENCE ACROSS ORIFICE PLATE (Pa)
P_v	VAPOUR PRESSURE (Pa)

Q	FLOW RATE (m^3/sec)
SEM	SCANNING ELECTRON MICROSCOPE
S_iC	SILICON CARBIDE
Si_3N_4	SILICON NITRIDE
T	TEMPERATURE (°C)
t	TIME (hrs)
U	FLOW VELOCITY AT THROAT (m/s)
U_o	UPSTREAM FLOW VELOCITY (m/s)
VL	VOLUME LOSS (mm^3)
VLR	VOLUME LOSS RATE (mm^3/hr)
σ	THROAT CAVITATION NUMBER
σ_o	UPSTREAM CAVITATION NUMBER
σ_{ob}	CHOKING UPSTREAM CAVITATION NUMBER
$\tilde{n}$	CYCLIC STRAIN-HARDENING EXPONENT
K_f	FATIGUE STRENGTH COEFFICIENT

1.0 INTRODUCTION

Erosion of a solid surface can take place in a liquid medium even without the presence of solid abrasive particles in the medium. Cavitation is one mechanism of erosion. Basically cavitation is defined as the repeated growth and collapse of bubbles or cavities in a liquid due to local flow induced pressure reduction. If the local pressure in a flowing liquid fall below its vapour pressure, because of sharp changes in geometry of the flow for example, cavities will be formed. These are transported downstream and when they reach a region of higher pressure, they collapse violently. The process by which material is removed from the surface is called cavitation erosion. And the resulting damage is termed cavitation damage.

Cavitation induced erosion can be a problem in many components. In the field of hydrodynamics, the effects of cavitation with very few exceptions, are undesirable. Uncontrolled cavitation can produce serious and even catastrophic results. It has been found that, all types of turbines, from a low specific speed Francis to the high specific speed Kaplan, are susceptible to cavitation to various degrees. Centrifugal and axial flow pumps are no exceptions. Cavitation also occurs in devices which do not require the input or output

of mechanical energy i.e the operation of valves and fittings of all kinds that produce a change in velocity of the liquid flowing through them. Cavitation continues to manifest itself in hydraulic structures such as spillway crest, gate and gateslots, bafflepeirs, conduit entrances, bends, tunnels and pipeline systems. In the naval field, it has been known that cavities formed around the propellers do limit thrust. It has also been found from observations on both surface and subsurface craft that, cavitation may also occur on rudders, struts and even on the hull itself.

The occurrence of cavitation in technological devices is evidenced in various ways and to various degrees depending upon intensity. Initially as the flow changes from a condition of no cavitation to one of some cavitation, the first occurrences are fine cavities (bubbles) which grow in streamwise favourable pressure gradients as they are carried along by the flowing liquid. These first cavitation bubbles are quite small, but are usually visible on careful observation. They are always evidenced by the characteristic cracking noise of their collapse. Hence, unless there is a considerable ambient noise, the first appearance of cavitation is best noted via acoustic listening devices. As the amount of cavitation increases, the noise level increases rapidly, and other features, generally of more importance to the mechanical engineer appear. These are modifications in the operating effectiveness of the fluid device, occurrences of vibration, and with time, progressive erosion of metal or other materials lying in the path of the collapsing bubbles.

Cavitation erosion occurs in the materials which are in the vicinity of the collapsing bubbles as they implode, that is, in the high pressure region of the system. In a flowing fluid, this would not be the location where the bubbles are created. Consequently the area of damage is often quite separate from the area in which cavities are generated, resulting in frequent incorrect diagnoses.

When the local pressure in a liquid is being reduced, a condition may eventually be reached where gas-filled bubbles (or cavities) nucleate and grow within the body of liquid. The gas in the bubbles may be vapour or molecules of a substance that was formerly dissolved in the liquid. If a bubble is formed by vaporisation, bubble growth will occur rapidly, but if gas dissolution is required for bubble formation, growth will occur more slowly. Growth of gas-filled bubbles (as opposed to vapor-filled bubbles) depends on the diffusion of dissolved gas to the cavity or on the rate of gas expansion due to pressure reduction. If cavities formed in a low-pressure region pass into a region of higher pressure, their growth will be reversed, and they will collapse and disappear as the vapor condenses or the gas is redissolved in the liquid. A vapor-filled cavity will implode, collapsing very rapidly (perhaps within a few milliseconds); a gas-filled cavity will collapse more slowly both being the exact or nearly exact reverse of the bubble-growth process. (the liquid dynamics of bubble growth and collapse are covered by Knapp et al (1970) & Hammitt (1980)).

There are two important effects arising from cavity collapse.

Firstly a broadband acoustic signal is generated. The second effect is that the nearby solid surfaces may be damaged. Material damage is initially apparent as small pits or cracks. Accumulation of these flaws will cause portion of the material to break off. As material is lost over a period of time, the eroded region will penetrate into the component which may lead to sudden failure long before the expected service life is expected. A given cavitating flow has a certain potential for generating erosion which may be termed cavitation intensity. The severity of material erosion may be termed the erosion rate or the erosion intensity and this will be a function of the cavitation intensity and the mechanical property of the material.

The collapse of cavities (bubbles) produces the damage in materials. The exact mechanism by which cavity collapse transmits severe localized forces to a surface is not fully understood. However, it most likely involves either waves produced by the collapse and immediate reformation of a cavity, a process known as rebound (fig.1), or impingement of a microjet of liquid through the collapsing cavity onto the surface being damaged due to nonsymmetrical cavity collapse (fig.2). Both rebound and nonsymmetrical collapse with formation of a microjet have been observed experimentally and partly computed analytically.

The source of the erosion damage has been known as early as 1917, when Rayleigh (1917) demonstrated theoretically that, the collapse of a bubble in a liquid due to an increase in pressure is accompanied by the emission into the surrounding liquid of a pressure pulse, which has the character of a shockwave, with

magnitude of order of 10kbar. However, the attenuation of the wave from a single bubble is so rapid that it can only damage a solid if it collapses no further than approximately its initial radius from the solid surface. Nevertheless when a cloud of bubbles collapse, it appears that the bubbles act in concert (i.e triggering each other's collapse Morch (1979)) and the combined shockwave can produce damage in a solid at a much greater distance. Moreover it has been shown both theoretically (Plesset & Chapman (1971)) and experimentally (Ellis & Naude 1961) that a bubble in close proximity to a solid surface does not collapse spherically, rather because of geometrical constraints, it becomes involuted and forms a jet of liquid which impacts the solid. Thus there are two sources of the mechanical component of cavitation erosion. The shockwave of the collapsing bubbles and the jet impact of those individual bubbles collapsing close to the surface. There are still conflicting opinions as to which of the above two mechanism is dominant during erosion.

Cavitation erosion as cited above can be a problem in many engineering components. Where it is possible to design components which do not cavitate, they may be unacceptably large and expensive. Additionally, a component which does not cavitate under design flow conditions may be subjected to cavitation attack if it operates away from the design point.

If an estimate is made of the amount of material which can be safely lost from a component, then knowledge of the material erosion rate will allow the safe operating life to be evaluated.

Estimating this amount will not be simple, as it will depend on other factors such the location of material loss and the stress on the component. However, the major difficulty in calculating operating life is that, as yet there is no means available for predicting cavitation erosion rates. Further difficulty in evaluating safe operating life arises from the fact that, the erosion rate is not constant. In the initial stages of attack, no mass is lost at all, termed the "Incubation Period". At the onset of mass loss, the mass loss rate is low, tending to increase after further exposure until a steady state value is reached. If the acceptable cumulative mass loss is large, then it may be permissible to ignore the incubation period and calculate the operating life by dividing the acceptable mass loss by the steady state mass loss rate. On the other hand, this will not be acceptable if the incubation period is a significant proportion of the safe operating life.

Many investigations during the past 40 years have attempted to obtain a correlation between erosion rate and some bulk mechanical property or a combination of properties of the material. The aim has been to permit the design engineer to select suitable materials for use in an erosive environment or to predict the lifetime of those materials already in service on the basis of properties which are readily available in handbooks. Unfortunately no simple correlation exists for wide or universal application, although various investigators have claimed success with different parameters for a limited range of materials.

Accelerated erosion testing has commonly been done using a vibratory testing apparatus, which has the great virtues of convenience and speed of operation. However such tests may produce anomalies because the cavitation is not hydrodynamically induced and because the cavitation intensity is much more severe than service conditions. An alternative to the vibratory test is the hydrodynamically induced cavitation produced in a venturi-type channel, usually placed in a recirculating flow loop. The cavitation intensity is increased to bring testing times down to acceptable levels by using a wedge-shape or cylindrical inducer and by employing a fairly high throat velocity. The rate of erosion measured in this way is unlikely to be equivalent to the erosion rate encountered in service and so comparative testing is necessary. There is a need for a consistent set of comparative test data encompassing a range of engineering materials, to assist in the choice of a suitable material in the early stages of a design.

In this purely experimental research program, various metals and non-metals have been evaluated for cavitation erosion resistance in a through flow system, i.e a venturi. The tested materials were produced under different manufacturing processes, hence rendering different surface morphology to be evaluated,

The plastic materials tested were produced in "ascast" and "machined" conditions. Two glass reinforced plastic (GRP) with an epoxy and vinylester matrices were tested. One had long unidirectional fibres, the other long and randomly dispersed fibre. The ceramics

tested were silicon nitride and silicon carbide. These had various surface finishes, from the as fired product to as ground and as lapped surfaces. A number of different metal alloys were also tested, ranging from aluminum alloys and brass, to nitrided and tool steel. The above materials were supplied by both industrial and research establishments, i.e. Dowty Fuel Systems, P.P.I Ltd., Worthington Simpsom, B.P Research, Polish Academic of Sciences and the Defence Research Agency.

The erosion resistance of the above materials were computed using the steady volume loss rate and norminal incubation periods for each samples. The effect of surface finish on erosion rate has been ascertained. The characteristics of erosion damage on the various materials tested have been classified. An appraisal on a comparative basis of the different erosion rates of the various materials tested under the same cavitation conditions is presented.

As mentioned earlier, in cavitation, the hydrodynamic conditions are so difficult to describe that no quantitative erosion prediction equation, based on independent measurable parameters exist. At the current state of knowledge better predictions can be made by purely empirical equations derived from compilations of test data. The process of accumulating data is only through experimental testing of real engineering materials. This testing process employing a venturi testing rig , though accelerated, is extremely time consuming and tedious. This is illustrated in the fact the Muosson (1937) has been the only one who has tested a comprehensive

range of engineering materials for the past sixty years. It is hoped that the results of this project will add and enhance the existing database on cavitation erosion.

FIG. 1 THE MECHANICS OF CAVITY GROWTH COLLAPSE, AND REBOUND

(a) Schematic representation of successive stages of growth, collapse and rebound of a travelling cavity. (b) Graph of cavity diameter as a function of time for the cavity in (a) (Knapp et al 1970)

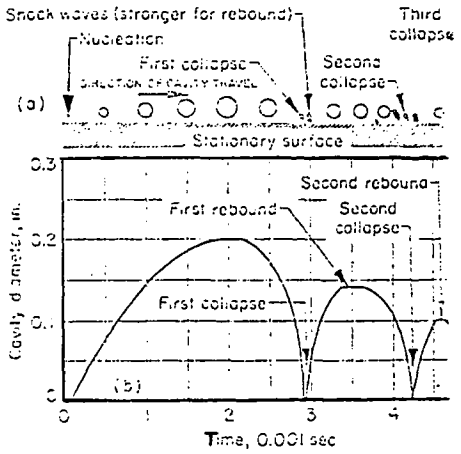

FIG. 2 SCHEMATIC REPRESENTATION OF SUCCESSIVE STAGES OF NONSYMMETRICAL CAVITY COLLAPSE WITH MICROJET IMPINGEMENT AGAINST A METALLIC SURFACE

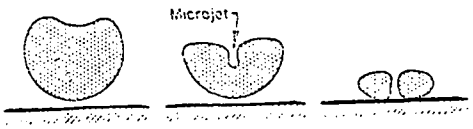

2.0 REVIEW OF HYDRODYNAMICALLY INDUCED CAVITATION

2.1 INTRODUCTION

Cavitation has been with us as a technological problem for some one hundred or more years since problems were encountered in applying the high shaft speed of turbines to ship propellers. It is generally recognised today that the flow phenomena called "cavitation" involving a general heterogeneous mixture of vapour and gas pockets or "voids", some of which can be approximately described as bubbles, frequently causes a rapid erosion of adjacent material structure. There is at present an enormous body of research literature concerned with the process of bubble collapse and cavitation damage, which has accrued at an increasing rate since the pioneering work of Rayleigh [1917] . However despite this one half century of research, there is still only a very incomplete understanding of the mechanisms by which a "cavitation field" causes rapid damage to adjacent solid materials.

It is the purpose of this chapter to summarise briefly the significant results of the very considerable research which has been concentrated on hydrodynamically induced cavitation over

the years, both from the view point of basic understanding of the phenomenon and of practical information of use to the designer of fluid machinery.

This review is particularly concerned with observations and experimental results obtained from hydrodynamically induced cavitation i.e. employing venturi and rotating disc devices. The above mentioned devices are briefly described, stating both their advantages and disadvantages. Some commonly agreed basic principles relating to cavitation damage are discussed, together with the time dependence of erosion rate. The influence of test parameters, flow characteristics and cavity dynamics in relation to cavitation damage are stated. Works investigating correlation of erosion rates with mechanical properties are also reviewed.

2.2 COMMONLY AGREED BASIC PRINCIPLE RELATED TO DAMAGE

Before discussing the issues mentioned in the introduction, it will be appropriate to review the various well-known undisputable experimental facts upon which consideration must be based. These are primarily as follows;

(i) Rapid pitting and erosion often occur in flows where cavitation is observed to exist. Its existence can be determined audibly by acoustic instrumentation, visually if the containment systemm is transparent, by means of machine vibrations, or through decrease or other change in performance from the single-phase flow condition. As for example a measurable decrease in head produced from a centrifugal pump for a given flow and rotating speed.

(ii) Cavitation pitting shows the characteristics of mechanical attack. Such well-known mechanical manifestations as slip lines in metals, have frequently being observed. The early damages which are formed in the early portion of the attack appear under a low power microscope as "moon craters" i.e. more or less symmetrical craters often with a raised rim.

(iii) Cavitation can, under certain conditions, damage even

the strongest materials such as stellites, tool steel, and any other structural materials. This damage can occur rapidly even in cases where chemical corrosion in single-phase flow with the same liquid-material combination would not be significant.

Certain obvious conclusions can be drawn from the general observations noted above. (a) Since observed cavitation fields usually contain large numbers of essentially spherical bubbles of various diameters and since as Rayleigh (1917) showed that the collapse of such bubbles could create pressures and velocities large enough to be damaging, it is likely that the surface of a material exposed to cavitation will experience a multiplicity of impulse impositions of widely varying intensities and with local random spatial distribution. The Rayleigh theory generally shows that the time of imposition of such impulses due to individual bubble collapses is extremely short. Furthermore the impulse magnitude and collapse times are greater for larger bubbles for a given collapsing pressure differential. Since individual symmetrical craters are observed, it is apparent that some of these impulses are sufficient to cause permanent material deformations. Since the spectrum of the impulses varies widely, it is also expected that individual craters with diameter covering a given range will be formed as has been observed (Hammitt (1963,1965)) and that many "blows" may be of insufficient

strength to cause permanent deformation. A large number of these weaker blows, however may be sufficient to contribute also to eventual fatigue failure. Thus it is to be expected that cavitation damage will eventually take the form of fatigue failures and this is in fact observed. (b) As the surface roughness increases due to accumulated cavitation damage, the flow pattern near the surface will frequently be importantly altered. In addition the substantial cold-working of the material surface may affect its ability to resist further damage. Increased strength and hardness will tend to increase its damage resistance, while increased brittleness will have the opposite effect. Thus it is to be expected that the rate of cavitation in a given situation will not be constant with time. Often an "incubation period" is observed before substantial material loss occurs, presumably while fatiguing processes proceed to a point necessary to cause failure. The damage rate then often increases to a maximum after which it decreases. This behaviour probably depends primarily upon the interplay of flow pattern alteration by virtue of accumulated roughness and material surface property changes, which are themselves due to the accumulated permanent deformations and stressings.

2.3 TESTING TECHNIQUE

There are many techniques for producing cavitation in the laboratory and many of these are described in detail by Hobbs(1962) and Holl and Wood(1964). Here only the rotating disc, the venturi and the vibratory device will be discussed.

2.3.1 ROTATING DISC :

One of the earliest devices employed for producing cavitation in the laboratory consist of a wheel attached to which are two or more samples symmetrically placed near its rim. The wheel which is submerged in water in a containment tank, is rotated via a spindle or shaft connected to a motor at very high velocity. Clouds of cavities are nucleated in the region of low pressure near the leading edge of the samples or at cavitation exciters. Exciters are normally of two kinds, protuberances or holes in the wheel. It is observed that more intense cavitation is produced with the protuberances than with holes as inducer.

In devices of this nature the liquid inlet and discharge ports to the disc enclosure are connected to external loops incorporating a heat exchanger, expansion tank, deaerating circuit and

auxilliary pumps and valves. The rig is instrumented for measurement and control of temperature, flow-rate, and pressure.

There are normally two configurations for wheel mounting. It could either be mounted horizontally or vertically. Fig(3a) shows a cross-section of a vertically mounted disc. with appropriate sealings as used by Hammitt(1967). It uses holes in the disc as exciters. Both sides of the disc are enclosed by walls of the containment tank each of which incorporate 24 stagnator vanes. These minimise half body rotation of the test liquid and generate the desired cavitation at the inducer holes. Fig(3b) shows the configuration and location of specimen on the wheel. Rao(1970) on the other hand employed or utilised the horizontal disc configuration. He uses protruding cavitation bodies as inducers. His rig is shown in fig(4a) in cross-section and fig(4b) shows the location of specimen. The advantages and disadvantages of the rotating disc method are as follows;

(a) ADVANTAGES;

(i) It provides a good simulation of in-service flow condition particularly for hydrofoil and properlers

(ii) Velocity of disc can readily be varied controlled.

(iii) Intensity of erosion can readily be varied by changing the size or geometry of the cavitation exciters.

(b) Disadvantages;

(i) Local pressure in the vicinity of samples cannot be readily varied or determined.

(ii) A fairly large volume of fluid is required.

(iii) It is difficult to prevent contamination and corrosion because the different materials, their relative motion, and the size of the system prohibit complete isolation of the construction materials from the sample.

2.3.2 VENTURI:

There are quite a number of designs of venturi for erosion studies. They generally consist of a high and low pressure vessel, a cooling system employing a heat exchanger for temperature regulation, a pump for liquid circulation, by-passes and valves for flow control and the necessary instrumentations. The basic principle involves the flowing fluid being allowed to flow through a constricted path in which the velocity is increased and the corresponding drop in pressure causes cavities to be nucleated.

Variations in venturi designs are centred around the working section, method of accomodating the specimen, and the position and type of inducer. In the first system fig.5a, the constriction is provided by stainless steel sample holder containing a hole at the upstream end where bubbles are nucleated, and the test specimen at the

downstream end where bubbles collapse (Hanson and Morch,1977). The upper figure shows a schematic plan view, and the lower figure shows a photograph of the side view. The cavity cloud **C** is generated at the exciter, the upstream hole at **B**, and travels downstream to collapse at the specimen **A**. In the system illustrated in fig(5b,c), the decrease in pressure is created by a reduced cross-section and the specimens are inserted into the wall of the tube as shown. Typical example of the latter is that used at the university of Michigan Fig(6) . Here the specimens are flush mounted on the side wall of the working section. The earlier design as used by Mousson (1937) is shown in (fig7), where cavitation is produced by means of a double weir arrangement. M.I.T and many other workers used a two-dimensional symmetric diffuser with plane parallel walls, where the test specimen could be mounted on or be an integral part of the wall. Fig(8) shows a test section as used by Rao(1970) on which different sizes and shapes of cavitating bodies could be inserted to constrict the flow round it, and the inducer itself could be the testing specimen. The side wall is made of transparent plastic for visual observation. Inducers would normally be of a cylindrical shape as used for example in Admiralty Research Establishment, Holton Heath or of a triagular prism as employed at City University and at Southampton University. The advantages and disadvantages of the venturi method are as follows;

(a) **ADVANTAGES;**

(i) They provide a good simulation of in-service flow cavitation.

(ii) The velocity and pressure of the liquid can be varied readily and independently.

(iii) The intensity of cavitation can be varied by throat design and by varying the position and orientation of the specimen with respect the to flow.

(iv) The size, number and distribution of bubbles can be determined more easily than in other devices

(b) **DISADVANTAGES;**

(i) A large volume of liquid is required and must be maintained at constant pressure.

(ii) Intensity of erosion is low, hence experiments take a considerable longer period.

(iii) The system can be expensive to construct and requires a large amount of laboratory space.

2.3.3 VIBRATORY DEVICE:

The most common and simplest device used for producing cavitation in the laboratory is the vibratory device. This is illustrated in figure 9. It consists of a magnetostrictive or

piezoelectric tranducer which vibrates in the kilohertz frquency range. Attached to the transducer is a stepped, exponential, or catanoidal metal horn which act to amplify the amplitude of the vibrations to approximately 20-100 m at the horn tip. When the lower portion of the horn is immersed in the operating fluid, a low pressure region is created immediately below it during its upward stroke and results in the nucleation and growth of a cloud of bubbles. During its downward stroke, the pressure is increased and the bubbles collapse.

The test specimen may be attached to the bottom of the horn itself or be held stationary below the horn. The former system is the basis of an ASTM standard (G32-72). Hobbs(1967) has shown that good reproducibility can be obtained with this device using a stationary sample, and that it can easily be modified for control of temperature and pressure. The advantages and disadvantages of the vibratory device are as follows:,

(a) ADVANTAGES;

(i) It provides a good simulation of vibratory cavitation.

(ii) It is simple and relatively inexpensive and requires little laboratory space.

(iii) Small volume of liquid is required.

(iv) Its high intensity of cavitation reduces testing time.

(v) The temperature and pressure of the

cavitating fluid can be readily controlled.

(vi) All metallic parts of the system, except the horn tip, can be readily isolated from the sample to minimise corrosion and contamination effects.

(b) DISADVANTAGES;

(i) The frequency cannot usually be varied over a significant range .

(ii) The size, number and distribution of bubbles cannot be readily determined.

(iii) The corrosion component of the damage cannot be studied as easily as in flow system because the high intensity of cavitation emphasises the mechanical component of erosion, and reduces the time available for corrosion.

2.4 TIME DEPENDENCE OF EROSION RATES

The most general procedure in the study of erosion is to compare the extent of erosion of different materials after the same period of exposure to cavitation. This procedure has a major flaw in that the rate of erosion is not constant with time. Hence the materials are compared at different phases of their erosion-time relationships, and their relative resistances to cavitation may vary with the period of exposure chosen for the test.

Extensive research has been done on this practice resulting to several forms of erosion rate versus time curve. Some of these curves are illustrated schematically in fig.10 below. According to Thiruvengadam and Prieser(1964) the curves consist of four zones (fig. 10a): (i) the "incubation zone" in which there is no detectable weight loss, (ii) the "accumulation zone" in which the erosion rate increases to a maximum level, (iii) the "attenuation zone" in which the rate of material loss decreases, (iv) the final "steady state zone". Eisenberg et al(1965) also agreed to the above form and stages. These investigators attributed the first three zones to the condition of the specimen surface and considered zone(iv) to be the rate which is characteristics of the material itself and recommend that this rate be used for comparison and correlation purposes.

Other investigators including Hobbs(1967) and Plasset and

Devine(1966) dispute both the form of the rate-time relationship and the significance of zone(iv). Fig10b is the curve they observed and it is also divided into four sections. (i) "incubation period", where no detectable weight loss is observed but the occurrence of plastic deformation or cracking, (ii) transition period, here erosion begins locally and the observed rate increases as it expands over the whole test area, (iii) constant rate period, and (iv) decreasing rate period, pits formed during zone (iii) deepen and cavitation colapse is attenuated by trapped air or water. Plesset and Devine have shown photographically that there is a reduction in the bubble cloud intensity "as a consequence of the hydrodynamic effects over the deeply damaged surface" and resulting in the decreasing rate period of fig.10b. Hobbs and Plesset and their co-workers, therefore base their correlations on the maximum (steady state) rate of erosion. Other investigators found that the type of erosion rate plot obtained was very dependent on the specimen's shape. Tichler et al(1970) was a proponent of this. He and his co-workers found that, flat samples resulted in plots similar to fig.10a, whereas those with raised rim gave peaked plots similar to fig.10b. However, Plesset and Devine(1966) also studied both flat and rimmed samples but could not detect any significant differences in the shape of the erosion plots. These then raised the possibilty that, the specific material under investigation determines the relative length and proportion of each zone. This facet of the problem was also

addressed by Tichler et al(1970) who identified two "steady state" periods of erosion (fig.10c). During the first, the erosion rate is high and the surface is rather uniformly attacked. In the second final, "steady state" region, the surface is saturated with deep isolated craters, and the erosion rate is relatively low. These authors illustrated the dependence of these two "steady state" regions on the metallurgical structure by showing the first "steady state" rate of tempered martensitic chromium steel to be considerably lower than that of an austenitic/ferritic steel, whereas the total volume loss of the former was higher than that of the latter after the same period in the second "steady state" period. This apparent discrepancy was attributed to the observation that the martensitic steel forms fewer and shallower craters than the soft austenitic/ferritic samples.

Experimental conditions such as temperature and material were observed to influence the shape of the plot according to Matsumura(1972). He observed a fourth type of curve showing two peaks as shown in fig.10d, for brass, tool steel, stainless steel, and mild steel but he found a single peaked curve similar to that shown in fig.10a to be typical of iron and aluminium.

Heymann(1967) concisely gave a simpler explanation to the erosion rate plots. He pointed out that the empirical data of cumulative weight or volume loss as a Function of time of exposure must be differentiated to provide an erosion rate versus time plot and this procedure will magnify all the scatter and

uncertainty of these data. In many cases, whether the resulting curve will be like that of fig.10a or 10b will depend very much on the investigator's opinion of what such a curve should look like. Heyman(1967) developed a statistical model in which he assumed erosion was caused by a fatigue-like process. From this model, he predicted rate versus time curve similar to those observed in fig.10. He then made the following inferences: (i) that the shape of the curve depends in part on the characteristic of the test, e.g on the distribution of bubble size and (ii) that, in the absence of other influences, the plot would tend toward a steady state value as postulated by Thiruvengadam and his co-workers, but the damage to the surface introduces geometric effect such as those described by Hobbs and Plesset and co-workers.

Rao and Young (1983) have investigated the method of curve fitting of erosion data. They found that normalised cumulative average erosion rate as a function of normalised time greatly reduces the individual variations of the instantaneous erosion rate versus time curves. Using this approach they analysed previous data and showed that the normalised cumulative erosion rate versus normalised time have significant advantage for erosion prediction with reduced data scatter.

2.5 INFLUENCE OF TEST PARAMETERS

2.5.1 EFFECT OF VELOCITY

In flow devices such as a rotating disc and a venturi using separate flow past a pin such as that pioneered by Shalnev(1955), or flow over an ogive as used by Knapp(1955), it has been observed that damage rates are proportional to a relatively high power of velocity. Keeping all other parameters constant, Knapp(1955) counted the number of pits per unit area per unit time produced on soft aluminium for various velocities. He plotted this measure of intensity against velocity and found that, the intensity varied with approximately the sixth power of velocity . His result was latter confirmed by Lichtman et al (1958), and Lichtman and Weingram(1964). Kerr and Rosenberg(1958) also found a power law , but their exponent varied from 5 to 7 . However Shalnev(1955) conducted experiment in a two-dimensional channel with a circular cylinder and reported that, the intensity of damage varied linearly with velocity. He defined his intensity as the average depth of erosion per unit time. Rasmussen(1955) using a rotating disc device also reported a linear relationship between intensity and velocity changes.,-

Hammitt and his co-workers (Hammitt et al 1965) observed a smaller dependence between erosion rate and velocity in a venturi test with mercury as the working fluid. They observed a maximun rate of erosion followed by a decrease as the velocity was increased further (Fig 11). Thiruvengadam (1971) also found a similar relation as Hammitt in a rotating disc. His experiment though was performed at constant free stream pressure P_o rather than constant cavitation number. Moreover, whereas Knapp studied pitting during the incubation period, other investigators have used data obtained at latter stages of erosion, and both Thiruvengadam(1971) and Wood et al(1967) have shown that the exponent "n" is not a constant, but is a function of the degree of erosion damage. Rao (1970,1980) found that copper, brass, mild steel, stainless steel and epoxy resin did not show the characteristic peak in erosion as velocity increases. He did however observe peaks with aluminium and plexiglass. Hutton and Selim (1983) experimenting with different cavitation source shapes found that the velocity exponent varies with different shape configuration, ranging from 2.95 to 7.13. This is contrary to the assumption that a single power law of cavitation erosion is applicable over a wide range of configurations. They attributed these differences to the fact that, each cavitation source shape produced different flow regimes(Fig12).

There seems to be an apparent discrepancy from the review above concerning the velocity exponent, and the relationship

between velocity and erosion rate. One set of investigators given a power law and the others reporting a linear law. It seems all the various factors as mentioned above would probably be responsible for these discrepancies.

2.5.2 EFFECT OF PRESSURE

The influence of pressure on the degree of erosion has been investigated for flow cavitation by Mousson(1937), Hammitt(1963) among many others. Results show that if the velocity is held constant and the pressure varied, cavitation damage increases through a maximum and decrease to zero at the pressure corresponding to cavitation inception, as illustrated in fig.13. Rao(1970) investigating with a rotating disc obtained the result shown in fig.14. Here the volume eroded seem to drop without any apparent peak with increase in pressure. However it is generally observed that, if the pressure were raised sufficiently, the cavitation would, in fact cease entirely. From this survey it is apparent that not a lot of research has been done on the effect of pressure. Though it looks obvious that the pressure of the flowing system must play an important part since it controls the energy of the collapse of the bubbles, and the relative length of the cavity. Another factor might be the fact that, variation in

velocity and pressure should not be considered independently because the intensity of cavitation, as represented by the cavitation number σ is a function of both parameters, where

$$\sigma = \frac{P_o - P_v}{1/2 \rho V^2} \qquad (1)$$

2.5.3 EFFECT OF GAS CONTENT

Two opposing effects appear to come in to play when this quantity is considered. If the total gas content is increased, it is likely that entrained gas, generally thought to be most important (as compared to dissolved gas) for bubble nucleation, will also increase. In this case, there should be more cavitation bubbles produced for the same pressure, temperature and velocity. Thus damage should increase. On the other hand, if the cavitation bubbles actually contained a higher quantity of noncondensible gas, the bubble collapses are restrained and reversed at a larger radius than otherwise, so that the resultant pressure waves in the liquid are reduced in amplitude. The analogous effect on the micro jet collapse mechanism is less clear. Still, for either mechanism damage would be reduced. The interplay of these opposing trends is uncertain in the general

case, but experience and some experimental work (Hutton 1992) appears to indicate that, large quantity of injected gas indeed substantially reduces cavitation damage.

2.5.4 EFFECT OF CAVITATION NUMBER (σ)

The effect of cavitation number as defined by equation 1 is similar to that of gas content in that, much the same opposing trends are evident. If cavitation number is increased for a given flow situation (i.e by raising the pressure and maintaining constant velocity) the number and mean diameter of bubbles will be decreased, but their collapsing pressure differential will increased. Thus collapse violence will be increased although the number of bubbles will be reduced. Hence, it is conceivable that a slight rise in the cavitation number, if accomplished by raising pressure at constant velocity, could cause an increase in the damage. And this has in fact been reported.(Young et al). It is of course clear that a sufficiently large pressure increase will cause a reduction in damage since cavitation will cease entirely if pressure is raised sufficiently.

If cavitation number is increased in a given situation by reducing velocity and maintaining constant pressure, the general evidence related to a velocity effect, already discussed, indicates that the damage will probably be decreased.

2.6 FLOW CAVITATION AND CAVITY DYNAMICS

Cavitation as mentioned in previous chapters ., occurs in flowing liquids when the pressure locally drops below the vapour pressure. Pressure minima develop at curved solid boundaries and when strong vorticity is present in the interior of the liquid.

In the flow over submerged bodies or through curved or converging-diverging ducts, streamline curvature is established by pressure gradients normal to the local flow direction. When the centre of curvature is towards the solid boundary, the minimun pressure will be at the wall, the pressure here decreasing with increasing curvature at constant free stream velocity and pressure. At sufficiently large curvature, the pressure drop results in liquid tension and cavitation inception occurs. This prevent further increase of the deflecting force on the liquid, and at large wall curvature, therefore, the liquid flow breaks off from the wall and a vapour filled cavity, fixed at the position of minimum pressure, is formed between the wall and the liquid. Generally, the liquid reattaches further downstream, but in some cases of submerged bodies, the cavity may contain the whole after-body, and its downstream termination point is in the liquid. Here the cavity is termed a supercavity. At the position were the cavity is initiated, a large number of travelling cavitation bubbles is

continuously produced. They grow explosively to their maximun size at the upstream end of the fixed cavity, and then are converted within a thin liquid layer along the fixed cavity interface toward its downstream end. These travelling cavities are important for the cavitation erosion observed in connection with fixed cavities as discussed below.

2.6.1 CAVITY MECHANICS

It is generally agreed that cavities in liquid flow are responsible for erosion. Hence a number of investigators have studied the mechanism of cavity growth, collapse and their resultant effect. Investigations of reattaching fixed cavities were performed by Knapp (1955,1956,1957) who found they may be steady or unsteady (cyclic) according to the attachment conditions at their downstream termination. Knapp(1955) using two-dimensional bluff bodies observed a cyclic behaviour of cavity growth, filling, and break-off. Briefly the mechanism he observed was as follows; A jet is formed at the trailing edge of the cavity and is directed upstream within the cavity. When the jet penetrates to the point of flow separation, or throat, the cavitation is momentarily interupted and the whole cavity is detached and convected downstream where it ultimately collapses and disappears. In the meantime, cavitation has started at the throat and the cavity grows until another "re-entrant" jet is formed and the whole process is repeated. Using other cavitation source

configurations, i.e con-div wedge, Furness(1974) and Lush and Skipp(1986) observed a similar process to Knapp's, but with one disimilarity. The main difference was that the cavity breaks off at some point downstream of the throat (termed partial break-off by Knapp) and only rarely did it break off cleanly at the throat. They claimed the re-entrant jet had insufficient energy to penetrate right to the throat. Lush's idealized cavity break-off and collapse sequence for a convergent-divergent wedge inducer is shown in fig.15. Fig.16 from the same author shows a typical cavity break-off and collapse sequence for a symmetrical inducer at $\sigma = 0.2$.

Hutton and Selim(1983) have done extensive work with various cavitation source shapes in order to classify cavity mechanics. They found that, there were differences in the damage pattern and the magnitude of damage at similar flow conditions produced by various configurations. They classified cavity mechanics into three types;

i) Cyclic Fixed Cavity Attached To A Rigid Body;

In this cavitation type, the flow detaches from the rigid boundary of the cavitation source to form pocket or cavity attached to the solid boundary and exhibits a cyclic nature (growth, filling and break-off). The pressure caused by the re-entrant flow striking the upstream end of the cavity, detaches the cavity from the body, after which it is swept on downstream by the surrounding flow,

and then start to collapse after it reaches the region in which the external pressure exceeds the pressure inside the bubble. The convergent-divergent wedge's cavitation sources are representative of this type.

ii) Travelling Cavitation Along A Solid Body;

This type of cavitation zone contains a great number of vapour bubbles of different sizes. These bubbles exist in the wake formed at the low-pressure points along the surface of the model and grow in the wake behind the model in the low-pressure zone with particularly well defined contours in the water. When the re-entrant jet collides with both the surface of the model and the upstream end of the cavity, it produces a high impact pressure, thus collapsing the bubble before any movement after the break-off of the cavity. The circular cylinder sources are the most representative of this type.

iii) Vortex Cavitation;

In this type of cavitation, the cavities occur in the cores of the vortices which form in the high shear zone behind the model. Bubble growth occurred somewhat far from the corners of the model. The cavitation bubbles while growing in size rolled up into two high shear layers regions downstream to formed a trailing cavity with well defined contour. For high cavitation numbers, the bubbles occur in dead-water zone behind the model. The

complete collapse of the bubbles occured when the re-entrant jet in the votex region surrounding them is striking the upstream end of the cavity generating high pressure after break-off of the cavity. The remaining smaller bubbles collapse as a cluster, and are shed downstream into a discrete wake. The 60 degrees symmetrical wedge cavitation sources are the most representative of votex cavitation.

2.6.2 EFFECT ON EROSION

In experiment with cavitation erosion of aluminium, Knapp(1955) found that the pitting rate had a peaked maximum close to the mean position of the downstream end of the fixed cavity. And he concluded that, erosion was caused by the collapse of travelling cavities in the stagnation zone. Fig.17 and fig18 shows Knapp's result.

Table 1 shows the result obtained by Hutton and Selim (1983). It demonstrates the relative intensity of cavitation erosion offered by the various cavitation source shapes operating at the same throat velocity and cavitation number. A comparison of the weight loss rates measured on the side wall specimen at σ = 0.035 reveals that, the weight loss rate produced by the 60 degrees symmetrical wedge is the most dangerous for side wall erosion. It generates approximately 21 times the weight loss rate produced by the circular cylinder and about 190 times that produced by the con-div wedge.

The differences in the magnitudes of the weight loss rate for the various configurations according to the authors should be attributed to the variation of many factors, such as the total number of collapsing bubbles, the sizes of the collapsing bubbles and the re-entrant jet. It seems obvious that the impact pressure generated by the re-entrant jet is the main contributor to the differences in the weight loss rates, because as the thickness of the re-entrant jet increases, the impact pressure collapsing the bubbles should increase, resulting in a higher damage, since the collapsing energy is proportional to the pressure difference between the outside and the inside of the bubble at the beginning of collapse.

2.7 CORRELATION WITH MECHANICAL PROPERTY

Cavitation damage rates are of course very strongly affected by material properties, but no general applicable relations appear to exist. Since the earliest days of cavitation damage investigations, it has been the practice to use hardness as a simple indicator of probable cavitation resistance for a material. It appears to be generally applicable within groups of material of the same general type. It is further recommended by the fact that it is extremely easy to measure.

The most extensive work for mechanical property correlation was by Mousson(1937), who measured the erosion resistance of 266 different alloys and considered the results relative to their yield and tensile strength, ductility, and hardness. He concluded that there is some consistent trend of increased erosion resistance with increase hardness. however he recognised that, grain size, strain hardening capability, surface treatment, impurity level, and alloy segregation all play a role in determining the resistance and may in fact, overshadow the influence of the original hardness. Laird and Hobbs (1971) and Lichtman and Weingram (1964) have also suggested hardness as the most suitable correlation - factor.

Thiruvengadam(1963) and Thiruvengadam and Waring (1964) considered the ability of the material to absorb the impact

energy of cavitation to be the determining factor and used the strain energy to fracture, as defined by the area under a stress-strain curve, as a correlation parameter. Experimentally they found a good correlation for a variety of materials. Their idea was expanded on by Backstrom(1967) to an elastic-plastic strain energy criterion and using Thiruvengadam's data, obtained an even better correlation. However, other investigators including Hammitt et al (1965)could not find any correlation between strain energy, yield stress, fracture stress or hardness, with erosion resistance. Rao et al (1970) attempted correlations among various parametres and the erosion resistance of seven alloys tested in a venturi, and rotating disc devices. He obtained the following percentage standard deviations of the experimental data shown in Table 2 from the equation

$$M\ v/t = \text{const.} \qquad (2)$$

where v/t is volume loss per unit time and M is a single mechanical property or group of them.

Hammitt(1967) using a comprehensive set of data generated both in a venturi and a rotating disc, found "Utimate Resilience" as the single mechanical property with best overall correlation. (Ultimate resilience =(Tensile strength) /(Elastic Modulus)). This term represents the energy per unit volume necessary to cause failure

if the failure were of a brittle type, so that ductility did not play an effective role. The relationship he found with the above mechanical property was as follows;

$$1/MDPR = C_1 UR \qquad (3)$$

where C_1 is a constant, MDRP is the mean depth of penetration rate and UR is the ultimate resiliance.

Most recently Richman and McNaugthon (1990) analysing cavitation data from two separate data bases, found that the key in understanding cavitation erosion is in the microscopic properties of the materials, i.e emphasis should be shifted to the micro structural characterization of damage. Their concept is based on the fact that material removal in cavitation erosion, in common with liquid droplet erosion and with solid particle erosion, is not a consequence of single impulses or impacts. They claimed damage accumulates for thousands of impacts before a particle is dislodged. This fatigue type process has been reported by other investigators. Thus, using cyclic deformation parameters, they obtained good correlation with material removal rates. Fatigue strength coefficient was the cyclic parameter that accounts for most of the differences among materials. The above parameter when plotted against mean depth of penetration yielded a correlation coefficient of -0.95. When cyclic strain-hardening exponent,

ñ is incorporated in a combined parameter with fatigue strength coefficient a further increase in correlation coefficient is obtained. i.e -0.989. In other words, 98% of the variability in maximum erosion rate is explained by the equation shown below which they obtained,

$$\text{Log(max. recession rate)} = 4.636\text{-}1.494\ (\text{Log}(K_f\ \tilde{n}\ )) \qquad (4)$$

where K_f is fatigue strength coefficeint and ñ is the cyclic strain-hardening exponent. Fig.19 shows the plot of the above results.

2.8 CONCLUSION

From the foregoing which relates primarily to the understanding of the phenomenon of cavitation damage, it is obvious that a considerable amount of research work has been done. However, it is also apparent that, many contradictions still exist. Thus, many years of additional research may well be required to delineate fully the presently rather sketchy picture of the cavitation damage mechanism. Such basic studies could well consider the following areas in which more precise information is required;

(a) Detailed bubble collapse behaviour; powerful tools are becoming increasingly available today which are useful in this respect, such as ultra-high-speed motion cameras and other sophisticated optical techniques. Since the critical path of a bubble collapse occurs in a few microsecond and involves an object only a few millimetres in diameter, it is clear that extremely sophisticated photographic equipment is required. Holographic photography with a nanosecond laser light pulse, could be another possible method.

(b) The effect of fluid properties, flow field parameters, and wall behaviour on bubble kinetics; It would be very desirable to know the effects of pressure and velocity gradients, boundary layer parameters, etc. on the very complex chain of events

apparently necessary to produce a damaging bubble collapse. If more detailed information of this type could be achieved, it might become possible to modify the design of fluid handling machines in such a way that cavitation damage would be largely avoided. It might also eventually become possible to measure the size and number distribution of the gas nuclei upstream of a cavitating region, and knowing the flow pattern approaching the region, predict the cavitation bubble distribution within the region. If the damage mechanism were understood to the extent necessary to predict the required size, location, and orientation of damaging bubbles, it would then be possible to predict the rate of damage to be incurred from a given flow situation. From here it might only require a small additional step to modify the flow path design in such a way that damage would be grossly reduced.

TABLE 1 SUMMARY OF EXPERIMENTAL RESULTS (HUTTON & SELIM)

CONFIGURATIONS	60° SYMMETRIC WEDGE					CIRCULAR CYLINDER						CON. - DIV. WEDGE					
EROSION PLACE	SIDEWALL																
EROSION TESTS AT CONSTANT VELOCITY OF 37 m/sec	S	P+	P_{o} AAA	$^{o}Q_{o}$ AA	WLR*	S	P	Po	$^{o}Q_{o}$	WLR	WLR	S	P	Po	$^{o}Q_{o}$	WLR	WLR
	.013	.131	5.75	12.5	133.28	.01	0.116	5.55	13.43	5.1	17	.01	.111	5.61	13.13	1.45	-
	.025	.221	5.84	12.5	250	.017	.016	5.6	13.43	10.2	37.3	.018	.171	5.67	13.13	1.84	-
	.035	.29	5.91	12.5	472.1	.025	.224	5.66	13.43	21	64.34	.025	.224	5.72	13.13	3.95	0.48
	.05	.393	6.02	12.5	618.6	.03	.255	5.69	13.43	28.6	55.2	.031	.263	5.76	13.13	2.953	0.59
	.065	.492	6.12	12.5	463.7	.035	.29	5.73	13.43	22.62	43.94	.035	.293	5.79	13.13	2.466	0.665
	.098	.724	6.35	12.5	347.3	.06	.458	5.9	13.43	12.05	37.56	.05	.385	5.88	13.13	1.236	0.27
	.13	.943	6.57	12.5	129.3	.098	.713	6.15	13.43	8.08	26.3	.075	.561	6.06	13.13	.669	-
	-	-	-	-	-	.15	1.08	6.52	13.43	14.15	16.48	-	-	-	-	-	-
EROSION TESTS AT CONSTANT CAVITATION NUMBER OF 0.035	U	P	P_{o}	$^{o}Q_{o}$	WLR	U	P	P_{o}	$^{o}Q_{o}$	WLR	WLR	U	P	P_{o}	^{o}Q	WLR	WLR
	40	.328	5.95	13.52	716.46	40	.33	6.68	14.52	41.4	74.56	40	.333	6.76	14.2	3.911	.79
	37	.29	5.91	12.5	472.11	37	.29	5.73	13.43	22.62	43.95	37	.293	5.79	13.13	2.466	.665
	34	.245	5.87	11.49	297.28	34	.256	4.85	12.34	9.8	24.88	34	.25	4.89	12.07	1.781	.465
	31	-	-	-	-	31	-	-	-	-	-	31	.21	4.07	11	1.411	.31
	28	.187	5.81	9.47	110.88	28	.18	3.29	10.16	4.3	12.25	28	.187	3.34	9.34	1.11	.27
	24	.151	5.77	8.11	34.12	24	.154	2.44	8.71	.875	5.66	24	.143	2.46	8.52	.75	-
σ_{ob}	4.6					3.86						4.08					
σ_{oi}	8.608					6						8.06					
σ_{cr}	0.045					0.045						0.024					
$\sigma / \lambda \alpha^{o}$	-0.785					-0.574						-0.932					

* WLR: Weight Loss Rate, mg/hr

+ P: Pressure at the throat, bar (absolute)

AAA ^{o}Q : Flow Rate, litre/sec

AAA P_{o}: Upstream pressure, bar (absolute)

TABLE 2

PERCENTAGE STANDARD DEVIATION OF EXPERIMENTAL CAVITATION EROSION DATA FROM THE RELATIONSHIP MV/T =CONSTANT

Mechanical property M	Percent standard deviation
Ultimate resilience × Brinell hardness	32
Strain energy × Brinell hardness	49
Ultimate resilience	204
Strain energy	242
UTS	559
Brinell hardness	622
Yield stress	771
% reduction in area	1131
% strain to fracture	2240

[a] From Rao *et al.* (1970).

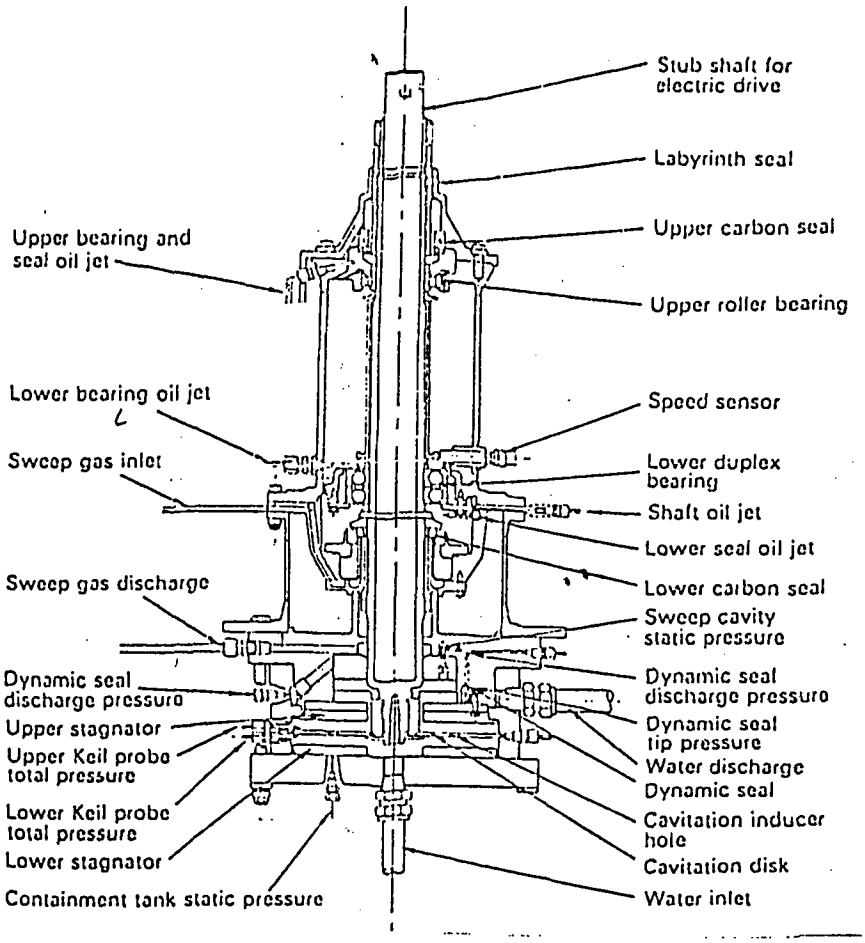

Fig.3a Cross section of a vertically mounted disc

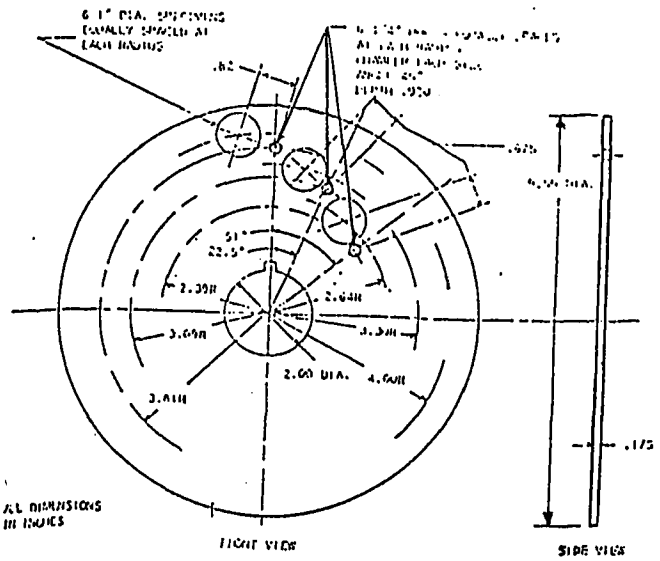

Fig.3b Test specimen and inducer location

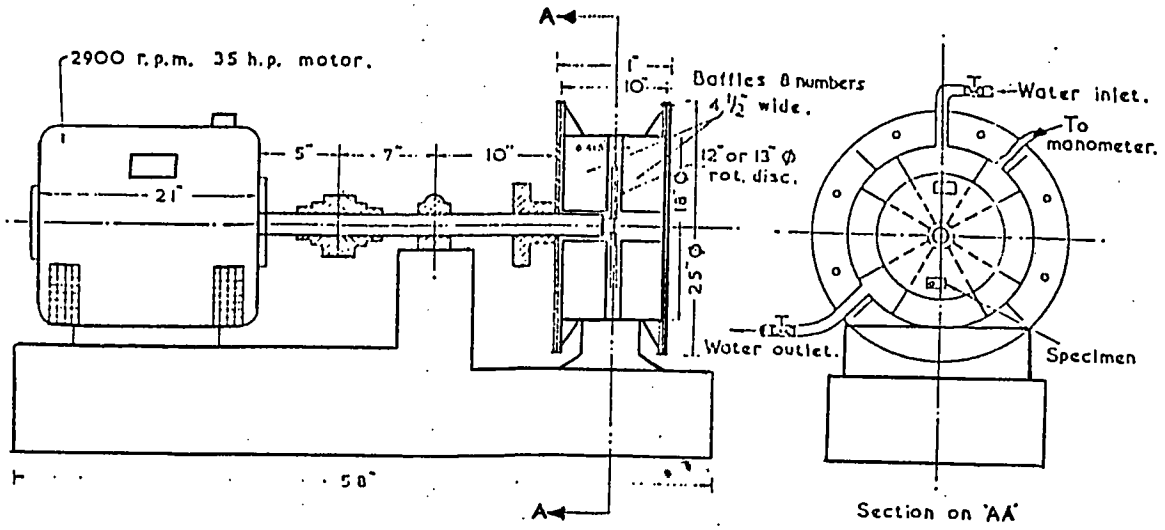

Fig.4a Horizontal arrangement of a rotating disc device

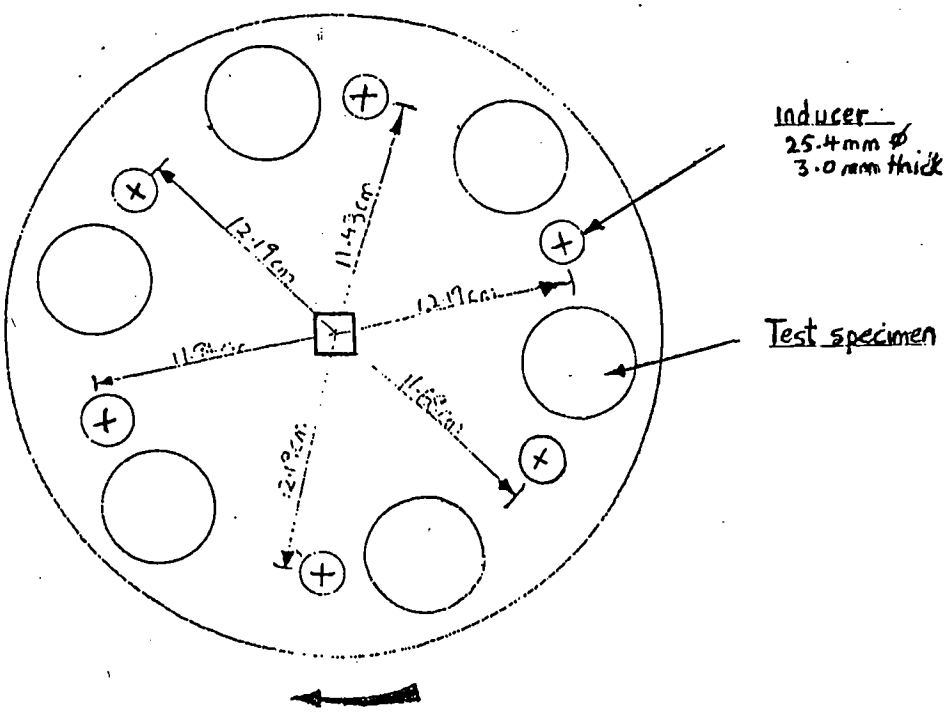

Fig.4b Test specimen and inducer arrangement

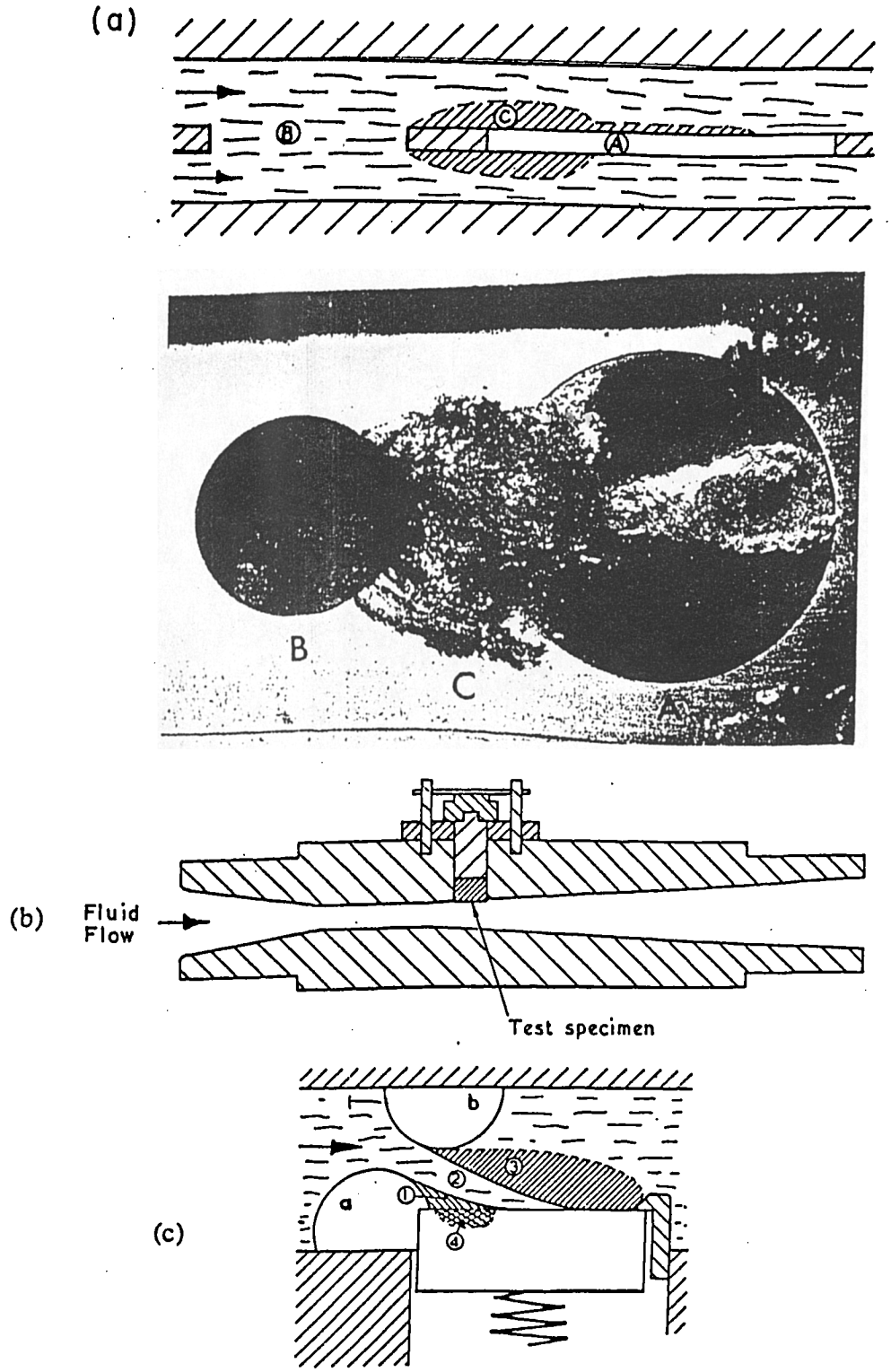

Fig.5 (a) Cavitation exciter and sample holder from flow system. Upper figure shows schematic plan view, lower figure shows photograph of side view. The cavity cloud *C* is generated at the exciter—the upstream hole *B*—and travels downstream to collapse at the specimen *A*. [From Hansson and Mørch (1977).] (b) A typical venturi tube in which the cavities are produced at the throat, and several specimens may be inserted through the wall. [From Knapp *et al.* (1970).] (c) A modified version of a venturi with offset constrictions *a* and *b* producing highly intense cavitation clouds 1 and 3 and erosion of the specimen 4. [From Erdmann-Jesnitzer and Louis (1974).]

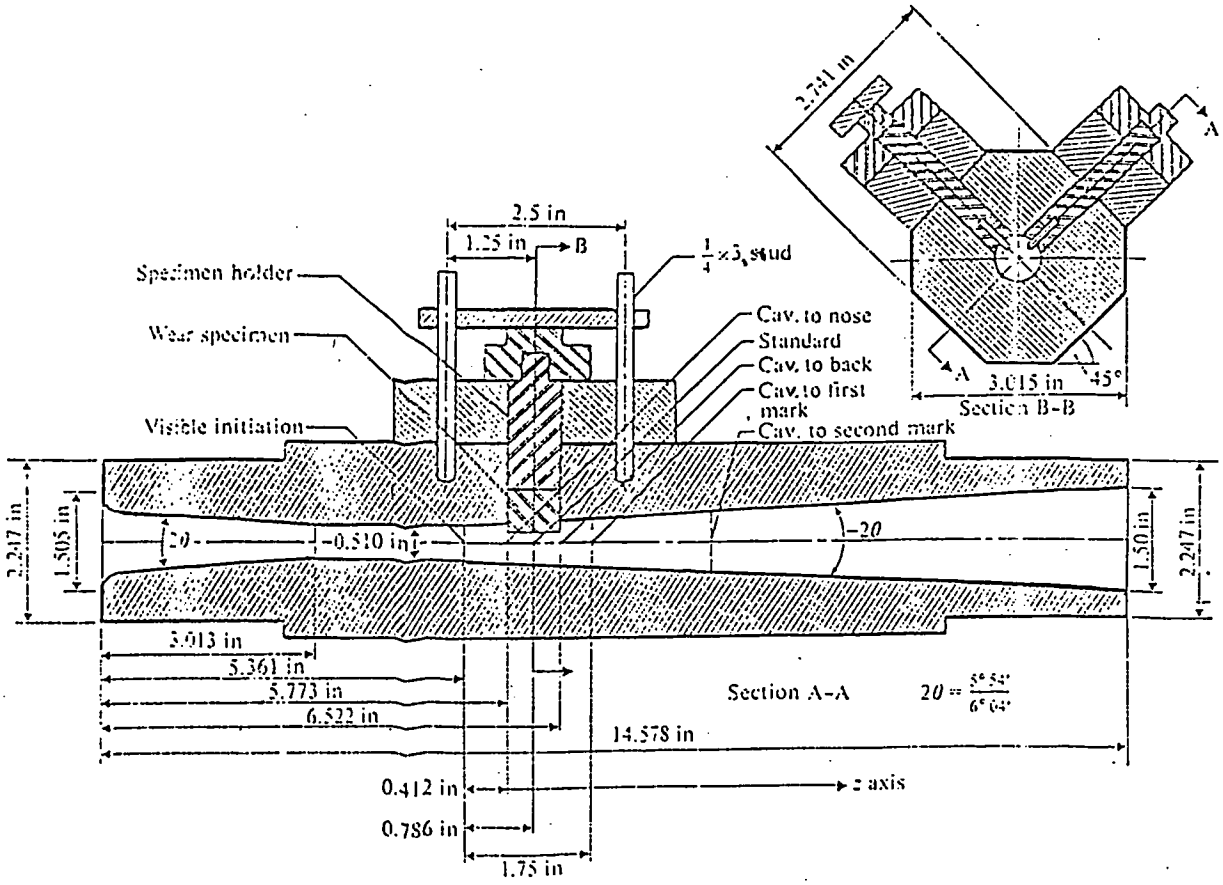

Fig.6 Test section at University of Michigan

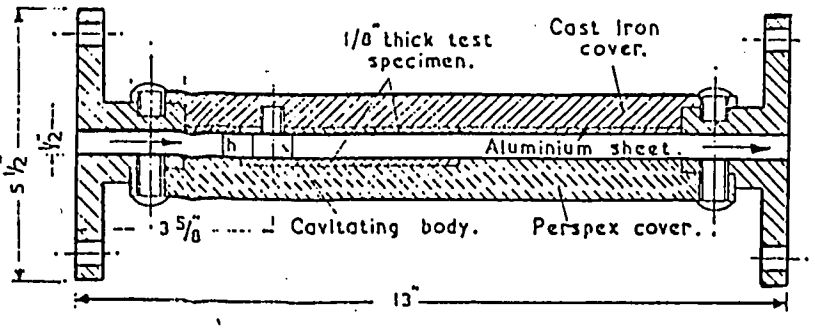

Fig.8 Test section as used by Rao (1970)

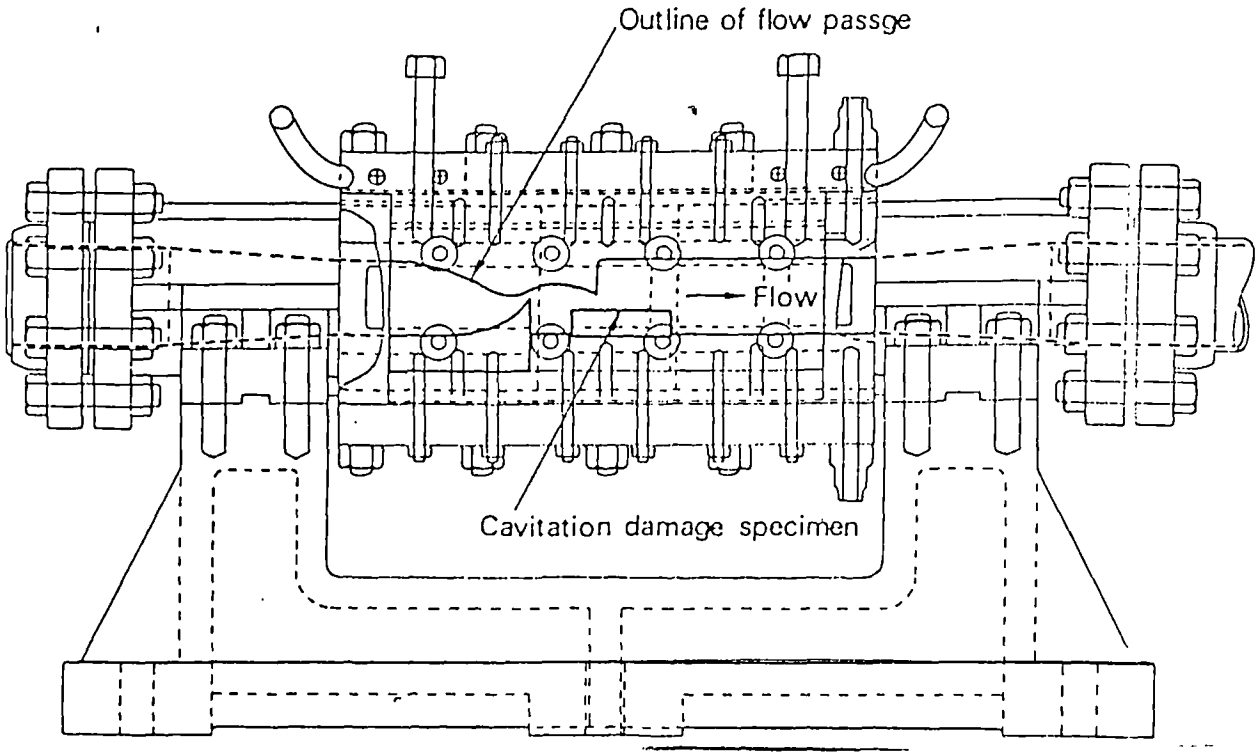

Fig.7 Holtwood Laboratory cavitation-damage test section (Mousson 1937)

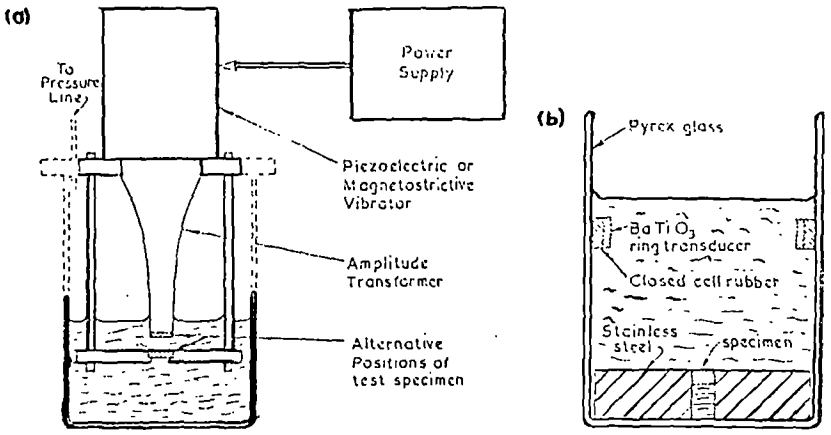

Fig.9

(a) A piezoelectric or magnetostric device for vibratory erosion testing in which a specimen is attached to, or held stationary below a horn. (b) A ring of piezoelectric material is attached to a beaker and produces a cavitating cloud of bubbles at the specimen surface (from Plesset and Ellis 1955)

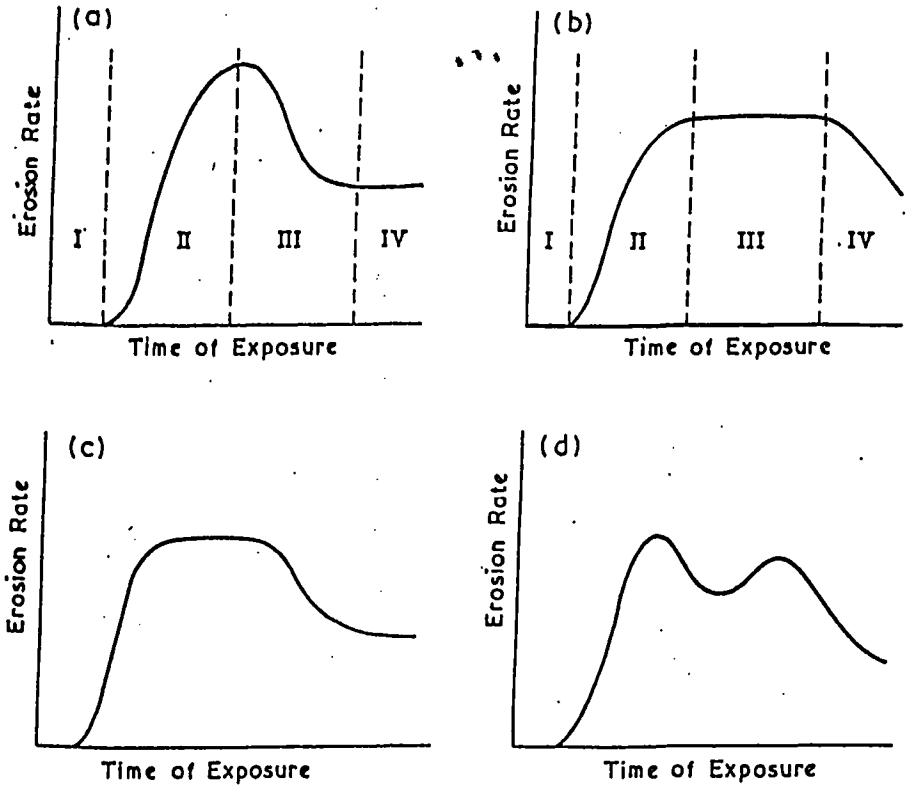

Fig.10 Schematic plots of the various form of erosion rate versus time curves obtained by different investigators

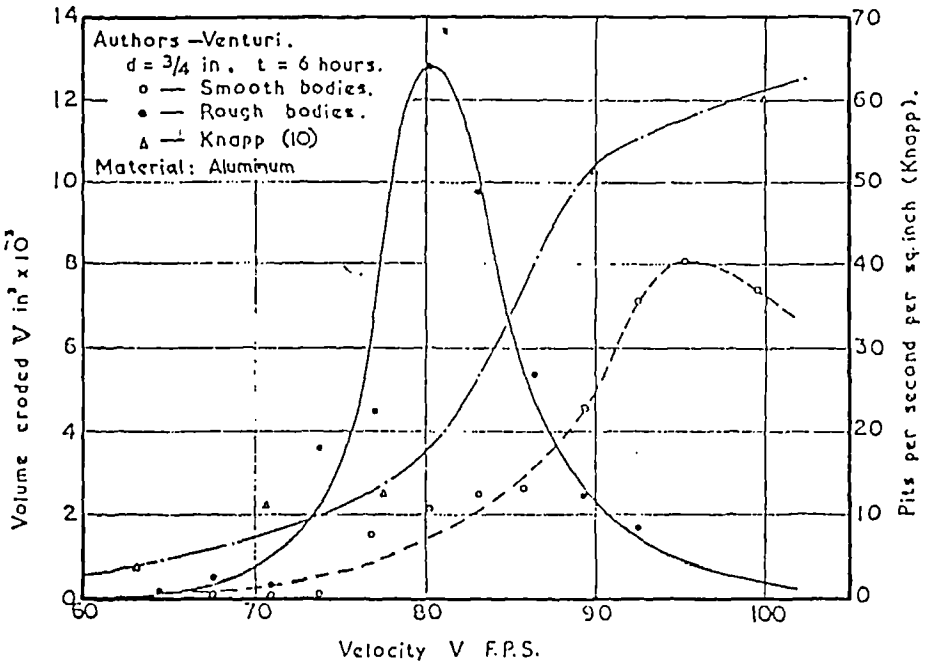

Fig.11 Relationship between volume eroded and velocity (Hammitt et al 1965)

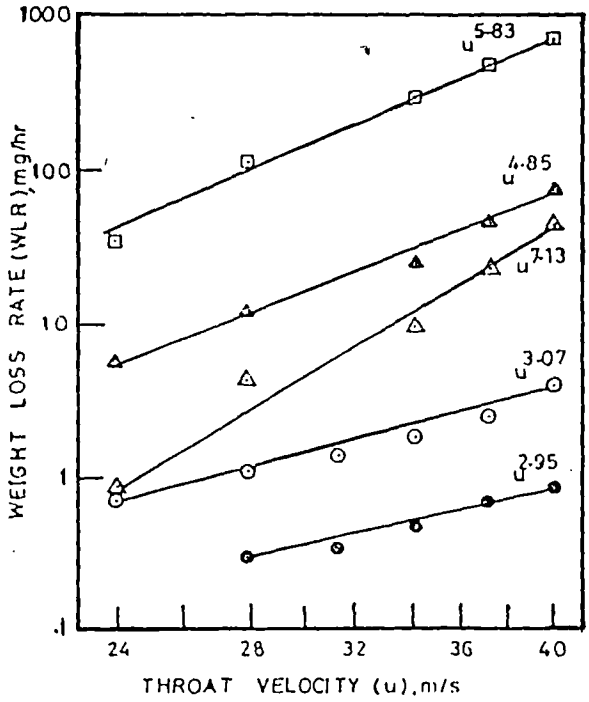

Fig.12 Variation of weight loss rate with throat velocity at a = .035 for 20 mm sources: ⊡ (sidewall), 60° symmetrical wedge; ⊙ (sidewall) and ▲ (cylindrical), circular cylinder; ⊙ (sidewall) and ● (divergent section), con-div wedge

(HUTTON & SELIM 1983)

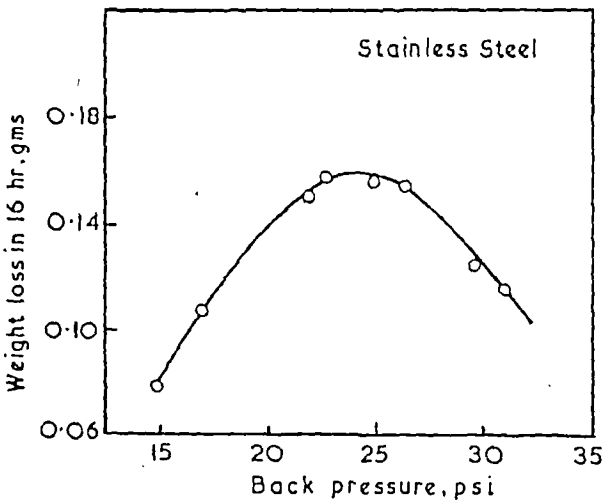

Fig.13 Influence of pressure on damage rate produced in a flow device [From Mousson (1937)]

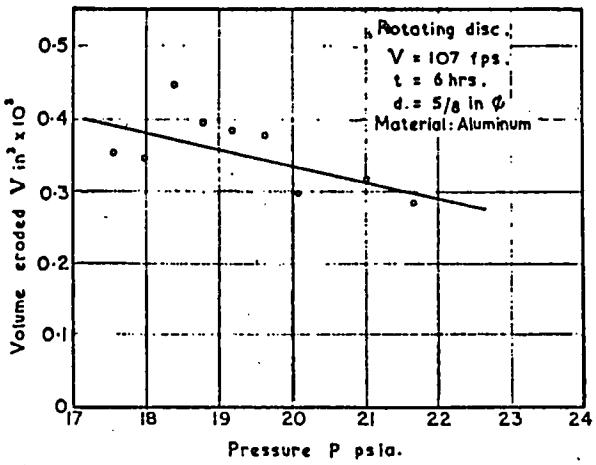

FIG. 14 **Relationship between Volume Eroded and Pressure** (Rao et al 1970)

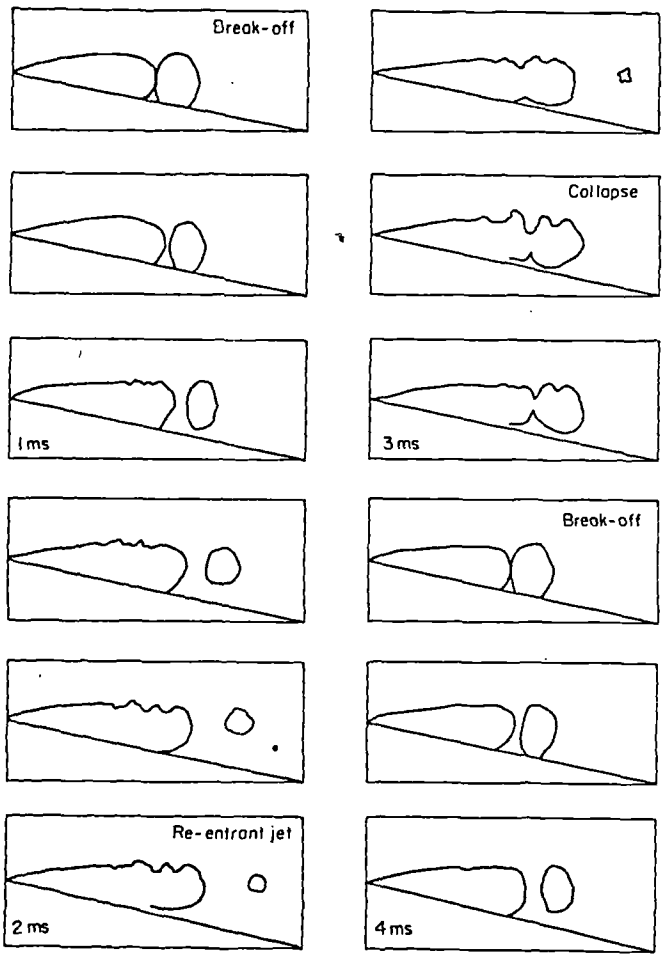

FIG 15 **Idealized Cavity Break-off and Collapse Sequence for a Convergent-Divergent Wedge Inducer** (Lush & Skipp 1986)

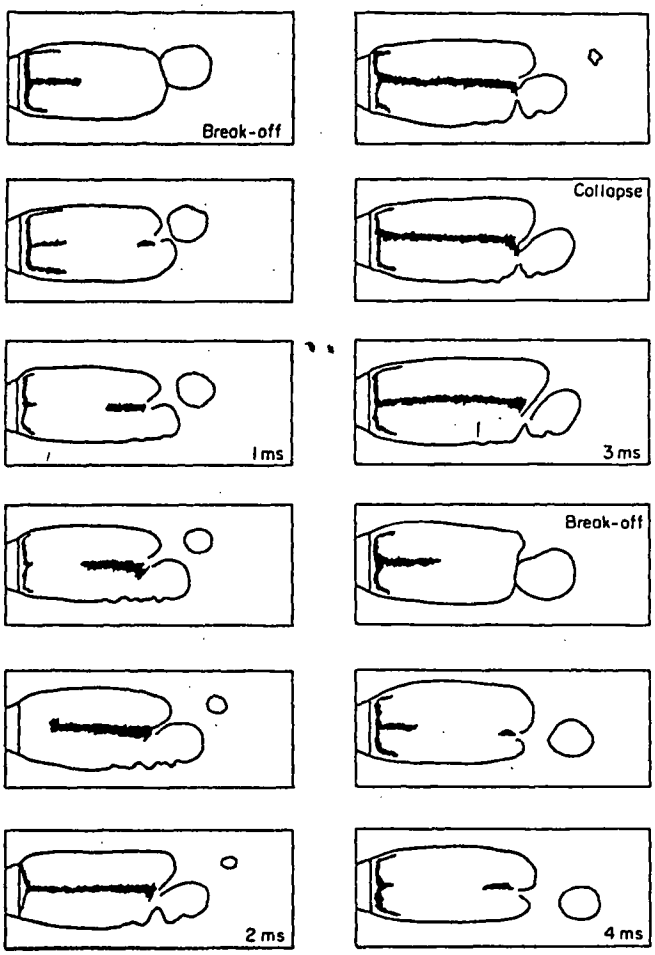

FIG 16 **Idealized Cavity Break-off and Collapse Sequence for a Symmetrical Wedge Inducer**
(Lush & Skipp 1986)

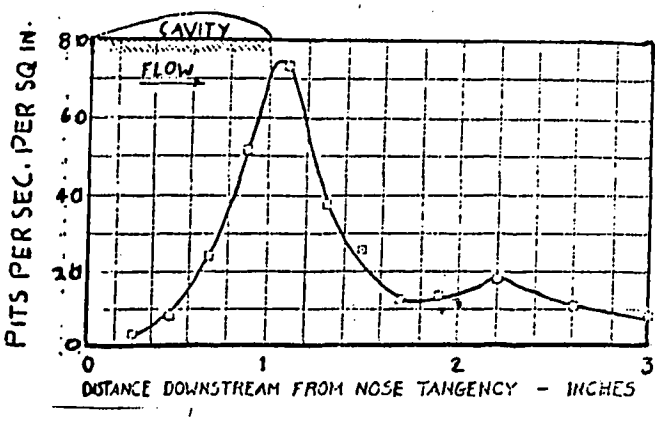

Fig.17 Distribution of Pitting for 1-in Cavity length

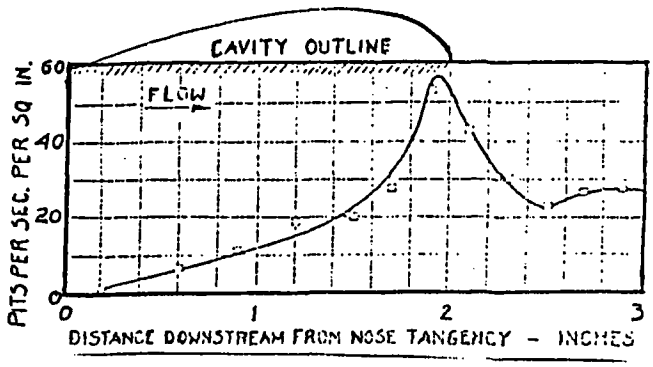

Fig.18 Distribution of Pitting for 2-in Cavity length

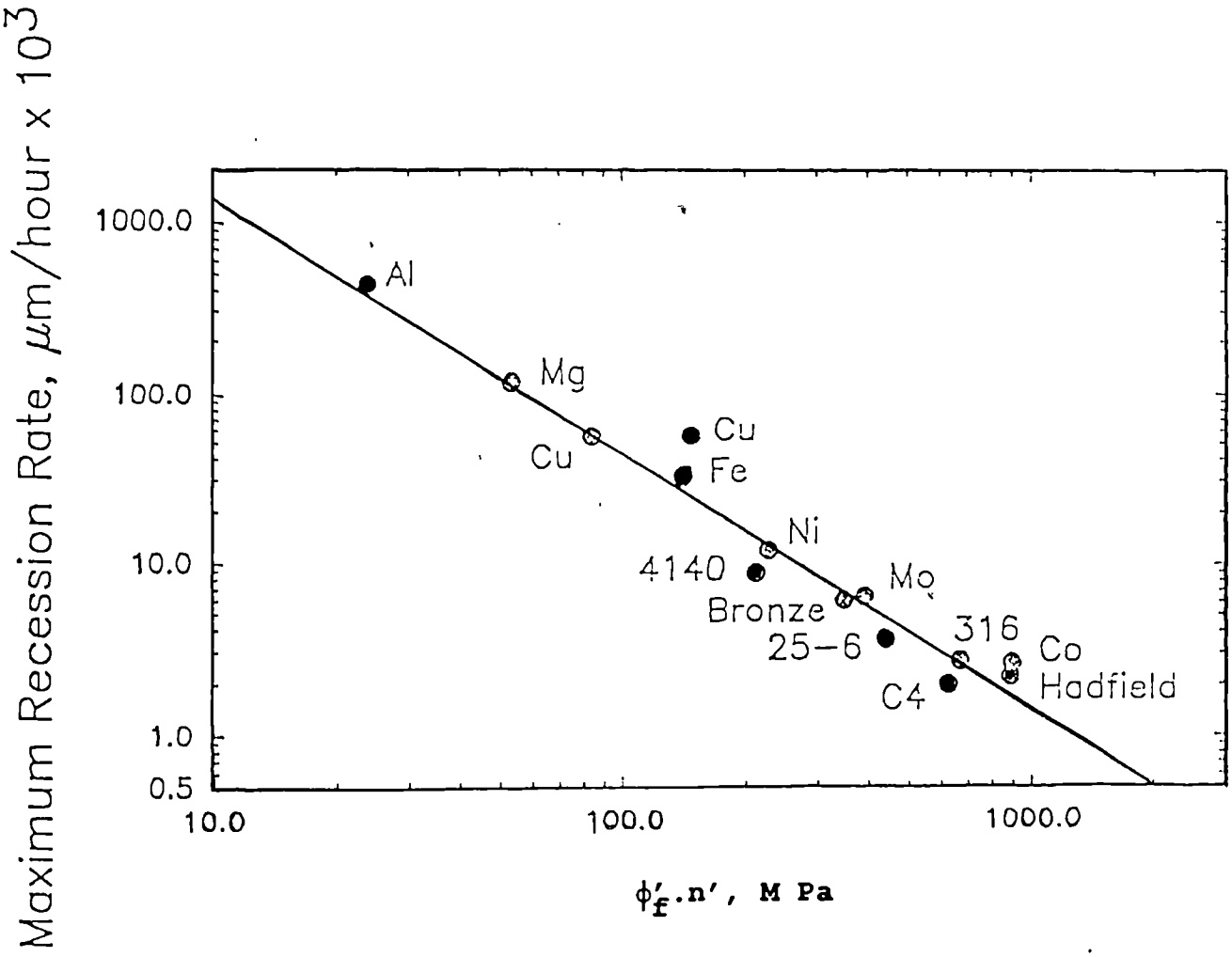

FIG. 19 Correlation between the combined parameter $\phi'_f.n'$ and maximum recession rate by cavitation erosion. (Richman & McNaugthon 1990)

(Richman & McNaugthon 1990)

3.0 TEST FACILITY

3.1 GENERAL DESCRIPTION

The test rig which simulate cavitation hydrodynamically is of the venturi type, and was originally designed by Dr. PETER LUSH (fig.20). It is a close circuit system with flow being generated by a 22kW two-stage centrifugal pump. The flow rate through the working section is controlled by a gate valve on the bypass. The rig is externally pressurised via a pneumatic-hydraulic transfer barrier. The rig includes a removable filter and it also incorporates a cooling system to regulate temperature. To reduce vibration to the working section, the pump is connected to its inlet and outlet via rubber couplings and all components are mounted on a 13mm resilient pads. The rig contains a total water volume of approximately 500 litres.

3.2 WORKING SECTION

The pipe run containing the working section can be isolated using ball valves to allow access without draining the rig. To minimise flow restriction theses valves are full flow, and all flanges on the working section run are neck welded. A 450mm long cruciform flow straightener is installed just downstream of the high pressure vessel to remove swirl. The working section has a cross section of 30mm by 15mm which is blended with the circular pipe work by a contraction upstream and a long diffuser downstream. The working sections, fabricated from stainless steel, are incorporated in two duraluminium walls as insert. The test sample is accommodated in a recess in one of the steel insert. Both walls which are removable, are held in position by 16 Allen bolts. A 60 degree symmetrical wedge inducer is used for accelerated testing, which produces a nominal 50% blockage. Figure 20C and 20D show both halves of the working section, While figure 20E is that of the inducer . Pressure and velocity are measured using two PLATON P25 series pressure transmitters (type P25LD & P25LA) with two Beka digital readouts (Type BA507 & BA508). The arrangement of pressure tappings is shown in fig.21. One digital readout gives the absolute pressure either upstream or downstream of the inducer. The other which gives

the differential pressure across the contraction upstream of inducer is also used to compute flow rate and velocity in the working section. The sensors could also be used to read atmospheric pressure using a pair of three way valves. This facility is used to check whether a change in reading during a run is due to a genuine change in flow conditions or instrument drift. Marked variation in flow condition in the working section will manifest as a change in noise level. This is picked up by a noise level meter or an oscilloscope via a piezo electric transducer, which is positioned at a sensitive point on the wall of the working section.

3.3 RIG PRESSURIZATION

The system is shown in fig.22. The rig is pressurized using air bottles which are recharged in the lab. A BIG bottle top regulator (Appollo 600) reduces the air pressure to approximately the level required. Safety valves on the gas line and high pressure vessel prevent the system being pressurized above its maximum rating of 14 bars. The pressure is set accurately by a Norgen (series11) pilot regulator, operating between 0 to 14 bars. Pressure is transferred to the rig water via a Greer Mercier hydraulic accumulator (model TB3.8 1.2

207). Bourdon pressure gauges connected to the high pressure vessel and air supply would indicate the same readings if the accumulator is functioning correctly. Dissimilar readings indicate that the accumulator bladder has reached the end of its travel in either direction.

3.4 TEMPERATURE REGULATION

The system for temperature regulation is shown in fig.23. Heat is transferred from the working fluid to the coolant by a Serck shell and tube heat exchanger (type AA44). The coolant is circulated by a Stewart 1KW. centrifugal pump, passing from the Serck to a large fan heat exchanger which transfers heat to the space outside the laboratory. The rig water temperature is monitored using two Pyrotenax NC/NA thermocouples. One is inserted 75mm into the low pressure vessel, and the other forms a cold junction. The signal from the thermocouple is stepped up using an operational amplifier (RS725CN) before being displayed on a digital readout. Laboratory and coolant temperature are measured using a thermometer. The rig is brought up to temperature by initially running with coolant circuit switched off. When the operating temperature is reached, the coolant circuit is switched on and

the temperature allowed to stabilise. The entire process takes about 40minutes. Varying the flow rate through the working section using the bypass also varies the flow rate through the heat exchanger. Thus a steady state operating temperature will vary for different flow settings. In practice the total variation was generally confined within the range of 38 to 43 degrees Celsius.

3.5 AIR CONTENT

Air content of the rig was measured using a Van-Slyke apparatus. A full description of the apparatus and its operation is given by Selim (1977). To ascertain that the Van-Slyke apparatus was operating correctly, measurement of saturation air content of water at various temperature were taken. It can be seen from fig.24 that, the result are in good agreement with those quoted by Douglas et al (1979).

In principle, the air content of the rig should not vary as the rig is closed loop. However, during the course of a test programme, the vessels will be vented to relieve pressure and the working section drained to have access to test samples. A series of twenty air content measurements were taken over a number of weeks while testing was in progress.

The mean air content was found to be 24.55ml/l with an average deviation from the mean of 2.74ml/l. All air volumes quoted are referred to 0 celsius and 1 atm. From a series of measurements on the same water sample, the deviation due to experimental error is taken as 0.24ml/l. When not in operation the water in the rig experiences an average pressure of 107.5kPa and is at a temperature of about 15 Celsius . The saturation content for these conditions is 22.05ml/l. This figure corresponds closely to the mean running air content .

3.6 FLOW VELOCITY AND CAVITATION NUMBER

The fluid flow rate through the working section was calibrated using a D and D/2 orifice plate (d/D =0.75) manufacture to BS.1042. The pressure difference across the orifice plate was measured using a mercury manometer and is shown plotted against the corresponding pressure difference across the contraction in Fig.(24). A linear correspondence could be seen indicating that both components are operating satisfactorily.

The volume flow rate is given by the equation

$$Q(m^3/s) = 0.00118668\left(\frac{P_{op}}{\rho}\right)^{1/2} \quad 5$$

Where P_{op} is the pressure difference across the orifice plate in Pa. and rho is the density of water in kg/m^3 . The fluid velocity in the working section upstream of the inducer, is given by the equation ,

$$U_o = 453.29\left(\frac{P_c}{\rho}\right)^{1/2} \quad 6$$

Where P_c is the pressure drop across the contraction in Pascal and U_0 is in m/s. The Cavitation number in the working section upstream of the inducer, is calculated by;

$$\sigma_o = \frac{P_o - P_v}{1/2\rho U_o^2} \quad 7$$

Where P_0 is the absolute pressure in the working section upstream of the inducer and P_v is the vapour pressure. Thus the upstream values of velocity and cavitation number can be calculated easily using the instrumentation

shown in Fig.(21). However, it is the throat conditions which are of interest. These can be inferred from the upstream values using the following equations which are derived in Appendix 3.8 ,

$$U_t = U_o(1 + \sigma_{ob})^{1/2} \qquad 8$$

$$\sigma_t = \frac{\sigma_o - \sigma_{ob}}{1 + \sigma_{ob}} \qquad 9$$

Where U_t and σ_t are the throat velocity and throat cavitation number respectively, and σ_{ob} is the choked or blocked value of σ_o . Since the working section of the rig is made of steel, it is not possible to check visually the occurrence of choked condition. This can however be overcome by checking that the downstream pressure tapping (fig.21) is giving a reading corresponding to the vapour pressure .

A simple interactive computer program is used to set the flow conditions. The desired values of U_t and σ_t are read in as is an estimated value of σ_{ob} and the measured temperature T, which is used to obtain P_v and rho . The program responds with the value of P_c which will give the correct velocity. This is set ensuring that the flow is choked and P_o is read and fed into the program. The program responds with a calculated value of σ_{ob} . If this is not close enough to the original estimate, a new estimated value of σ_{ob} is fed in and the whole process repeated. Once the estimated and calculated values are in good agreement the program will then give the correct values of P_c and P_o for the required flow conditions.

In calculating U_o there is an error of 0.25% from calibrating the flow rate, a maximum error of 0.5% due to unsteady fluctuations in the differential pressure and an estimated error of 0.25% in ascertaining the cross sectional area of the working section. The cumulative error in U_o is therefore 0.61%. The error in calculating σ_o includes the error for U_o and the error in measuring P_o which is a maximum of 0.3% . The accuracy of temperature measurement is better than $\pm 0.5^{\circ}$ C therefore errors in P_v and ρ are negligible. The cumulative error in σ_o is therefore 0.91%. The cumulative error in U_t is 0.73%

APPENDIX 3.7

3.7.1 OPERATION OF CAVITATION RIG

These notes should be used in conjunction with the guide to rig operation given by Grant (1982b);

(1) By opening the pressure tappings to the atmosphere, the digital readouts should be adjusted periodically to read atmospheric and zero pressure as appropriate. This is achieved via the back of the control board, where the zero adjustments of the digital readouts are situated. In performing the above procedure, a second person is needed since the controls are behind the control board and the readout display is infront.

(2) The filter in the rig has an element which can be replaced . This should be carried out if the rig water becomes discoloured. The valve upstream of the filter should only be open one quarter of a turn, since any more and the excess pressure will rupture the filter.

(3) Water samples from the Van Slyke can be taken, using pipette, from the tappings either side of the orifice flange.

(4) The orifice plate is removed unless calibration of flow rate is being performed.

(5) Although there are 16 tappings for Allen bolts to hold the working section sidewall in position only 6 of these need be used.

(6) When replacing water lost after the working section has been drained, it is important that all air is expelled. This is done by venting both pressure vessels while the rig is pressurized from the mains for about two minutes.

(7) Occasionally the Serck shell heat exchanger is clogged with debris and corrosion product. This will be noticeable when the temperature of the rig water start drifting from the mean of 40 Celsius during runs appreciably. If this occurs, the heat exchanger should be dismantled and thoroughly cleaned following manufacturer's cleaning procedure.

APPENDIX 3.8

3.8.1 CALCULATION OF THROAT VELOCITY AND CAVITATION NUMBER

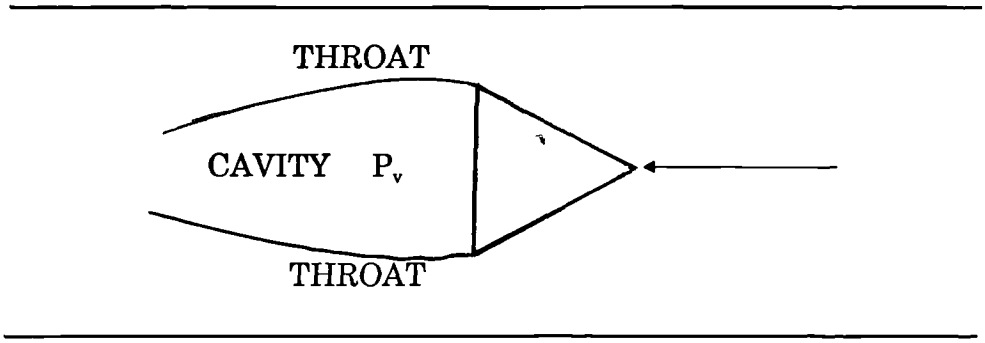

Defines P, U, σ and A as the pressure, velocity, cavitation number and area at the throat respectively . P_o, U_o, σ_o, and A_o are the same parameters at a point in the working section upstream of the inducer. P_v is the vapour pressure of the working fluid. σ_o is the upstream cavitation number at blocking (σ =0) i.e. when the cavity is, in principle, infinitely long. Rho is the density of the fluid.

Applying Bernoulli's Equation:

$$P + 1/2\rho U^2 = P_o + 1/2\rho U_o^2 \qquad 10$$

at blocking;

$$P_v + 1/2\rho U^2 = P_o + 1/2\rho U_o^2 \qquad 11$$

$$\frac{P_o - P_v}{1/2\rho U_o^2} + 1 = \left(\frac{U}{U_o}\right)^2 \qquad 12$$

$$U = U_o(1 + \sigma_{ab})^{1/2} \qquad 13$$

rearranging equation 10

$$\frac{P_o - P_v}{12\rho U^2} + 1 = \left(\frac{P_o - P_v}{1/2\rho U_o^2} + 1\right)\frac{1}{1 + \sigma_{ab}} \qquad 14$$

$$\sigma = \frac{\sigma - \sigma_{ab}}{1 + \sigma_{ab}} \qquad 15$$

Thus, using equation 13 and 15, the conditions at the throat can be inferred from the conditions upstream. The analysis implies that the ratio U/U_o remains at the value calculated at breakdown for any σ. The ratio U/U_o is recalculated for each velocity as it shows a weak dependence on velocity.

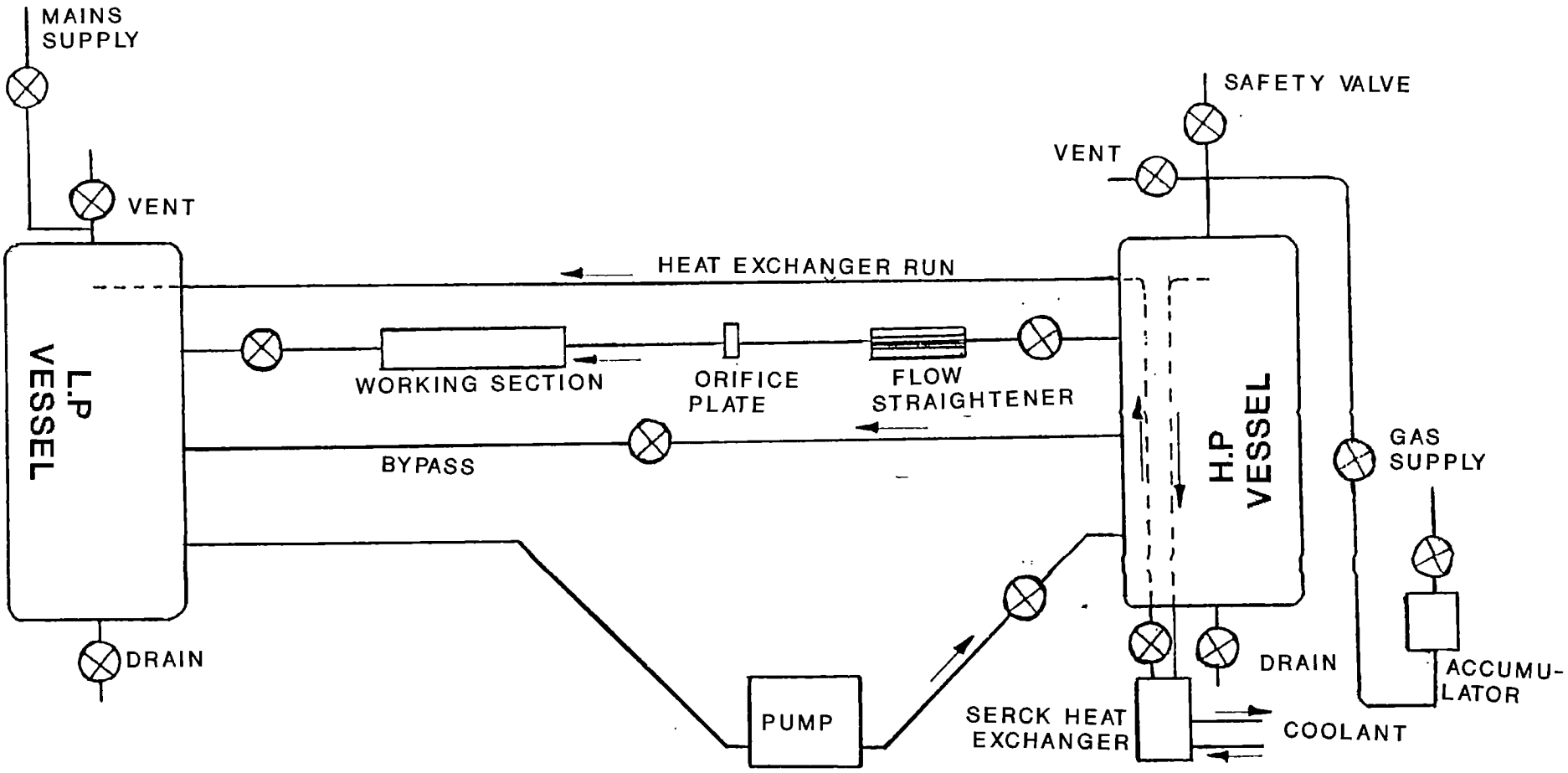

Fig.20 CAVITATION EROSION TEXT FACILITY

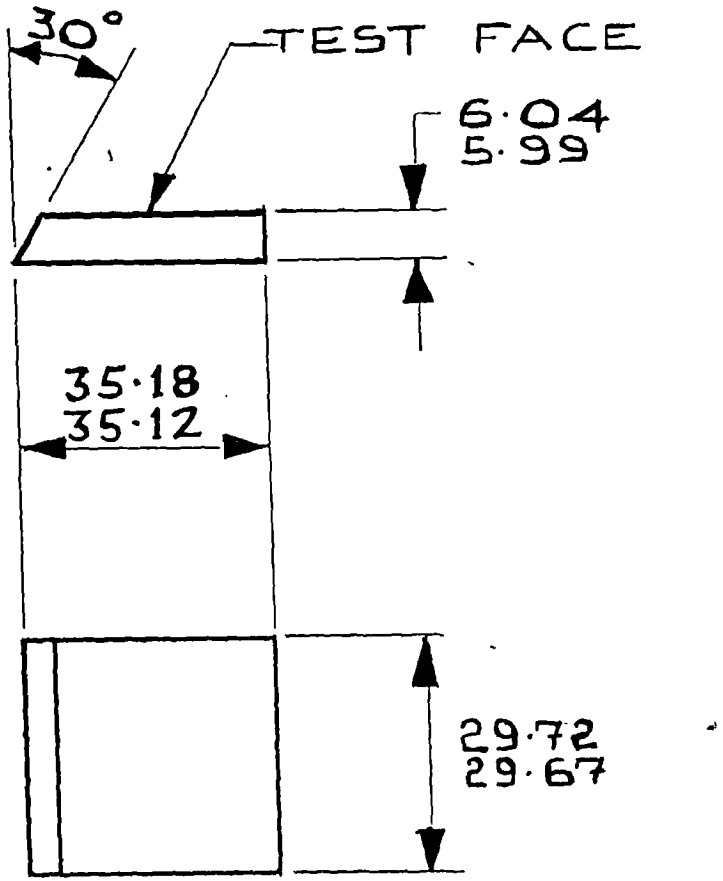

Fig.20b CAVITATION EROSION TEST SPECIMEN

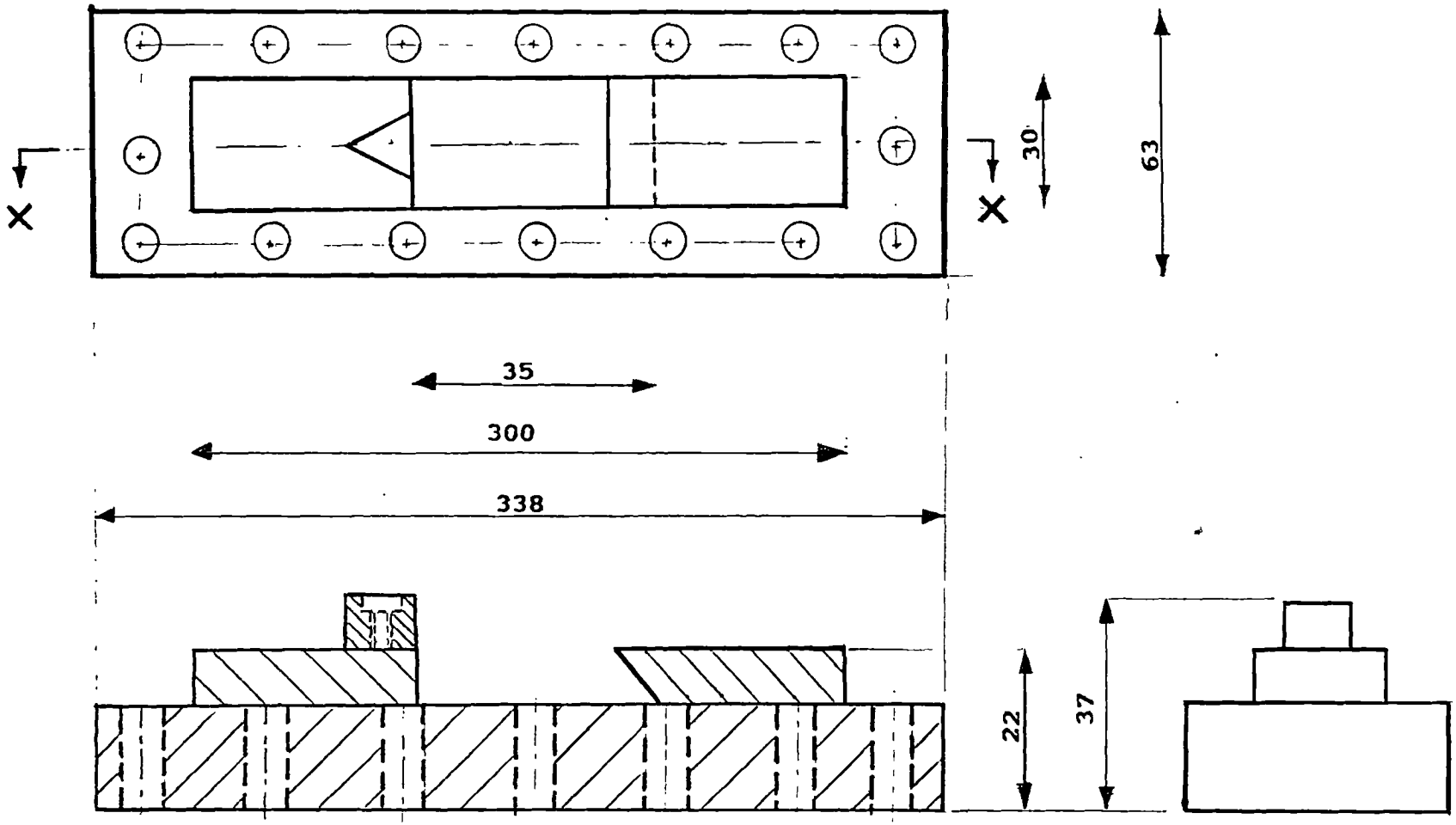

FIG. 20C: SECTION ACOMMODATING INDUCER AND TEST SPECIMEN

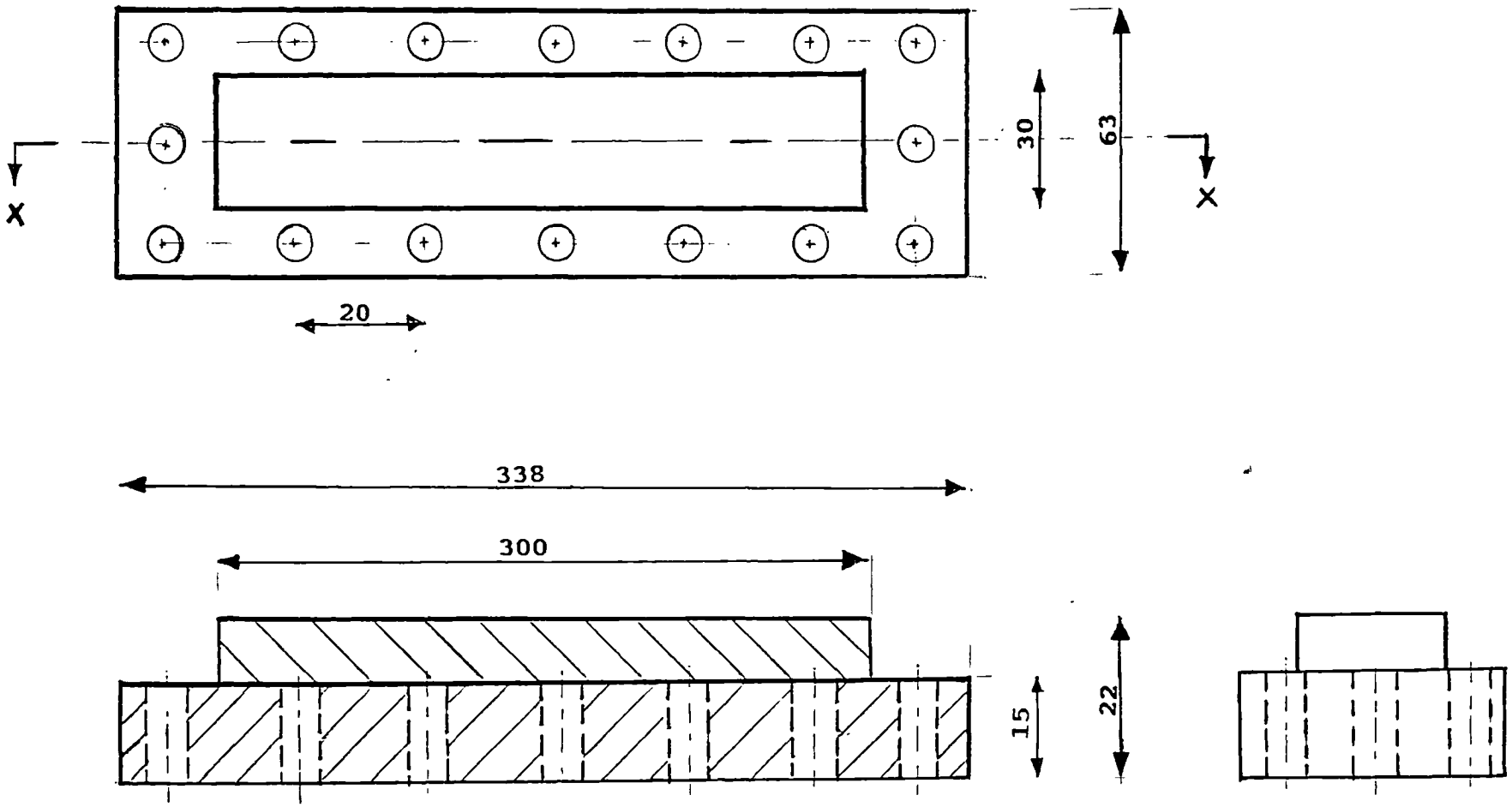

FIG. 20D; ONE HALF OF WORKING SECTION

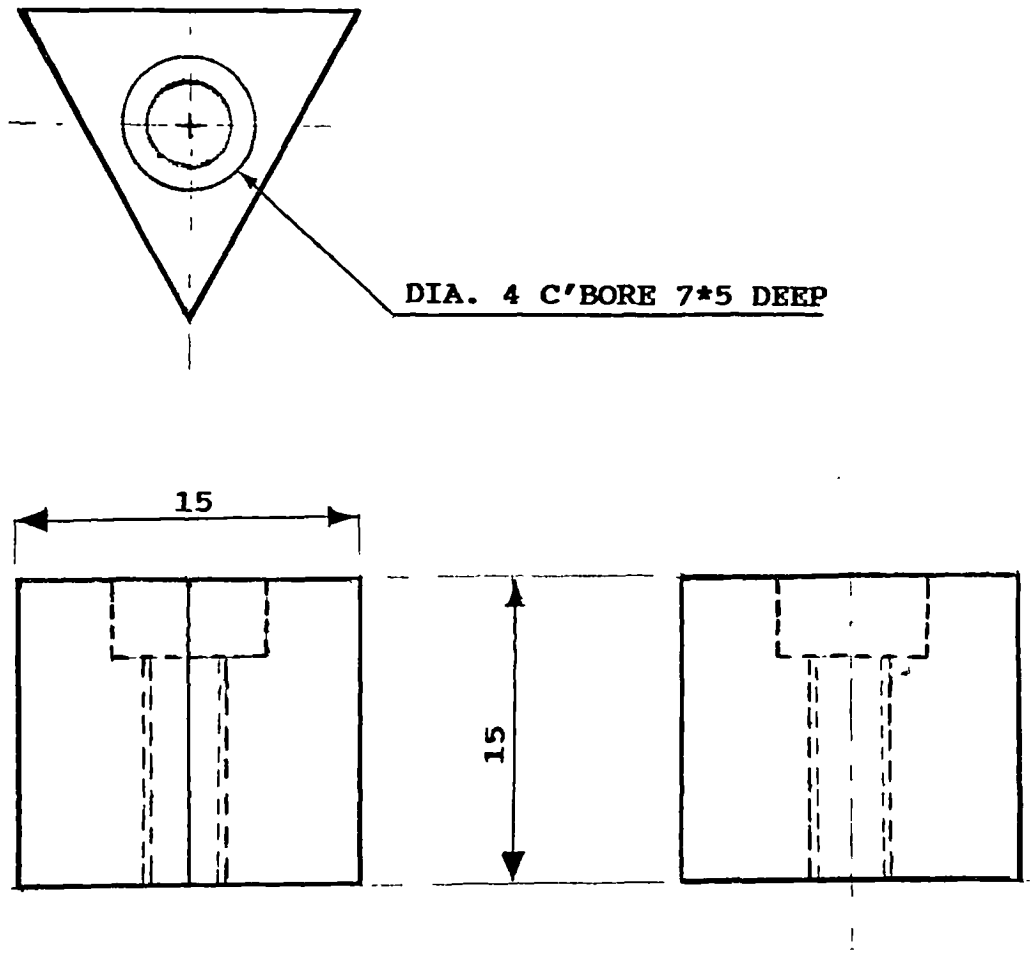

FIG. 20E: SYMMETRICAL WEDGE INDUCER

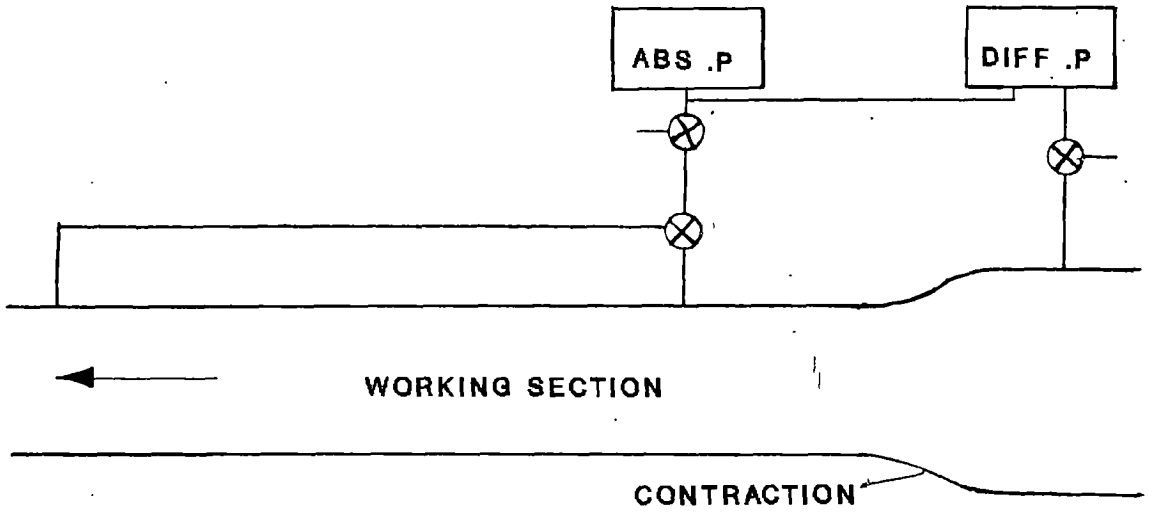

Fig.21 WORKING SECTION PRESSURE TAPPINGS

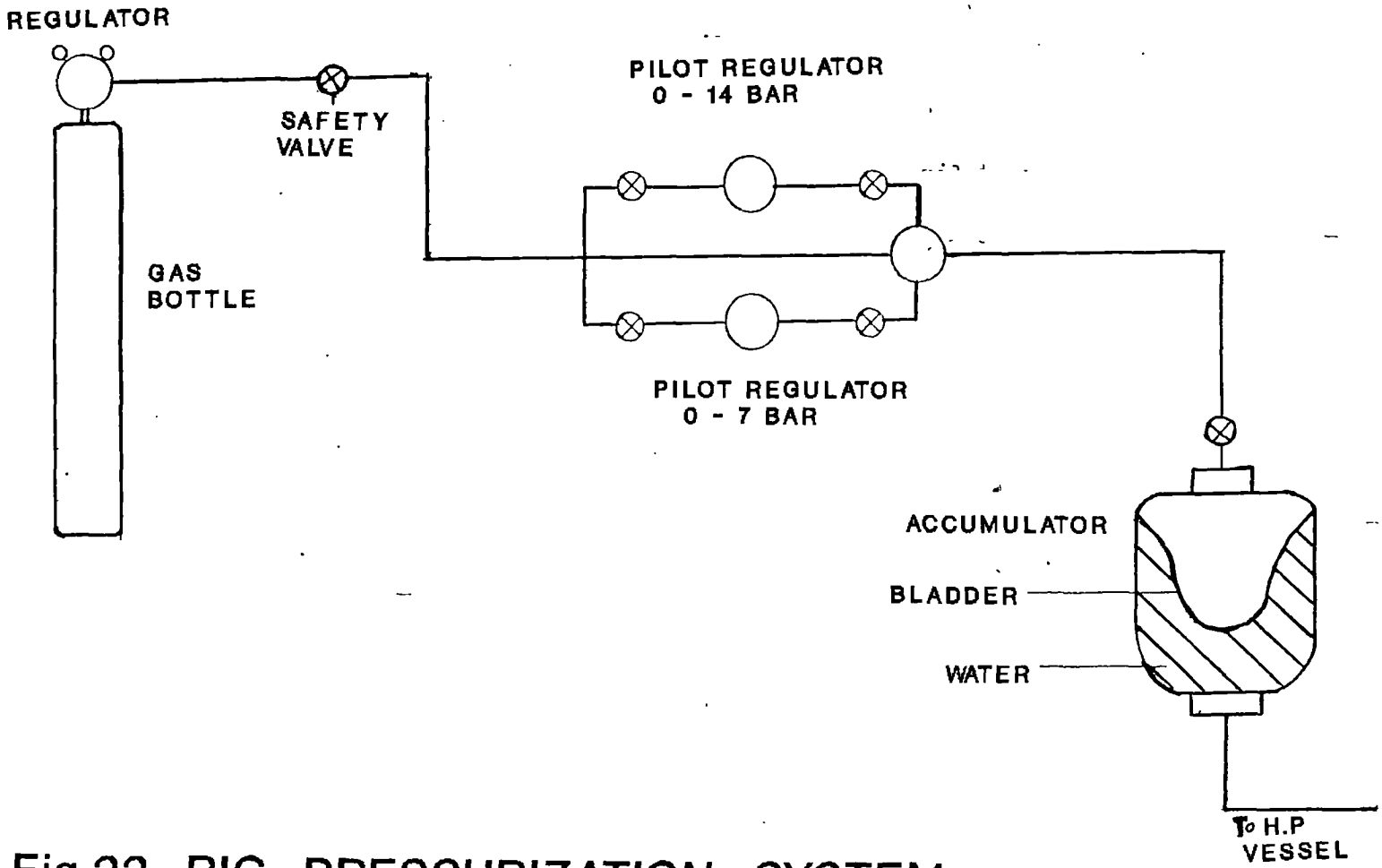

Fig.22 RIG PRESSURIZATION SYSTEM

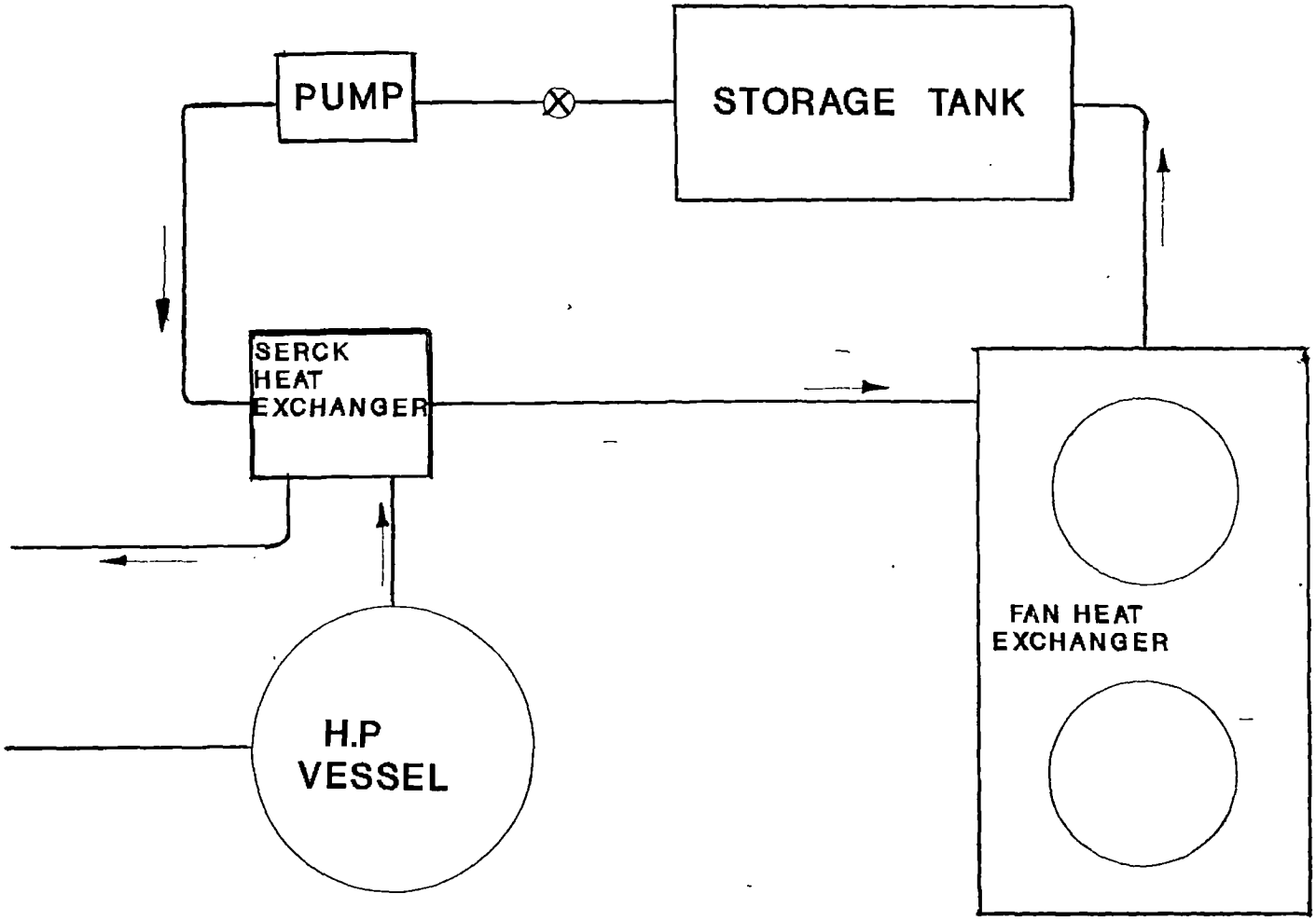

Fig.23 TEMPERATURE REGULATION CIRCUIT

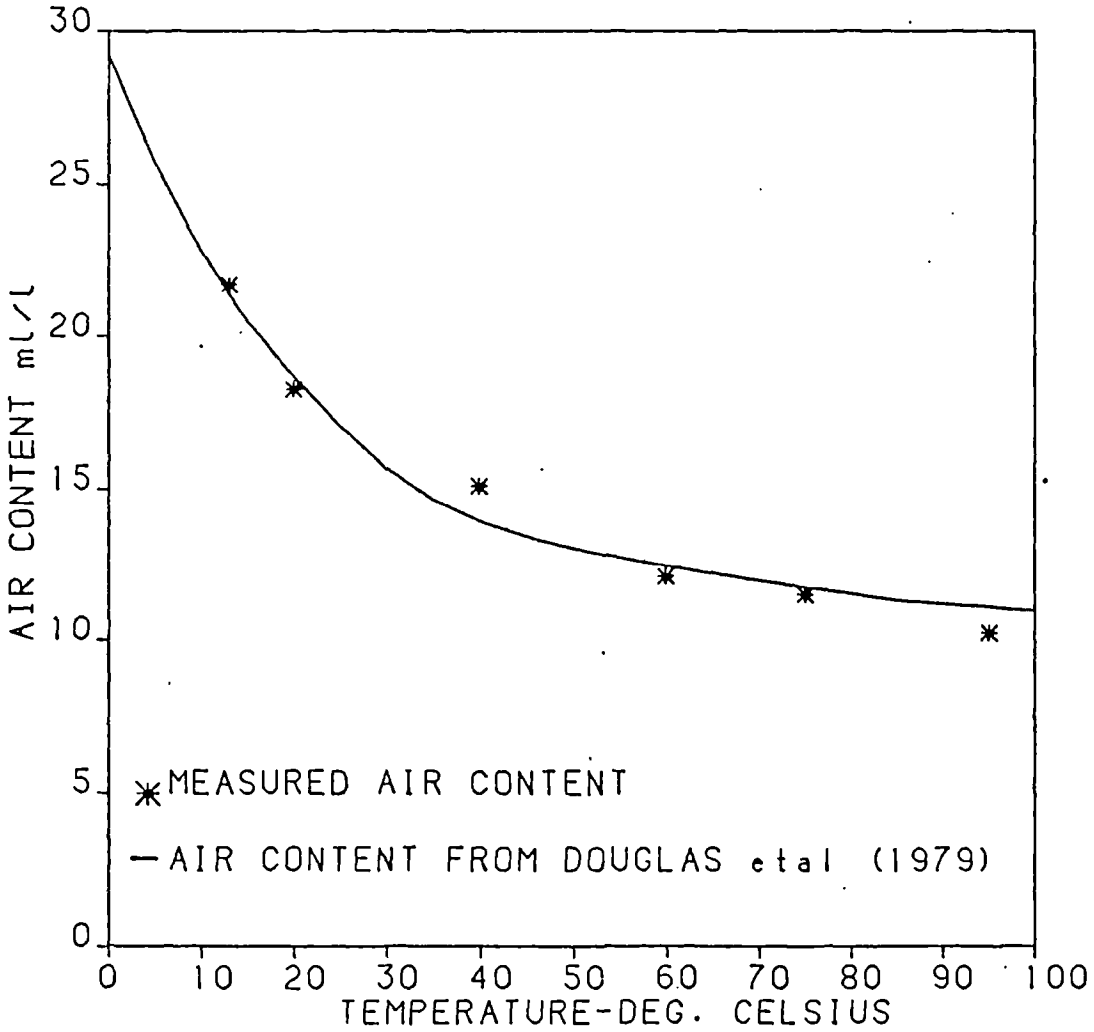

Fig.24 COMPARISON OF MEASURED AND EXPECTED VARIATION OF AIR CONTENT WITH TEMPERATURE
Air Volume referred to STP

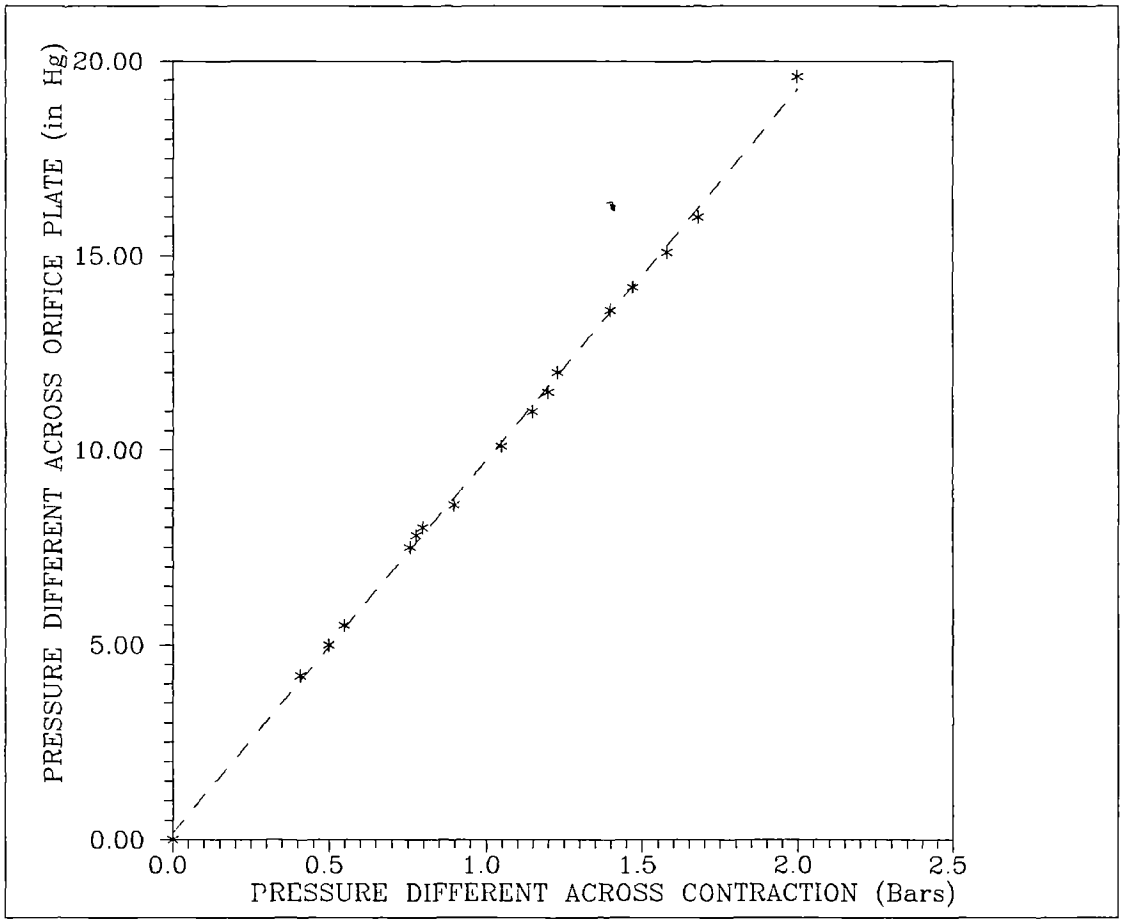

Fig25 CALIBRATION OF CONTRACTION USING ORAFICE PLATE

4.0 EXPERIMENTAL PROCEDURE

4.1 RIG OPERATION

The rig working fluid is drawn from the mains and contains a total water volume of approximately 500 litres. The mean air content of the water has been measured to be 24.5ml/l with an average deviation of 2.7ml/l. In principle, the air content of the rig should not vary as the rig is closed circuit. However, during the course of a test, the vessels are vented to relieve pressure and the working section drained to allow access to the test sample. The mean pH value during the course of testing was found to be 7.5 with deviation of ± 0.2. Working temperature of the water was between 38-42 degrees celsius having a 40 degrees celsius mean. Before commencement of a test, the working fluid is warmed up to the working temperature, by restricting flow to the working section via the bypass and with the heat exchanger circuit turn off. This would last for approximately 30 minutes depending on the ambient condition.

4.2 TEST MATERIALS

Materials used in this project were either supplied from industrial firms or were produced in the department's workshop. Majority of those that came from companies were not of the right specification. Some were short in length and others in thickness. Hence shims of various sizes were made to compensate.

The working section of the rig and in particular the sidewall that accommodates the test specimen is designed such that, the specimen is flush mounted. The test specimen measures 30mm by 30mm on the exposed face and is held in position by a 30 degrees chamfer at the trailing edge and by being overlapped by about 2mm by the inducer at the leading edge. The overall dimensions of the specimen are approximately 33.5mm * 30mm * 6mm thick (see fig20b). Thus, the two linear dimension of thickness and length play a vital role in fixing the specimen rigidly in position during a test run. Any slight movement of the specimen during a run will alter the specified flow conditions. However, as mentioned earlier, any marked variation in flow condition could easily be detected by the pressure gauge upstream of the inducer, or in extreme situations by changes in cavitation noise level.

4.2.1 CERAMIC

In recent years, high performance ceramics have been successively improved both in terms of the materials themselves and of sintering technology. Ceramic components are however, damaged to an unacceptable extent through the introduction of residual stresses and cracks during finishing processes. Fracture of ceramics typically starts with a flaw at or near the surface and hence the properties of the suface have a major influence in determining the strength of the material. In many applications, the component must be made to very close tolerances which, owing to the variability due to sintering, can only be achieved by machining .

Finishing difficulties with high performance ceramics stem precisely from their excellent material properties which entail corresponding machinability problems . Owing to the extreme hardness and strength of ceramics, only a limited range of processes are available. In industrial applications, only lapping and grinding have found wide acceptence. Grinding is invariably carried out with diamond tools, while hard materials such as boron carbide can be employed for lapping.

Apart from the conventional processes, however, innovative techniques such as ultrasonic lapping, electro-discharge machining and laser beam processing can be applied, enabling

even complex shape to be processed. Owing to the nature of the materials, each of these processes involves the problem of damage to the product surface. In practice therefore, damage to the materials is avoided by selecting extremely low removal or cutting rates, entailing very high processing times and costs. To these must be added extreme tool wear, making machining even more expensive. Technological development of finishing processes to overcome these problems take two major directions; On the one hand, material-oriented and at the same time cost effective process control - strategies need to be developed for existing processing technologies. On the other hand, new ceramic processing methods have to be developed and applied, in order to extend the range of finishing options.

The importance of the final machining of ceramic component is not only concerned with producing the required form and surface quality, it is intrinsic in the production of strength, wear, and the high temperature characteristics of the component.

In this investigation, two ceramic base materials were utilised. These were silicon carbide and silicon nitride. The silicon nitrides were produced via two manufacturing processes; " hot pressed" and " hot isostatic packing" (HIP). Hot pressing consolidates and sinters the powders all in one step. Silicon nitride are hot-pressed in order to achieved

a high density as close to 100 percent of theoretical density as possible . The greater the density the body has, the lower the contained residual porosity. Porosity is detrimental to the mechanical properties of the ceramic, so it is desirable that it be minimised. Hot isostatic packing is a process that applies pressure in all directions on a powder preform using a higly-pressurized gas atmosphere inside a specially constructed pressure vessel. Heat and pressure are applied in sintering, resulting in a highly-dense and uniform part. The silicon carbides samples were reaction sintered. Reaction-sintered silicon carbide is formed by pressing silicon carbide powder and graphite powder together and impregnating the preform with liquid silicon. The silicon reacts with the graphite to form more silicon carbide, which reaction-sinteres all the components together. Excess silicon is usually left over, and this limits the high-temperature strength of the material. Both materials then went through indentical surface finish processes, ie. grinding and lapping. Thus, the objectives here were twofold, first to investigate the erosion resistance offered by the surface finishing processes, and secondly to evaluate and compare the cavitation erosion performance of both silicon carbide and silicon nitride. Table 3 give the general condition of the ceramic materials prior to testing.

4.2.2 PLASTICS

Epoxy resins are a highly versatile class of thermosetting plastics. Because of the many different constituents used, the epoxy formulations are presented to the user in many different forms; liquid, solutions, paste solids, one-part, two-part and sometimes three-part packs. The term epoxy, epoxy system etc. as commonly used, normally pertain to the complete system, i.e resin plus hardener plus any other constituent.

The success of epoxy resin in a diverse range of applications is based on a number of characteristics. Epoxy resin systems do not evolve volatiles during curing and shrinkage is low. Dimensional changes are negligible thereafter. Epoxy resins are presently used for far more than other matrices in advance composite material, especially for structural aerospace applications.

Mechanical properties are good for an amorphous non-crystalline polymer, having toughness and reasonable impact strength. Being thermosetting, epoxies are not susceptible to plastic flow under stress.

Three epoxy resin formulations were used in this project. These were produced in as cast and machined conditions. Their general conditions prior to testing are shown in table 4.

4.2.3 COMPOSITE

For many applications it is possible to increase the modulus and strength of plastics by means of reinforcement. A reinforced plastic consists of two main components; a matrix which may be either thermoplastic or thermosetting and a reinforcing filler which usually takes the form of a fibre. In general, the matrix has a low strength in comparison to the reinforcment which is also stiffer and brittle. To gain maximum benefit from the reinforcment the fibres should bear as much as possible of the applied stress. The function of the matrix is to support the fibres and to transmit the external loading to them by shear at the fibre-matrix interface. Since the fibre and matrix are quite different in structure and properties, it is convenient to consider them separately.

The reinforcing fillers usually take the form of fibres. A wide range of amorphous and crystalline materials can be used as reinforcing fibres. These include glass, carbon, boron, and silicon carbide.

Glass in the form of fibres is relatively inexpensive and is the principal form of reinforcement used in plastics. The fibres may be chopped strands or continous filaments. They are produced by drawing off continous strand

of glass crucible which contains the molten glass.

The matrix in a reinforced plastic may be either thermosetting or thermoplastic. Nowadays the major thermosetting resin used in conjunction with glass fibres reinforcement are unsaturated polyester resins and epoxy resins. The most important advantages with these materials can offer are that they do not liberate volatiles during cross-linking and they can be moulded using low pressures at room temperature.

In this project two composite materials were utilised. These were glass reinforced plastic (GRP) and Fybroc. They both employed two thermosetting plastics as the matrix, i.e. epoxy resin for the former and vinyle ester for the latter. E-glass fibre was utilised as the reinforcing element in both matrices. The fibre content of both GRP and Fybroc were approximately 60% and 30% by volume respectively. The GRP samples had a laminated structure with unidirectional fibre in each lamina. The fybroc had chopped strand that were randomly dispersed. Table 5 list their general formation.

4.2.3 FERROUS AND NON FERR0US METALS

Together with the non metals, a number commercial alloys were also tested in this project. They range from pure alluminium to tool steel. These are tabulated in table 6, listing their basic compositions and conditions prior to testing.

4.3 TESTING PROCEDURE

The masses of the sample before and after a test run were taken using a Mettler electronic balance (type AE160) which was accurate to within 0.1mg. During a test, two sets of mass measurement would be recorded, one for the test specimen and the other for a control sample. The control would give an indication of any drift in instrument reading. Before a test proper, the test sample would be weighed, and the mass recorded. It will then be inserted in the rig for about 5 minutes without being subjected to cavitation. After which it will be removed cleaned and dried, then reweighed. Ideally there should not be any mass loss. In practice, a variation of not more than $\pm$0.2mg was observed.

A test run would last for either 20, 25 or 30 minutes, depending on the material being tested. The harder the material the longer the duration was the scheme adopted. Runs conducted at 30 minutes duration would raise the working temperature to just under 45 degrees Celsius. This was the limiting value for the working fluid. Hence, when temperature rose above this value, the run would be aborted and the temperature allowed to fall to an acceptable value before a

re-run. For the materials tested, a typical test sequence would be as follows; The masses of the control samples would be recorded. The test specimen would then be loaded in to the rig. After setting flow conditions, it would be subjected to cavitation for 25 minutes. It would then be removed, cleaned, dried and weighed. Three readings of the test specimen and control would be obtained and an average recorded. This sequence of testing and mass recording would be continued until a significant mass loss or steady state mass loss rate is reached. For a less resistant material, cumulative testing time could be as short as 1.5 hours, while a more resistance one would last for up to seven or more hours.

A similar set of testing procedure would then be performed on an identical specimen to assess or ascertain the repeatability of the test.

MATERIALS TESTED

CERAMICS *

TABLE 3:

MATERIAL	PRODUCTION PROCESS	FINISHING PROCESS
SILICON CARBIDE	REACTION SINTERED	FIRED GROUND LAPPED
SILICON NITRIDE	HOT PRESSED	FIRED GROUND LAPPED
SILICON NITRIDE	HOT ISOSTATIC PACKING (HIP)	GROUND

* SUPPLIER DOWTY FUEL SYSTEM

PLASTIC (EPOXY RESIN) *

TABLE 4:

DESIGNATIONN	EPOXY SYSTEM	FINISHING PROCESS
ER BROWN G	BISPHENOL EPOXY WITH PARTICULATE FILLER	AS CAST MACHINED
ER BLACK Q	NOVALAC EPOXY WITH PARTICULATE FILLER	AS CAST MACHINED
ER BROWN MG	BISPHENOL EPOXY WITHOUT PARTICULATE FILLER	AS CAST MACHINED

* SUPPLIER WORTHINGTON SIMPSON

COMPOSITE *

TABLE 5:

MATERIAL DESIGNATION	MATRICE	FIBRE	STRUCTURE *	FIBRE VOL.%	FIBRE ORIENTATATION
GRP	EPOXY RESIN	E-GLASS	ANGLE-PLY LAMINATE	60	UNIDERECTIONAL
FYBROC	VYNLE ESTER	E-GLASS	BULK SOLID	40	CHOPPED STRAND RANDOMLY ORIENTATED

* SUPPLIER BP. RESEARCH

METAL ALLOYS

TABLE 6a:

No	MATERIAL	NORMINAL COMPOSITION wt %
1	ALUMINIUM SIC	99.99A
2	AL.ALLOY HE9	0.75Mg 0.5SI BAI Al
3	AL.ALLOY HE15	0.5Mg 0.5SI 1.0Mn 4.0Cu BAL. AL.
4	AL.ALLOY HE30	1.0Mg 1.0SI 0.7Mn BAL. AL.
5	AL.ALLOY PA2	2.7Mg BAL. AL.
6	BRASS M63	36.26Zn BAL. Cu.
7	CUPRO-NICKEL	10NI 1.5Fe. 0.23Mn. BAL Cu
8	GREY CASTIRON	3.29C 0.28MN 1.27SI BAL Fe
9	ARMCO IRON	0.035C 0.1Mn 0.01SI 0.026P 0.035S BAL. Fe.
10	CARBON STEEEL (AISI 1020)	0.22C 0.12Mn 0.01SI 0.01P 0.03S BAL. Fe.
11	CARBON STEEL	0.43C 0.063Mn 0.26SI 0.03P 0.03S BAL. FE.
12	ALLOY STEEL	0.4C 1.37Mn 0.55SI 17.7Cr 9.4NI 0.6TI BAL.Fe
13	TOOL STEEL M4	1.3C 4.2Cr 0.3NI 0.25Mn 4.5Mo 5.5W 4.0V BAL.Fe
14	TOOL STEEL (CPM10V)	2.5C 5.3Cr 0.5Mn 1.3Mo 0.9SI 9.8V BAL. Fe
15	NITRALLOY (BS.S106)	0.24C 3.2Cr 0.5Mn BAL.Fe
16	NITRIDED STEEL (BS.S134)	
17	CAST STAINLESS STEEL (BS316C16)	0.08C 18Cr 10NI 2Mn 2.5Mo BAL.Fe

5.0 EXPERIMENTAL RESULT

The results presented in this chapter have been obtained from testing a number of different engineering materials. These ranged from plastic, ceramic, composite to commercial alloys. For the purposes of comparison, all samples were tested in identical conditions as mentioned in chapter 3 under testing procedure. Hence a constant cavitation number was maintained. This also had the added advantage of producing a constant area of erosion on the test specimen. Variation of cavitation intensity was achieved through changes in throat velocity.

The physical form of damage in the tested materials were examined by both optical and electron microscope. With some materials, particular attention was paid to the transition zone between the areas of simple surface deformation and those exhibiting actual loss of material.

5.1 EROSION RATE TIME PATTERN

Much information on cavitation erosion rates for numerous materials in various types of tests have been published over the past half century. However, much less information is available from testing real engineering materials and from field devices. Also many attempts have been made to correlate erosion rate with mechanical properties of materials as cited in the review chapter 2 .

In any cavitation erosion test, the damage rate is generally time dependent. Ideally (but not always) the plot of volume loss versus time follows an S-shape curve as shown in figure 26a. The exact shape or time behaviour of the curve will depend on the specific material, fluid and other parameters of the test.

In general, the erosion history for a particular material specimen could be divided into stages as shown in figure 26b, which are defined as follows;

i) INCUBATION PERIOD :

This is the initial stage of the erosion rate-time pattern during which the erosion rate is zero or negligible compared to latter stages, and also the exposure duration associated with this stage. No material lost is detectable, but damage to surface is caused by pitting in ductile materials and cracking in brittle

materials, or a combination of both. If a material exhibits work-hardening, this may extend the incubation period.

ii) ACCELERATION PERIOD:

Once deformation or cracking becomes sufficiently advanced, mass loss will commence, and the rate of material removal increases. Initially, material is removed only from localised sites, but gradually the removal will extend over a large area similar in size to the cavitation zone.

iii) STEADY STATE PERIOD :

During this period, the rate of mass loss of material is more or less constant, corresponding to material removal from the entire cavitation zone area.

iv) DECELERATION PERIOD :

The steady state mass loss rate will apply until a large cumulative mass has been lost. Eventually the erosion rate declines, probably because the loss of material is so great that local flow conditions have changed and reduced the cavitation intensity, or the eroded surface is protected by a captive layer of liquid or stagnant fluid

In practice, for a venturi-type erosion test, the acceleration period is rather indistinct in some cases, and the deceleration is rarely reached because the time required is prohibitive or

very long.

The overall erosion behaviour under cavitating conditions could be described in terms of four parameters, as express by the simple equation below.

$$ML = MLR\,(T - NIP) \qquad (16)$$

or

$$VL = VLR\,(T - NIP) \qquad (17)$$

Where ML(mg) is the cumulative mass lost, VL(mm^3) is cumulative volume lost, MLR(mg/hr) is the steady state mass loss rate, VLR(mm^3/hr) is the steady state volume loss rate, T(min) is test duration, and NIP(min) is the nominal incubation period. The latter is defined as the intercept on the time axis of a straight line extrapolated at the maximum slope portion of the curve of cumulative volume loss against time. On some occasions, the curve for volume loss rate against time for some materials would produce two distinct steady state periods. Whenever this is encountered, the one with the higher erosion rate is computed or taken.

Although weight or mass loss is actually measured, neither gravitational nor inertial effects are reckoned to be

important, and the amount of material removed is properly described by its volume. This is particularly true when comparing erosion rates of different materials. The steady state volume loss rate is considered here as being the principal parameter which characterises the erosion resistance for a given test.

5.2 RESULT ANALYSIS

The result for each material or sample tested in this project is given as a graph of cumulative volume loss versus time. The test data have been analysed using the method of least squares, the slope given the steady state volume loss rate, and the intercept on the time axis giving the nominal incubation period. The least square line is drawn in each graph. The 95% confidence limits for the slopes are also included. The above process is quite straightforward when there is an obvious linear or steady state region. However if there is a substantial acceleration or deceleration period, it is not appropriate to include all the data points. In order to deal with this in an objective way, the linear regression analysis is performed repeatedly with fewer data points until the 95% confidence limits reach a minimum value. This condition is then taken to define the slope and intercept of the best fit line and consequently the volume loss rate and nominal incubation period.

In many flowing devices such as rotating disc, jet impact devices, and tunnel devices using separated flow pass a pin such as that pioneered by Shalnev(1955), or flow over an ogive as used by Knapp(1955), it has been observed that damage rates are proportional to a relatively high power

of velocity. The 6th power was suggested by Knapp (1955), and these seems fairly representative for the damage obtained with these types of devices. Later tests have shown that the exponent varies with many factors. Grant (1984) testing model materials of aluminum and perspex in the same rig used in this project, and under identical conditions found a power law equation to fit the data best. He found the velocity exponent for both aluminum and PMMA to be 6.9 and 9.0 respectively.

In this project as mentioned earlier, the cavitation intensity was varied by changing the throat velocity in the working section in the venturi. For samples were this has been done the velocity exponent has been obtained. This has been computed assuming the simple power law equation of

$$VLR \propto V^n \qquad 18$$

With the application of simple algebra, the above law could easily be written as

$$\frac{VLR_1}{VLR_2} = \left(\frac{VELOCITY_1}{VELOCITY_2}\right)^n \qquad 19$$

from where the exponent is calculated. Subscript 1 and 2 represent the lower and higher values of velocity and volume loss rate respectively.

To verify the above relationship in equation 18, tests were performed on GRP using four different velocities, ranging from 45 to 30 in steps of 5 m/s. Although it would have been more objective to test a wider range of velocities, it is important to point out that, 45 and 30m/s were the maximum and minimum velocities the rig could sustain while cavitating conditions were maintained.

Also the characteristic curves of erosion rate against time for the non-metals have been produced. The erosion rate values have been obtained by computing the slope of the line joining the origin and each data point on the cumulative volume loss versus time curve (tangent slope) for each data file. i.e for each material sample considered.

Both hardness and micro-hardness values for all samples tested were measured. The hardness values were got using a Vickers hardness machine with a 20kg load. While the micro-hardness values were obtained using a Shimadzu micro hardness tester with a 500kg load.

Cavitation erosion tests generally are very time consuming, this is particularly so when a venturi rig is employed. However, in this project effort were made to duplicate test with each sample specimen.

It was observed generally that deviations or percentage difference between repeated tests did not exceed 5% with regards to VLR and NIP . Typical graphs showing degree of repeatability have been plotted. This essentially have been done by plotting both test data on a single graph

5.2.1 PLASTIC

From table 4 it is seen that the plastic materials employed in this project were all derivatives of epoxy resin. Table 7 list their nominal mechanical properties. The primary objective in testing these materials were twofold. Firstly, to ascertain the erosion resistance of the two production processes employed in producing both surfaces, and secondly, to compare the erosion performance of the three epoxy resin systems.

Fig.27 to 36 shows the characteristic plots of volume loss against time for each epoxy resin sample tested. Using least squares regression analysis to those points adjudged to lie in the steady state region the mass loss rate (MLR), volume loss rate (VLR) and the nominal incubation period (NIP) were calculated for each sample. These together with the running conditions are shown in each plot of volume loss against time.

Table 8 and 9 list the results for both the as machined and "as cast" samples at both high and low cavitation intensities respectively. Also included in the above tables are results for the hardness and micro-hardness values of the test samples. Table 10 list the velocity exponent for the epoxy resins. In the above table, the velocities and volume loss rates from which the exponents were computed are also given. Fig.37-46 shows the comparison graphs between the epoxy resin systems

and also between the two surface conditions. Here the erosion data of the two samples or surface conditions being compared are plotted on the same graph to illustrate their performance differences. Fig.47-49 shows the characteristic erosion rate versus time curves for the epoxy resin systems.

5.2.2 CERAMIC

The ceramic materials used in this project are listed in table 3. It shows their production process and surface conditions prior to testing. The basic parameters used to characterise these materials are shown in table 11 under the heading of mechanical properties.

Silicon carbide and silicon nitride are covalently bonded compounds, and tend to dissociate at temperatures well below their melting points, a property that introduces some problems in the attempt to process and form these materials. Both silicon carbide and silicon nitride are extremely hard, and thus very difficult and expensive to machine. Therefore in order to avoid the necessity of expensive machining of the final parts from the material, the only cost-effective and practical processing method is through powder technology. Powders from these materials can be pressed and sintered into a shape that may then only need minor machining to produce the final product.

However, no matter the extent to which the final machining or surface finishing processes are carried out, they will always introduce surface defects such as roughness, surface and sub surface cracks and would leave the surface

with a residual stress. There have been a number of studies into the strength of silicon carbide and silicon nitride machined and treated under a variety of conditions. (Allor et al (1983), Anderson et al(1979), Hakulinen.M (1985)). Some of the effects reported are considerable, and they are a cause for concern to the producer, not only with respect to the manufacture of the component but also to its possible behaviour in service.

As seen from table 3, three surface morphologies were tested for their cavitation resistance and consequently the performances of both the surface finishes and the bulk ceramic materials were ascertained. The surface roughness of the above surface finishes are shown in table 12a. These were measured using a Talysurf profilometer. As would be expected the as lapped surface was the finest. However, visually and under low magnification the differences between the above surface roughness was not very apparent.

Figures 50-62 show the characteristic plots of cumulative volume loss against time for the individual samples tested, from were the cavitation parameters of MLR, VLR and NIP are obtained. These values together with the test conditions are shown in each figure. Variation in cavitation intensity i.e changing velocity from 40 m/s to 45 m/s enabled computation of the velocity exponent. Assuming a power law relationship between erosion rate and velocity, and

using equation 19, the velocity exponent for silicon carbide and silicon nitride were obtained and these are shown in table 12b .

The general result for both silicon carbide and silicon nitride in all three surface conditions are tabulated in table 13 and 14 respectively. In these tables the MLR, VLR NIP, Hv , Hv and test velocity of the respective material-surface combination are given. The above cavitation parameter i.e MLR, VLR and NIP were obtained using regression analysis as discussed in this chapter under section 5.2.

The performance of the various surface finishes and the two ceramic base materials are shown in comparison graphs in figures 63-70. In these plots the data of the materials or surface finishes to be compared are plotted on the same graph. Typical erosion rate versus time plots for both silicon carbide and silicon nitride are shown in figures 71-76.

5.2.3 COMPOSITE

A composite consists of two or more physically distinct materials which are combined in a controlled way to achieved a mixture having more useful properties (to defined criteria) than any of the constituents on their own.

Polymer composites with continuous fibre reinforcement of high volume fraction and perfect alignment are known to possess very high values of specific strength and stiffness. Their properties can be tailored according to the load system acting on a structural part made from these materials. Besides these advantages, the wide variety of different fibre and matrix materials permits the design of composites with unique properties for different kinds of applications.

The composites materials tested in this project are listed in table 16 These were GRP and Fybroc (glass fibre in a matrix of Vinyl ester) . The GRP had a laminated structure with unidirectional fibre orientation, while Fybroc was manufactured with chopped strand randomly dispersed in the matrix.

Graph of volume loss against time for GRP at various cavitation intensity (i.e at different velocities) are shown

in figure 77-80. On these graphs, the regression line is shown, together with the running conditions. The GRP samples were tested at four different velocities i.e, 45, 40, 35, and 30 m/s, respectively. This provided enough data to compute the velocity exponent for this sample. Figure 81 shows the variation of volume loss rate with velocity. The used of log scales resulted in the data lying approximately on a straight line, suggesting that a power law relationship is appropriate. Using least square regression on the data yields the relationships;

$$VLR \propto V^{6}.14 \qquad 20$$

The characteristic curve of erosion rate against time for GRP is shown in figure 82. The data for the above characteristic curve were obtained at high cavitation intensity , i.e 45m/s.
For the Fybroc sample two tests were done at 40 and 35m/s respectively. The individual graphs of cumulative volume loss against time for this sample are shown in figure 83 and 84. Figure 85 shows the graph of average cumulative erosion rate against time at both low and high cavitation intensities respectively for the Fybroc sample.

Comparison graphs for both GRP and Fybroc tested

at comparable velocities are shown in figure 86 and 87. The summarised results for both GRP and Fybroc are tabulated in table 17.

5.2.4 METAL ALLOY

Together with the non-metals, a number of metal alloys were also tested for their cavitation resistance. Table 6a and 6b list both their nominal composition and condition respectively prior to testing. It is seen from the above tables that quite a wide range of materials were employed. These range from soft aluminum to hard materials such as tool steel and nitrided steel. Also noticeable from table 6b, is the fact that various heat treatment processes have been performed on these alloys.

The data obtained from this class of materials were also analysed using the method of least squares mentioned in section 5.2. The result for each sample plotted as cumulative volume loss against time are shown in figure 88-98. Similar to previous results, their running conditions are also included in these plots. Table 17 gives the summarised result of all the metal alloys tested in the programme. As with the 0previous result tables, this also list values of VLR, NIP, Hv and Hv respectively.

5.3 GENERAL OBSERVATION OF EROSION PATTERN

The physical form of damage in the tested materials were examined by both optical and electron microscope. With some materials particular attention was paid to the transition zone between the areas of simple surface deformation and those exhibiting actual loss of material.

The observed erosion pattern shows obvious differences between the damage sustained by the various classes of engineering materials both in terms of extent and morphology. In some respect this is not surprising since the materials belong to distinctly different groups.

5.3.1 PLASTIC

Before testing of the epoxy resins, the surfaces of both the "as cast" and the as machined samples were measured using a Talysurf profilometer. The as cast samples had a smoother surface with an average roughness of less than 0.7 m . The machined surface had an average roughness of 1.2 m (centre line average). Figure 100a and 100b shows the

surface morphology of the above two conditions using an optical microscope prior to testing. The contrast between the two surface is very evident in the above micrographs. The cast sample is apparently smooth apart from microscopic pores. The effect of machining, as seen in figure 100b, completely removed the smooth skin layer. The machined surface is relatively rough, full of machined markings.

For the two surface conditions tested i.e, "as cast" and machined, there were no apparent difference in the erosion pattern observed, from pits or crack formation to full scale material removal. It was evident after the first run at high cavitation intensity (45m/s), and after the second run at low intensity (40m/s) that, no significant plastic flow occurred prior to material removal. Although the impact sequence could not be traced precisely due to interaction of a large number of impact by micro jets, the epoxy resin clearly shows crack initiation, growth and removal of material as shown in the damage progression sequence in figure 101.

Figure 101a shows an optical micrograph of the initial damage on a machined surface tested at 45 m/s. A network of micro-cracks predominates during this initial stage. It then developed into a network of macro-cracks and travelled in all directions. As erosion progresses, small and large crevices would form at the sites of the intersecting cracks. Figure 101b shows localised damage and cracking which

resulted in the removal of large pieces of material. The micrograph clearly shows initiation of brittle fracture as demonstrated by the sharp boundaries. As erosion progresses further, large fragment of material would be dislodged, leaving a large crevice behind as shown in figure 101c.

Another mechanism which resulted in the removal of large fragment of material, was the propagation of cracks into the material, and then parallel to the surface, only to return at a different point on the surface. Figure 102a is a typical example resulting from this mechanism.

Although brittle failure was observed as the primary mode of fracture, individual grain disintegration from the resin was also observed on fractured surfaces as illustrated in Figure 102b. This secondary mode of failure generally occurred on the sharp edges of a fractured surface or in large crevices.

The final damage profile sustained was in the form of a trench, elongated in the direction of flow, with the central zone deeply pitted, while the surrounding or adjacent sites showed sign of extensive surface pitting. A typical macroscopic view of gross damage on one eroded area is shown in Fig 102c.

5.3.2 CERAMIC

5.3.2.1 SILICON CARBIDE

Photomicrographs taken from an optical microscope of the three surface finishes employed are shown in fig 103. From figure 103a and 103b it is seen that both the ground and lapped samples had similar surface features. Both surfaces were covered with little tiny pores or pits. The grinding marks on the ground sample are still very evident. In the lapped sample in figure 103b, it is seen that the grinding marks have been removed. The as fired or sintered sample in figure 103c had more or less a pore free surface. The microstructure in the form of grain boundaries could just be seen in the above figure. At a higher magnification , one could easily see areas of "free" silicon (light areas) in the reaction sintered silicon carbide as shown in figure 103d.

The observed material removal mechanism from the three surface finishes was not significantly different. It was observed generally that the failure mode was predominantly brittle in nature, as will be seen later. Figure 104 shows a typical damage progression sequence from both optical and scanning election microscopes respectively. Figure 104a shows initial pitting formation. These were shallow and very irregular in both size and shape. As exposure increases these

pits tend to coalesce or link up and consequently increasing in size. As the above process was occurring, there would be further pit formation inside existing ones and on plain areas thus producing further deeper pits as shown in figure 104b. There was no appreciable plastic flow prior to the formation of these pits or craters. At this early stage, material loss was noticeable though not properly resolved in the above optical micrograph. The scanning electron micrograph of figure 104c which shows a magnified view of the pit in figure 104b clearly depicts several features which are not visible under the light optical microscope. Areas of complete destruction with fracture planes, cracks, and isolated irregular-size pits are clearly evident. Further exposure resulted in a network of micro-cracks and macro-cracks propagating in all directions. The overlapping of these network of intersecting cracks will result in fragments of material being removed as shown in figure 104d, taken from an optical microscope. The sub surface crack propagation not seen in figure 104d is clearly depicted in the scanning electron microscope of figure 104e. In the above micrograph, crack growth or propagation into the material is clearly illustrated. The fractured surfaces are unquestionably smooth and sharp showing evidence of brittle failure.

Apart from material removal by both micro-crack and macro-crack intersections, chipping was also

observed to be another major mode of failure. A sizable chip would be observed to have been removed repeatedly around the central zone area during the advanced stages of erosion. Figure 105a shows a typical photograph of gross damage on one eroded area, clearly showing the chipping effect. It is also seen from this photograph that the damage area, exhibits a propensity for cracks to propagate well beyond the cavitation zone. This effect thus gives a conservative result of the actual cavitation damage area. A scanning electron micrograph taken inside the central damaged zone in figure 105a is shown in figure 105b . Here again brittle features such as cleavages in transgranular fractures are evident. Figure 105c show a localised crack in the central erosion zone. Figure 105d shows an optical micrograph of the surface topography of a chipped surface. Figure 105e shows a typical picture of gross damage sustained in silicon carbide after a completed test. The characteristic trench type crater elongated in the direction of flow as common in venturi-type test is very evident.

5.3.2.2 SILICON NITRIDE

Optical micrographs of the three surface finishes employed, i.e, ground, lapped and as fired are shown in figure 106. Here as well, the contrast amongst the three surface finishes was not that pronounced. Figure 106a shows the as ground sample with its characteristic grinding marks. Figure 106b is of the lapped sample, where it is clearly seen that, almost all of the grinding marks have been removed. The surfaces of the above two finishes were pore free. In the as fired sample shown in figure 110c tiny little pores or pit were observed on the surface. These obviously were developed during the sintering process. It should be noted that the surface roughness amongst the three finishes was not that significantly different as shown in table 12a.

Erosion damage progression sequence for this material were taken by an optical microscope and are shown in figure 107. Figure 107a shows the plain surface prior to testing. After being subjected to induce cavitation erosion for just under 50 minutes, the surface topography was changed to that shown in figure 107b. It shows a clouding effect of the damaged area. This was caused by the formation of a large number small depressions as a consequence of the micro jets impact. No material loss was observed at this stage. As exposure time increases, it was obseved that, small isolated pits would

emerge from the "clouded" surface. (This is shown in figure 107c though not properly resolved). Further exposure would result in deeper and wider pits as shown in figure 107d. Material loss just after the incubation period was observed to be as a result of the coalescence of the large pits or craters. At advanced stages of erosion, the material removal process was concentrated around the vicinity of the central zone as shown in figure 107e, which shows a typical gross picture of one eroded area. The adjacent region surrounding the central zone had a "ripple" surface topography. In the central zone itself material removal was occuring primarily as a result of intergranular fracture as illustrated by figure 107f and 107g. These were taken using the optical microscope from two local regions in the central zone. The characteristic cracking and chipping observed with silicon carbide was very much absent with silicon nitride. Figure 107h shows a typical photograph of gross damage as sustained on silicon nitride after a completed test.

5.3.3 COMPOSITE

5.3.3.1 GRP

Before testing the GRP samples their surfaces were examined under the optical microscope. They were observed to possessed macroscopic pores, typically in the range 50 to 100 m in diameter. These were circular in shape and randomly distributed over the entire surface. Figure 108 shows an optical micrograph of the above mentioned surface with typical pores disposition.

Initial cavitation induced erosion damage on this material were centered on the resin top surface. Here the micro jet impact would initially form micro-pits which tend to grow in size as erosion progresses. If these pit formations interact with pre-existing pores, the process is accelerated with subsequent fibre exposure as shown in figure 108a.

As erosion progresses it was observed that material removal was essentially due to fibre and matrix debonding as a result of the micro jet impact, and the subsequent stress waves. Typically a layer will be removed together with the impregnating resin. It was observed during this high cavitation test (45m/s) that it took less than 10 minutes for the first ply to be partially eroded. Figure 108b shows a micrograph of the skeleton nature of the fibre totally devoid of resin. At the

left side of the micrograph one could see the fractured end of the fibres that were oriented at 90 degrees to the bottom ply which is just about been damaged. Figure 108c clearly shows the effect of delamination, and the selective nature of layer by layer erosion. Three plies are easily distinguished from their fibre orientation. Figure 108d is an optical micrograph depicting three fractured fibres, clearly indicating the fibre-matrix interfacial separation. Typical of venturi-type test , the cross-sectional area of damage was observed to decreased with increasing thickness of composite. However, unlike other materials the central cavitation zone of the eroded GRP sustained a greater depth of penetration. This tunneling effect is clearly seen in Figure 108e, which shows a photograph of gross damage on one eroded area.

5.3.3.2 FYBROC

The surface of the Fybroc specimen was rough and full of scratches as depicted in figure 109, prior to testing. Erosion progression as observed with this specimen was typically brittle in nature.

Figure 110 shows the overall development of pits. These are progressively chosen to depict specifically typical growth of

undamaged surface to transition and finally to complete destruction. These micrographs not only exhibit the progression of damage on the surface as individual pits enlarge and develop, but also the erosion process causing material loss.

Initially, the pits are small and as the exposure increases, the size of pits increases. Figure 110a shows initial damage in the central zone, where the vinyl ester matrix has been damaged, and the glass fibres are just exposed. Also visible in this micrograph is the random disposition of the fibres. As erosion progresses more of the brittle matrix is crushed as illustrated in figure 110b, exposing more of the fibre as a result of debonding. On further exposure as shown in figure 110c, the entire strand of fibre is broken easily as a result of no protection. Clearly the delamination effect observed with GRP is totally absent with this specimen. Figure 110d shows a photograph of gross damage on one eroded area.

5.3.4. METAL ALLOYS

Detailed studies were also done on the material removal mechanism on a number of commercial alloys. These are listed in table 6. Similar to the non-metals, the observations studies with these metal alloys were done at high cavitation intensity i.e. at 45 /s.

5.3.4.1 ALUMINIUM ALLOY (PA2)

Figure 111 shows a series of damage progression photomicrographs using the optical microscope for recrystalised annealed aluminum. The very early damage observed in this specimen is shown in figure 111a. It shows isolated depression at the centre of which are deeper faceted pits. They are normally circular in shape with raised rim. The area adjacent to the pits show sign of extensive work hardening.

Increased exposure would produce an increase in pit density. As the pits size increases they would subsequently overlap producing a surface topography as shown in figure 111b. Material removal was noted at this stage, and the process was observed to be by "necking" or tearing of the extruded ridges between adjacent pits. Figure 111c shows a scanning electron micrograph of damage in the central zone during the final

stages in the erosion process. It clearly depicts a surface topography that has been fractured by tearing or ductile rupture. Macroscopic view of gross damage with the above specimen after testing for two hours and twenty minutes is shown in figure 111d.

5.3.4.2 CUPRO-NICKEL (90/10)

Figure 112 shows the damage progression sequence for cupro-nickel in the annealed condition using an optical microscope. Figure 112a. shows the specimen surface prior to testing, indicating slight artifacts resulting from machining. During the initial stages of cavitation attack no significant changes occurred. As the exposure time within the incubation period increases, signs of plastic deformations were observed on the surface as shown in figure 112b. They had the effect of diminishing the reflectivity of the surface. As cavitation attack progresses, pits of varying sizes, and mostly circular in shape with raised rim would appear randomly on the surface. As erosion progresses so does the pit density, as shown in figure 112c. With further increase in exposure, the pits would broaden, and initial material removal would commence between ridges of pits. This was similar to the process of necking observed in aluminum. Figure 112d shows the material removal process after necking. Scanning electron micrograph taken from the

central zone during the final stages in the erosion process is shown in figure 112e. In the above micrograph large dimples are clearly seen on the fractured surface, showing evidence of ductile failure. Figure 112f shows a photograph of gross damage on the above specimen after being subjected to cavitation for two hours.

5.3.4.3 BRASS (single phase)

Observation on single phase brass were in all respect very similar to the sequence described above for cupro-nickel. Damage during the final stages of the erosion process is shown in figure 113a, and a scanning electron micrograph of damage in the central zone is shown in figure 113b. The above fractured surface show signs of tearing or ductile rapture, with ill-defined dimples.

5.3.4.4 ARMCO IRON

The damage progression for Armco iron recrystalised and annealed is shown in figure 114. Figure 114a shows the surface of the specimen before testing. After initial exposure to cavitation attack lasting about 30 minutes, the surface was observed to have deformed appreciably with little

tiny depressions covering the affected area. No material loss was observed at this stages. The effect of the above depressions were mainly on the reflectivity of the surface as shown in figure 114b. As exposure is increased further, some of the depressions would turn in to pits, which would then eventually grow and link up with adjacent ones. The first detectable material loss occurs by a ductile mechanism akin to those described for cupro-nickel. It results in severe surface distortion as shown in figure 114c.

Damage sustained during the final stages of the erosion process is shown in figure 114d using a scanning electron microscope. The ductile nature of failure with this specimen is very evident in the above micrograph. It shows large dimples from micro void coalescence. A further scanning electron micrograph taken from another area in the central zone further indicate another mode of fracture, "ductile tearing" as shown in figure 114e. A photograph of gross damage on this specimen is shown in figure 114f.

5.3.4.5 CARBON STEEL

For the two carbon steels tested in this project, the initial deformation and subsequent material removal process were similar to those described for armco iron above. However material loss during the final stages of the

erosion process were obviously different as the following scanning electron micrographs illustrate. Figure 115a and 115b shows ductile tearing and intergranular fracture respectively for the hyper quenched carbon steel (45). The above micrographs were taken from two separate areas in the central damage zone. Figure 115c is the damaged surface of the annealed carbon steel (AISI1020). In the above micrograph the topography of the damaged surface clearly reveals a fractured surface with dimples.

5.3.4.6 STAINLESS STEEL (Acid resistance)

The damage progression for the heat refined, acid resistance steel is shown in figure 116. Figure 116a shows the undamaged surface prior to testing. After the first 60 minutes of testing, the surface was observed to be intact, i.e there was virtually no markings or depressions as observed with the previous alloys. On further exposure the familiar tiny depressions were observed. They were typical of those found in carbon steel. Initially they turn to diminish the reflectivity of the surface as shown in figure 116b. As exposure time increases the tiny depression marks would nucleate into sites for pit formation as shown in figure 116c. As more and more pits were formed as a result of increased exposure, material loss was detected after a lengthy incubation period lasting over two hours.

Figure 116d shows the initial stages of material removal. More exposure led to a very deformed surface topography as shown in figure 116e. In the above photomicrograph adjacent craters are seen to be connected by thin or skeleton ridges. On further erosion, these skeleton ridges are removed, leaving a bigger crater as in figure 116f. At the final stages of the erosion process, scanning electron micrographs taken from two separate areas in the central zone are shown in figure 116g and 116h respectively. Figure 116g shows clearly the brittle nature of failure i.e intergranular fracture, while figure 116h shows a surface topography akin to ductile rupture.

5.3.4.7 TOOL STEEL (CPM10V)

Initial pitting in tool steel is shown in the scanning electron micrograph of figure 117a. They were shallow and non-circular in shape. The characteristic raised rim found in pits in ductile alloys were very much absent. This is clearly shown in the optical micrograph in figure 117b. As erosion progresses micro-cracks from the edges of the pits would tend to propagate, and subsequently link up with adjacent pits as shown in figure 117c. This would tend to increase the size of the damaged area. Initial material removal was observed to be as a result of micro-cracks interaction. Once this is widely spread, the surface becomes highly deformed as

shown in figure 117d. With increase cavitation attack, the surface is deformed further with the emergence of large pits and craters as shown in figure 117e.

Scanning electron micrograph taken from the central zone during the final stages in the erosion process is shown in figure 117f. Quasi-cleavage facets and shallow ill-defined dimples are evident in the above micrograph. A macroscopic view of gross damage on this specimen is shown in figure 117g.

5.3.4.8 NITRIDED STEEL

The damage progression sequence observed with nitrided steel is shown in figure 118. Initial pitting formation was very similar to those of tool steel, in that they were non-circular, shallow, and without the raised rim found in ductile alloys. Figure 118a shows a typical photomicrograph using an optical microscope to illustrate the above feature. Figure 118b shows initial pitting in nitrided steel as seen using the scanning electron microscope. During this initial stage, the depth of an individual pit is very much less than its mean surface diameter. With further increase in cavitation attack, the pit density i.e, number per unit area will also increase. They will subsequently link up as micro-cracks from the edges of adjacent pits propagate and intersect. This formation is shown in figure 118c. Increased exposure would further produce a highly deformed surface with isolated pits having a

very high ratio of depth/diameter emerging. Figure 118d shows a photomicrograph of the above process. Three pinhole pits could just be seen in the centre of the above picture . With further exposure the above pits would tend to widen, and eventually formed a surface topography as shown in figure 118e.

It was also observed with this specimen that, material would occasionally be removed from an area far off from the cavitating zone, without any sign of pitting or plastic flow prior to removal. The above process could best be defined as "spalling". The spalled surface is in complete contrast with that in the cavitation zone in terms of the surface - topography. Figure 118f shows a photomicrograph of a typical example, with lines radiating from the centre of impact at the bottom of the photomicrograph.

Scanning electron micrograph taken from the centre zone during the final stages of the erosion process is shown figure 118g. Here also the are signs of quasi-cleavage facets with ill-defined dimples. A microscopic view of gross damage with this specimen is shown figure 118h, where the effect of spalling is clearly seen adjacent to the central cavitation zone.

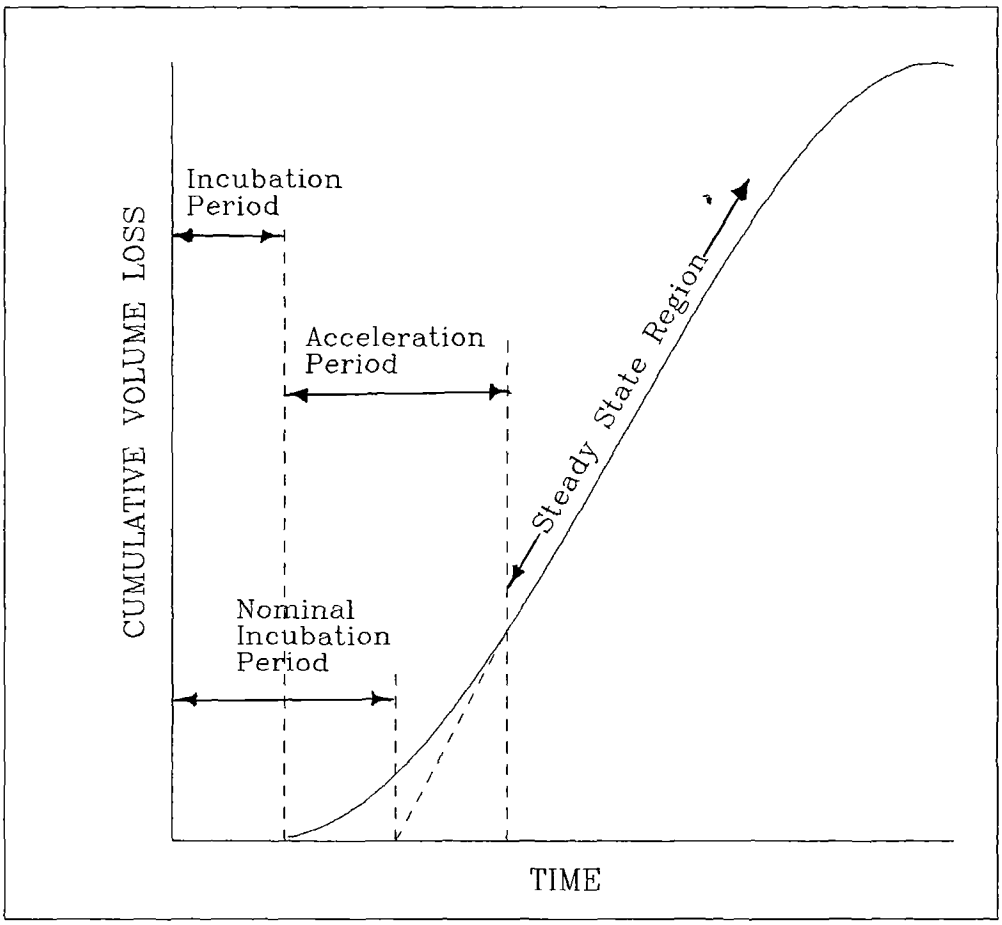

Fig26A. Typical Cumulative Volume loss Versus Time Behaviour

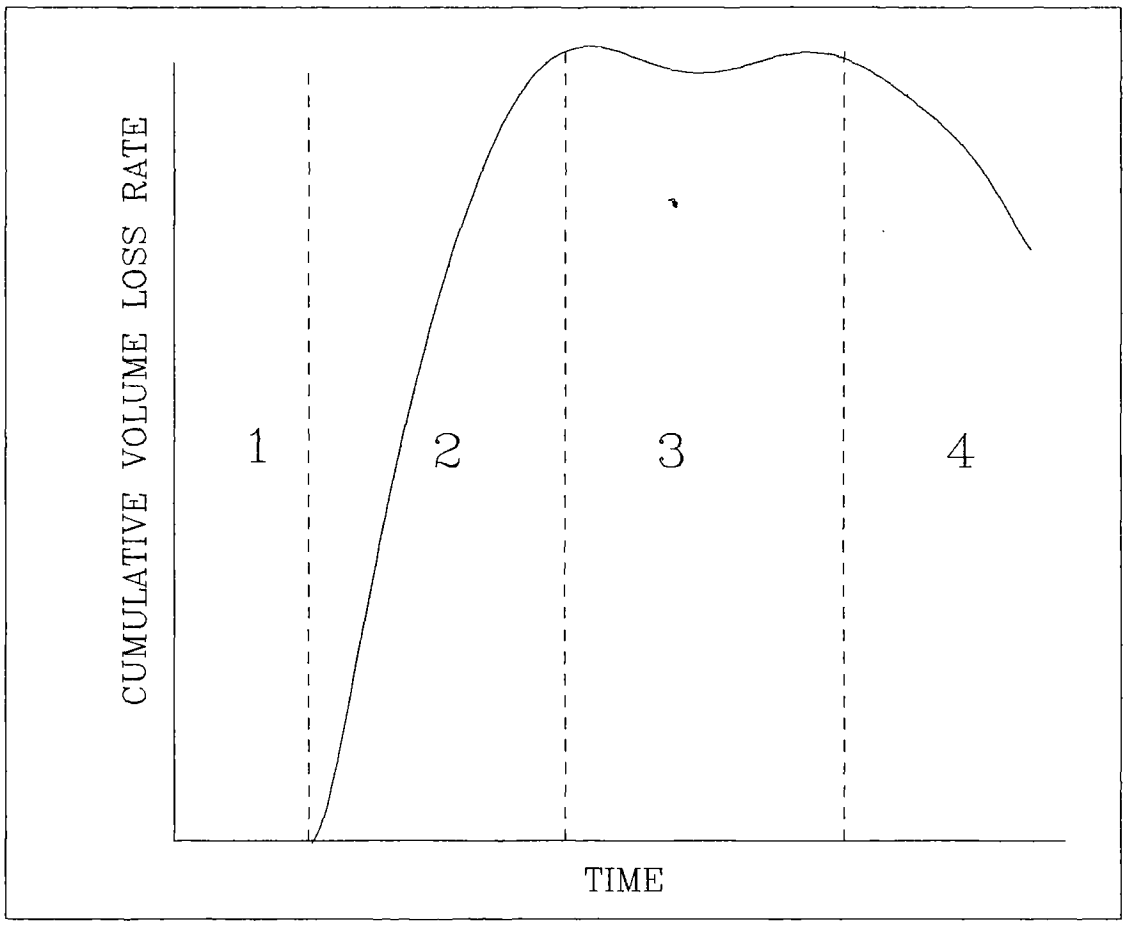

Fig26B. THE FOUR STAGES OF EROSION

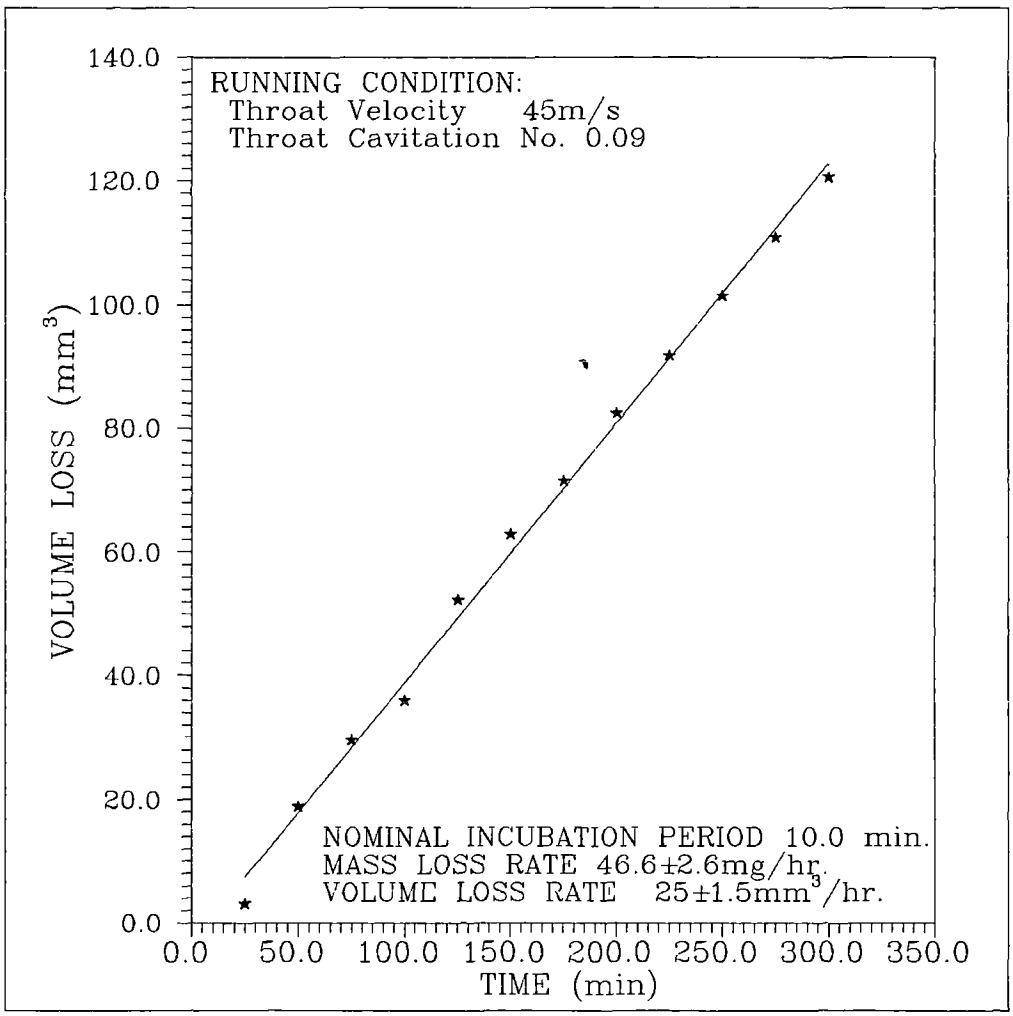

Fig.27 GRAPH OF CUMULATIVE VOLUME LOSS AGAINST TIME FOR EPOXY RESIN (BLQ) AS CAST

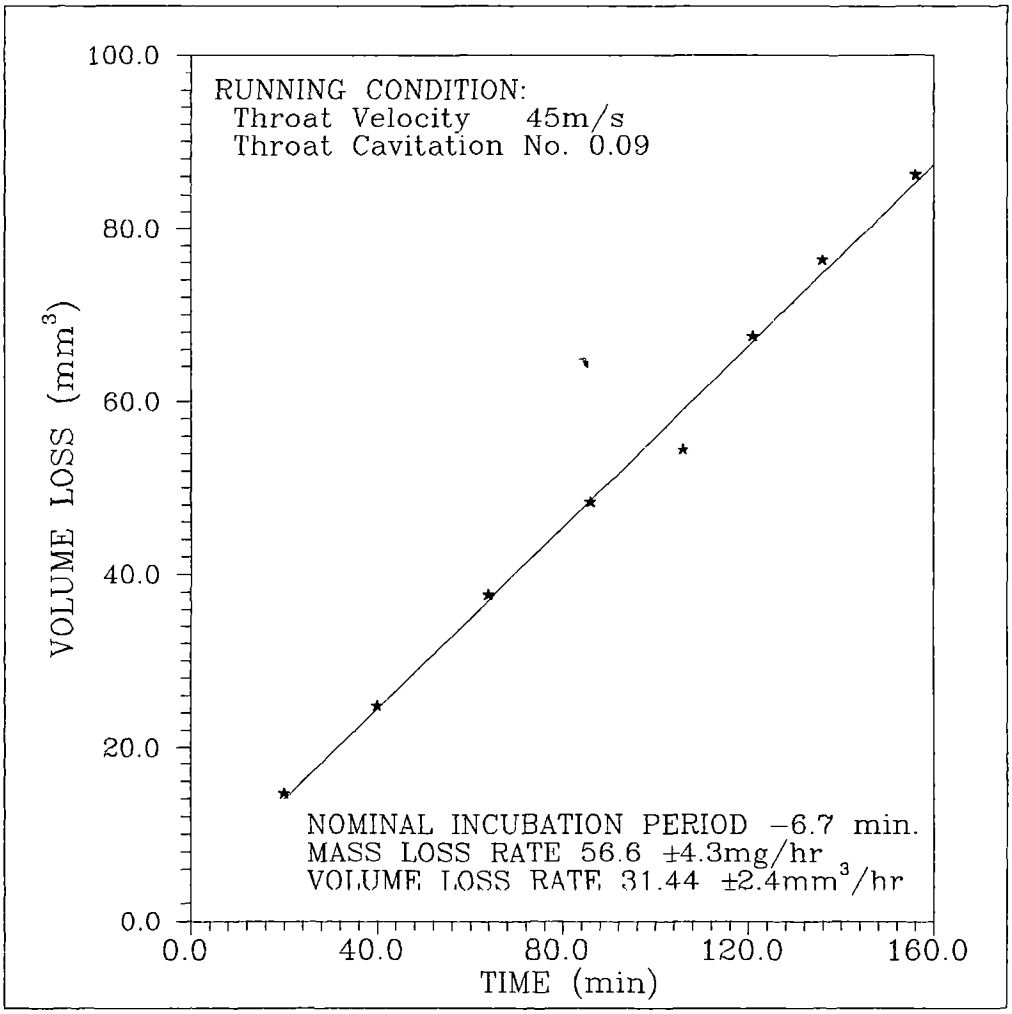

Fig.28 GRAPH OF CUMULATIVE VOLUME LOSS AGAINST TIME FOR EPOXY RESIN (BL.Q) MACHINED

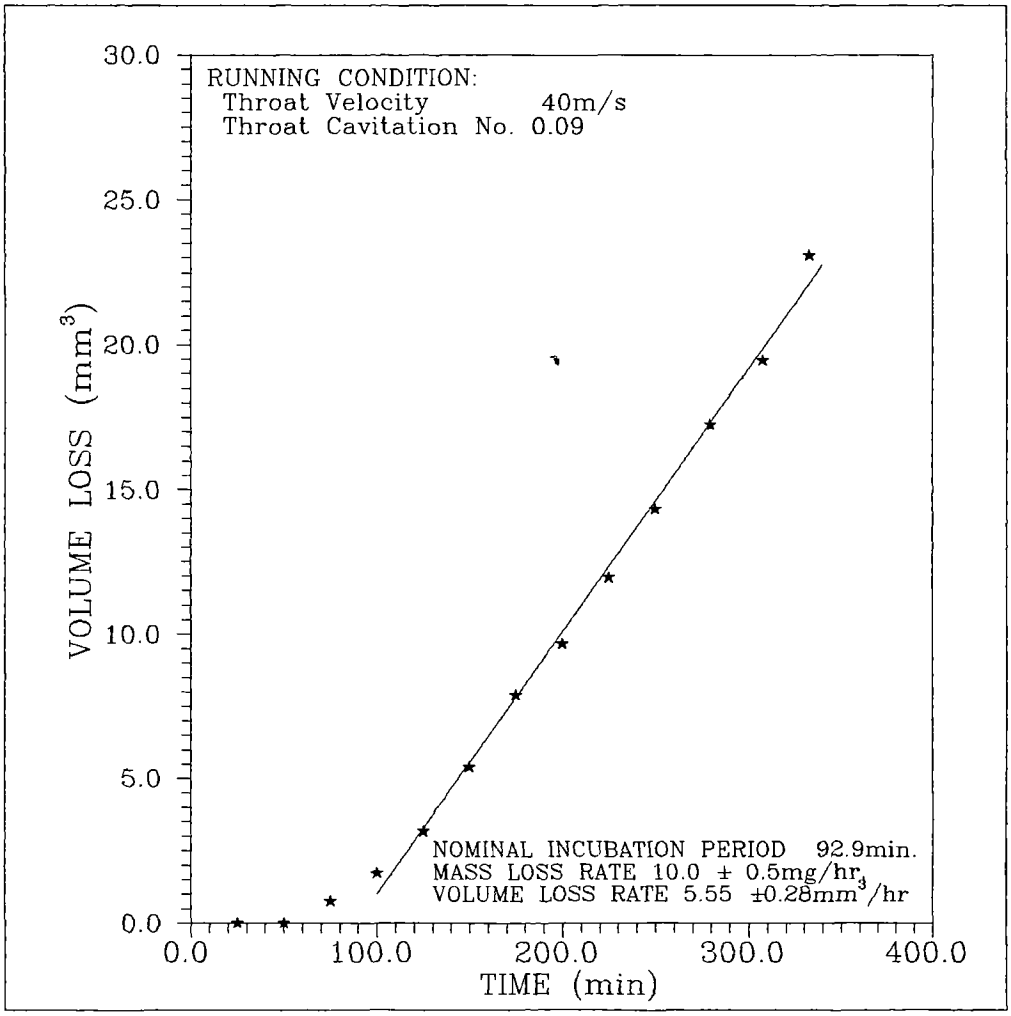

Fig.29 GRAPH OF CUMULATIVE VOLUME LOSS AGAINST TIME FOR EPOXY RESIN (BL.Q) AS CAST

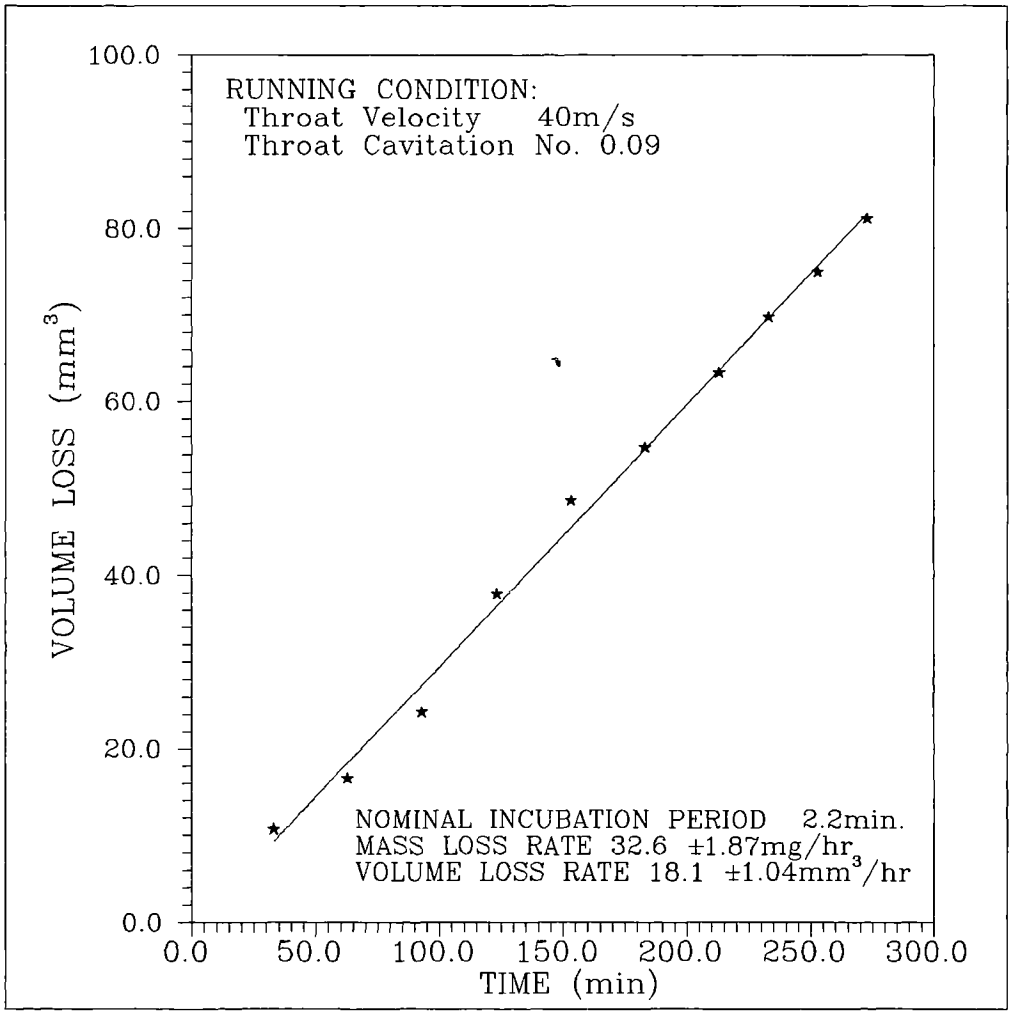

Fig.30 CUMULATIVE VOLUME LOSS AGAINST TIME FOR EPOXY RESIN (BLQ) MACHINED

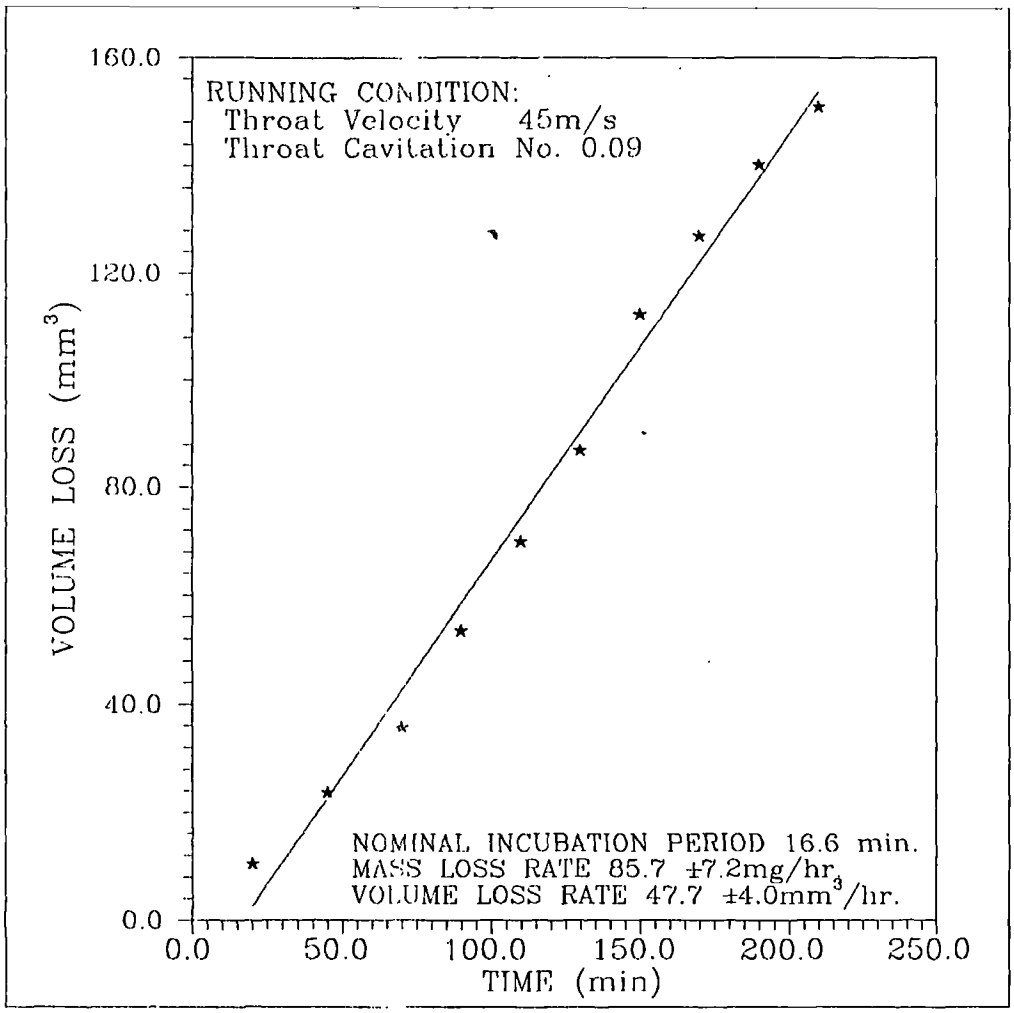

Fig.31 CUMULATIVE VOLUME LOSS AGAINST TIME FOR EPOXY RESIN (BR.G) MACHINED

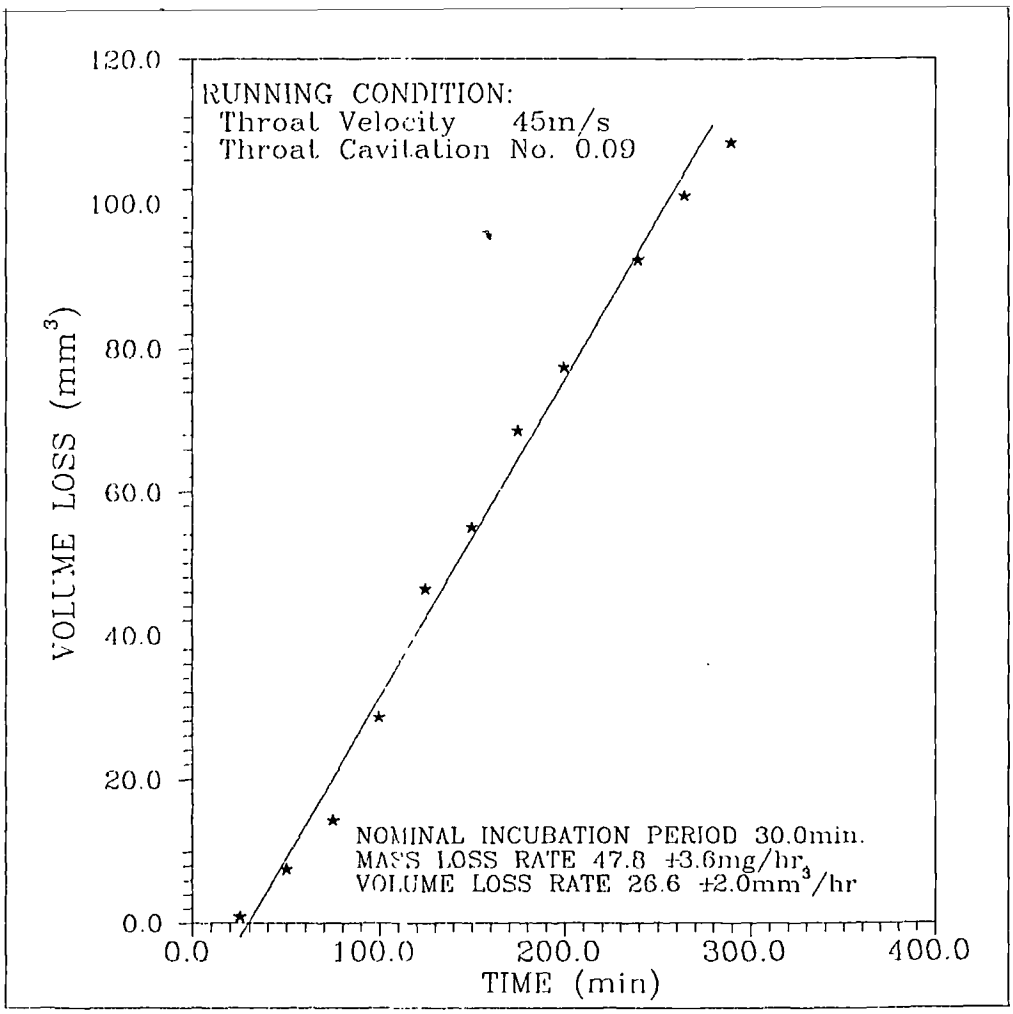

Fig.32 GRAPH OF CUMULATIVE VOLUME LOSS AGAINST TIME FOR EPOXY RESIN (BR.G) AS CAST

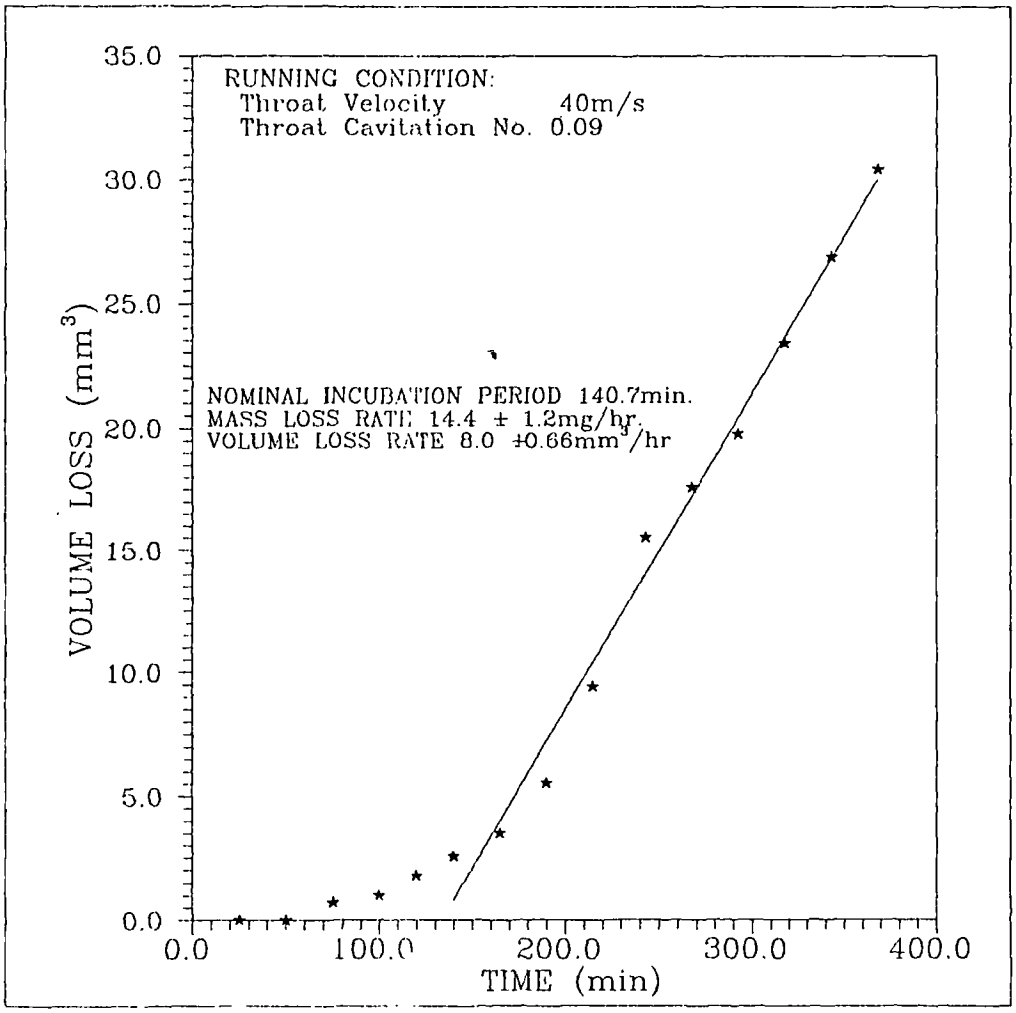

Fig.33 GRAPH OF CUMULATIVE VOLUME LOSS AGAINST TIME FOR EPOXY RESIN (BR.G) AS CAST

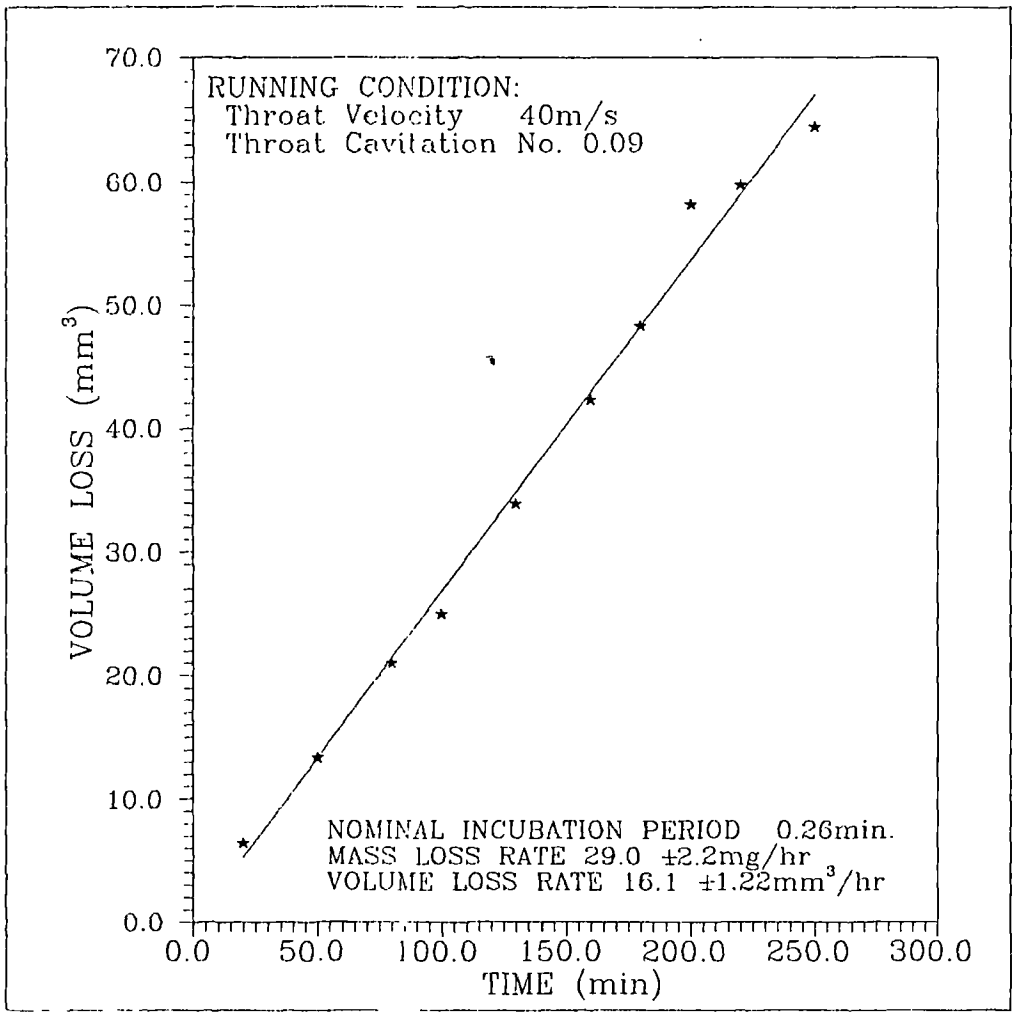

Fig.34 CUMULATIVE VOLUME LOSS AGAINST TIME FOR EPOXY RESIN (BR.G) MACHINED

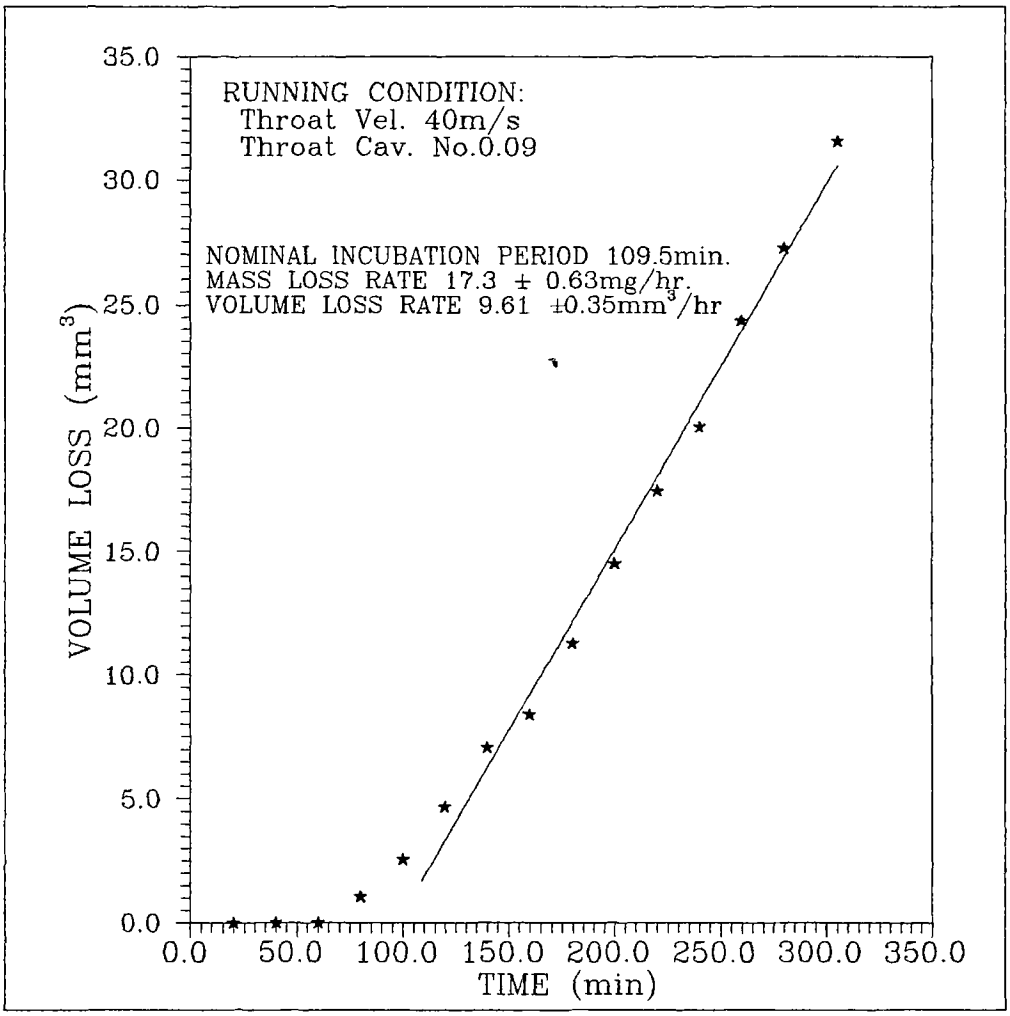

Fig.35 GRAPH OF CUMULATIVE VOLUME LOSS AGAINST TIME FOR EPOXY RESIN(BR.MG) AS CAST

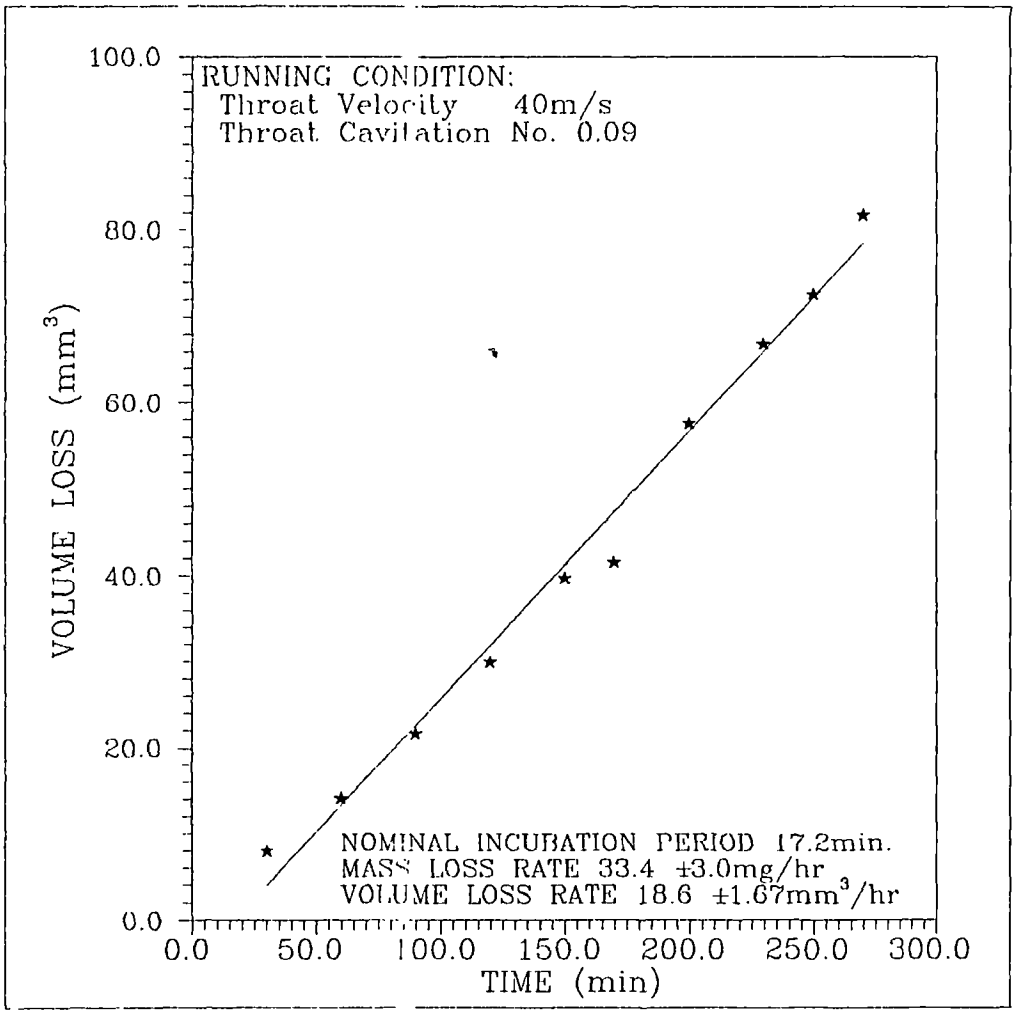

Fig.36 Cumulative Volume Loss Against Time For Epoxy Resin (Br.MG) Machined

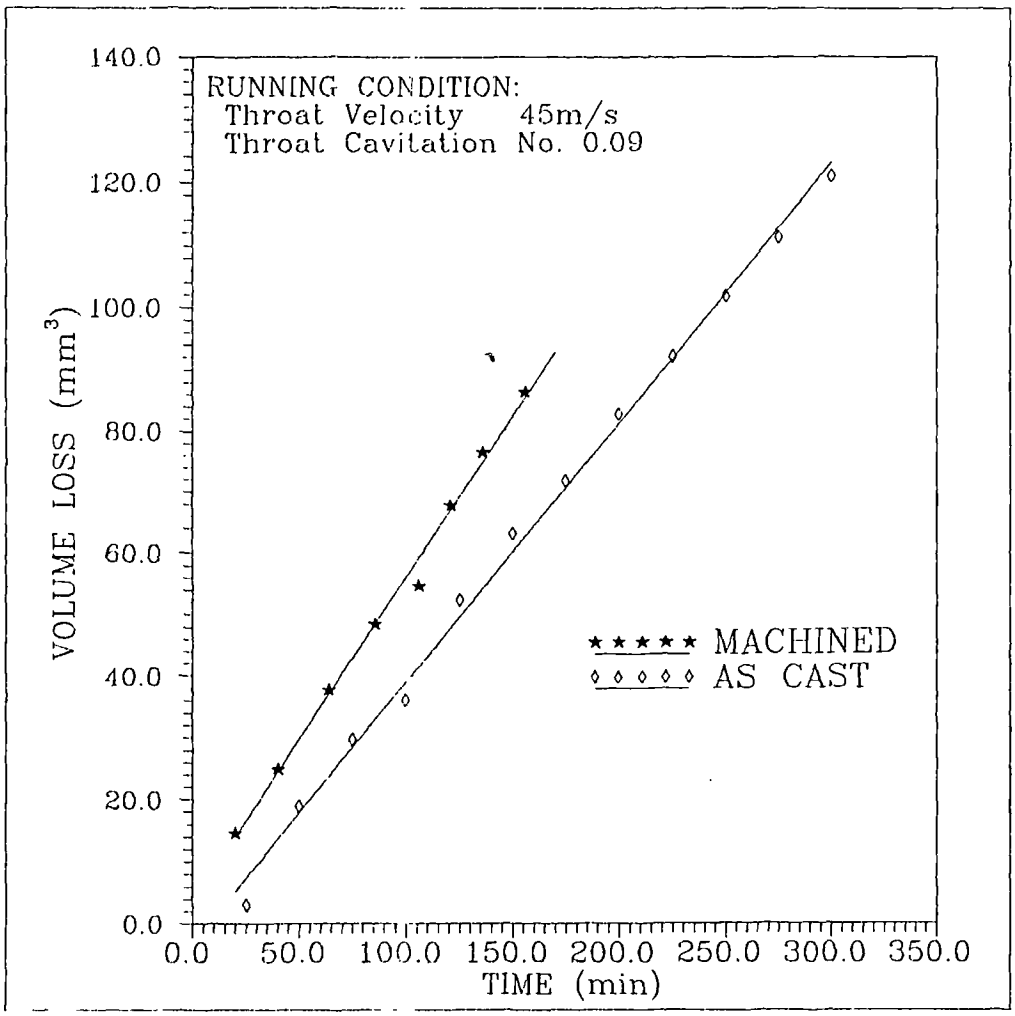

Fig.37 COMPARISON GRAPH BETWEEN AS CAST AND MACHINED NOVALAC EPOXY RESIN SYSTEM (BLO)

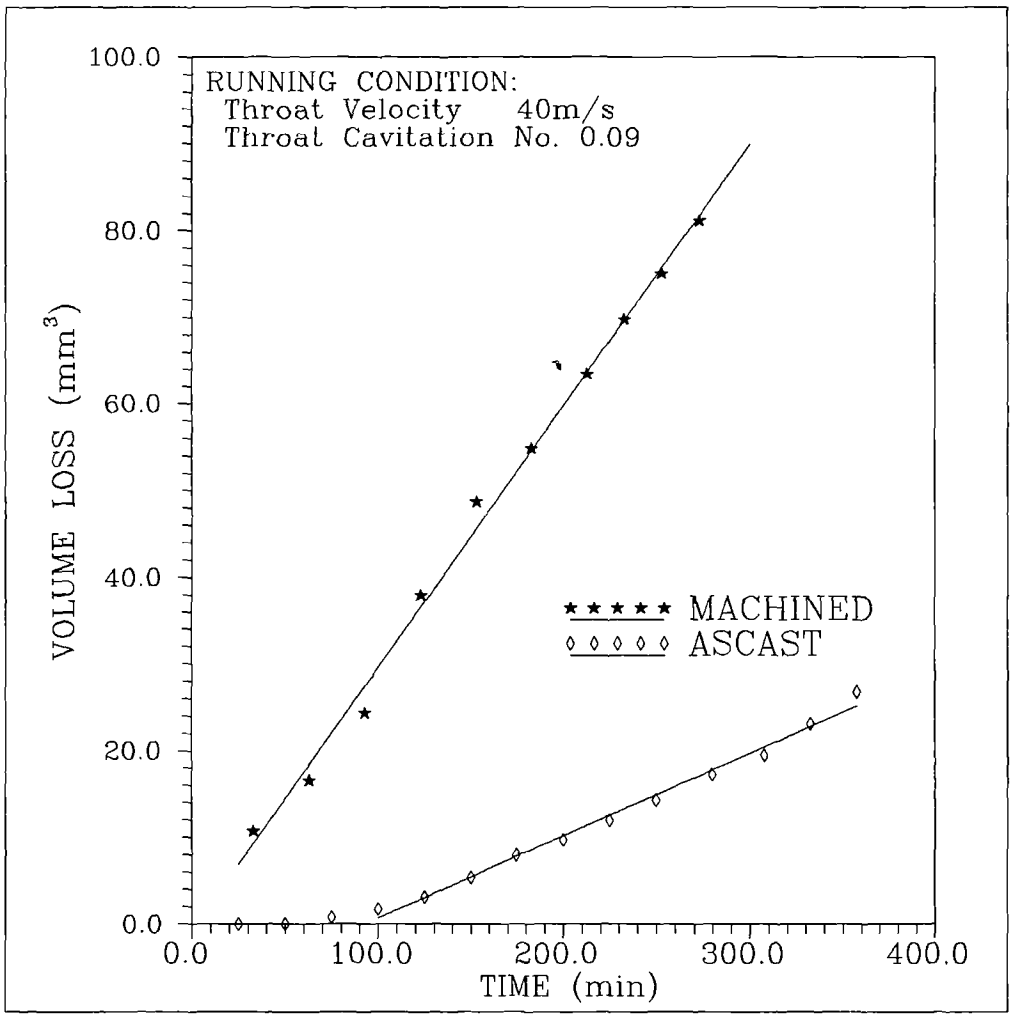

Fig.38 COMPARISON GRAPH BETWEEN ASCAST AND MACHINED. NOVALAC EPOXY RESIN SYSTEM (BL.Q)

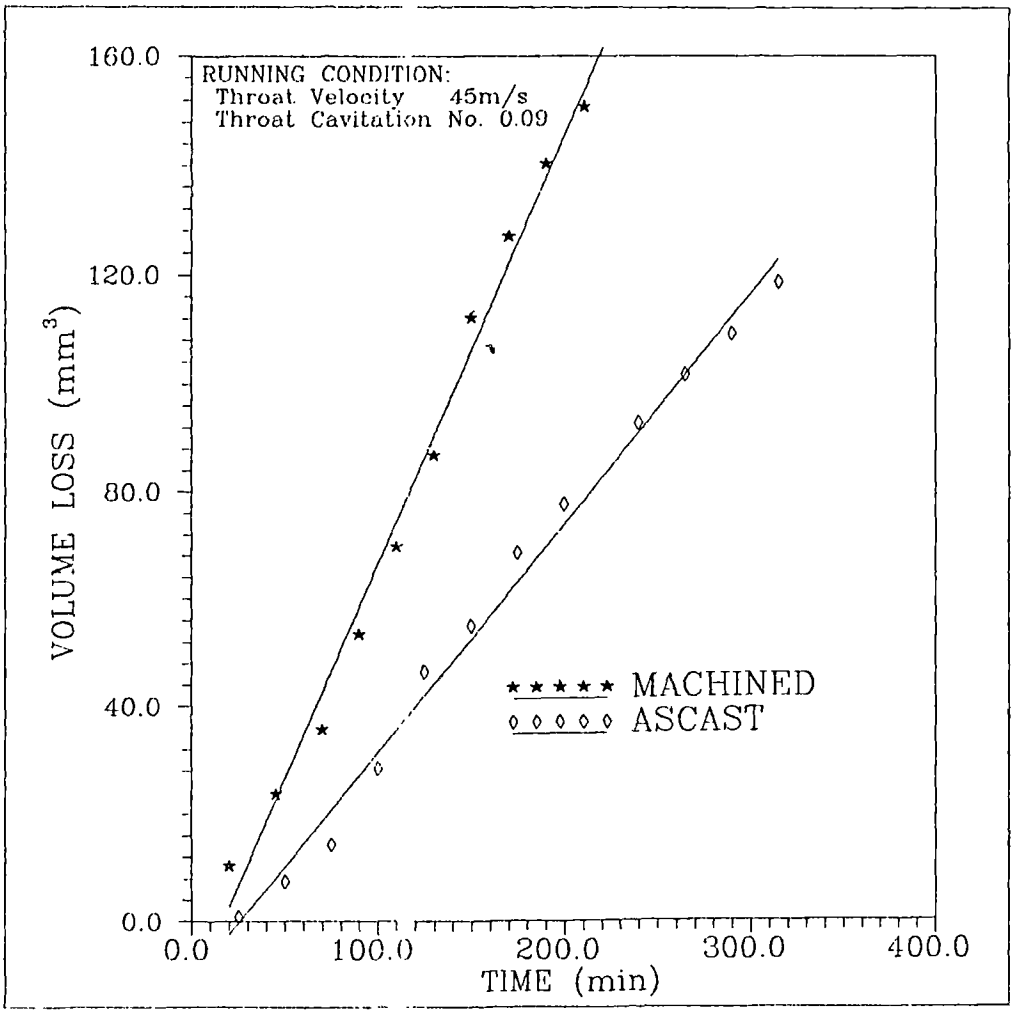

Fig.39 COMPARISON GRAPH BETWEEN AS CAST AND MACHINED BISPHENOL EPOXY RESIN SYSTEM(BR.G)

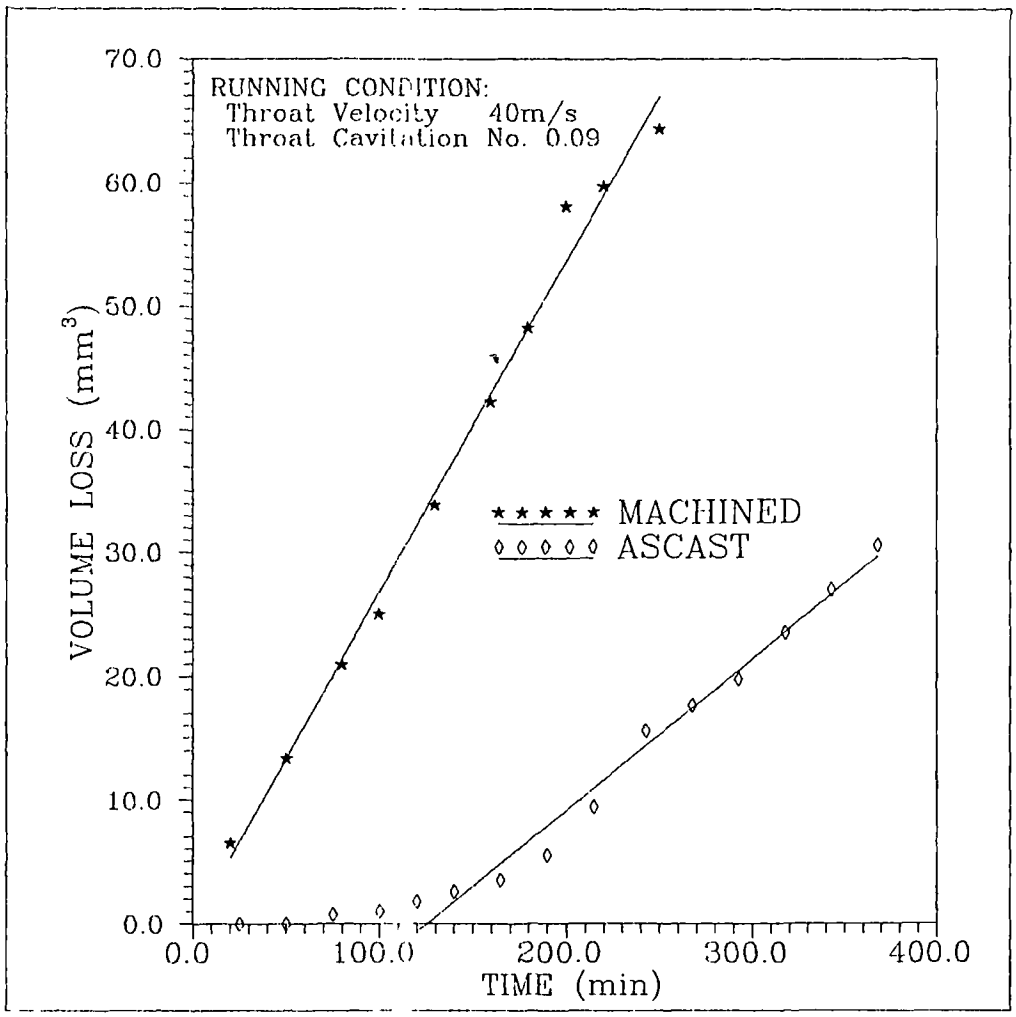

Fig.40 COMPARISON GRAPH BETWEEN AS CAST AND MACHINED BISPHENOL EPOXY RESIN SYSTEM(BR.G)

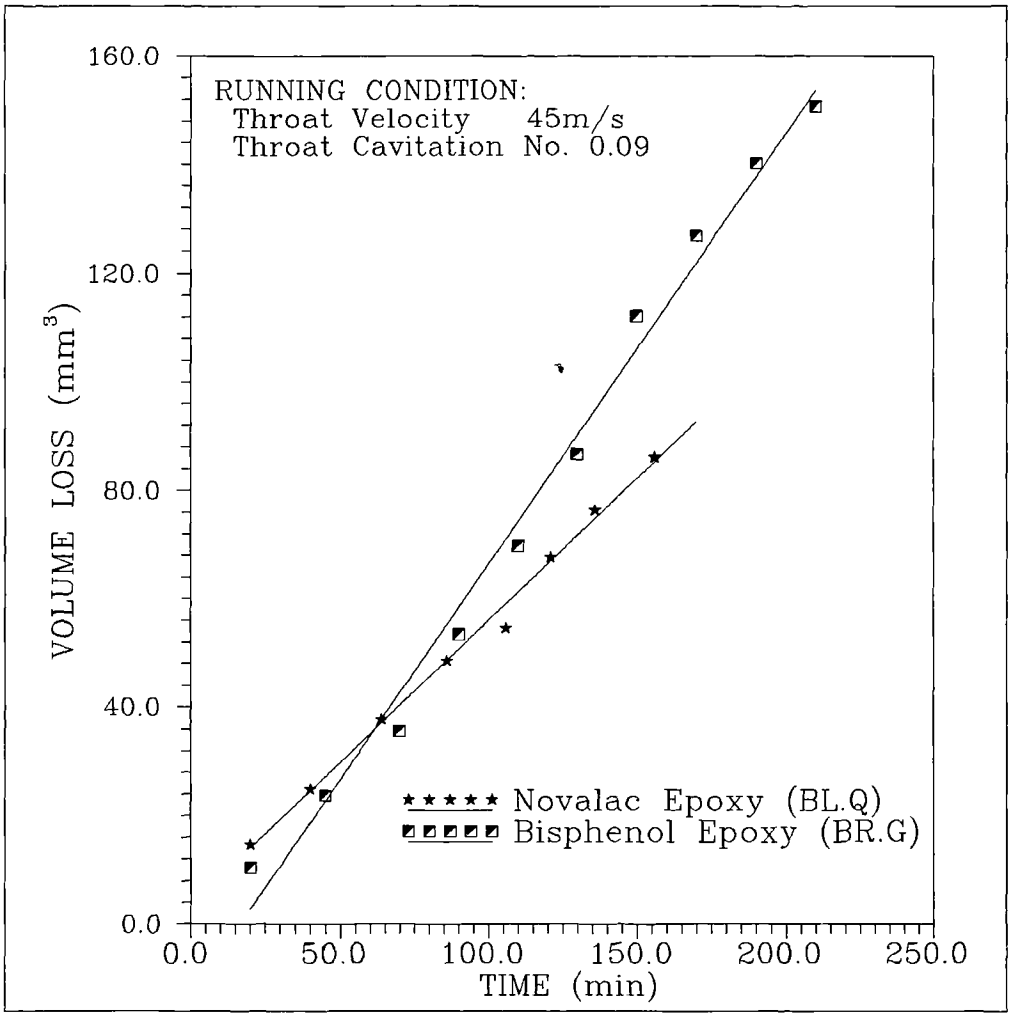

Fig.41 COMPARISON BETWEEN EPOXY RESIN SYSTEMS IN THE MACHINED CONDITION AT 45 m/s

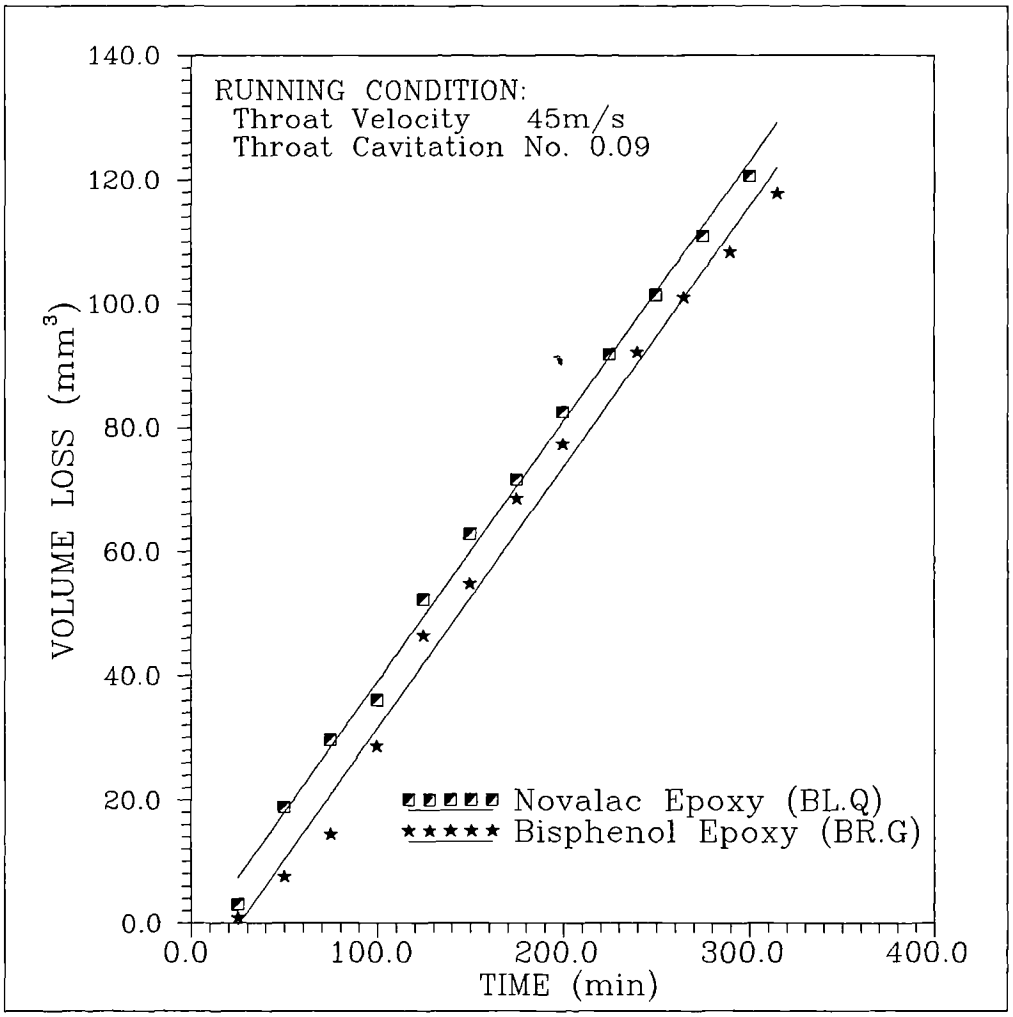

Fig.42 COMPARISON BETWEEN EPOXY RESIN SYSTEMS IN THE AS CAST CONDITION AT 45 m/s

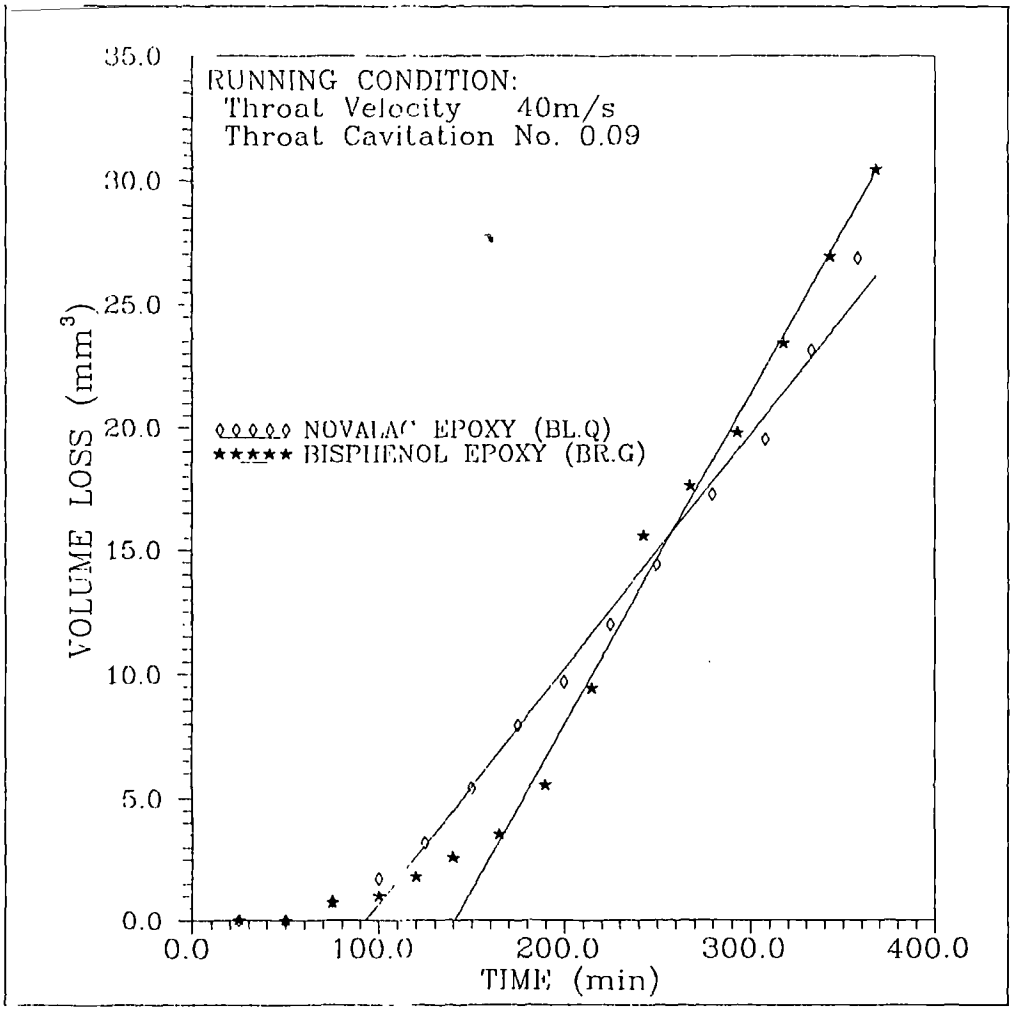

Fig.43 COMPARISON BETWEEN EPOXY RESIN SYSTEMS IN THE AS CAST CONDITION

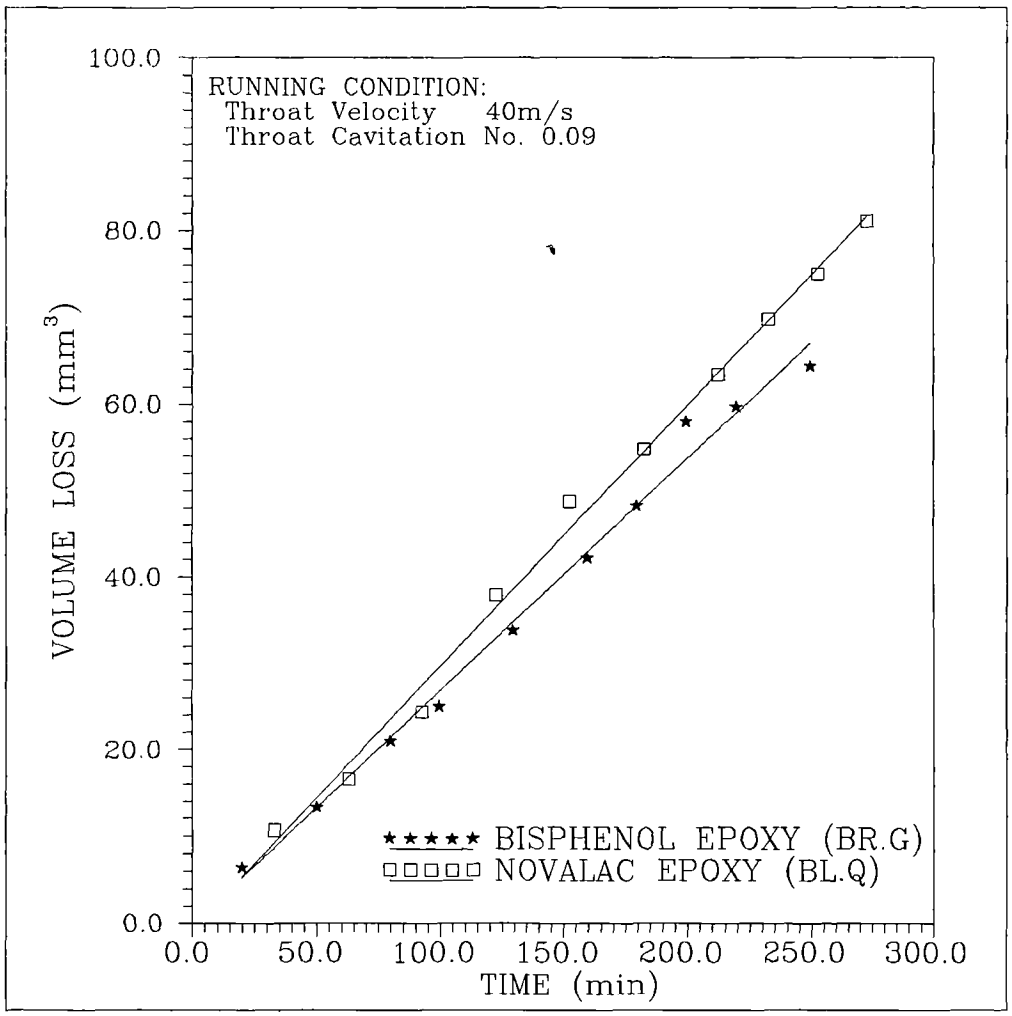

Fig.44 COMPARISON BETWEEM EPOXY RESIN SYSTEMS IN THE MACHINED CONDITION

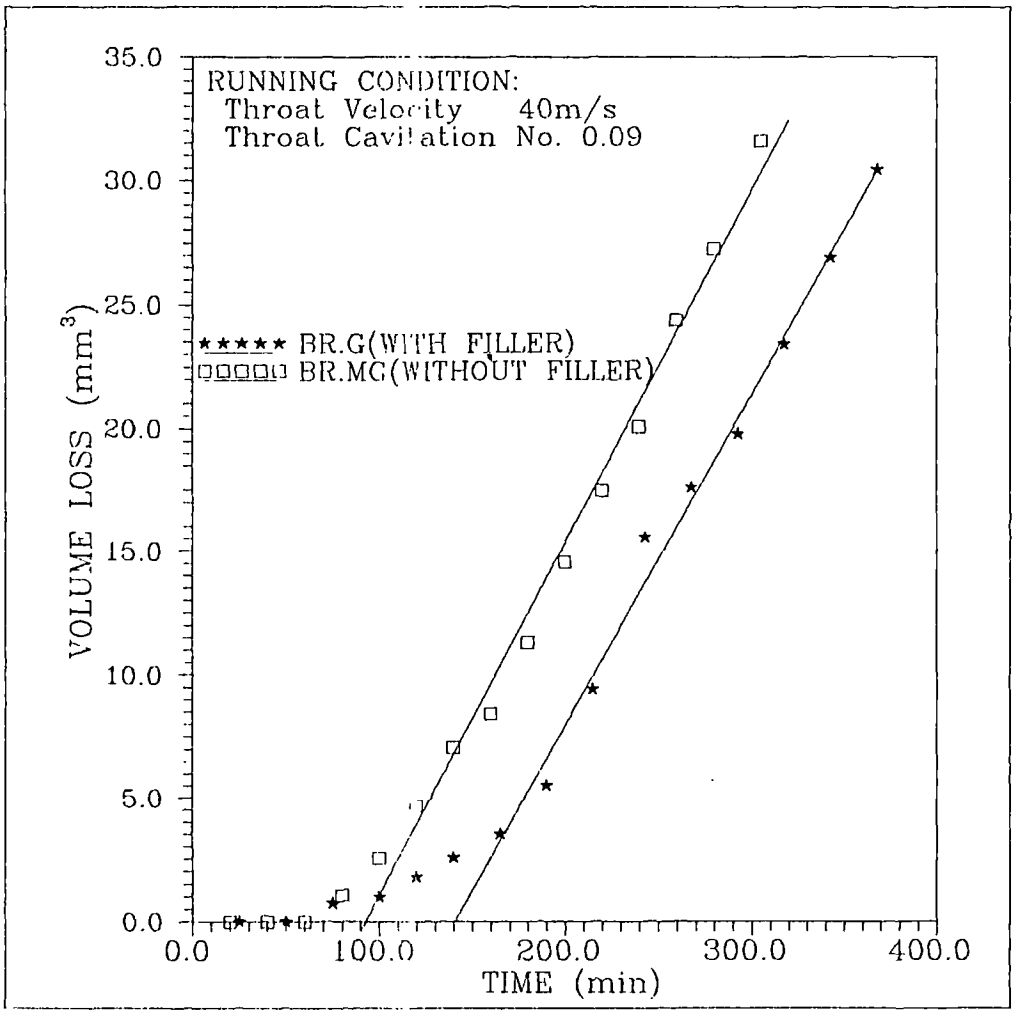

Fig.45 COMPARISON GRAPH OF BISPHENOL EPOXY RESIN WITH AND WITHOUT PARTICULATE FILLER IN AS CAST

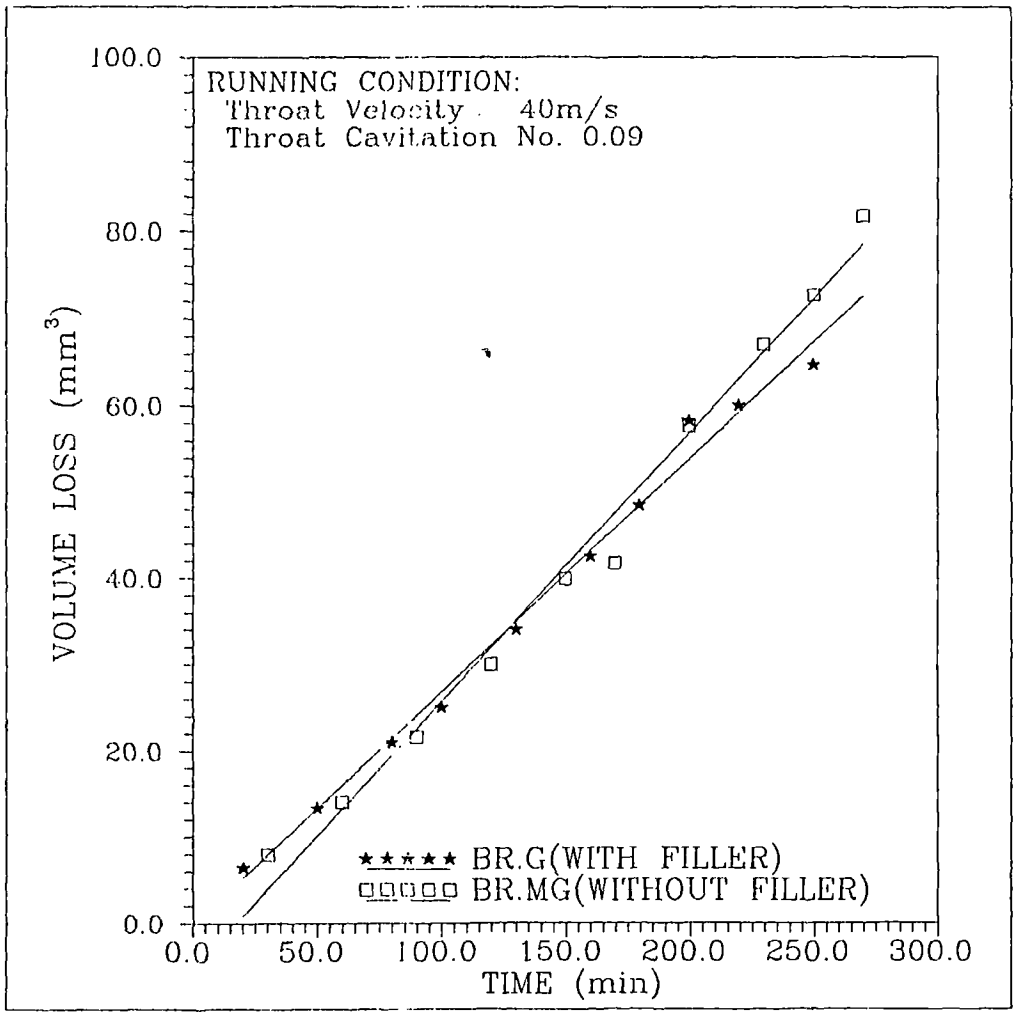

Fig.46 COMPARISON GRAPH OF BISPHENOL EPOXY RESIN WITH AND WITHOUT PARTICULATE FILLER AS MACHINED

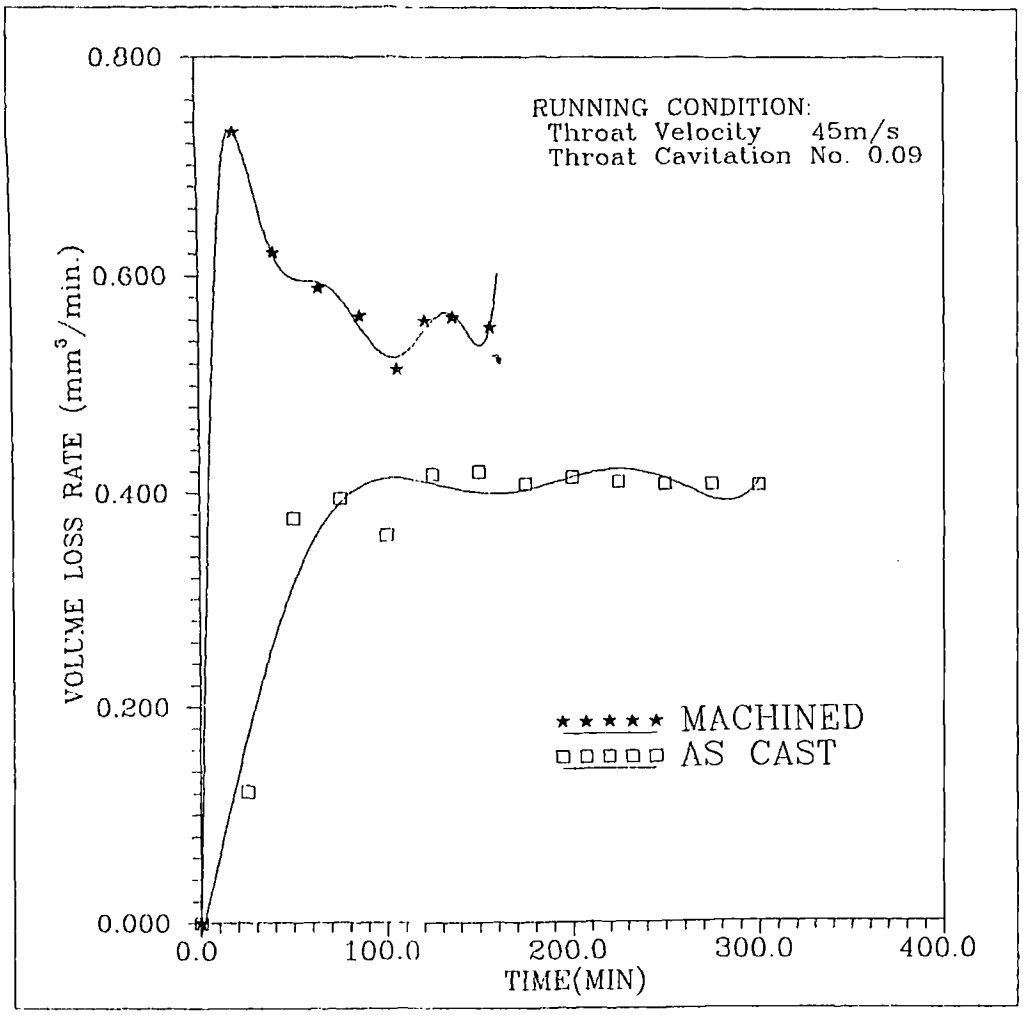

Fig.47 EROSION RATE–TIME CURVES FOR NOVALAC EPOXY RESIN (BL.Q) IN AS CAST AND MACHINED CONDITIONS

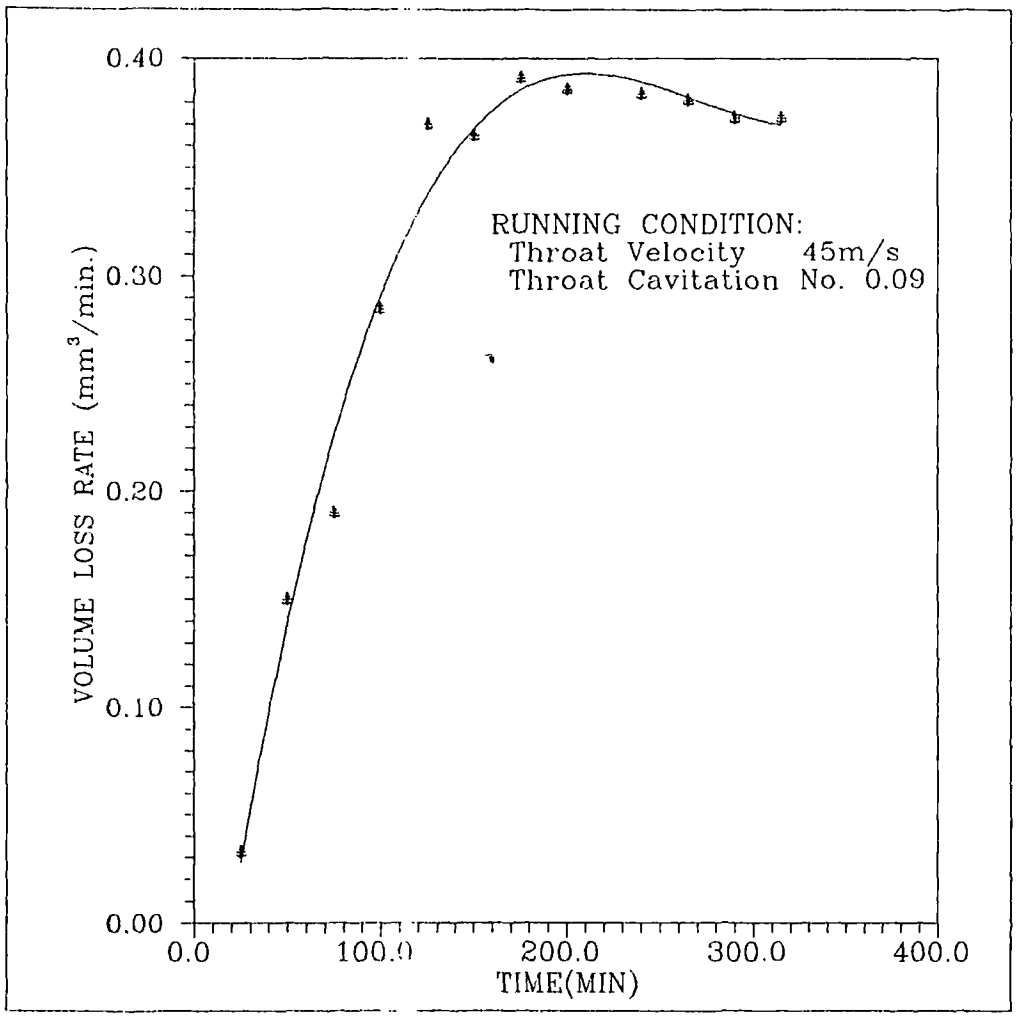

Fig.48 EROSION RATE–TIME CURVE FOR BISPHENOL EPOXY RESIN SYSTEM (BR.G)IN AS CAST

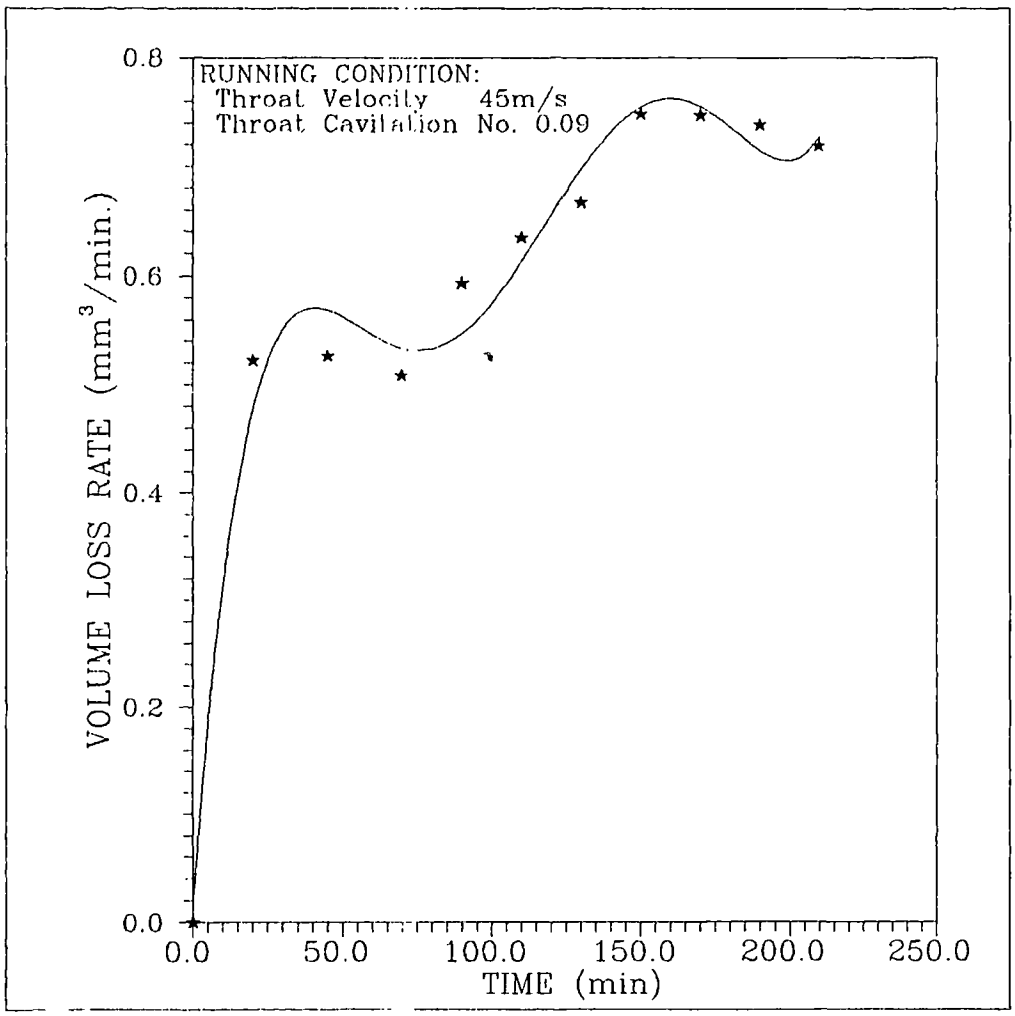

Fig.49 EROSION RATE–TIME CURVE FOR BISPHENOL EPOXY RESIN(BR.G) MACHINED

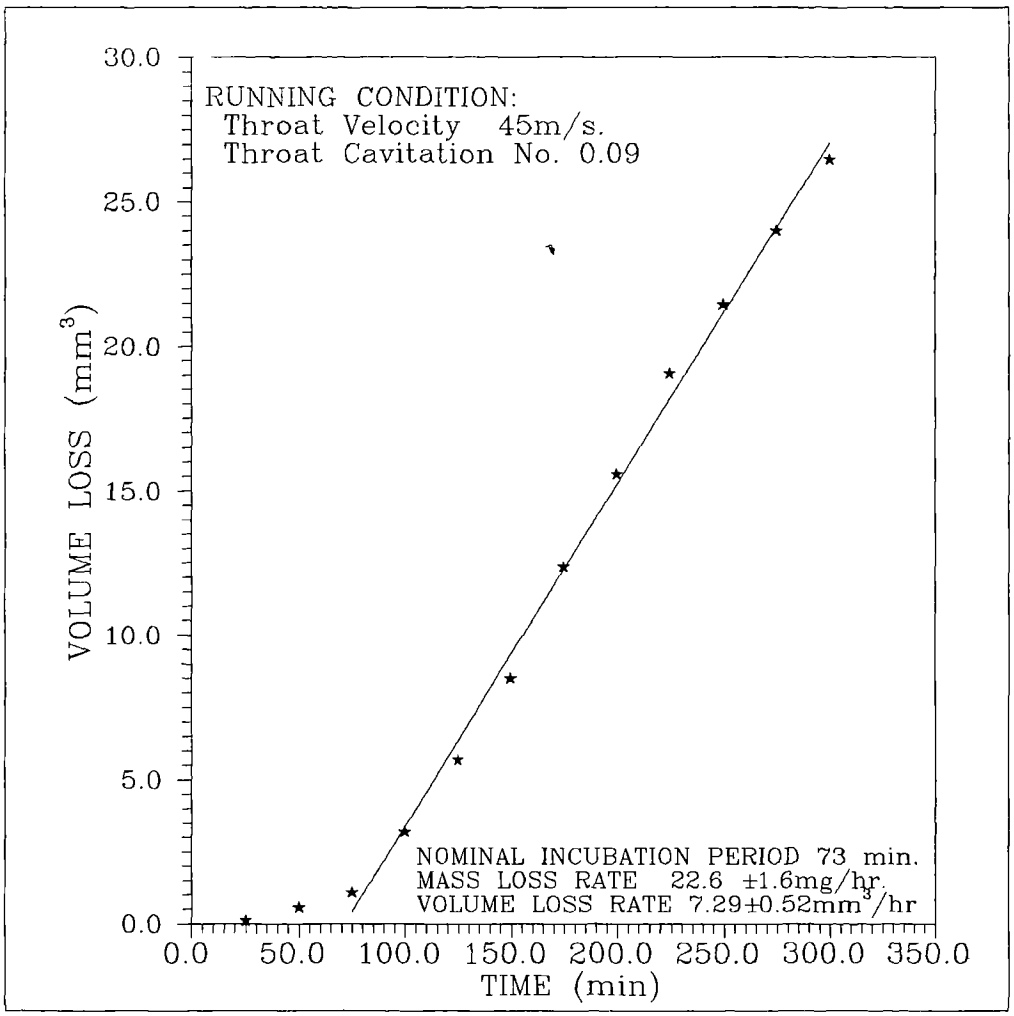

Fig.50 CUMULATIVE VOLUME LOSS AGAINST TIME FOR SILICON CARBIDE AS GROUND

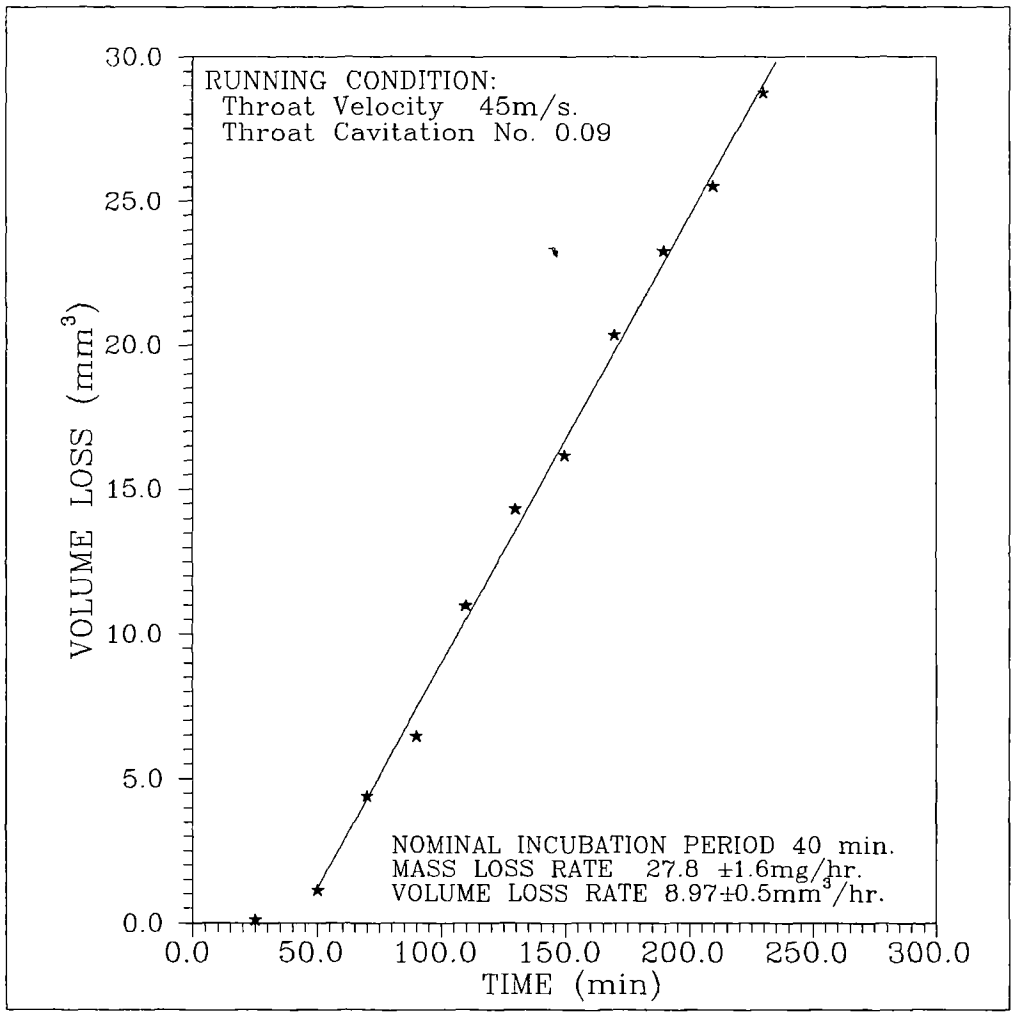

Fig.51 CUMULATIVE VOLUME LOSS AGAINST TIME FOR SILICON CARBIDE AS LAPPED

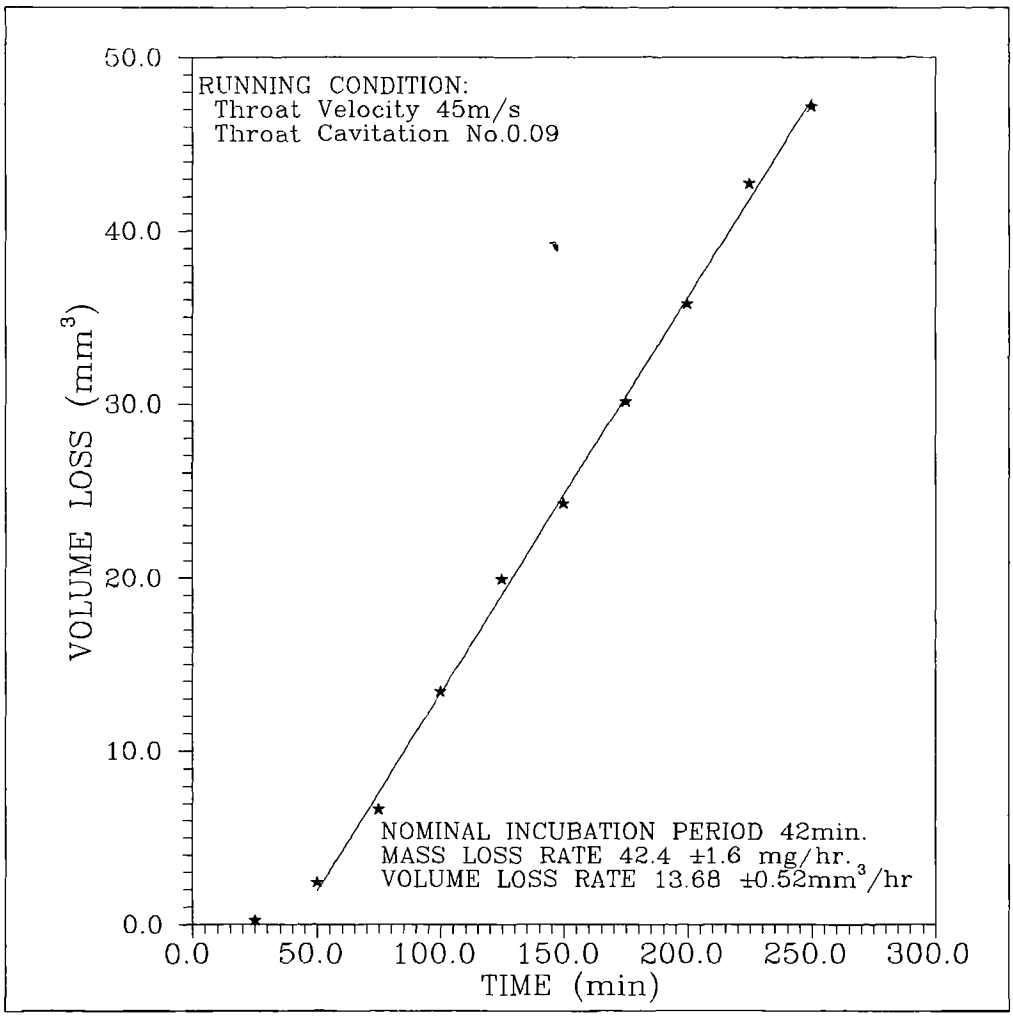

Fig.52 CUMULATIVE VOLUME LOSS AGAINST TIME FOR SILICON CARBIDE AS FIRED

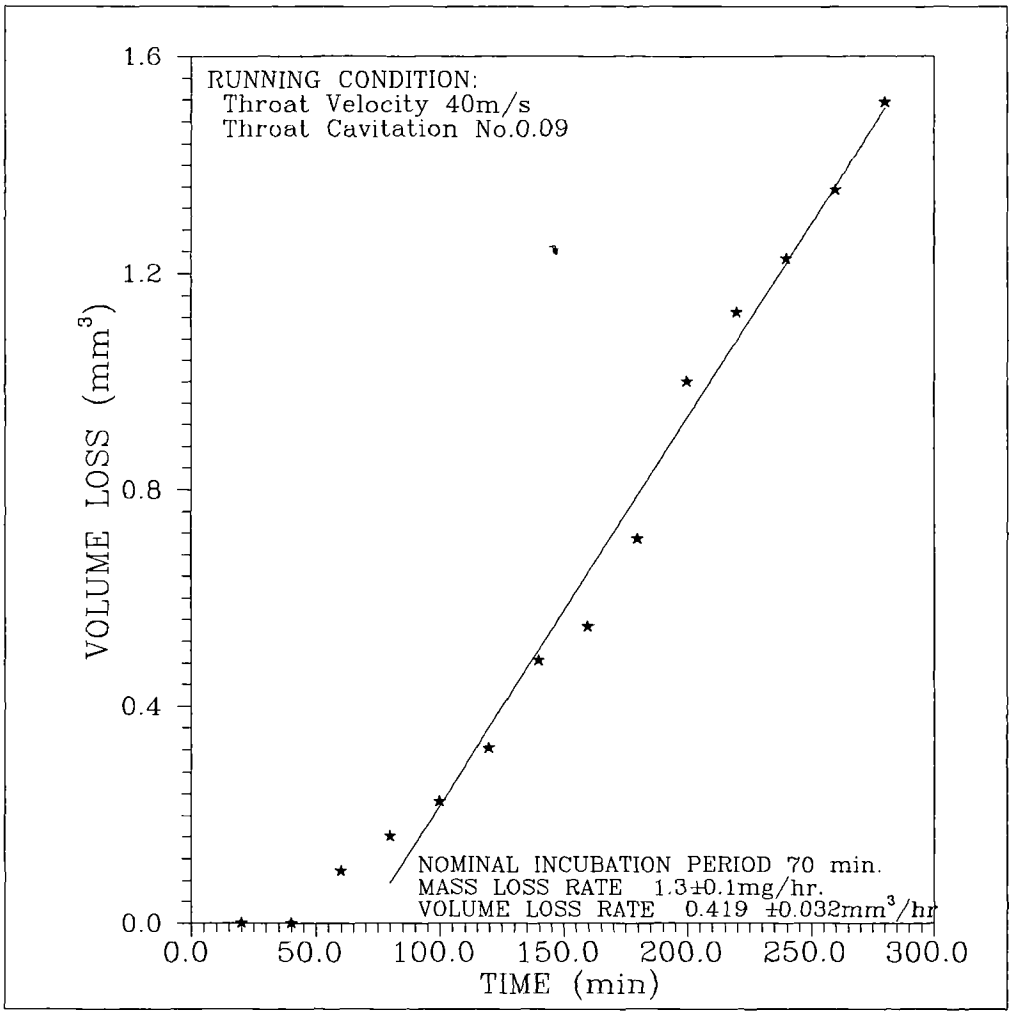

Fig.53 CUMULATIVE VOLUME LOSS AGAINST TIME FOR SILICON CARBIDE AS GROUND

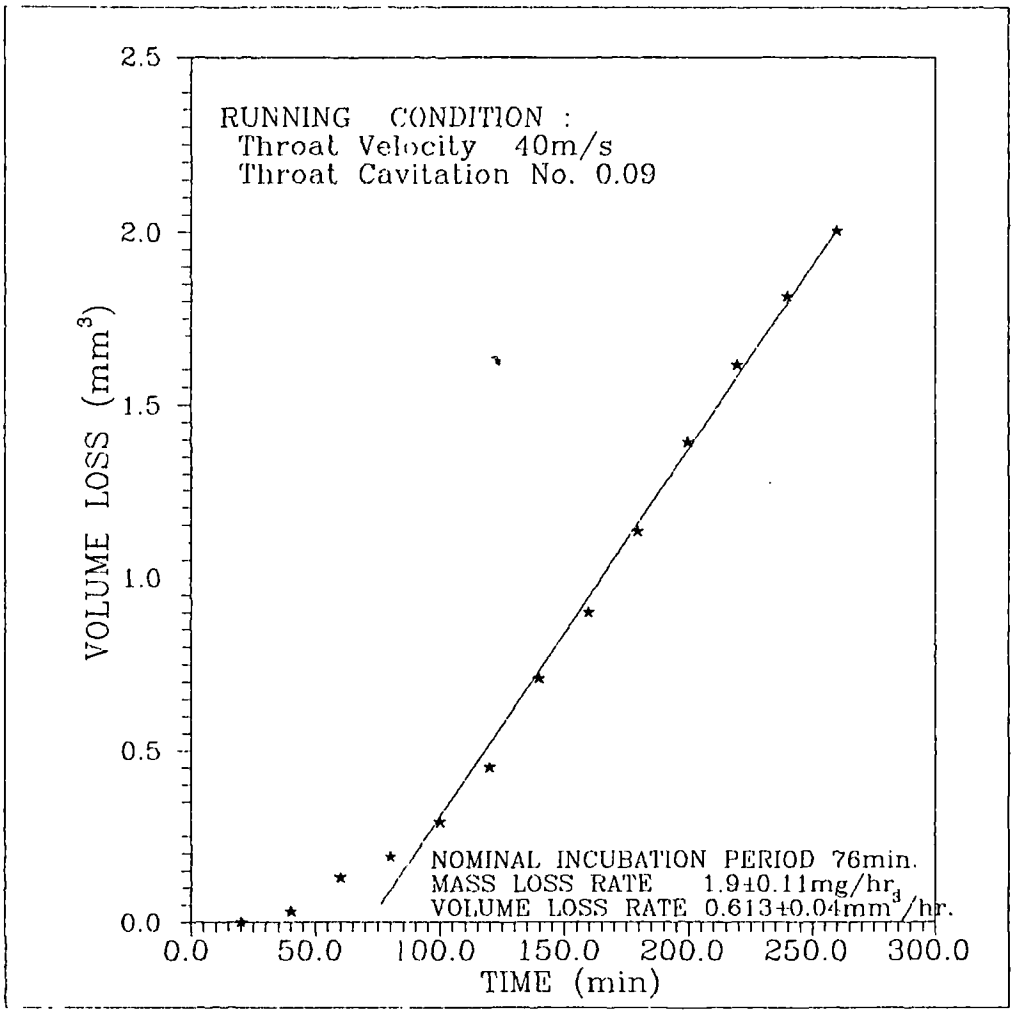

Fig.54 CUMULATIVE VOLUME LOSS AGAINST TIME FOR SILICON CARBIDE AS LAPPED

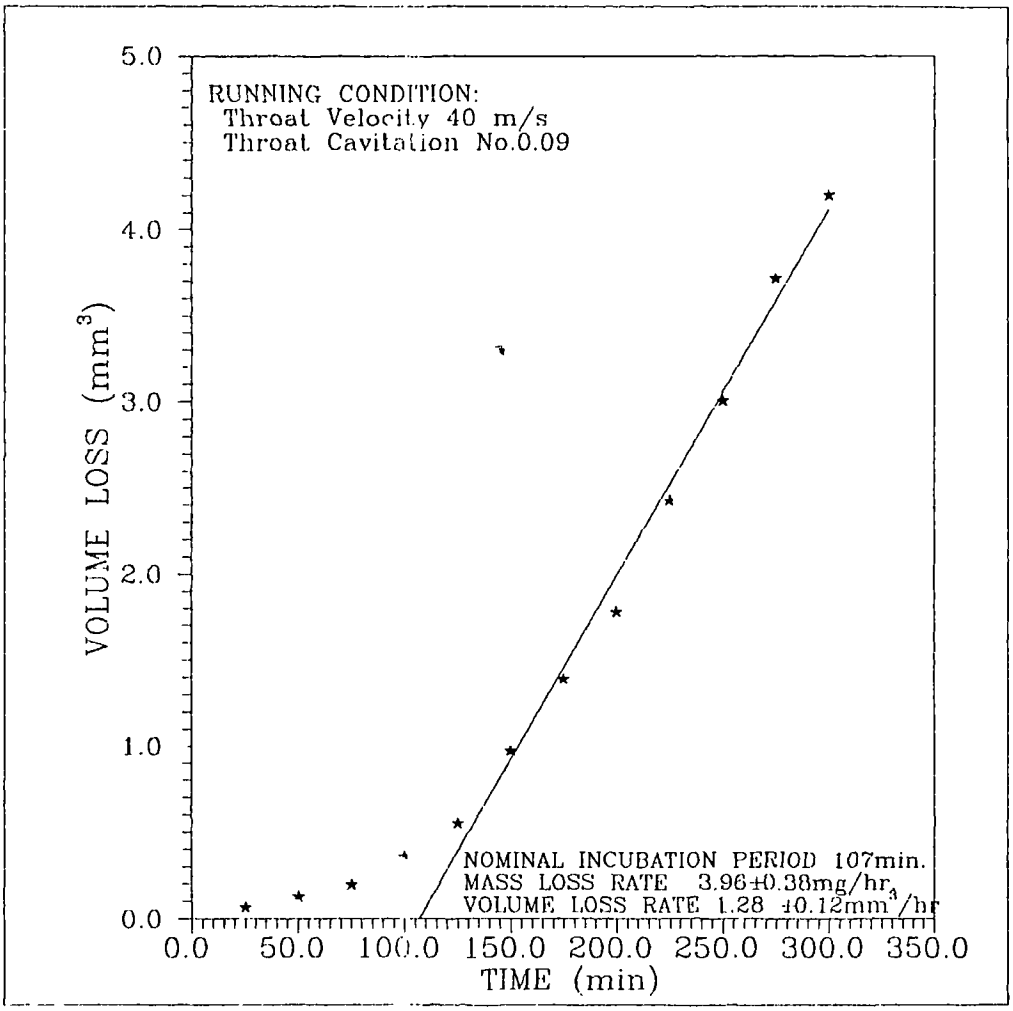

Fig.55 CUMULATIVE VOLUME LOSS AGAINST TIME FOR SILICON CARBIDE AS FIRED

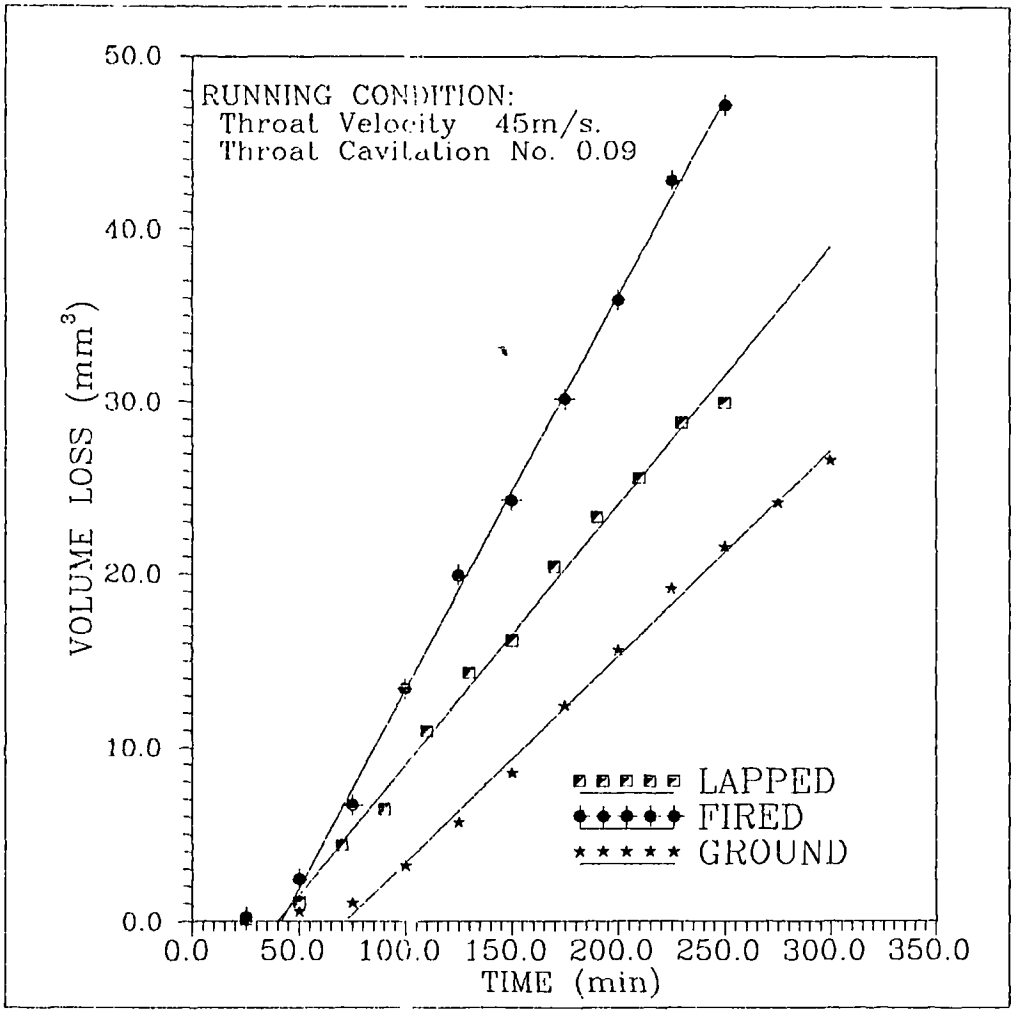

Fig.56 COMPARISON OF SILICON CARBIDE IN AS LAPPED, GROUND AND FIRED CONDITIONS

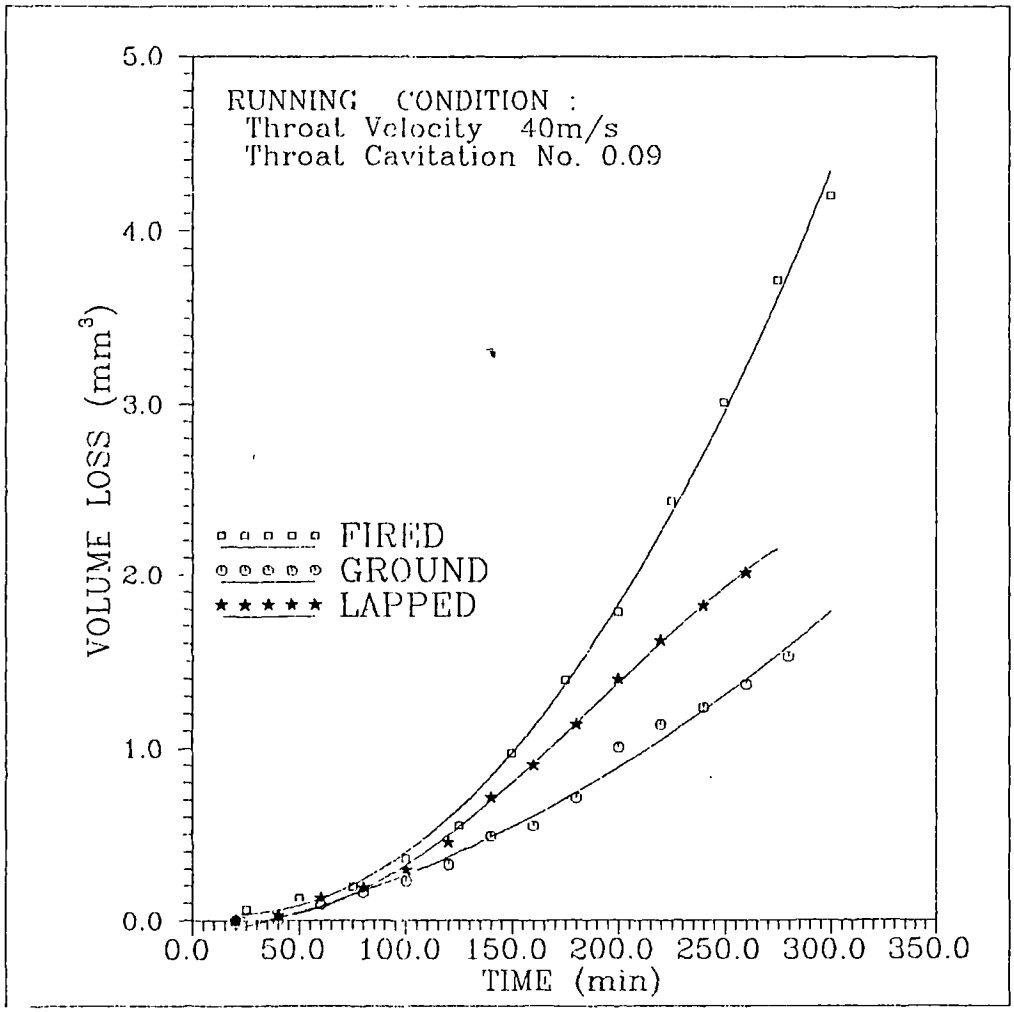

Fig.57 COMPARISON OF SILICON CARBIDE IN AS LAPPED, GROUND AND FIRED CONDITIONS

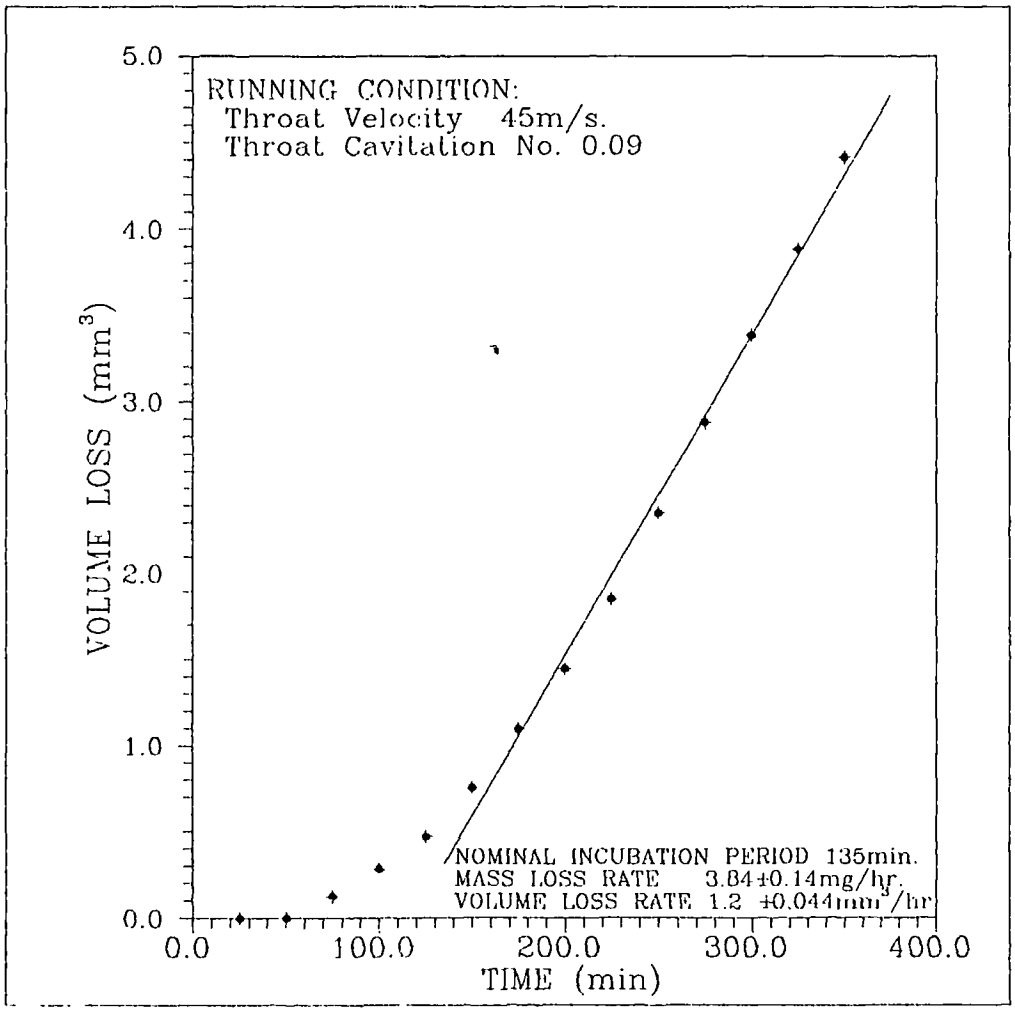

Fig.58 CUMULATIVE VOLUME LOSS AGAINST TIME FOR SILICON NITRIDE AS GROUND

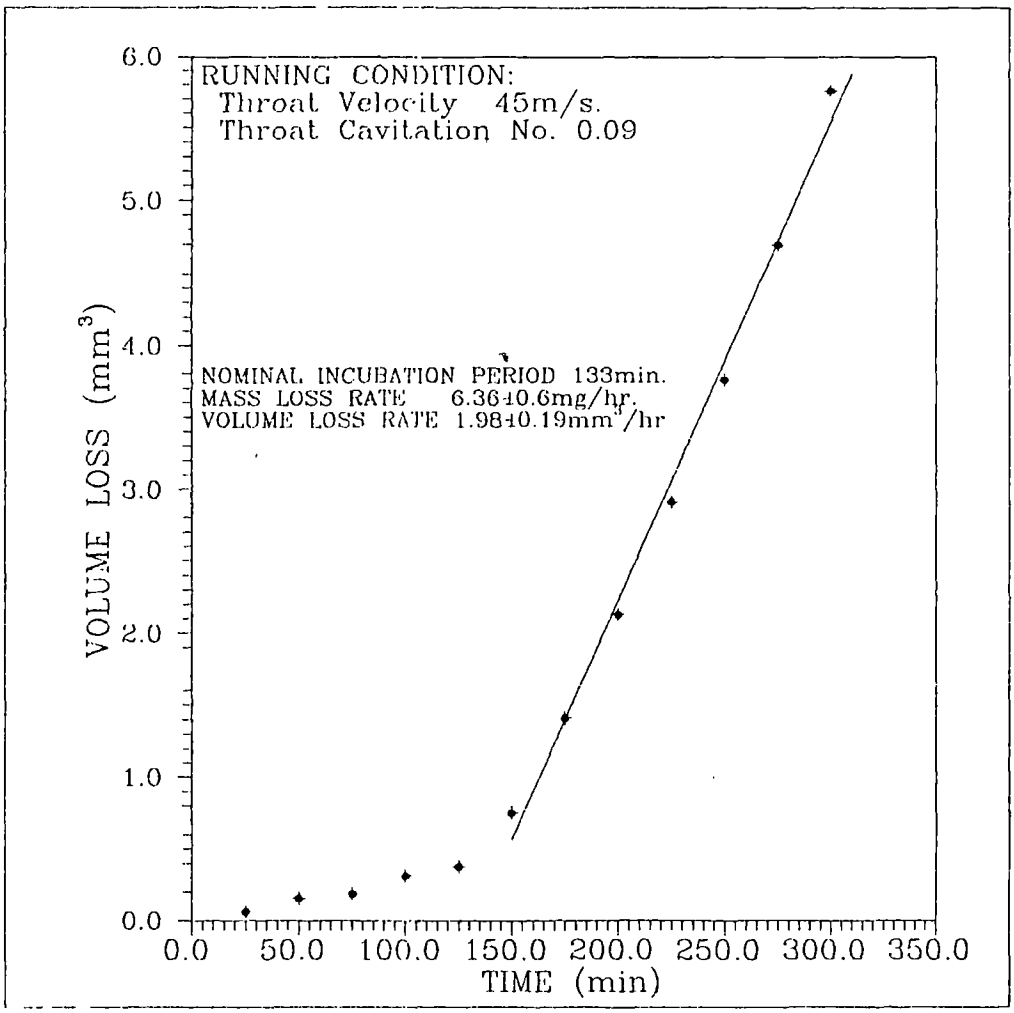

Fig.59 CUMULATIVE VOLUME LOSS AGAINST TIME FOR SILICON NITRIDE AS LAPPED

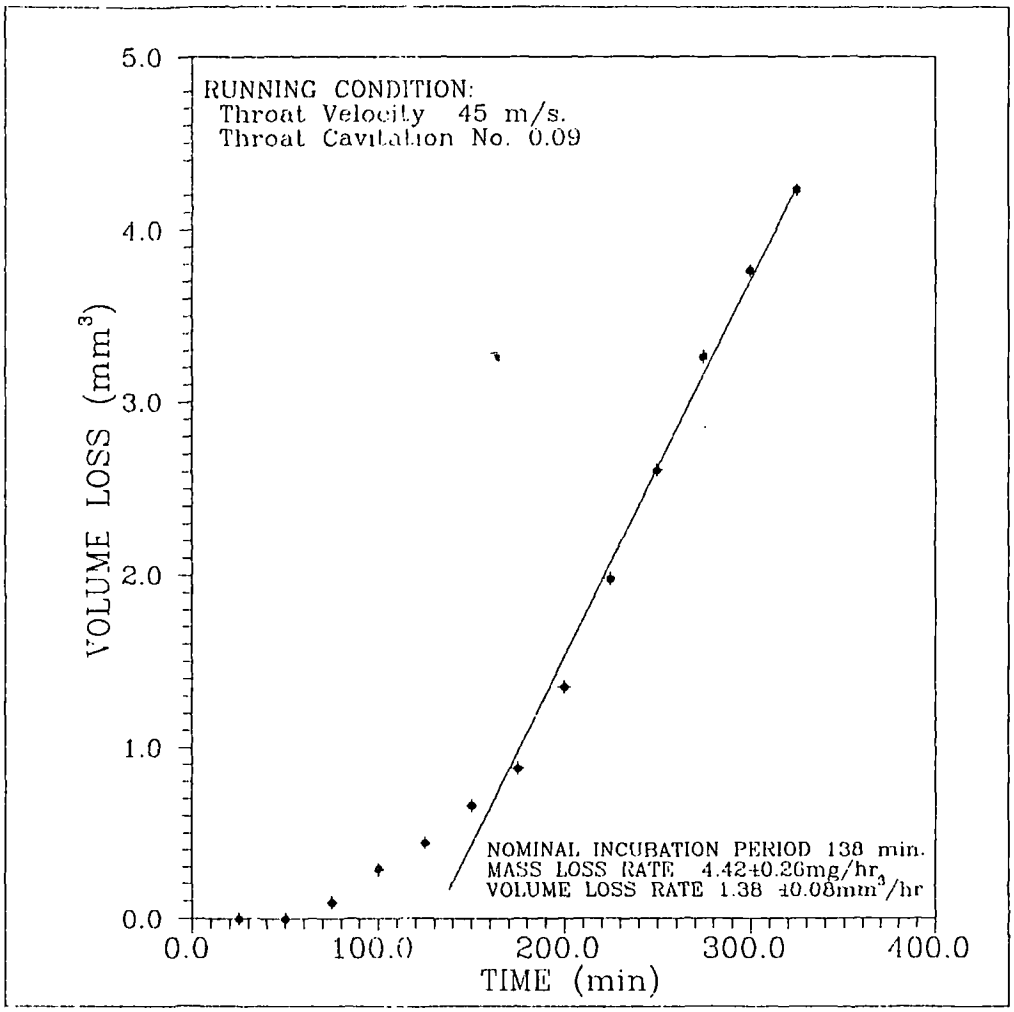

Fig.60 CUMULATIVE VOLUME LOSS AGAINST TIME FOR SILICON NITRIDE AS FIRED

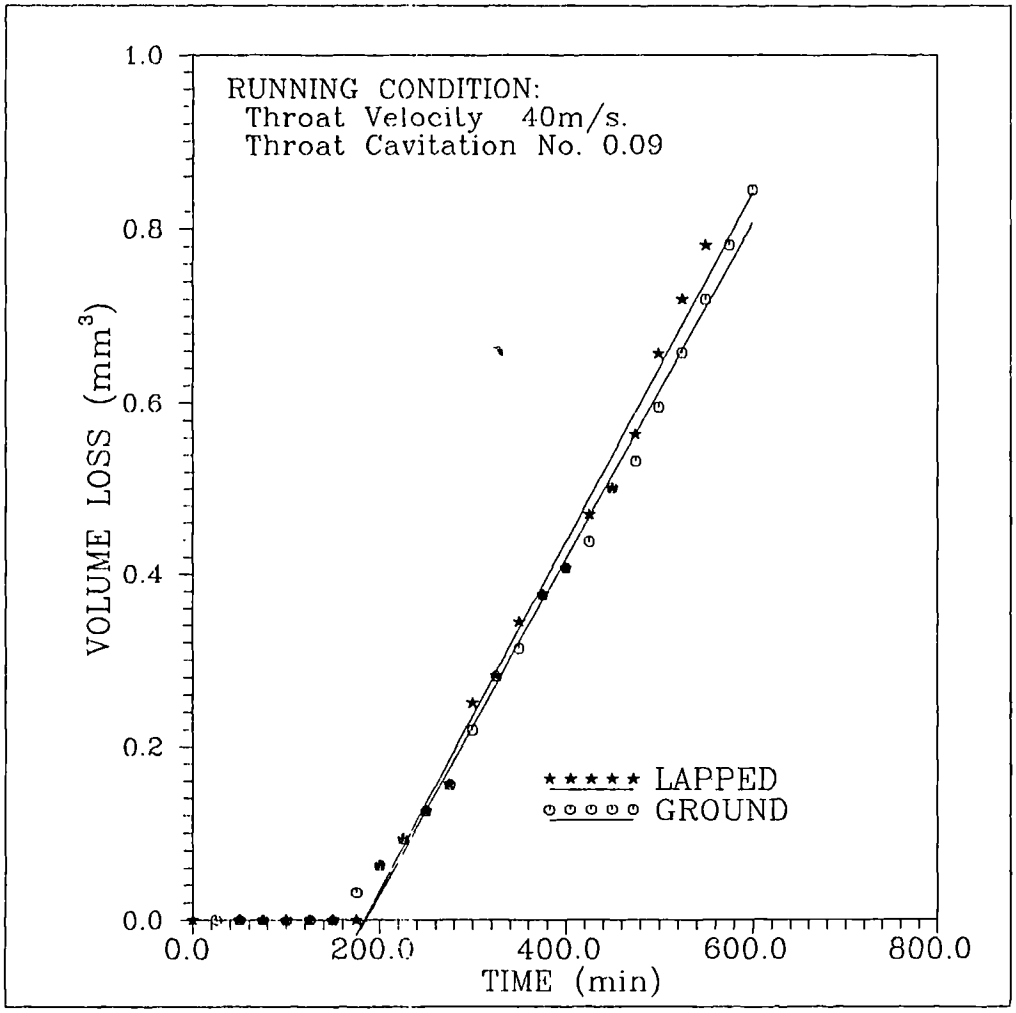

Fig.61 COMPARISON OF SILICON NITRIDE IN AS LAPPED AND GROUND CONDITIONS

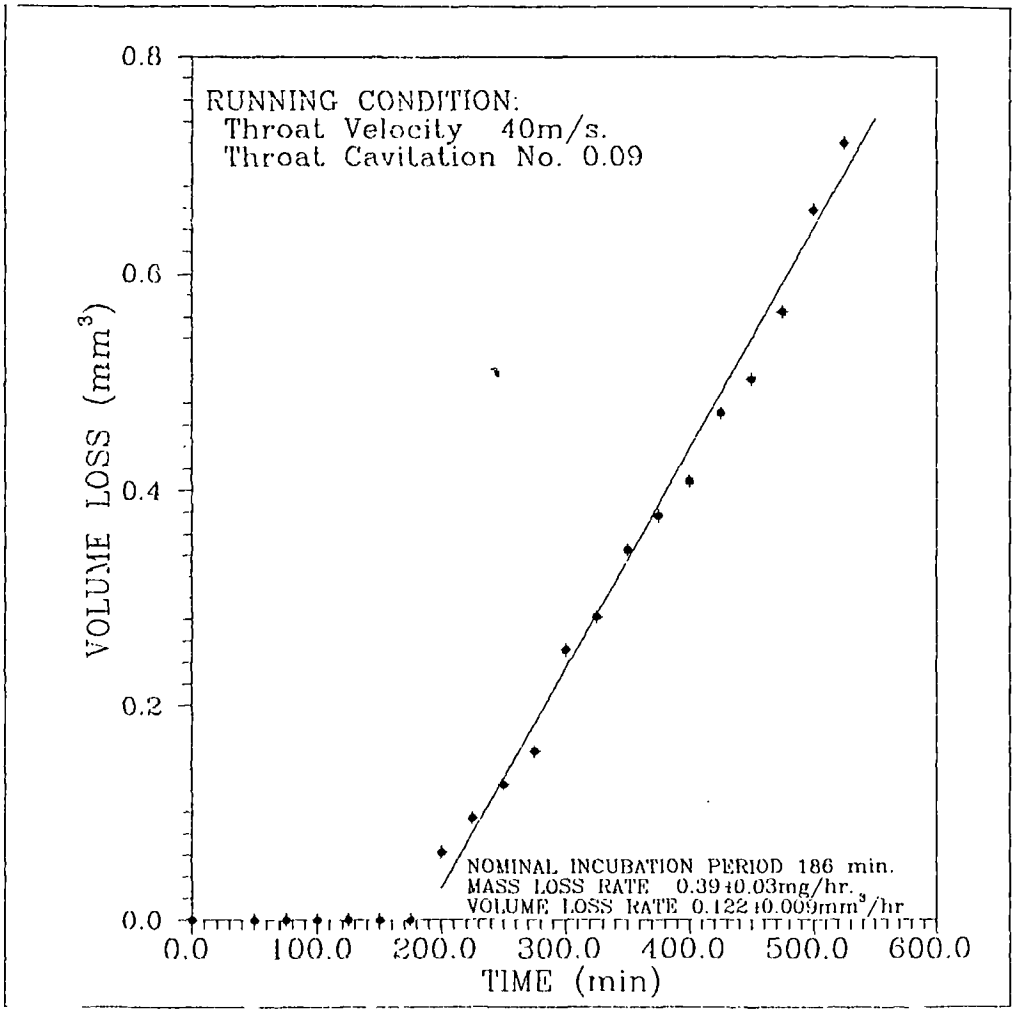

Fig.62 CUMULATIVE VOLUME LOSS AGAINST TIME FOR SILICON NITRIDE AS LAPPED

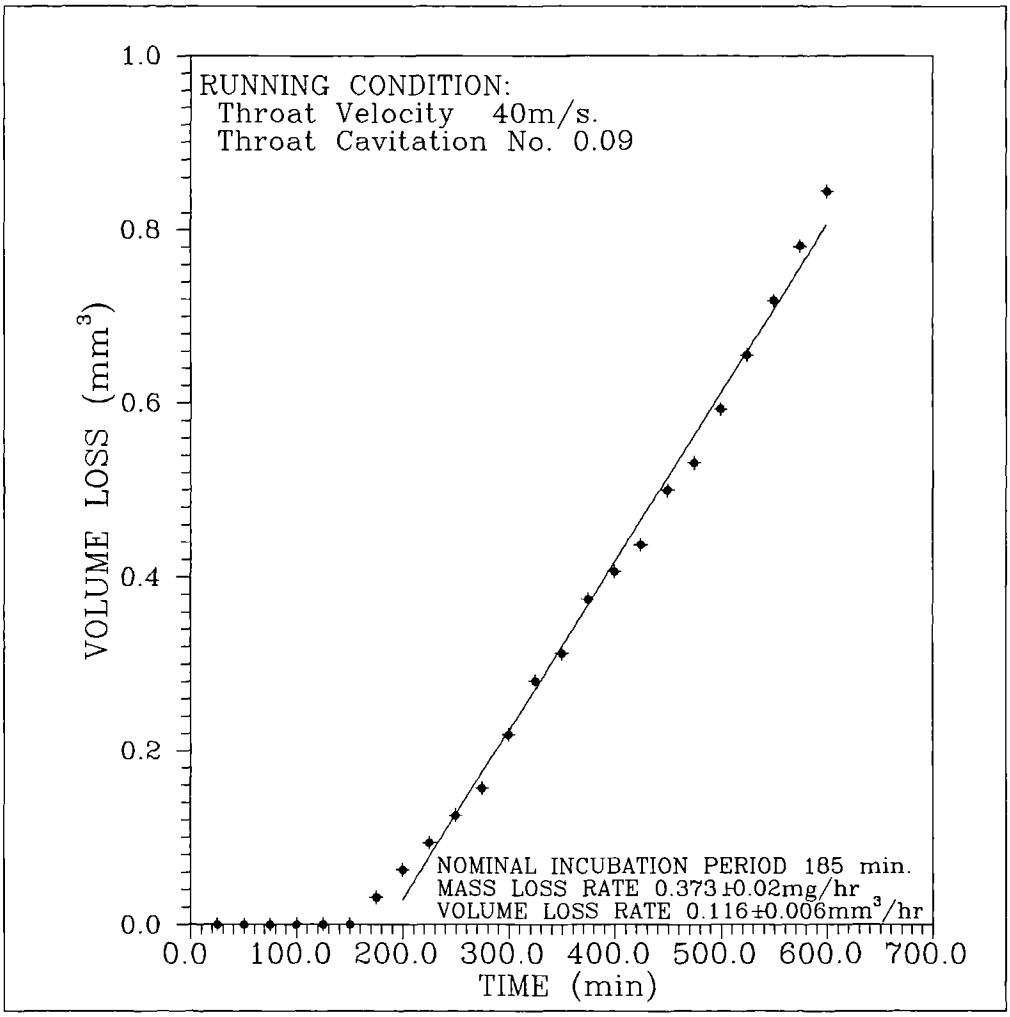

Fig.63 CUMULATIVE VOLUME LOSS AGAINST TIME FOR SILICON NITRIDE AS GROUND

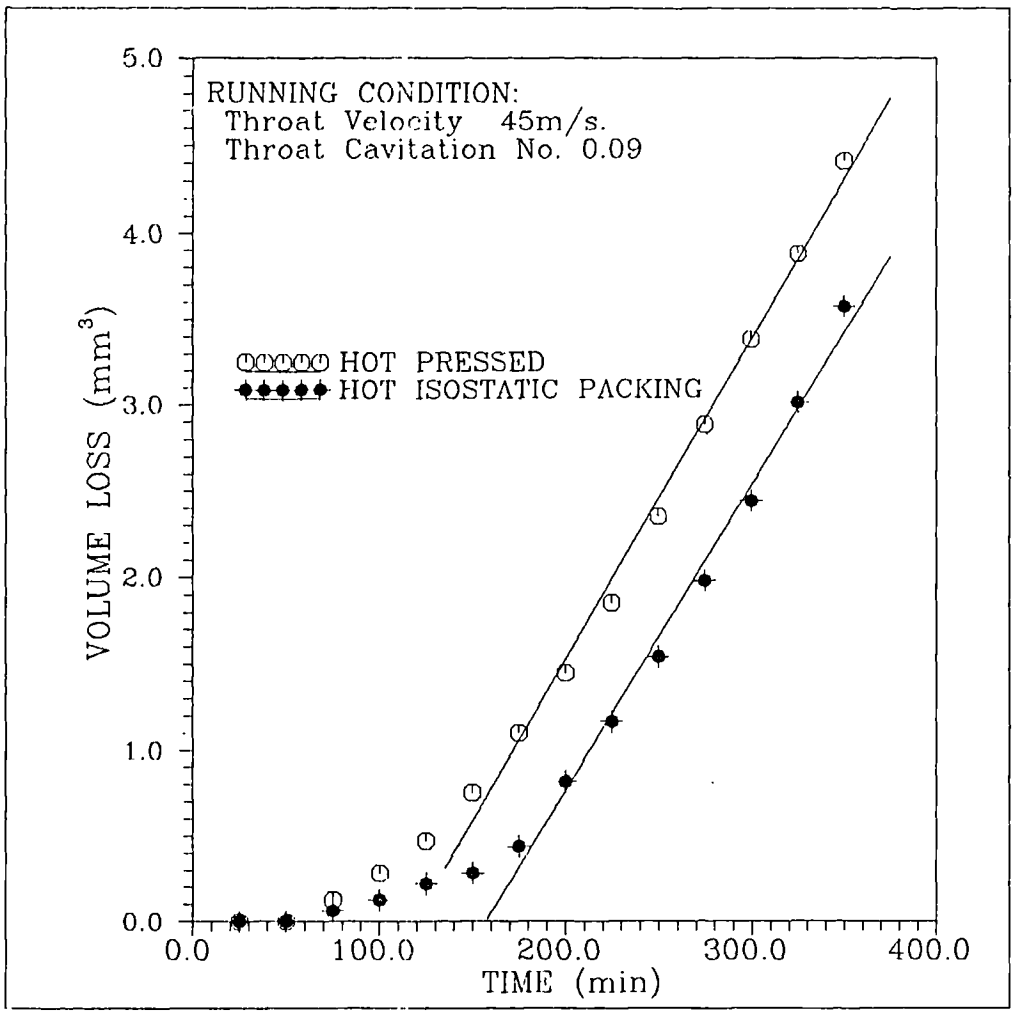

Fig.64 COMPARISON BETWEEN HOT PRESSED GROUND AND HIP GROUND IN SILICON NITRIDE

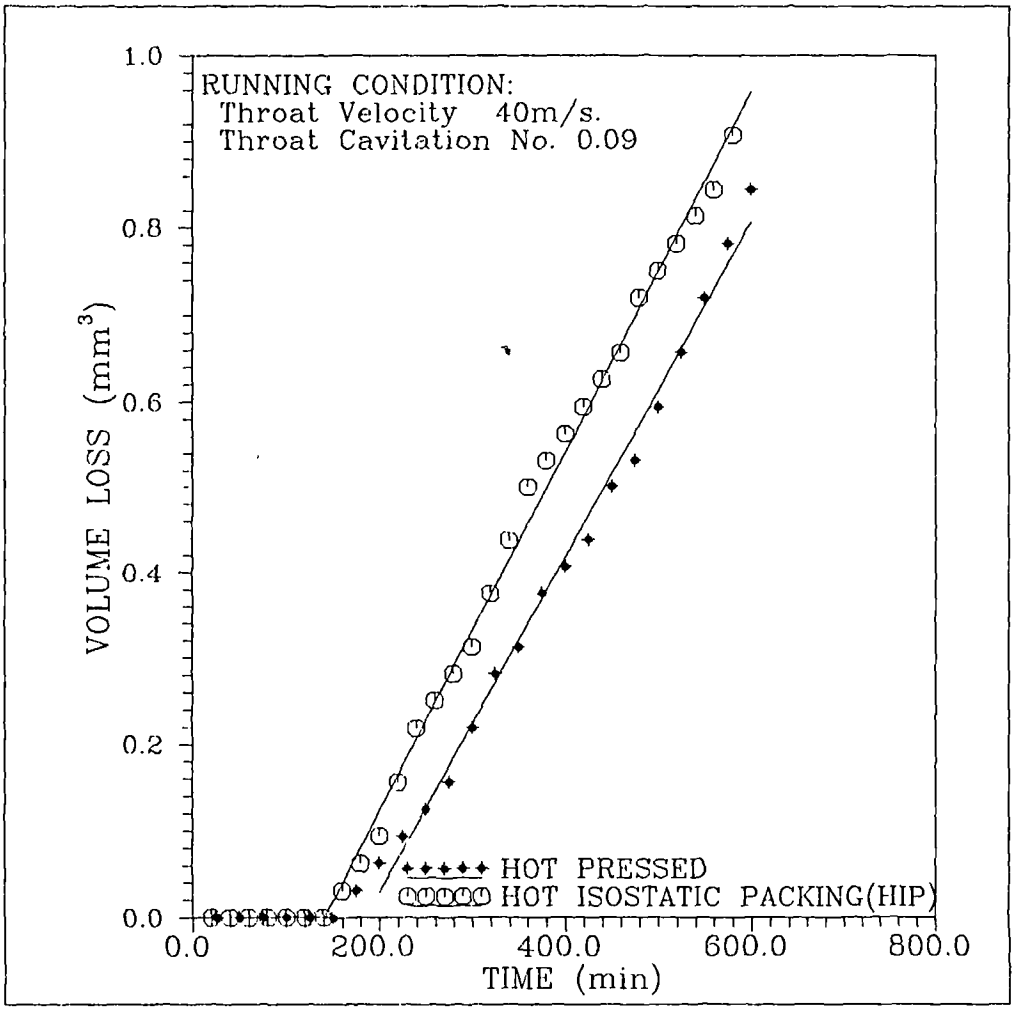

Fig.65 COMPARISON BETWEEN HOT PRESSED GROUND AND HIP GROUND IN SILICON NITRIDE

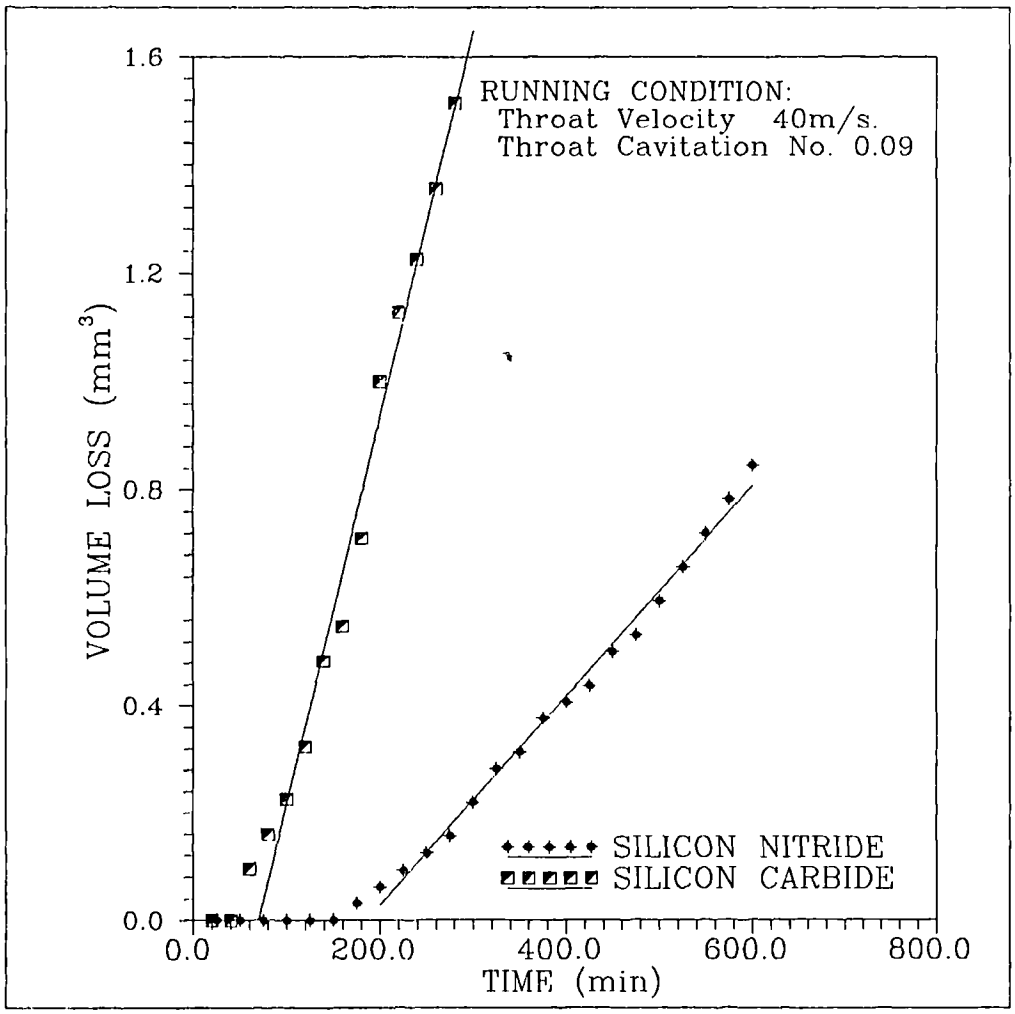

Fig.66 COMPARISON BETWEEN SILICON CARBIDE AND SILICON NITRIDE IN THE GROUND CONDITION

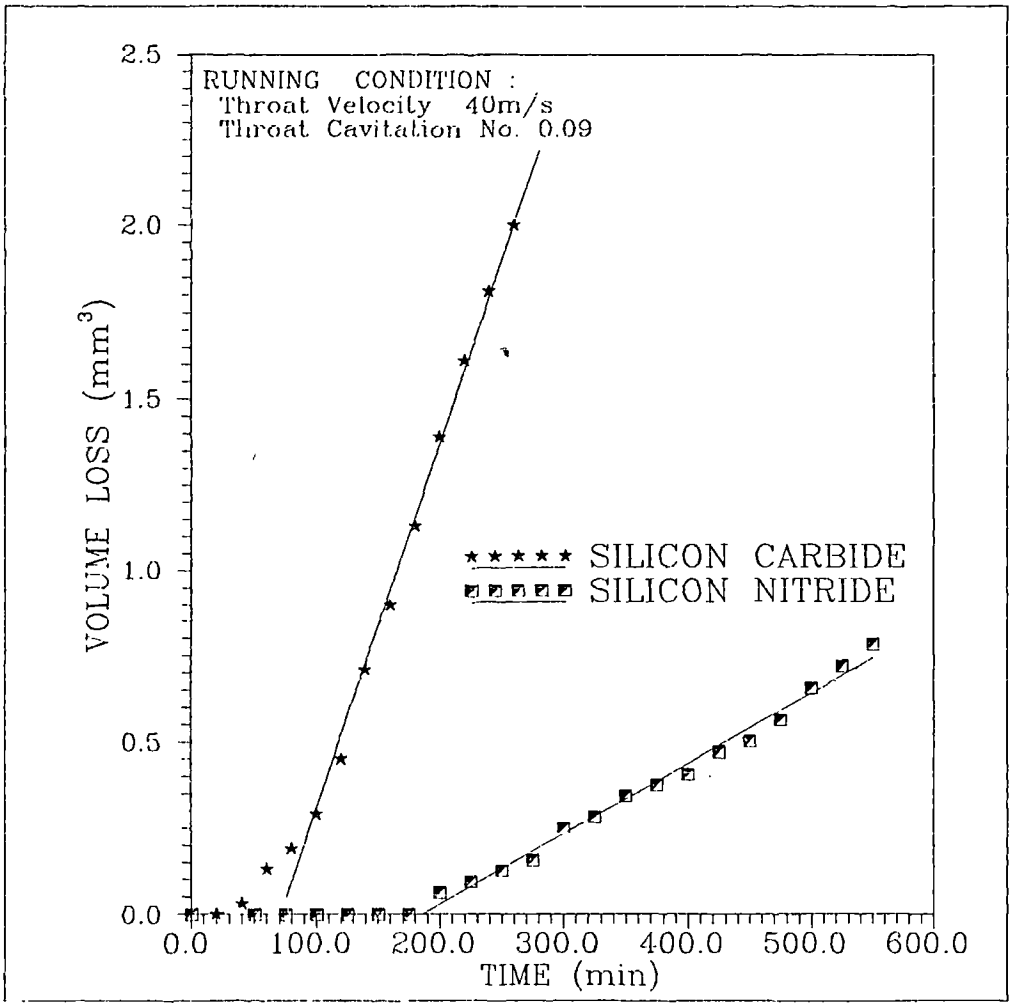

Fig.67 COMPARISON BETWEEN SILICON CARBIDE AND SILICON NITRIDE IN AS LAPPED CONDITION

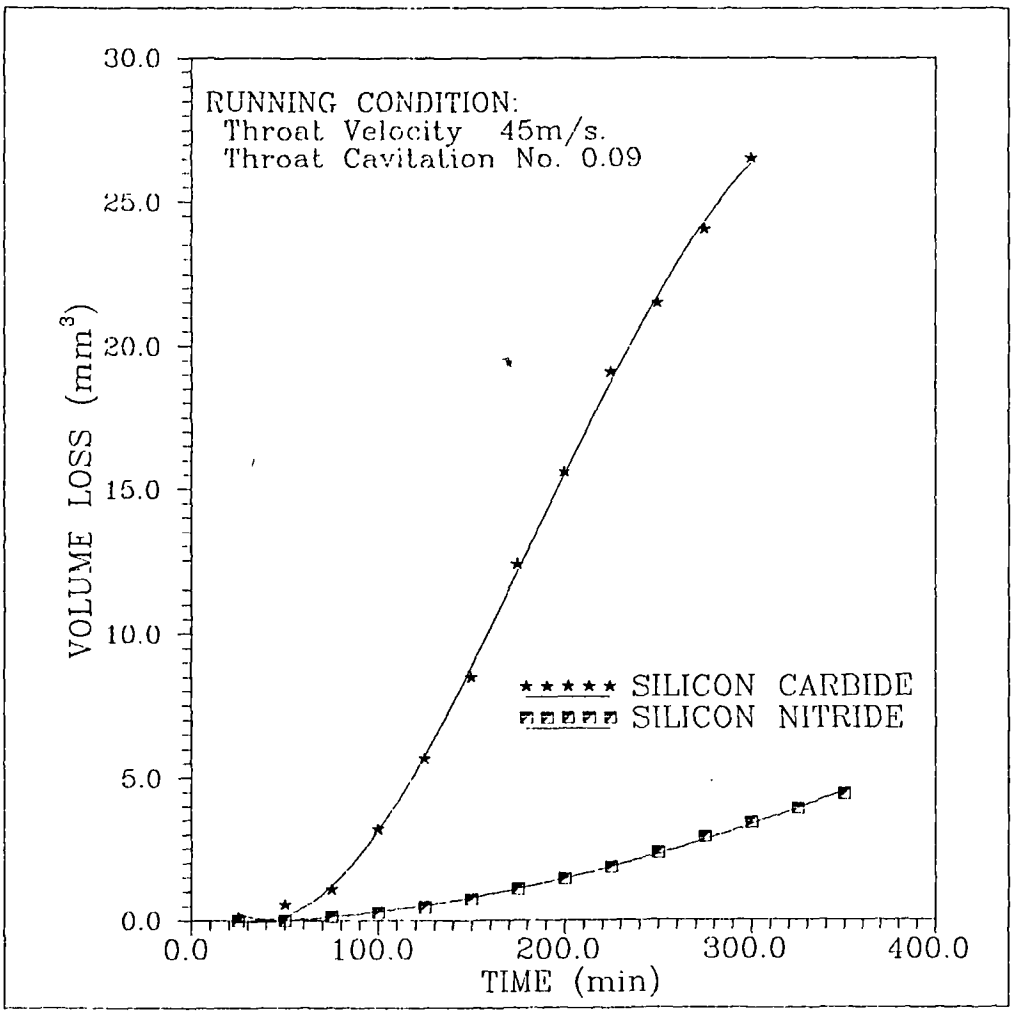

Fig.68 COMPARISON BETWEEN SILICON CARBIDE AND SILICON NITRIDE IN THE AS GROUND CONDITION

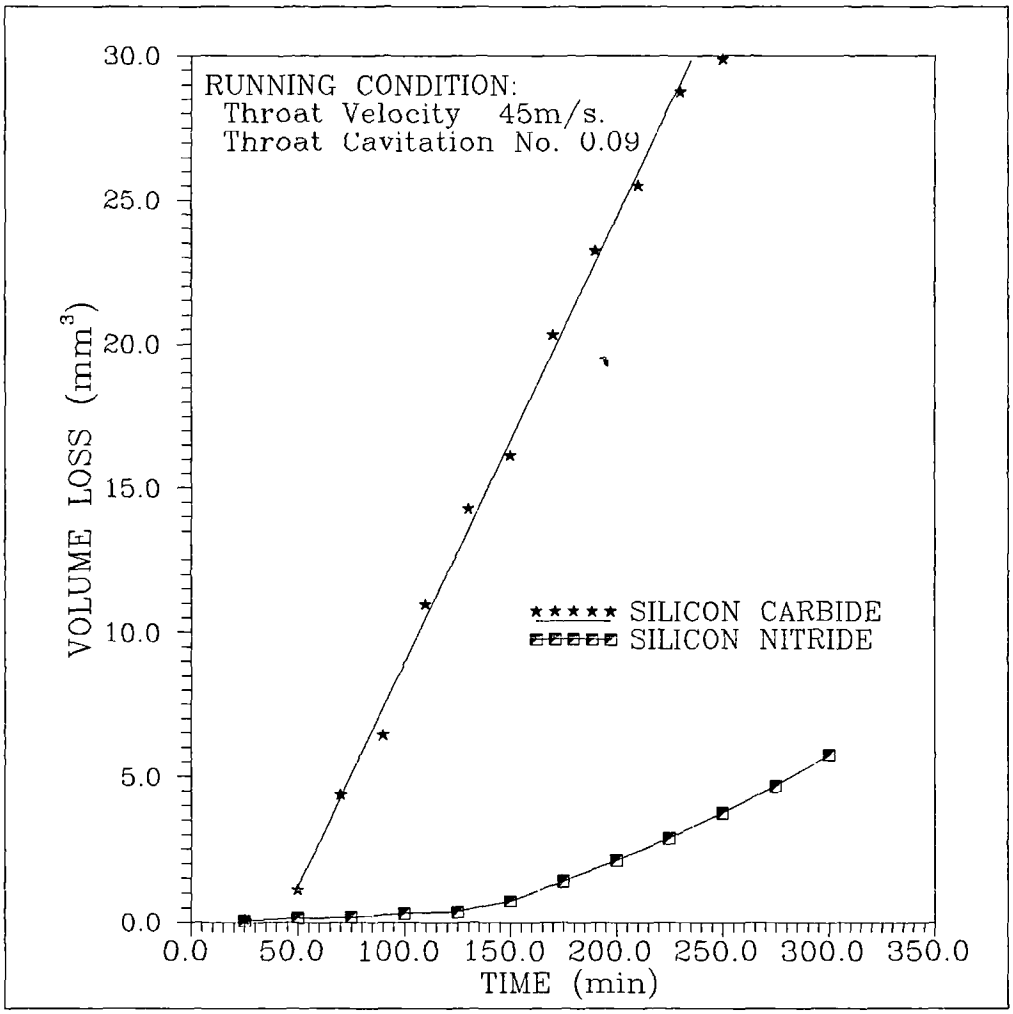

Fig.69 COMPARISON BETWEEN SILICON CARBIDE AND SILICON NITRIDE IN THE AS LAPPED CONDITION

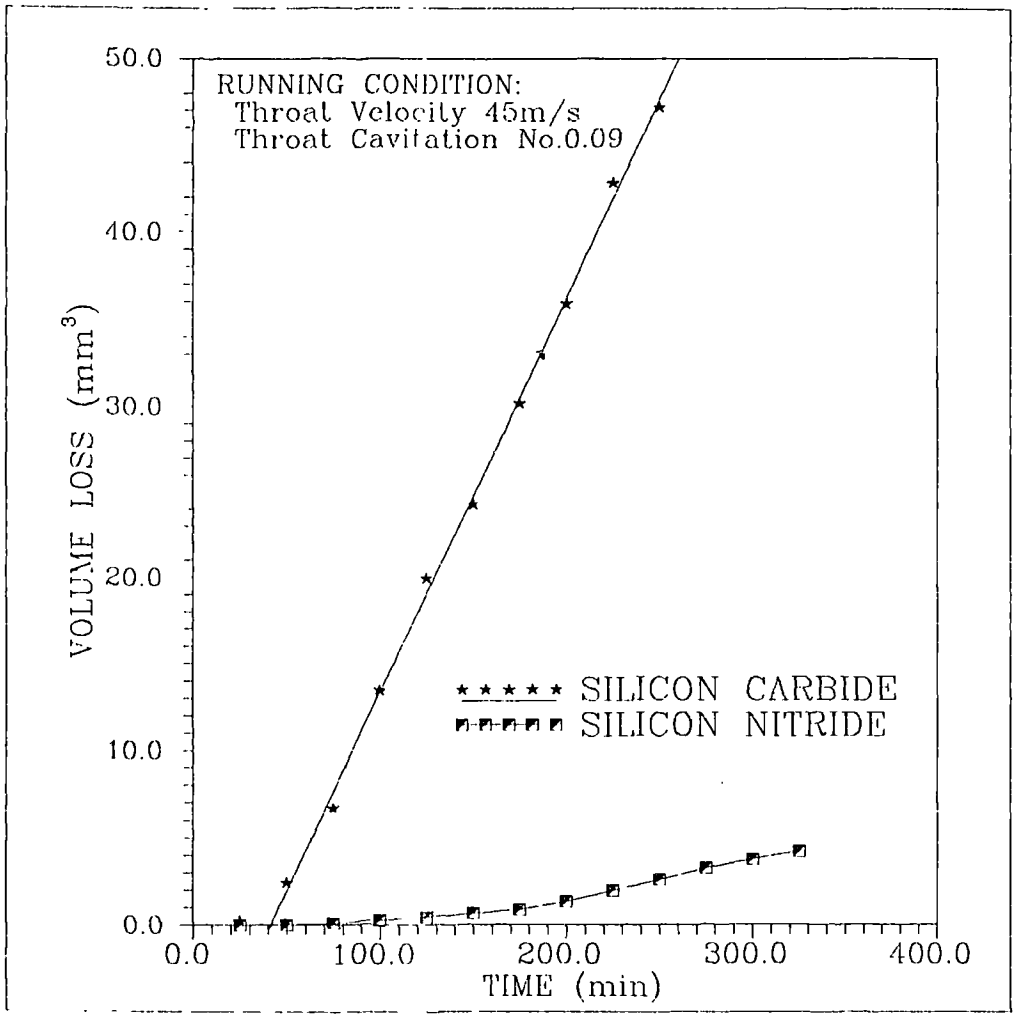

Fig.70 COMPARISON BETWEEN SILICON CARBIDE AND SILICON NITRIDE IN THE AS FIRED CONDITION

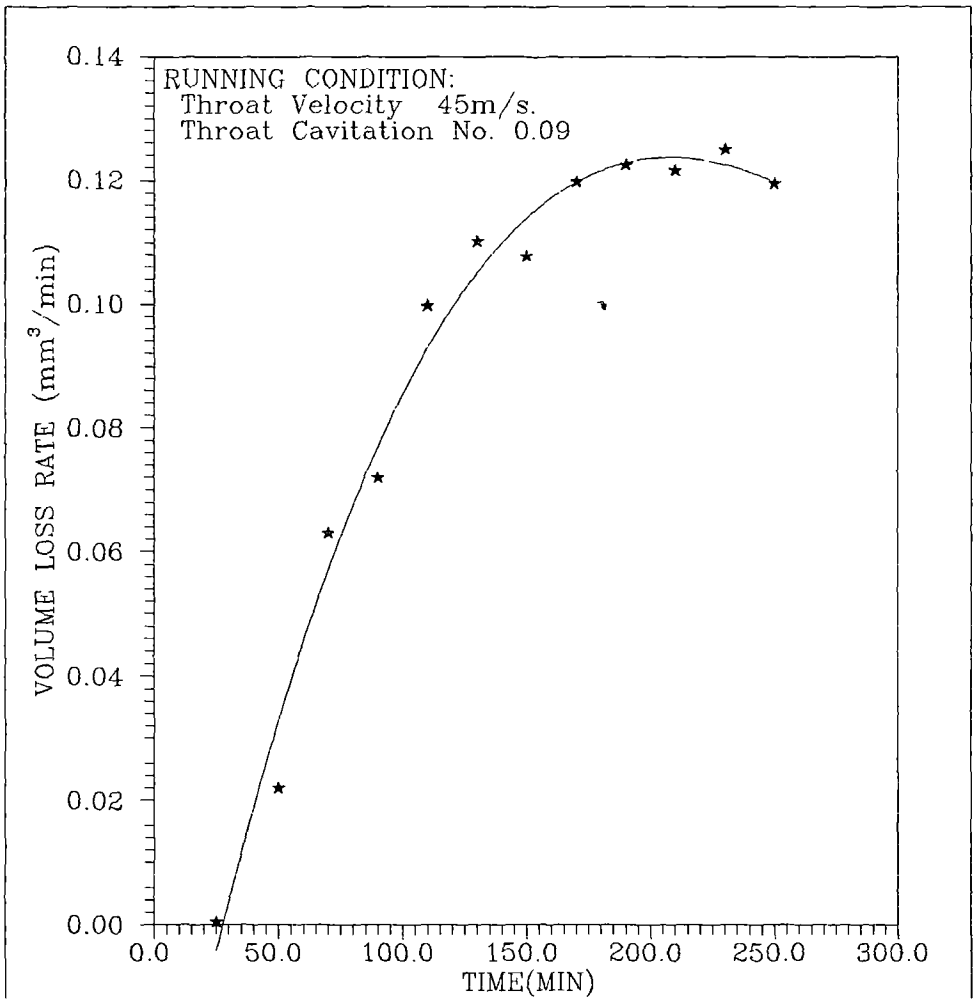

Fig.71 GRAPH OF EROSION RATE AGAINST TIME FOR SILICON CARBIDE AS LAPPED

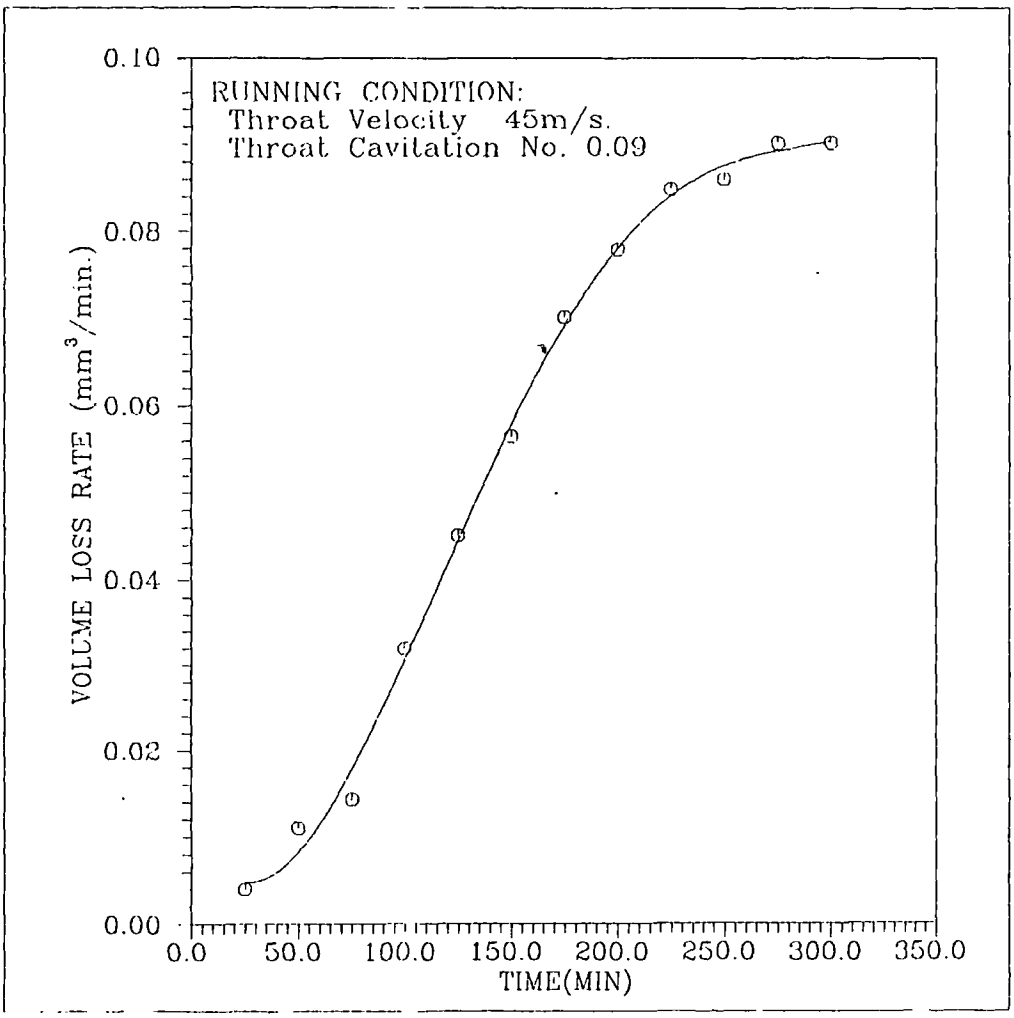

Fig.72 GRAPH OF EROSION RATE AGAINST TIME FOR SILICON CARBIDE AS GROUND

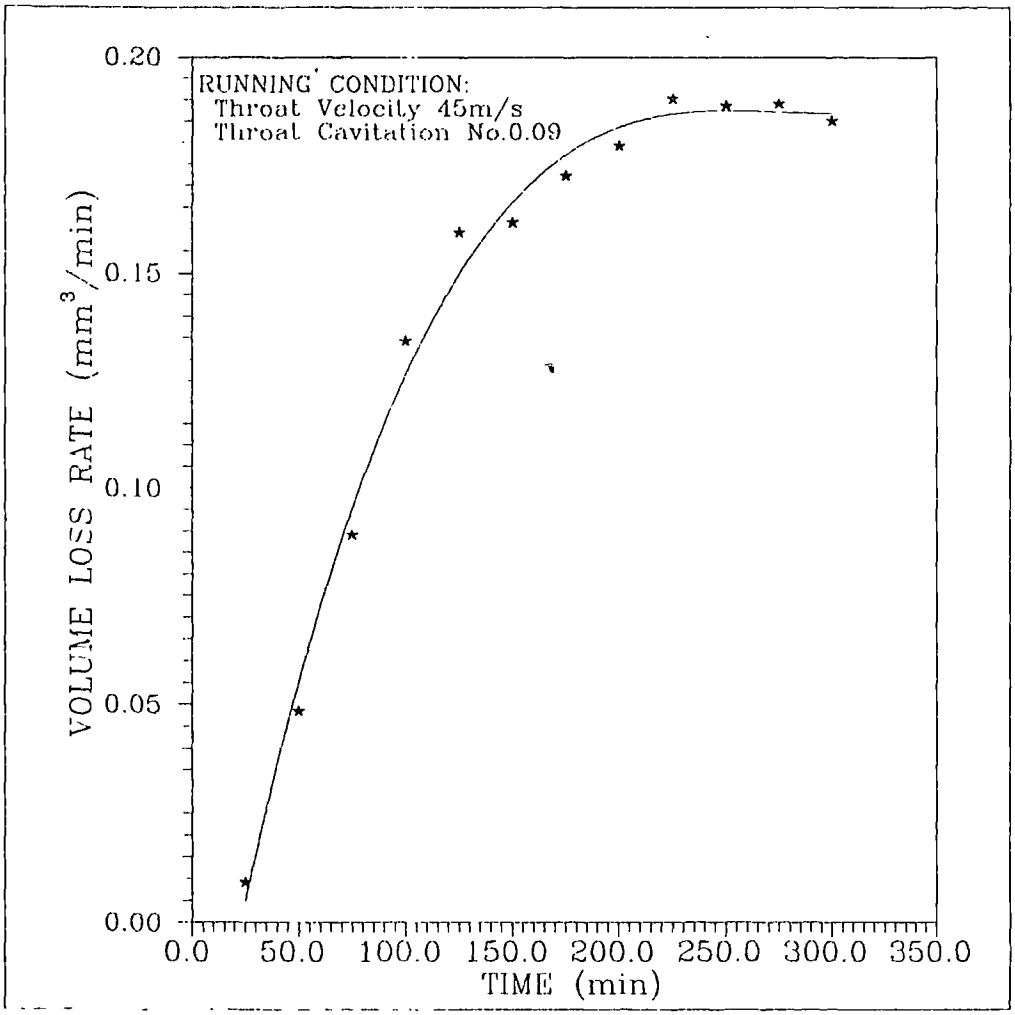

Fig.73 GRAPH OF EROSION RATE AGAINST TIME FOR SILICON CARBIDE AS FIRED

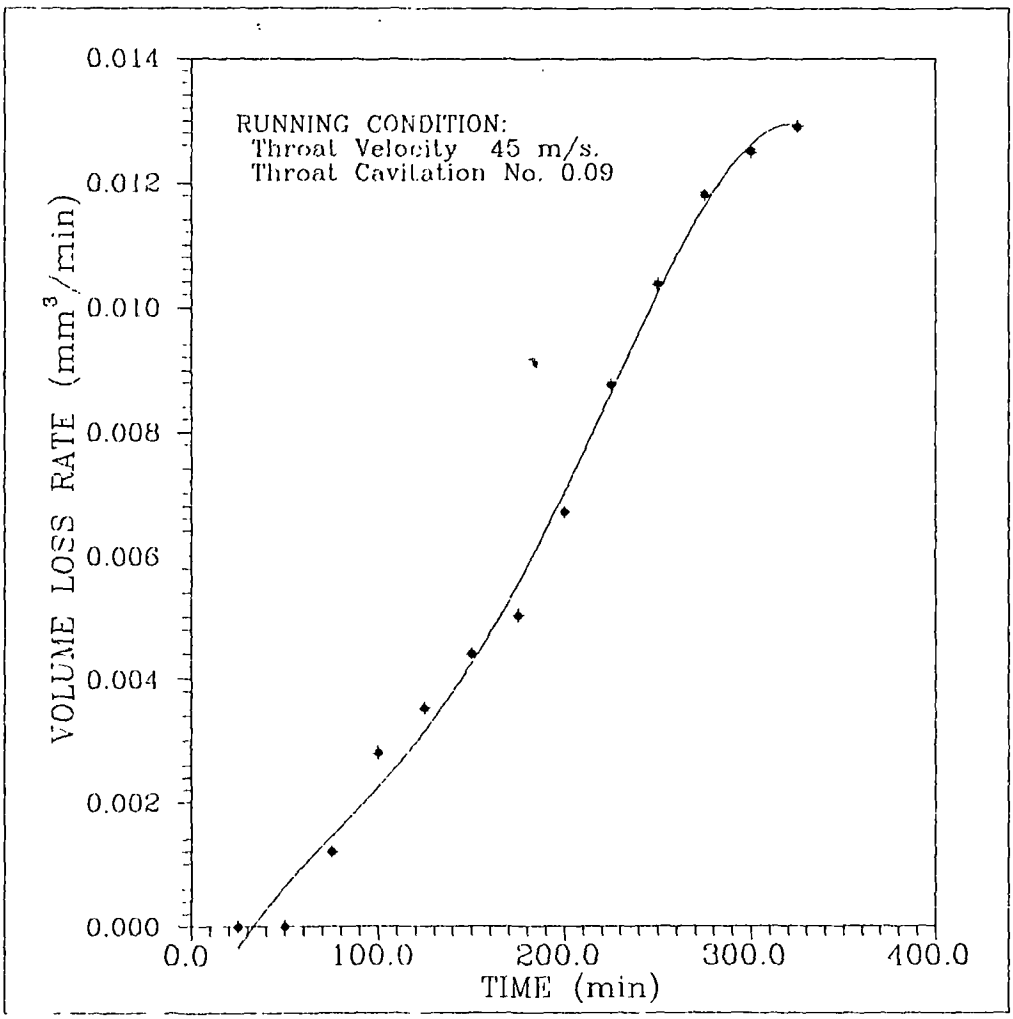

Fig.74 GRAPH OF EROSION RATE AGAINST TIME FOR SILICON NITRIDE AS FIRED

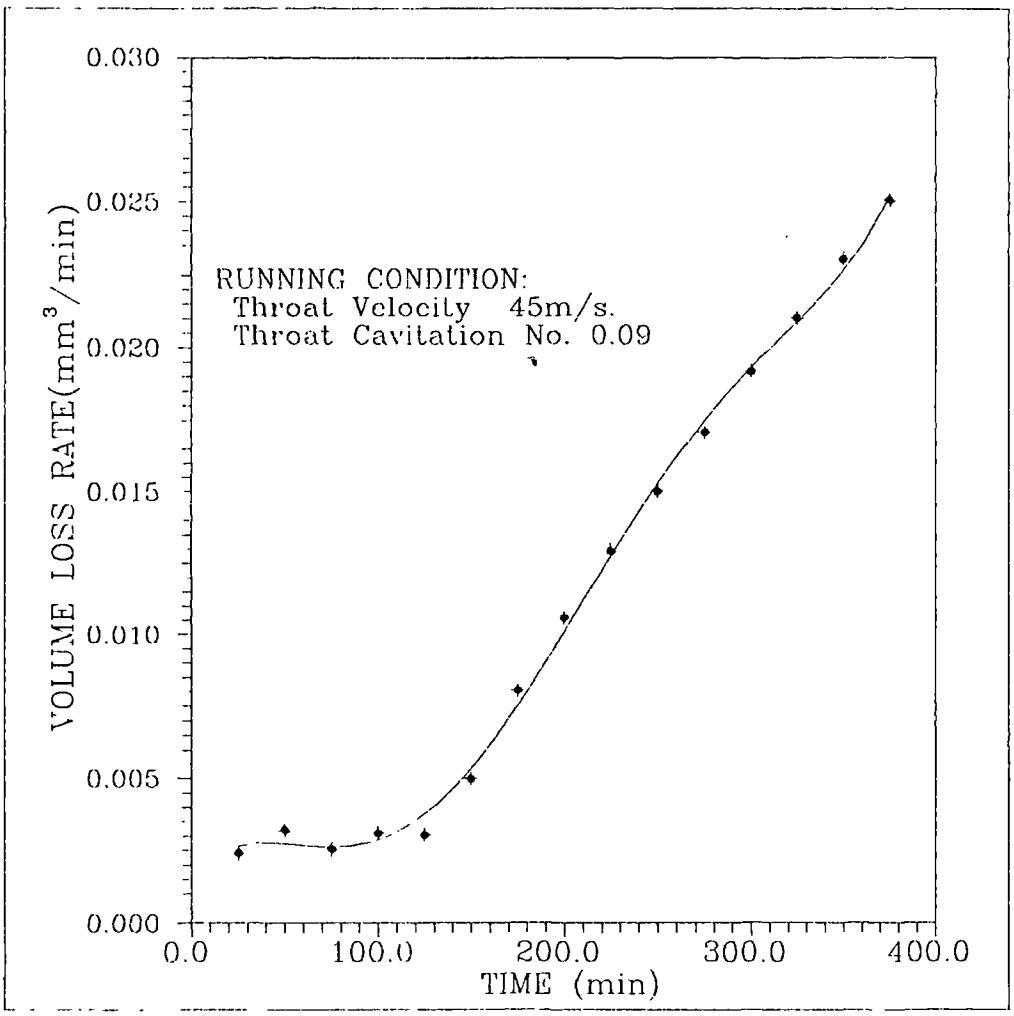

Fig.75 GRAPH OF EROSION RATE AGAINST TIME FOR SILICON NITRIDE AS LAPPED

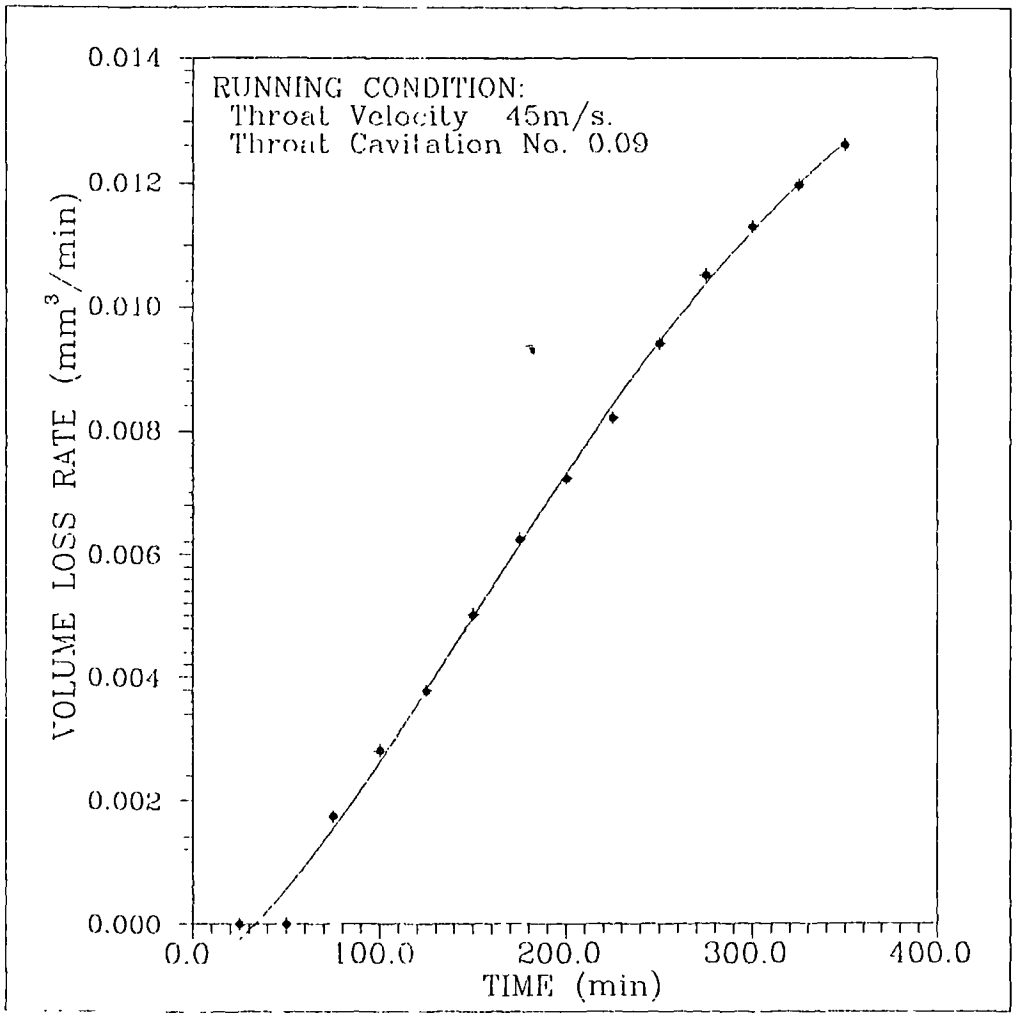

Fig.76 GRAPH OF EROSION RATE AGAINSTB TIME FOR SILICON NITRIDE AS GROUND

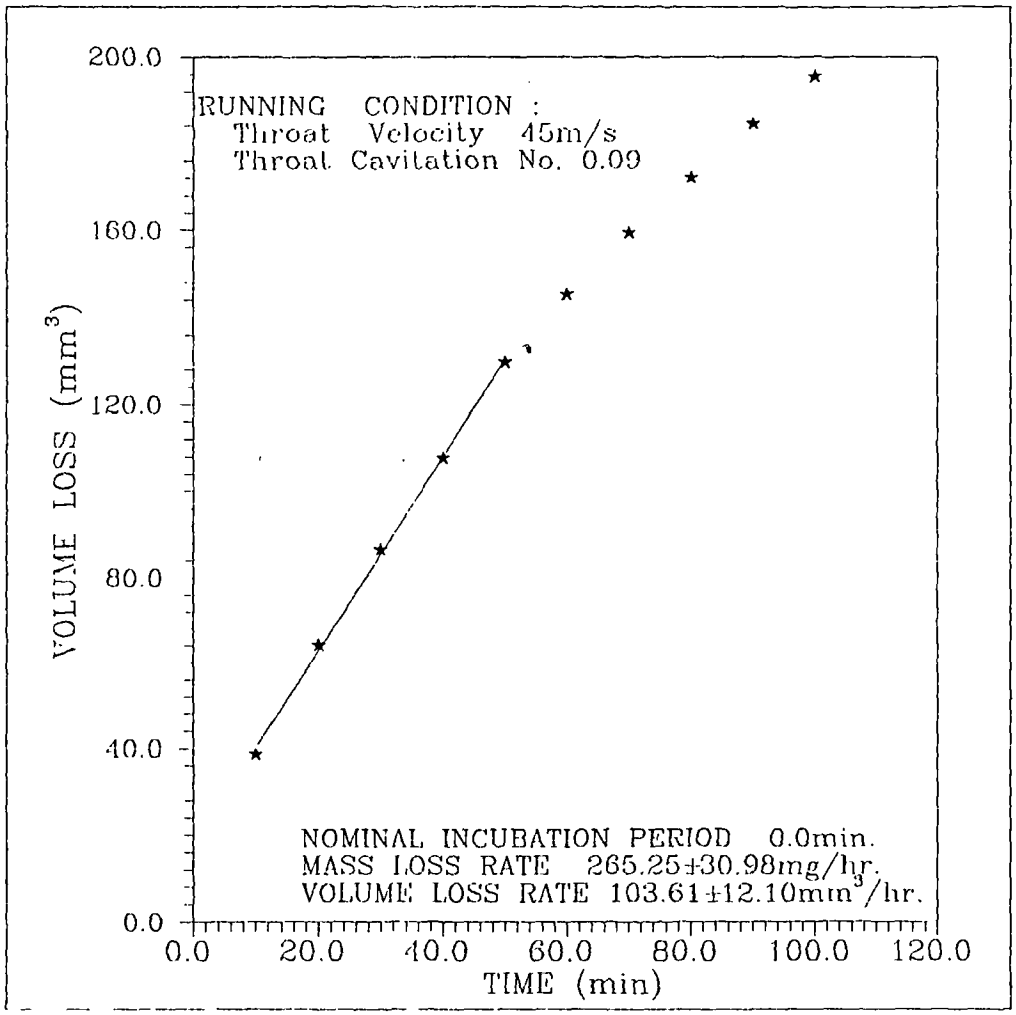

Fig.77 CUMULATIVE WEIGHT LOSS AGAINST TIME FOR G R P

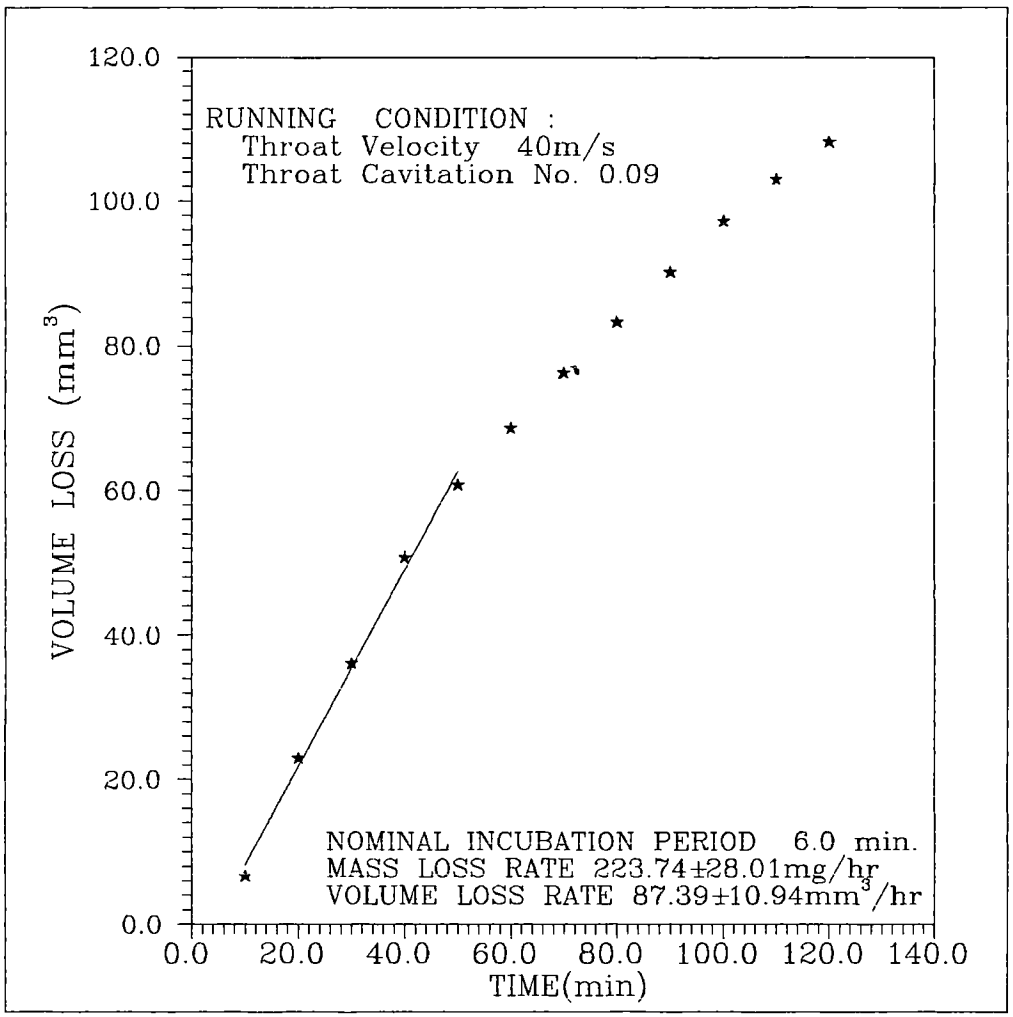

Fig.78 CUMULATIVE WEIGHT LOSS AGAINST TIME FOR G R P

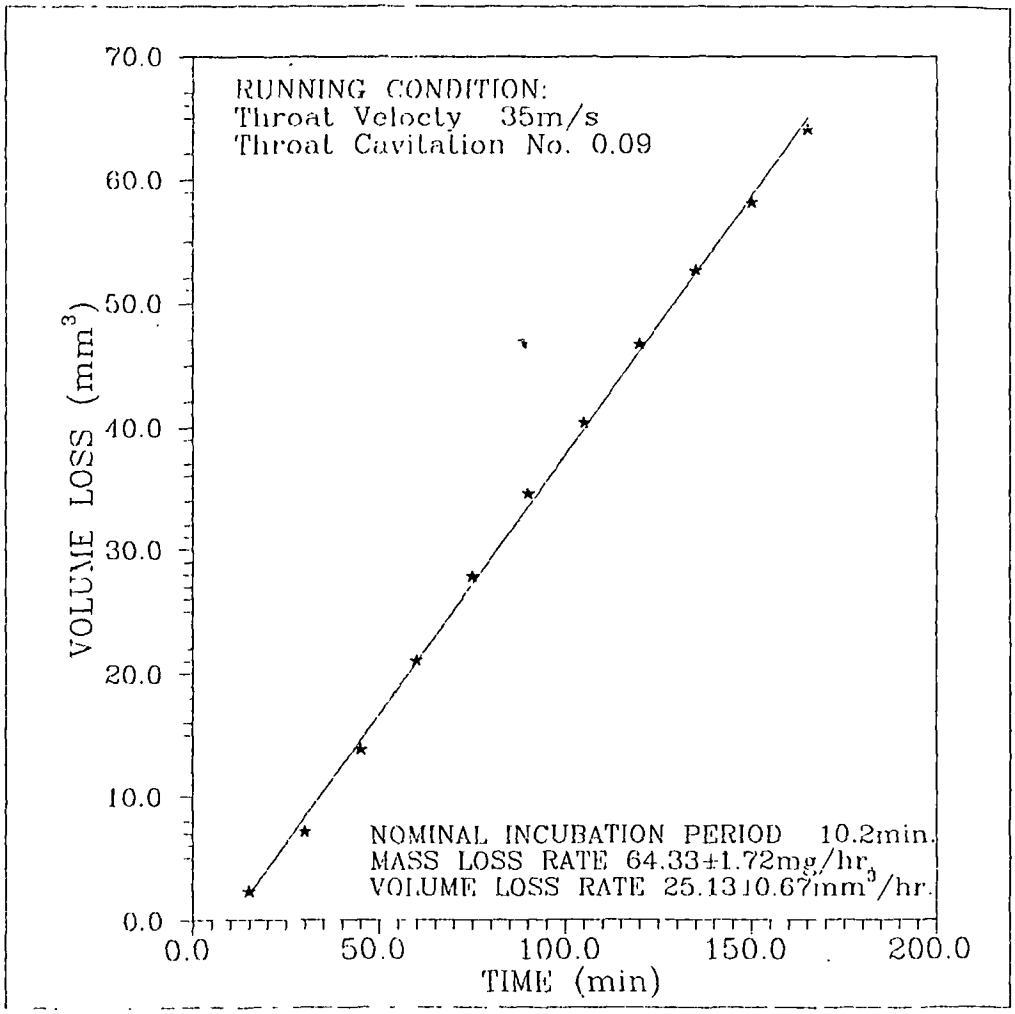

Fig.79 CUMULATIVE WEIGHT LOSS AGAINST TIME FOR G R P

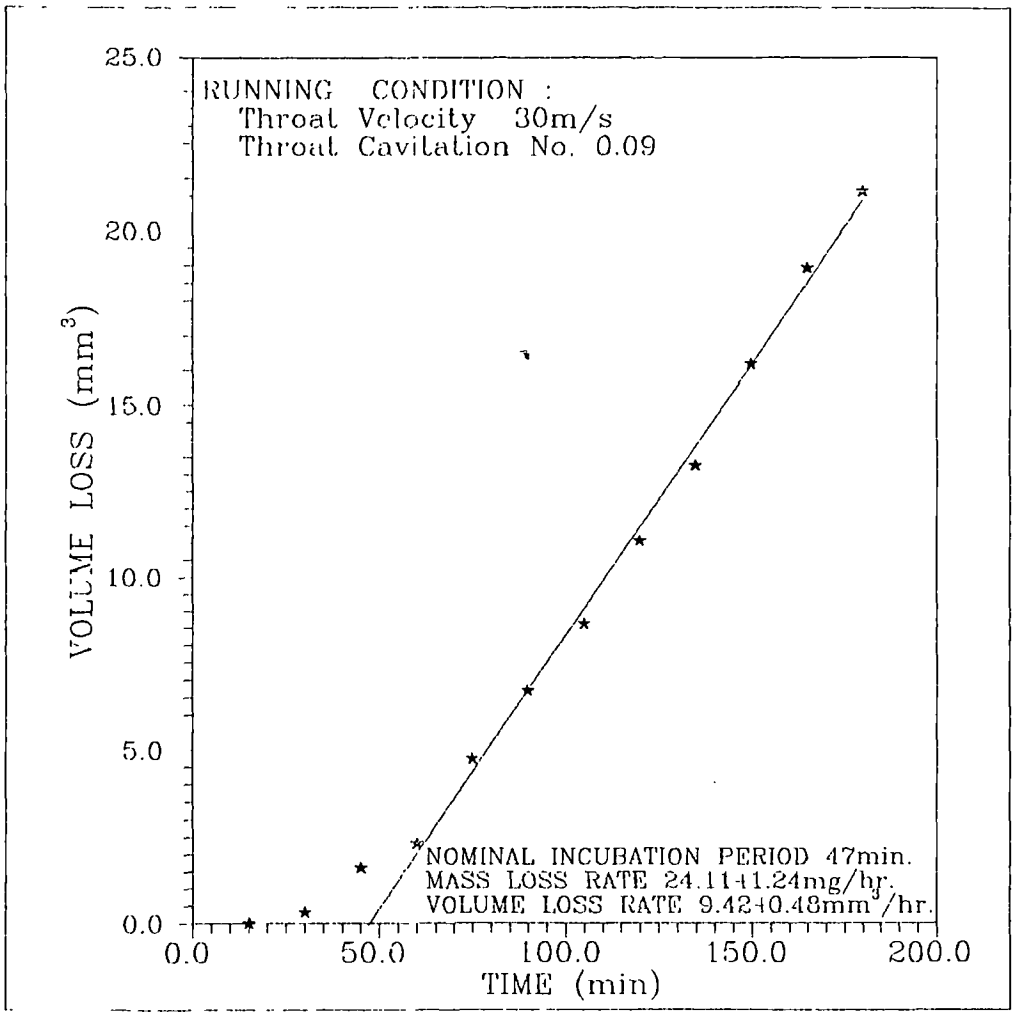

Fig.80 CUMULATIVE WEIGHT LOSS AGAINST TIME FOR G R P

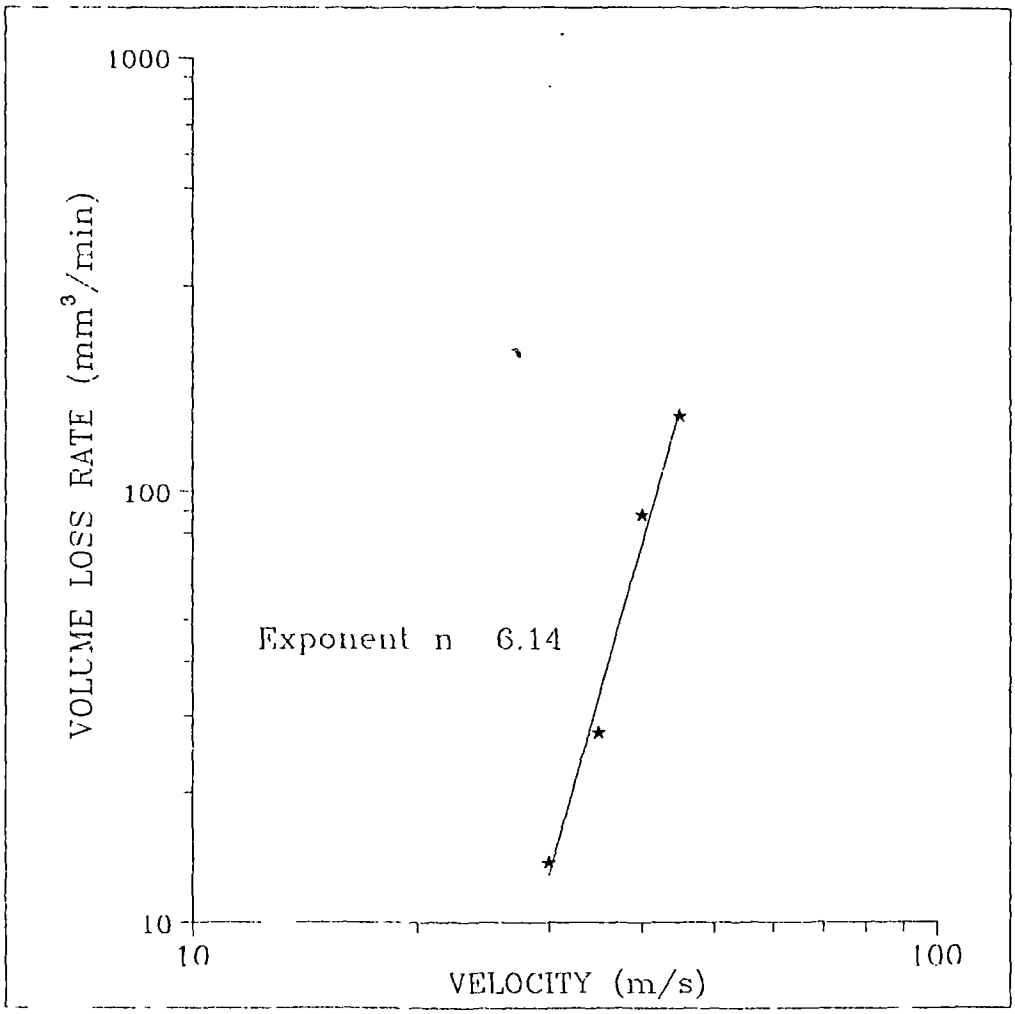

Fig.81 VOLUME LOSS RATE VERSUS VELOCITY FOR GRP

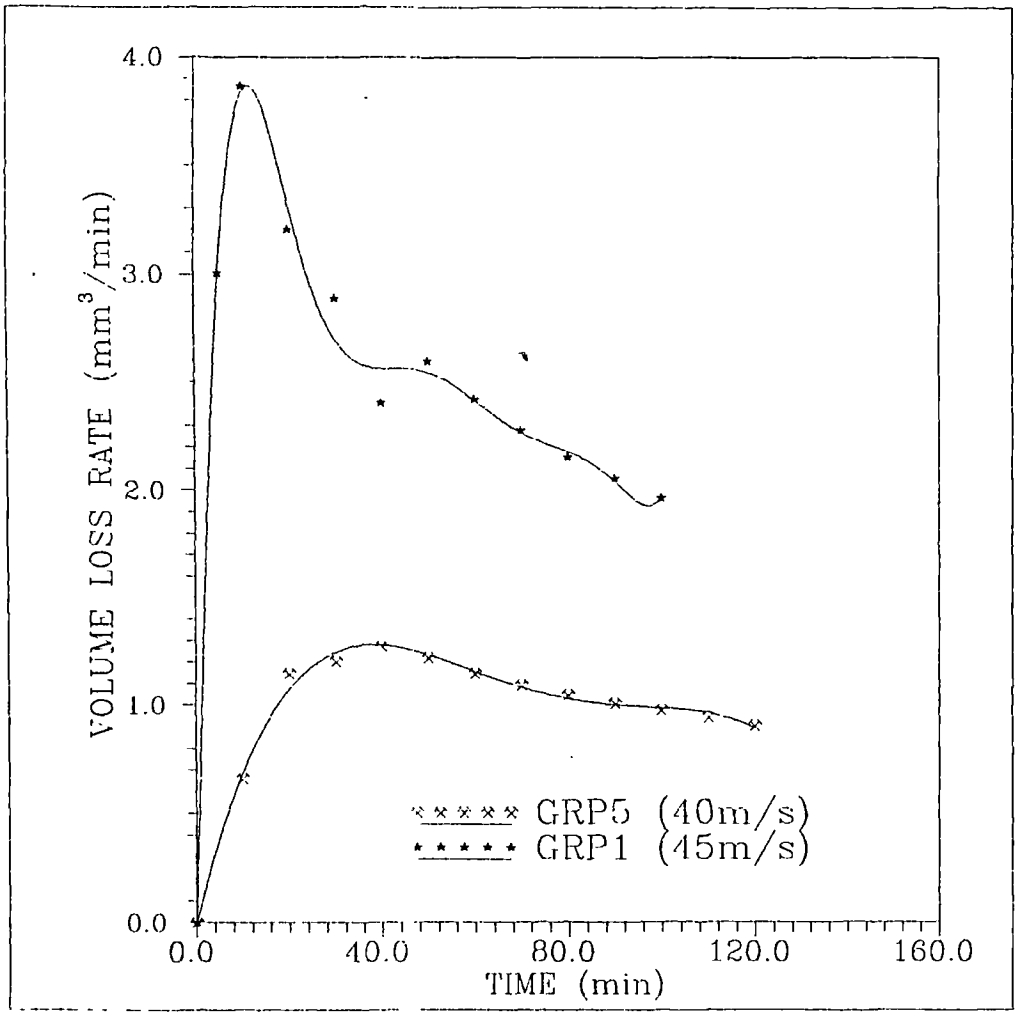

Fig.82 EFFECT OF CAVITATION INTENSITY ON EROSION RATE CURVE ON GRP

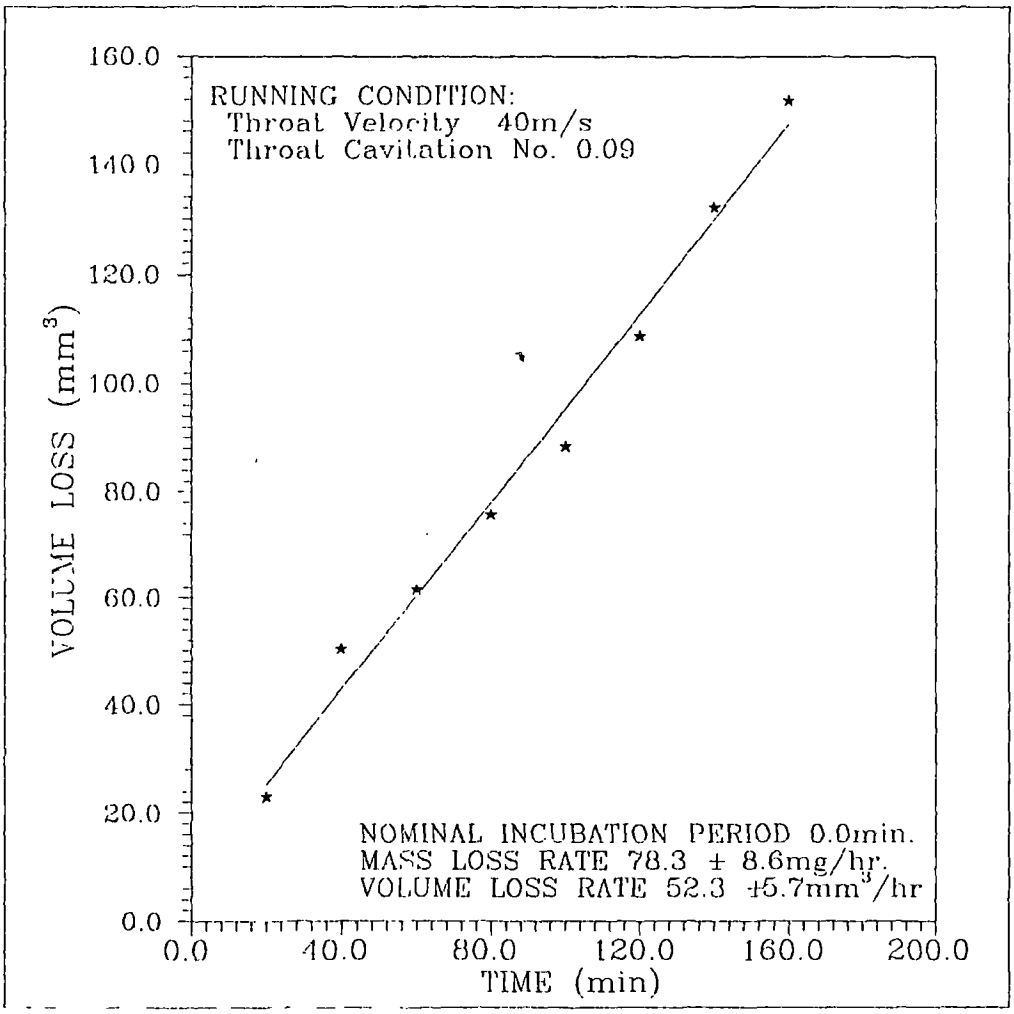

Fig.83 GRAPH OF CUMULATIVE VOLUME LOSS AGAINST TIME FOR FYBROC

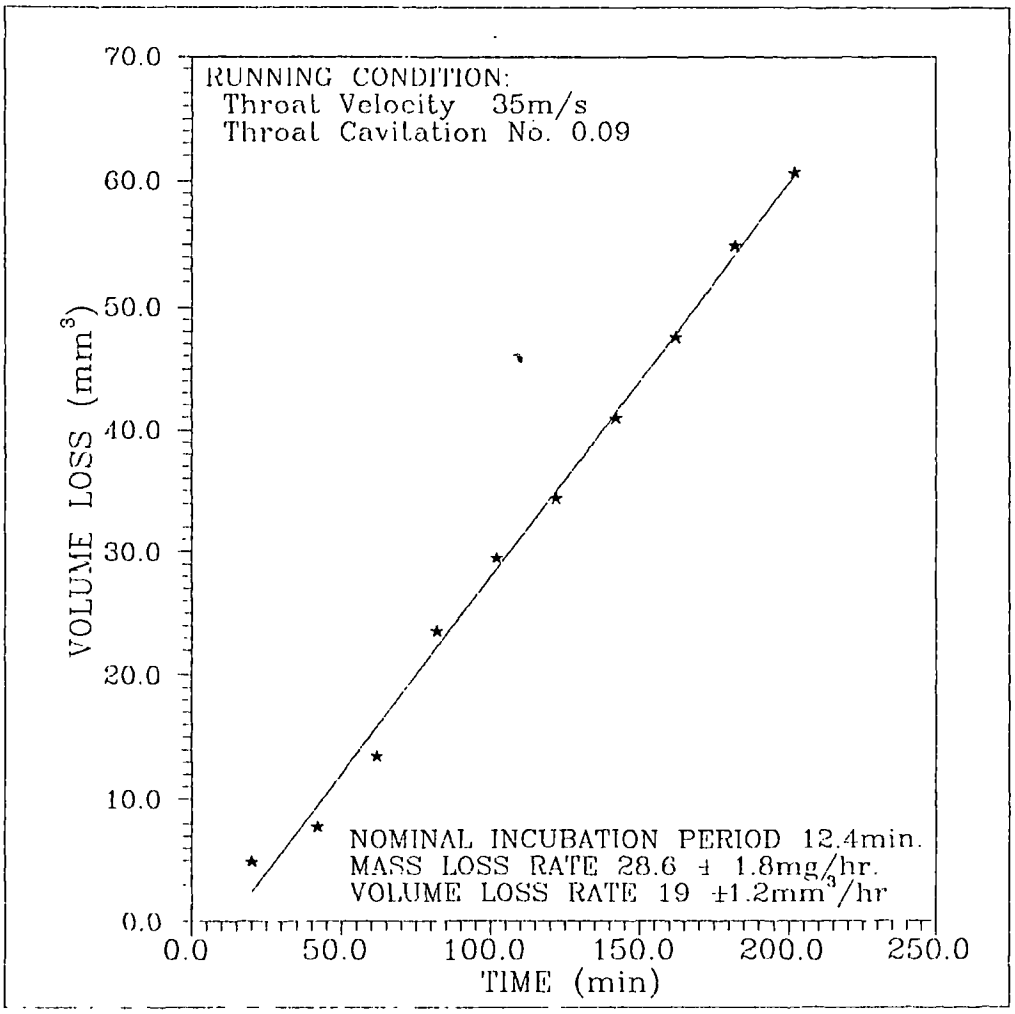

Fig.84 GRAPH OF CUMULATIVE VOLUME LOSS AGAINST TIME FOR FYBROC

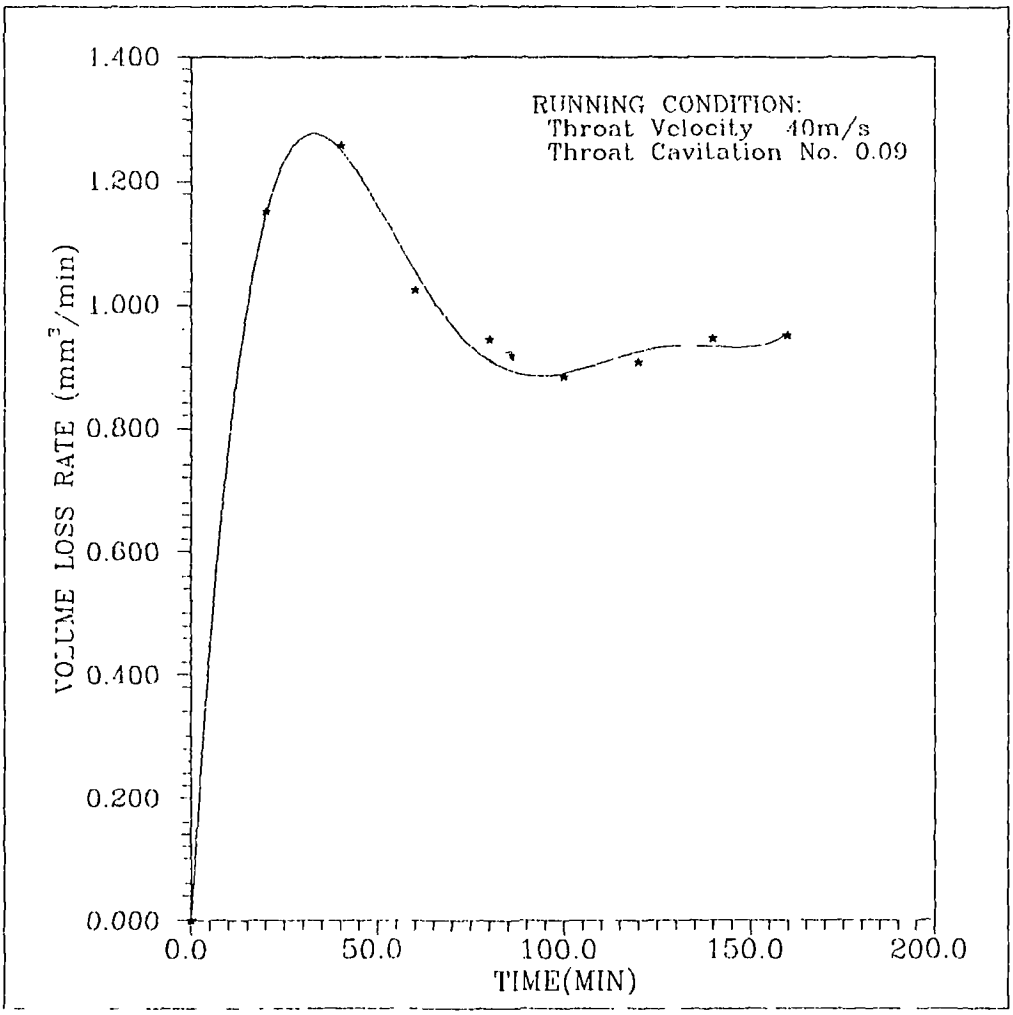

Fig.85 GRAPH OF EROSION RATE AGAINST TIME FOR FYBROC

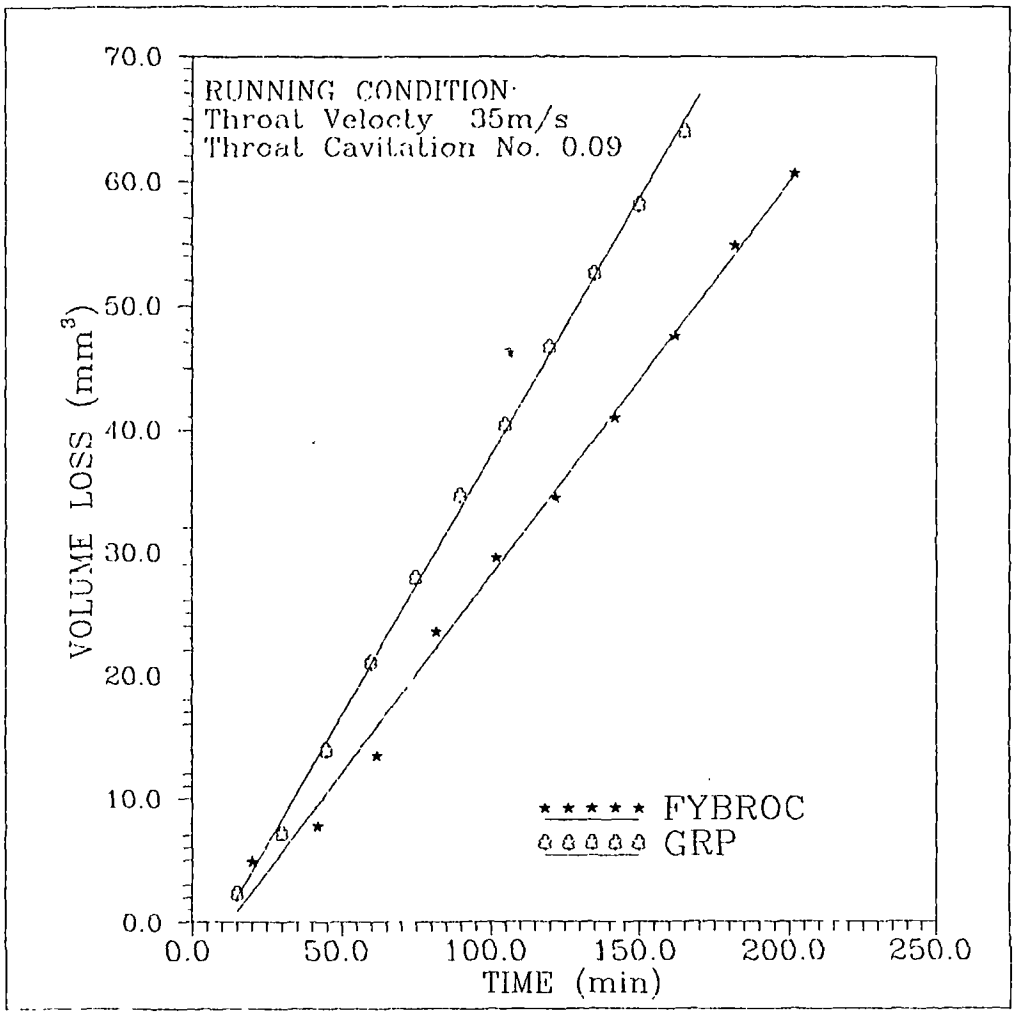

Fig.86 COMPARISON GRAPH BETWEEN GRP AND FYBROC

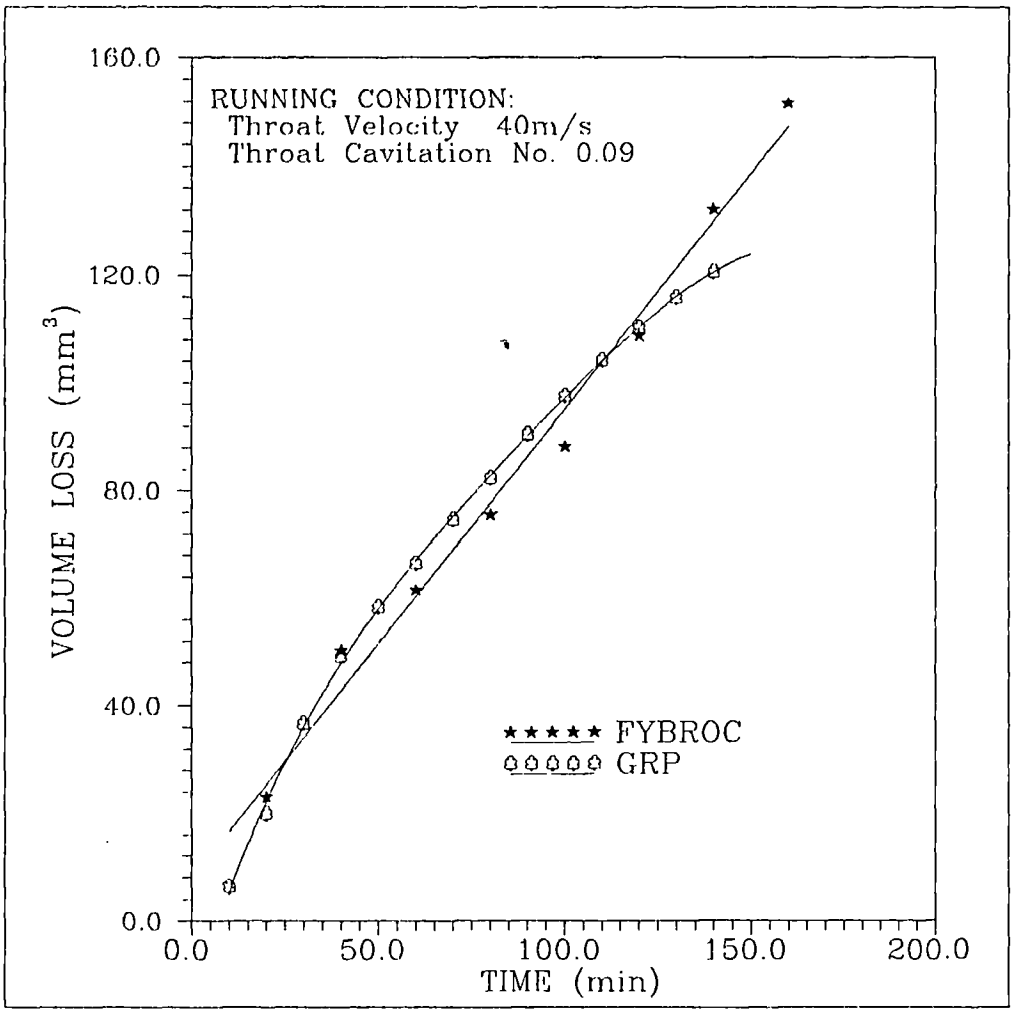

Fig.87 COMPARISON GRAPH BETWEEN GRP AND FYBROC

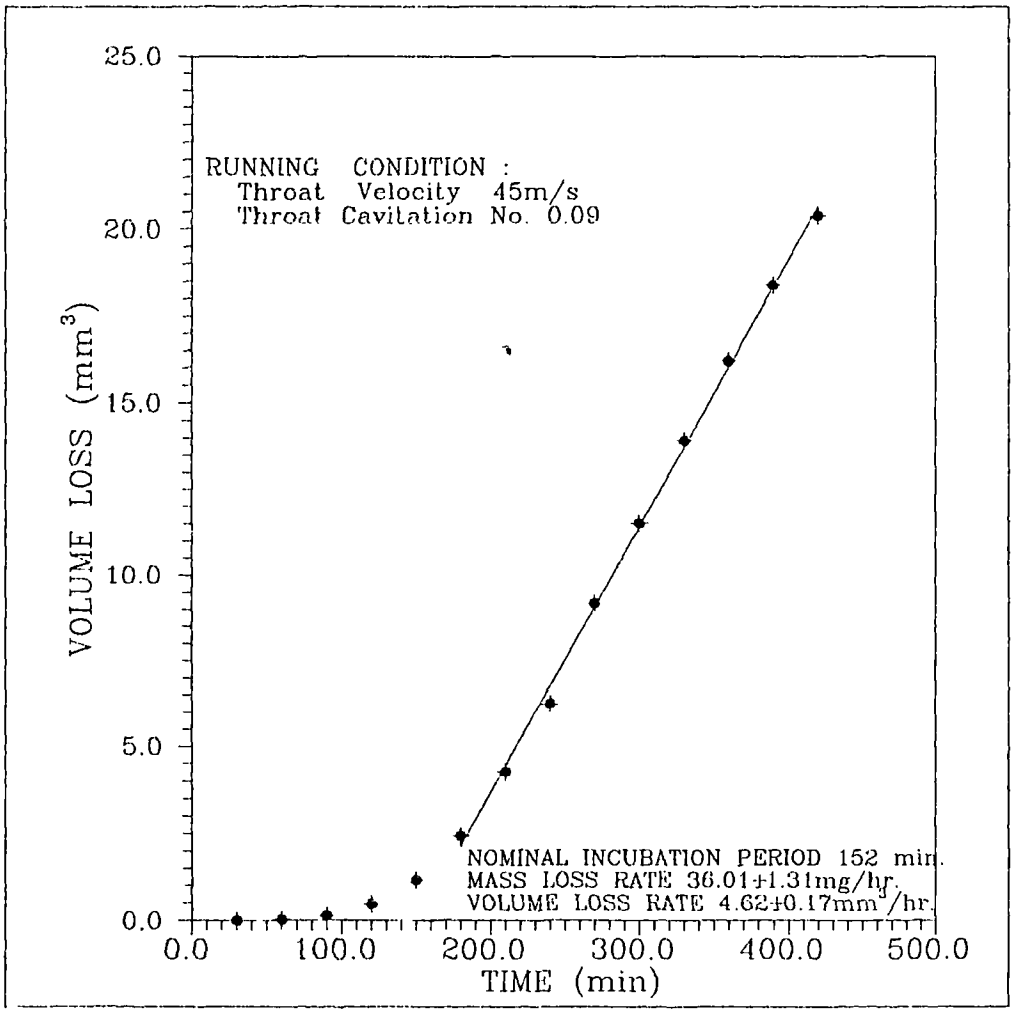

Fig.88 GRAPH OF CUMULATIVE VOLUME LOSS AGAINST TIME FOR CARBON STEEL (AISI 1020)

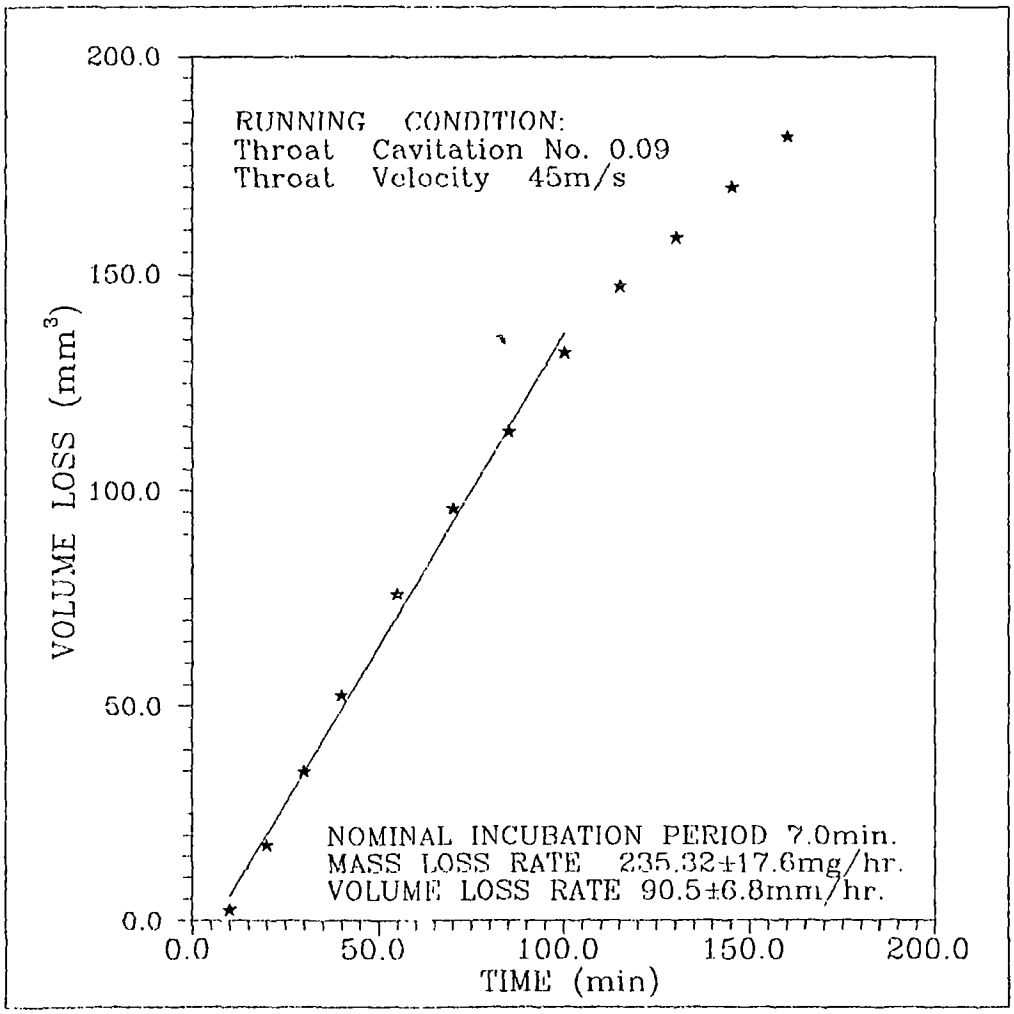

Fig.89 GRAPH OF CUMULATIVE VOLUME LOSS AGAINST TIME FOR ALUMINIUM(PA2)

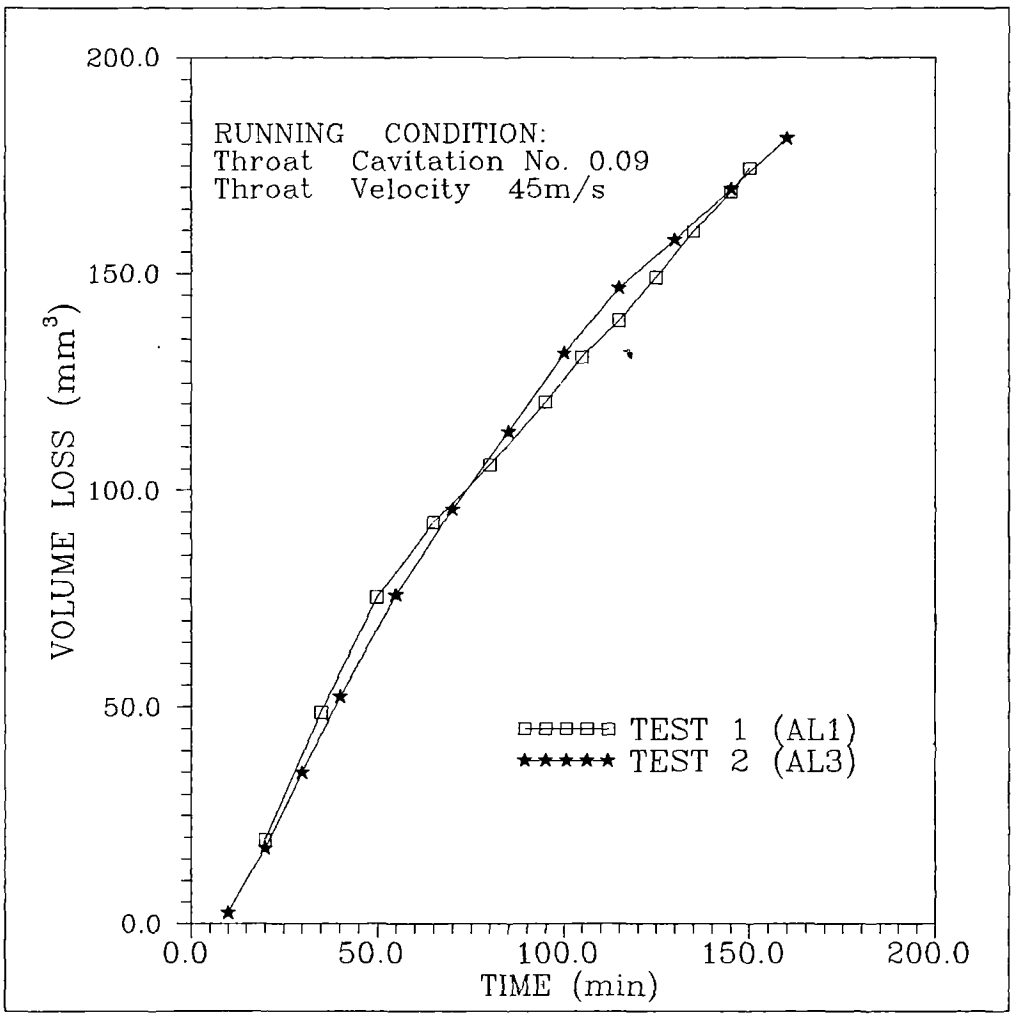

Fig.89B REPEATABILITY TEST FOR ALUMINUM ALLOY

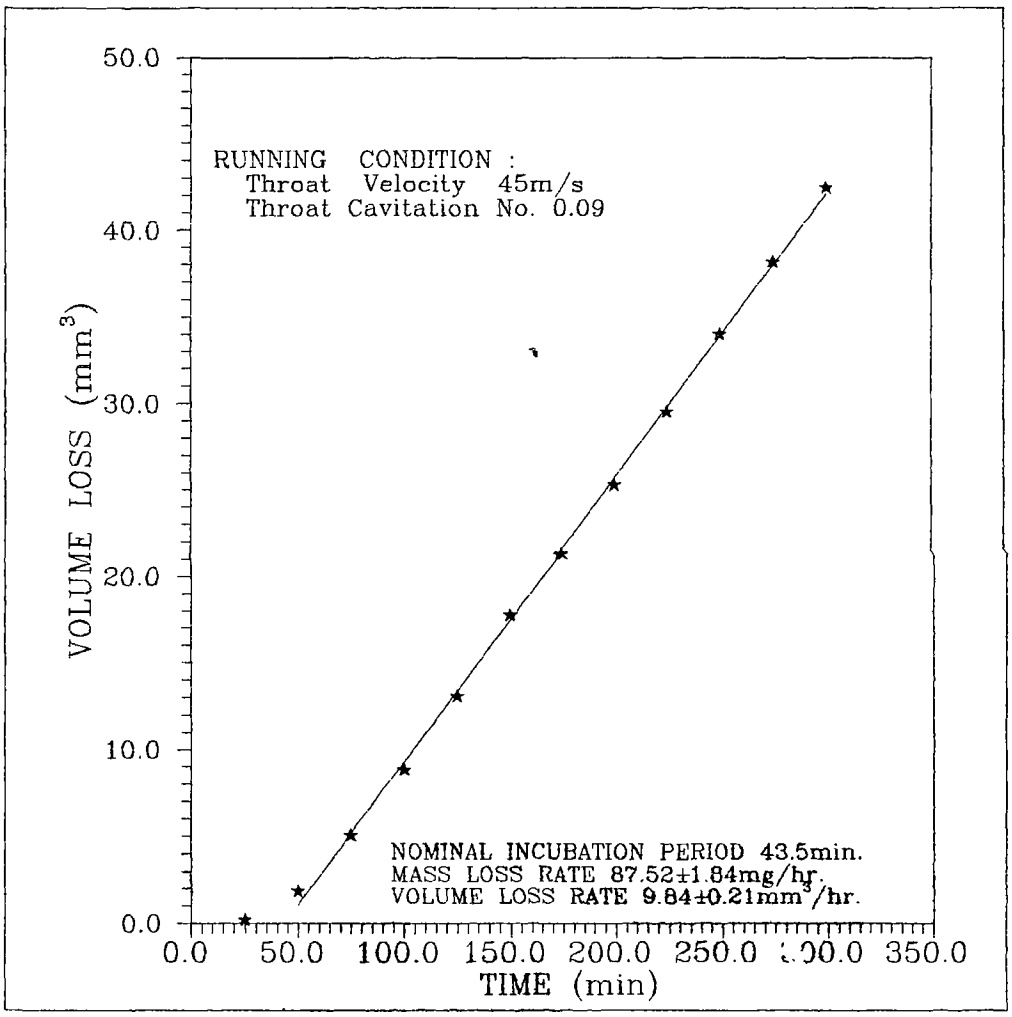

Fig.90 CUMULATIVE WEIGHT LOSS AGAINST TIME FOR CUPRO-NICKEL

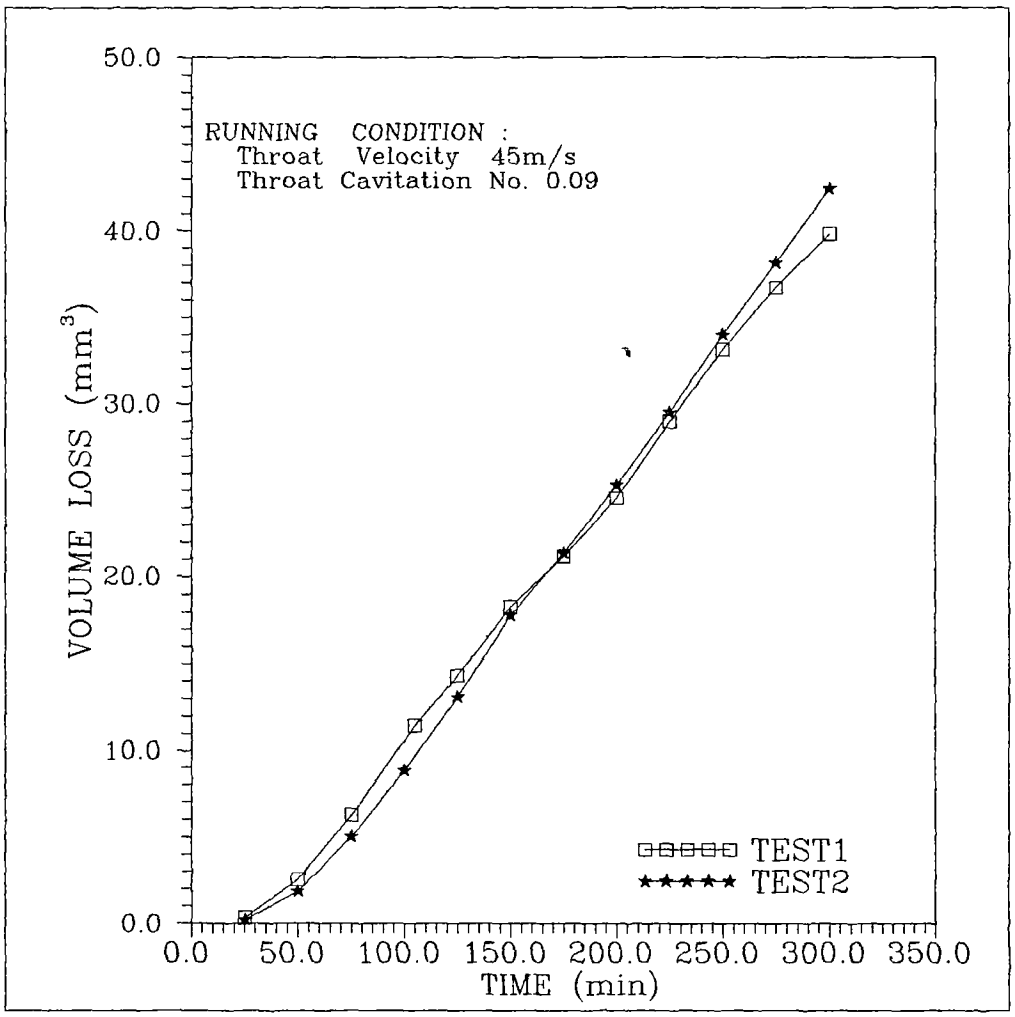

Fig.90A REPEATABILITY TEST FOR CUPRO-NICKEL(90/10)

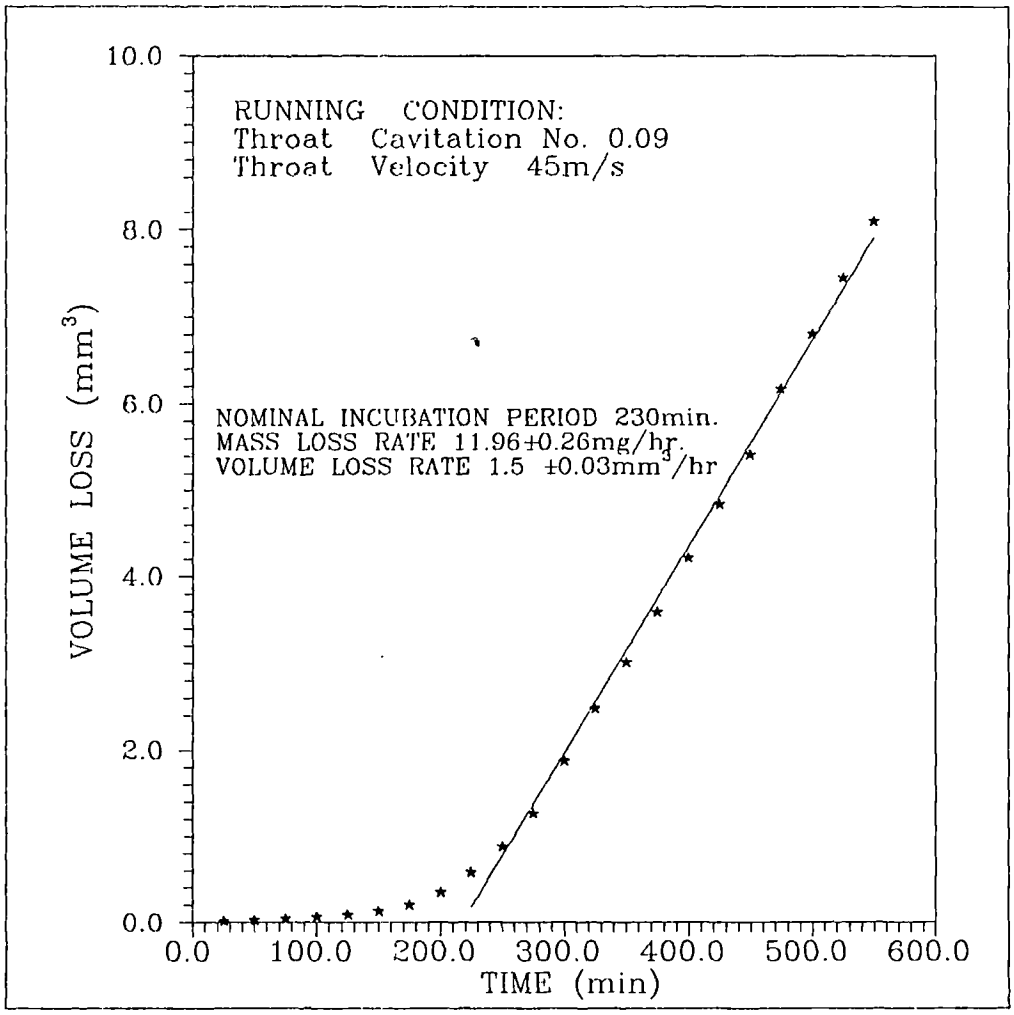

Fig.91 GRAPH OF CUMULATIVE VOLUME LOSS AGAINST TIME FOR ARMCO IRON

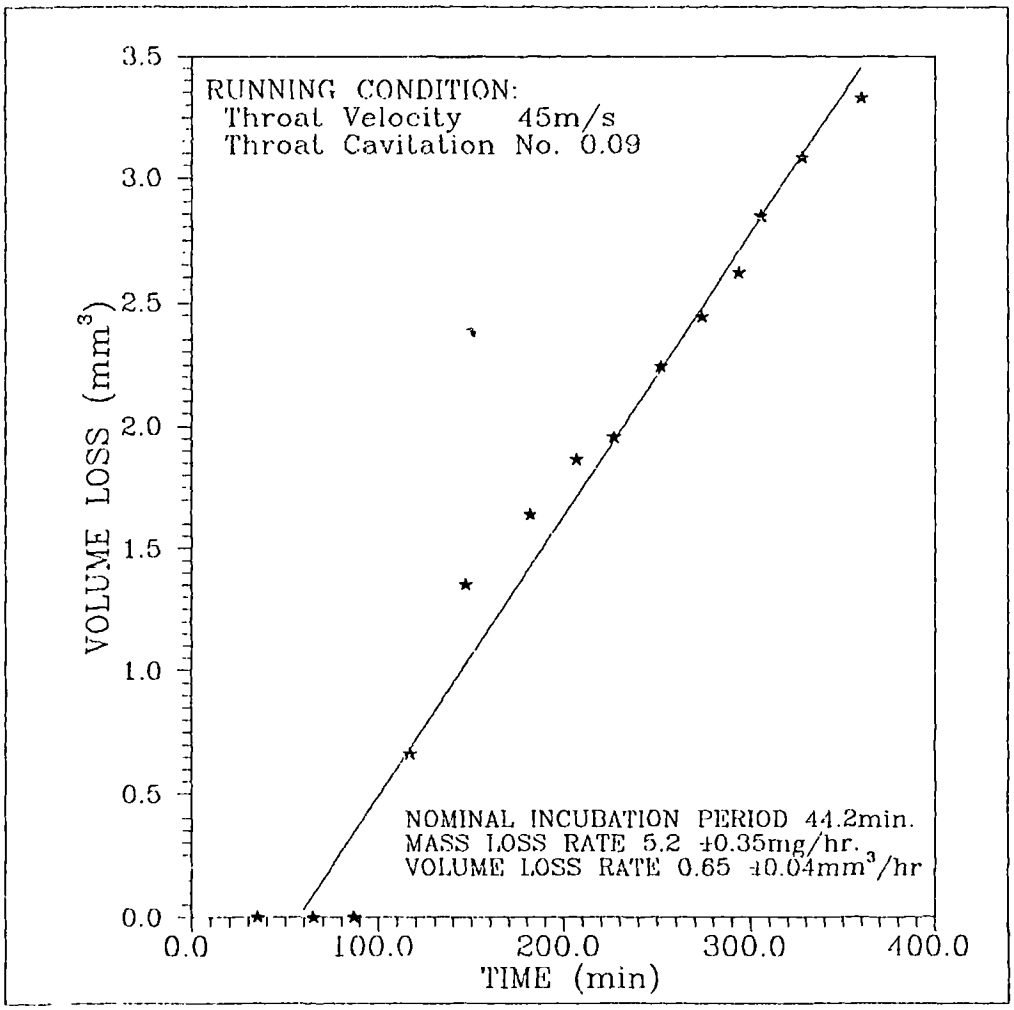

Fig.92 CUMULATIVE VOLUME LOSS AGAINST TIME FOR CAST STAINLESS STEEL

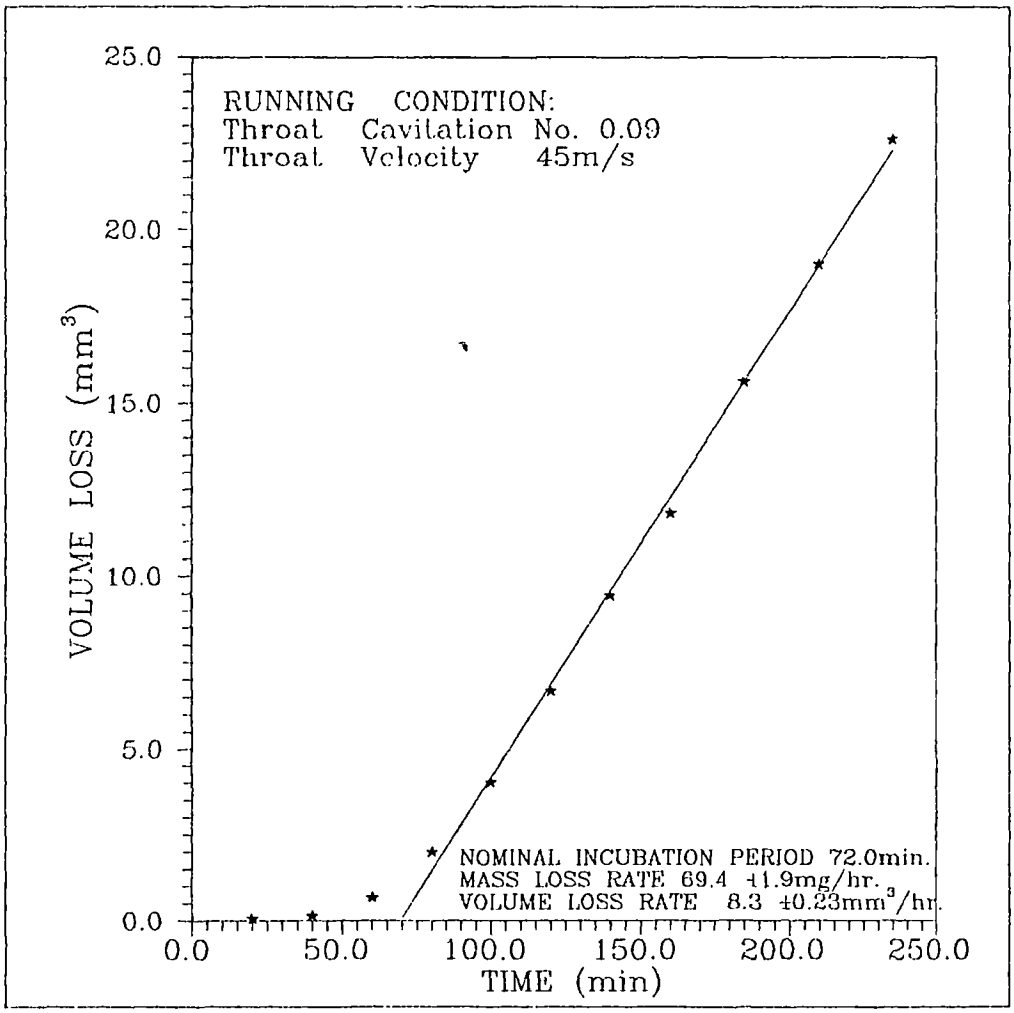

Fig.93 CUMULATIVE VOLUME LOSS AGAINST TIME FOR BRASS (M63)

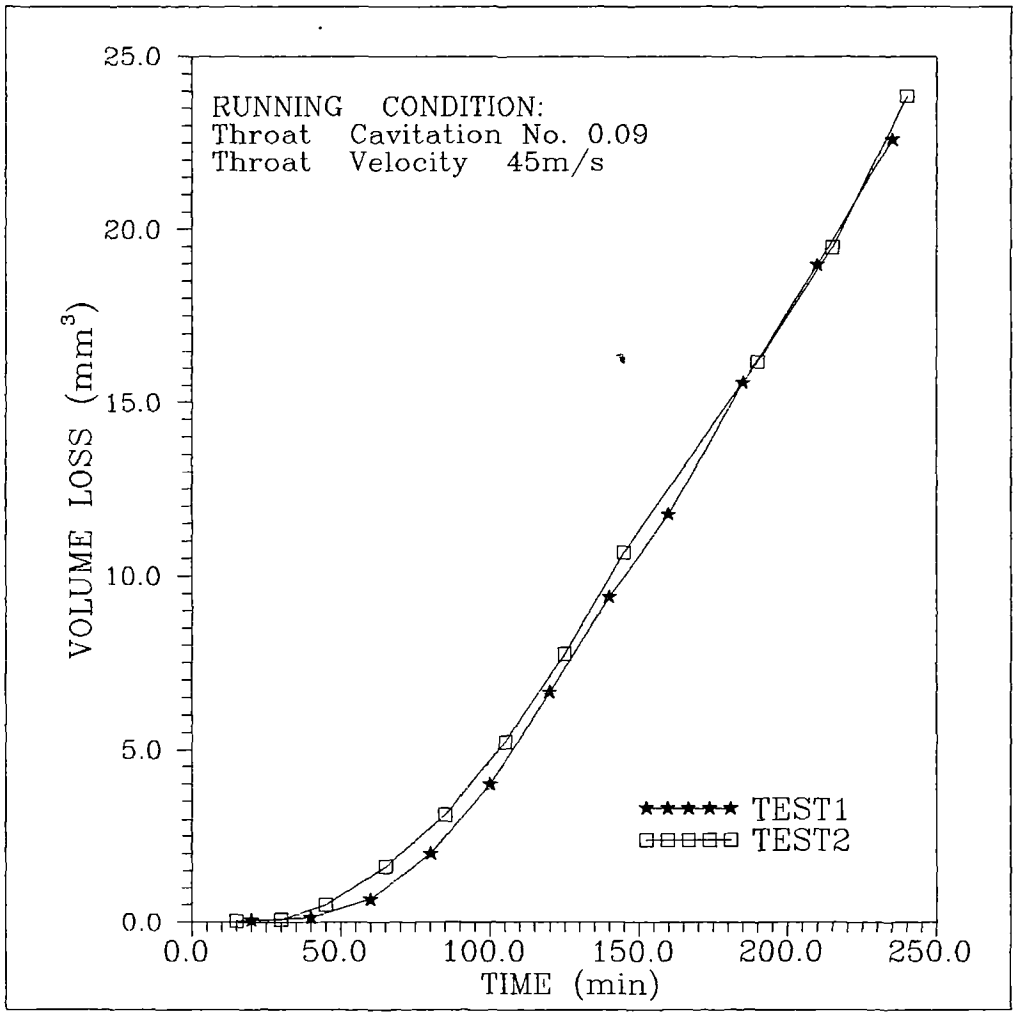

Fig.93A REPEATABILITY TEST FOR BRASS (M63)

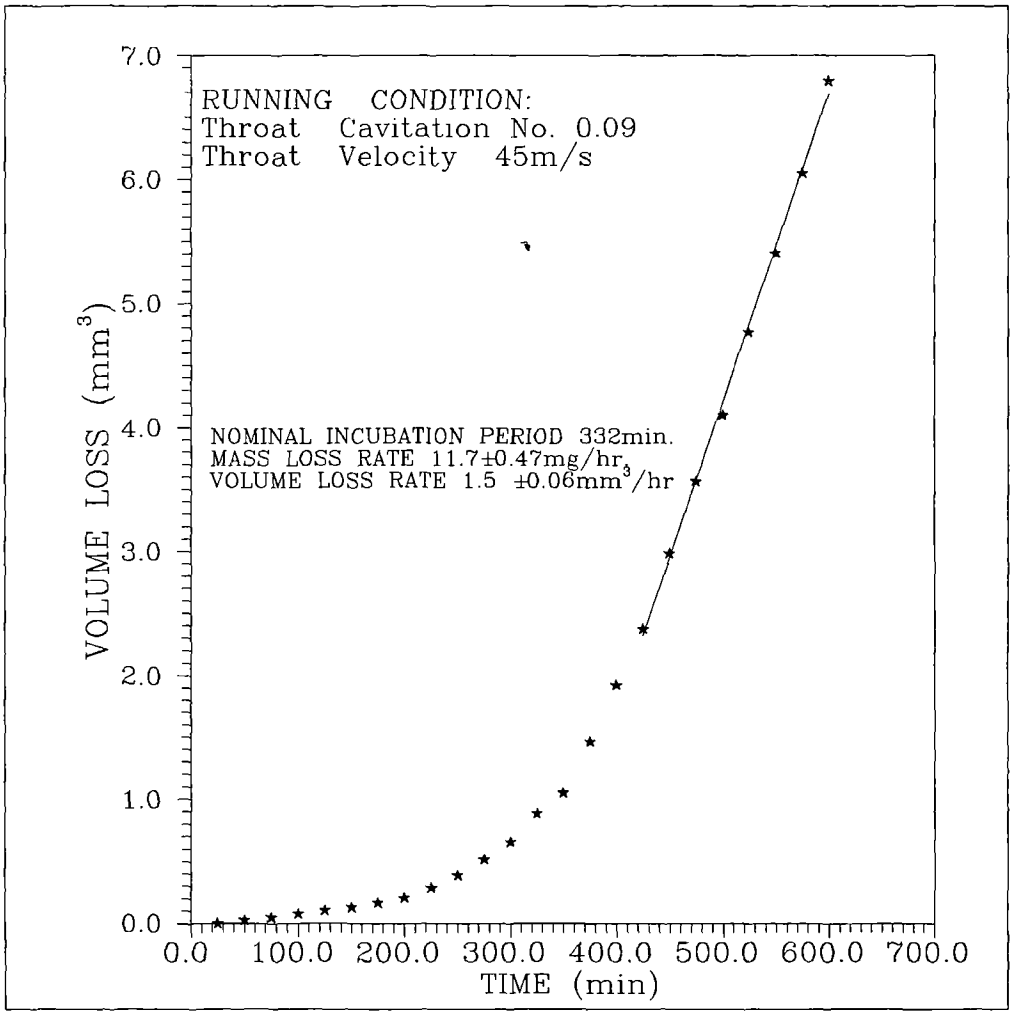

Fig.94 CUMULATIVE VOLUME LOSS AGAINST TIME CARBON STEEL (45)

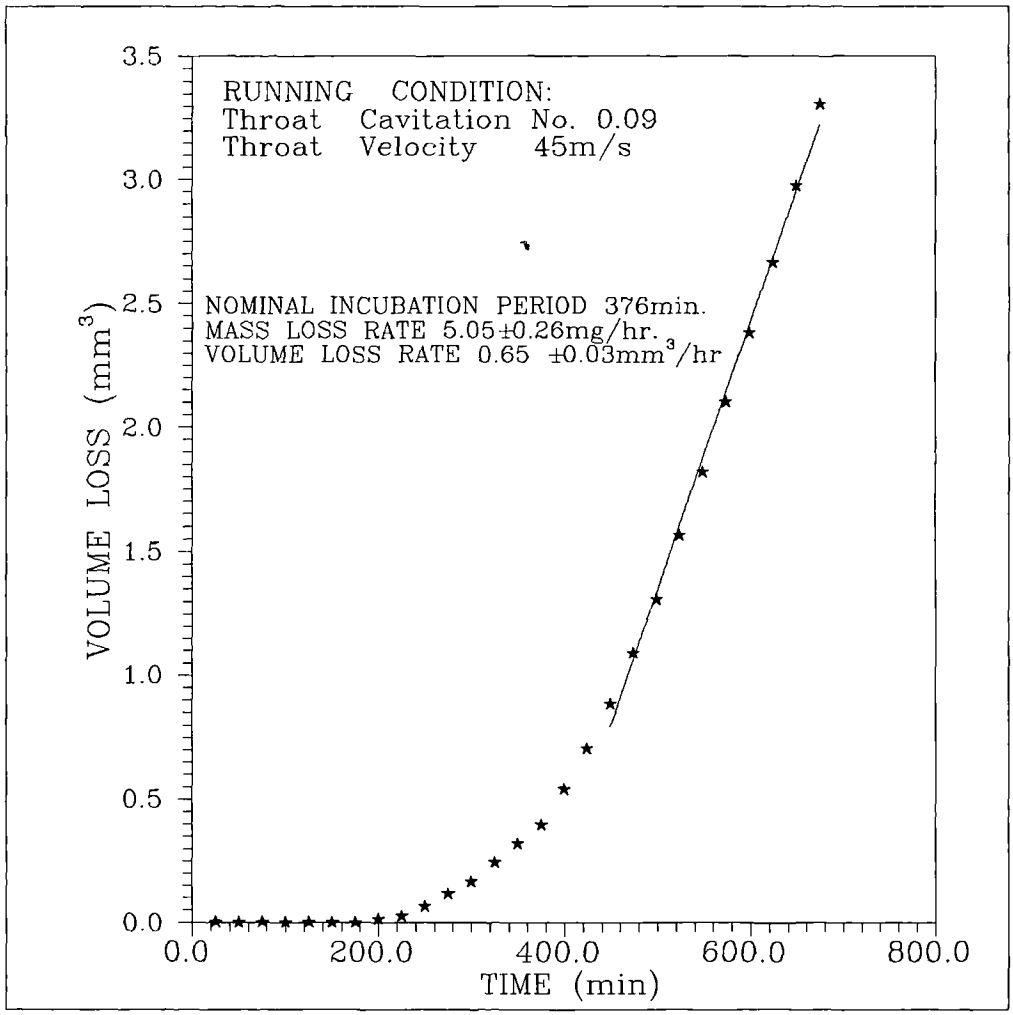

Fig.95 CUMULATIVE VOLUME LOSS AGAINST TIME FOR STAINLESS STEEL(ACID RESIST.)

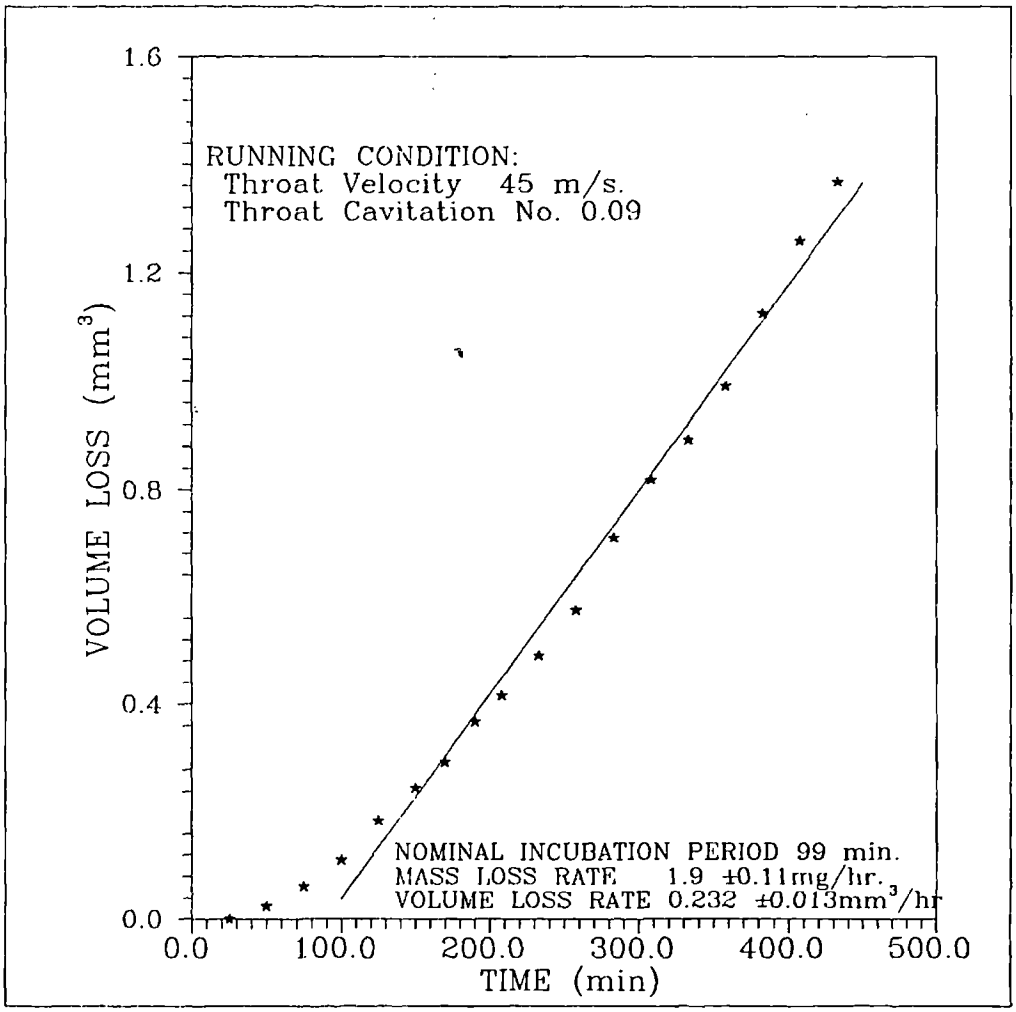

Fig.96 CUMULATIVE VOLUME LOSS AGAINST TIME FOR NITRIDED STEEL

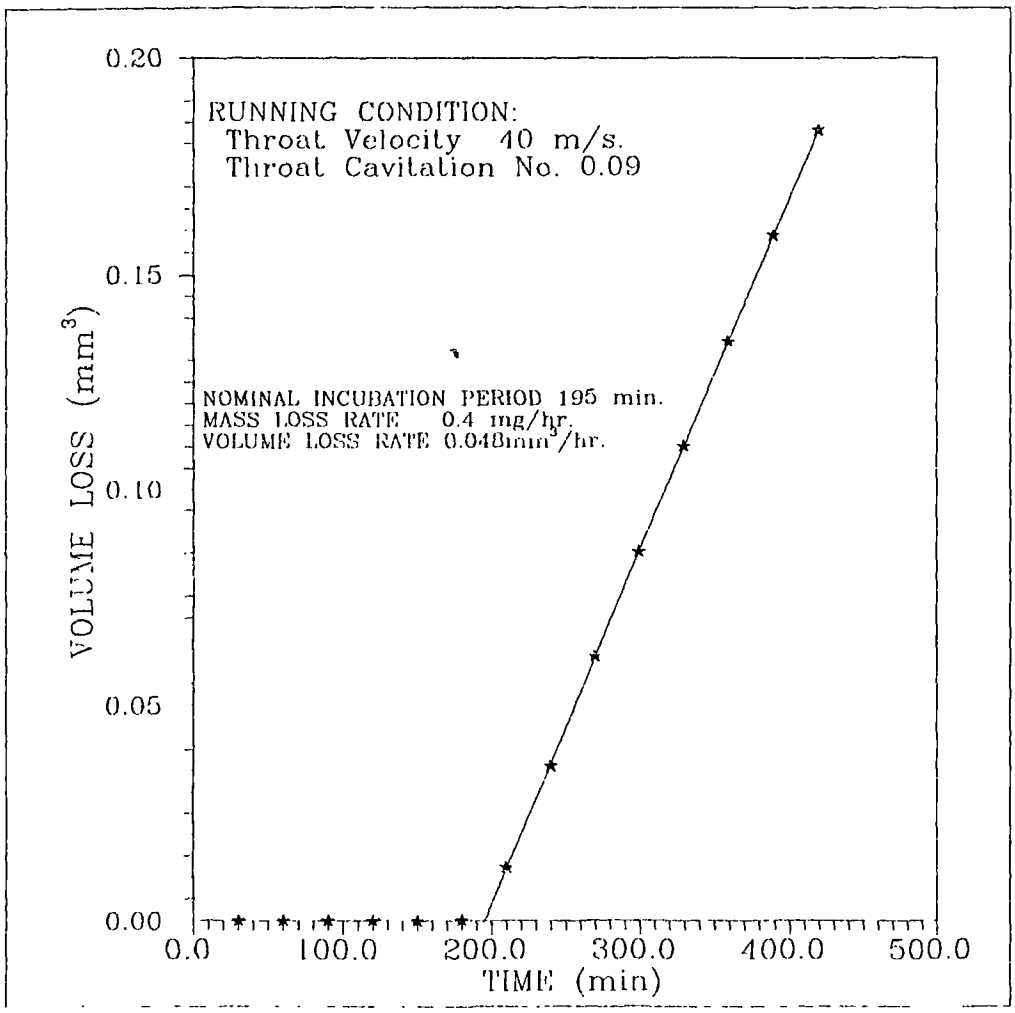

Fig.97 CUMULATIVE VOLUME LOSS AGAINST TIME FOR NITRIDED STEEL

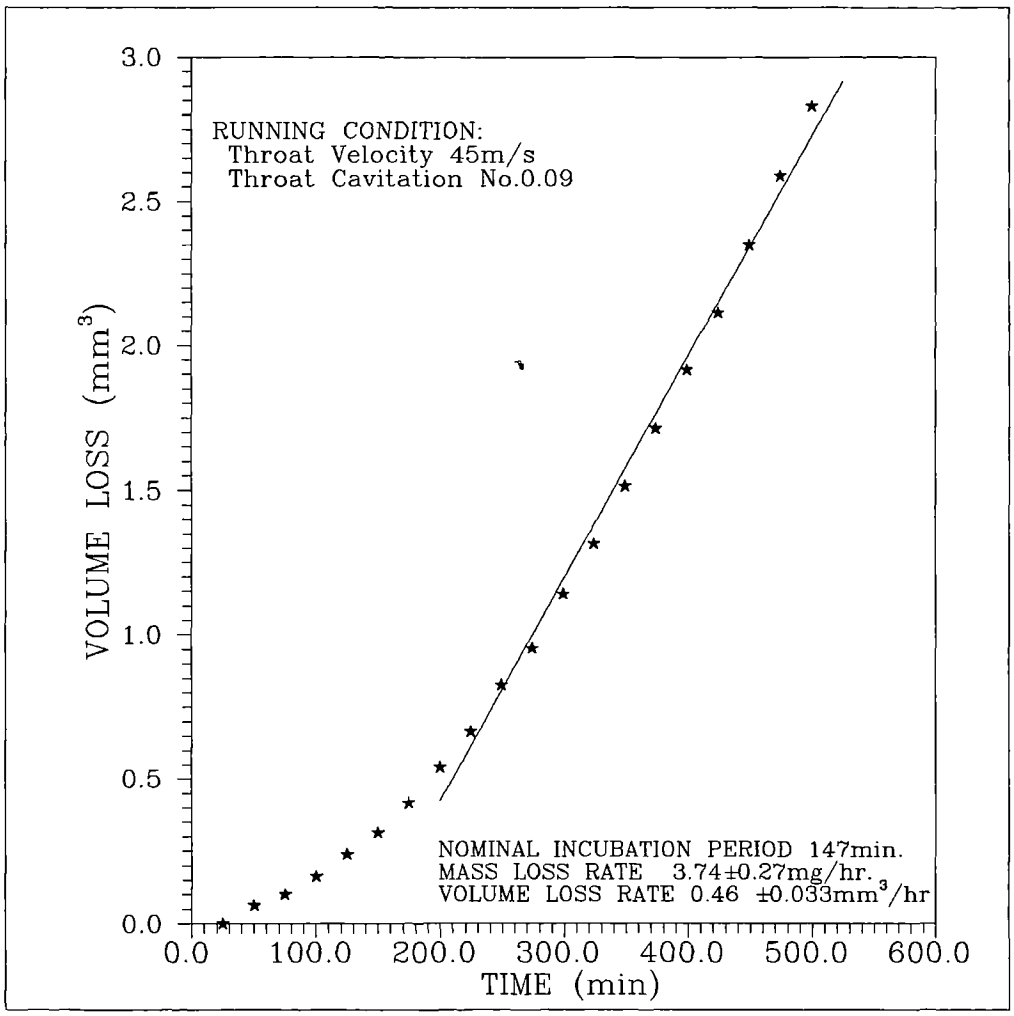

Fig.98 CUMULATIVE VOLUME LOSS AGAINST TIME FOR TOOL STEEL

Fig.99 COMPARISON PLOT OF VARIOUS MATERIALS

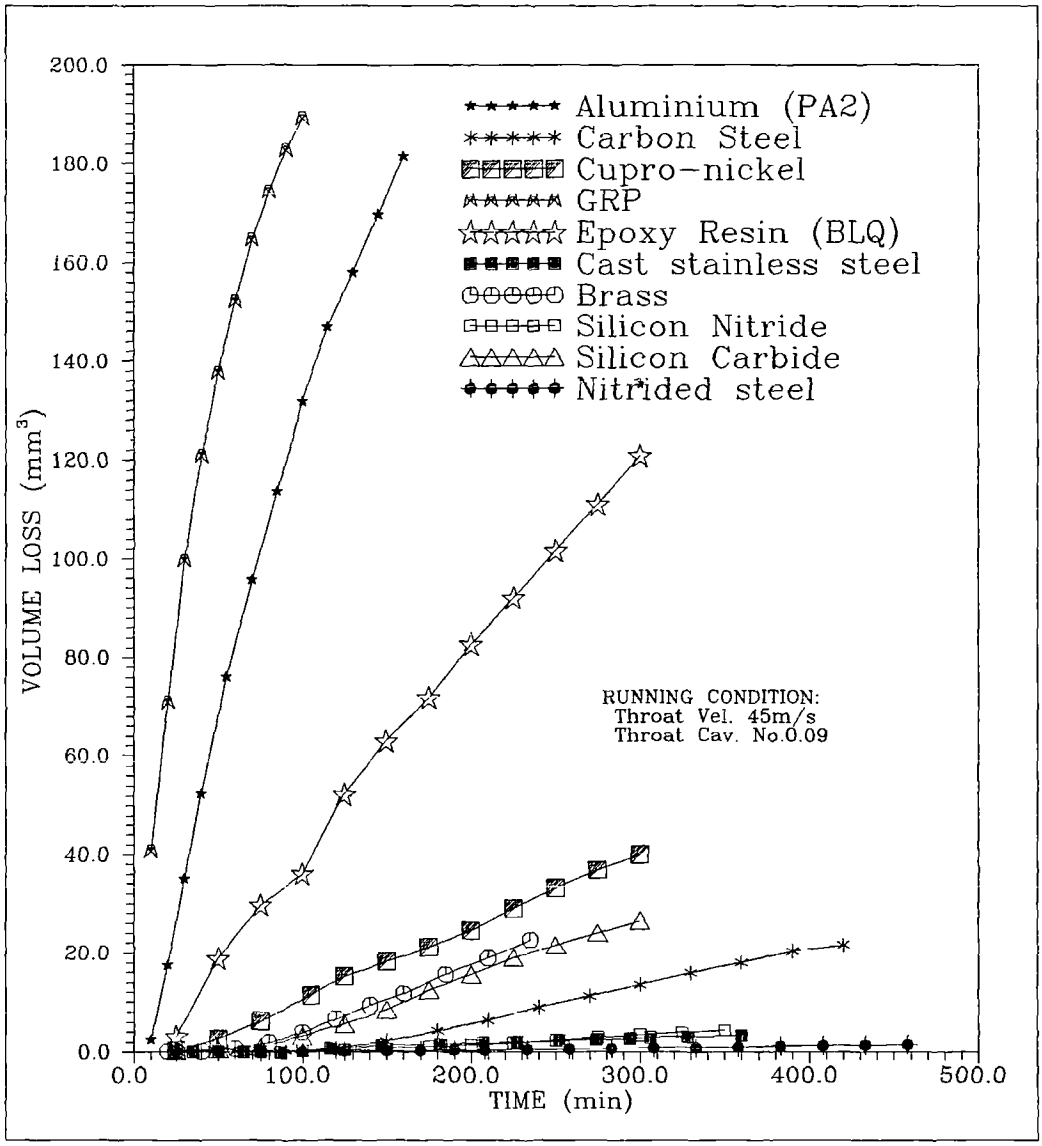

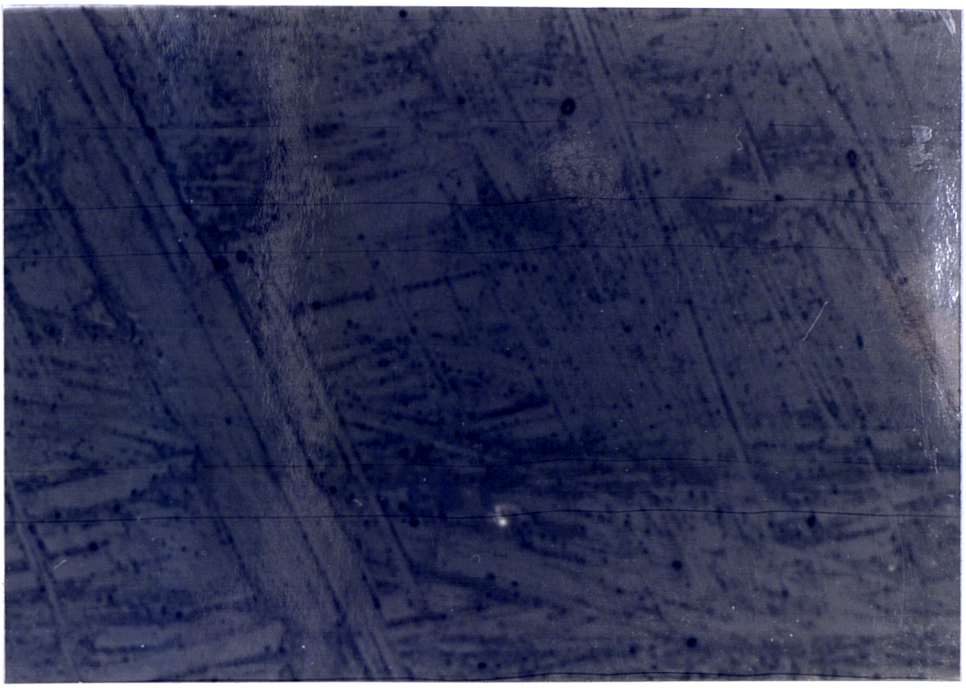

FIG. 100a (as cast)

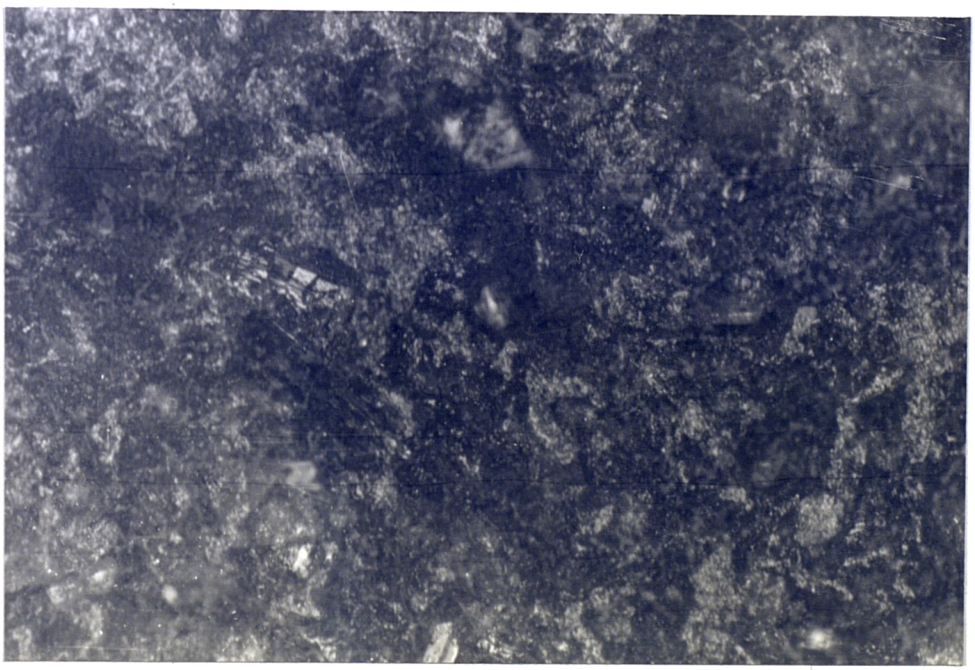

FIG. 100b (machined)

OPTICAL MICROGRAPH OF AS CAST AND MACHINED SURFACE OF EPOXY RESIN PRIOR TO TESTING

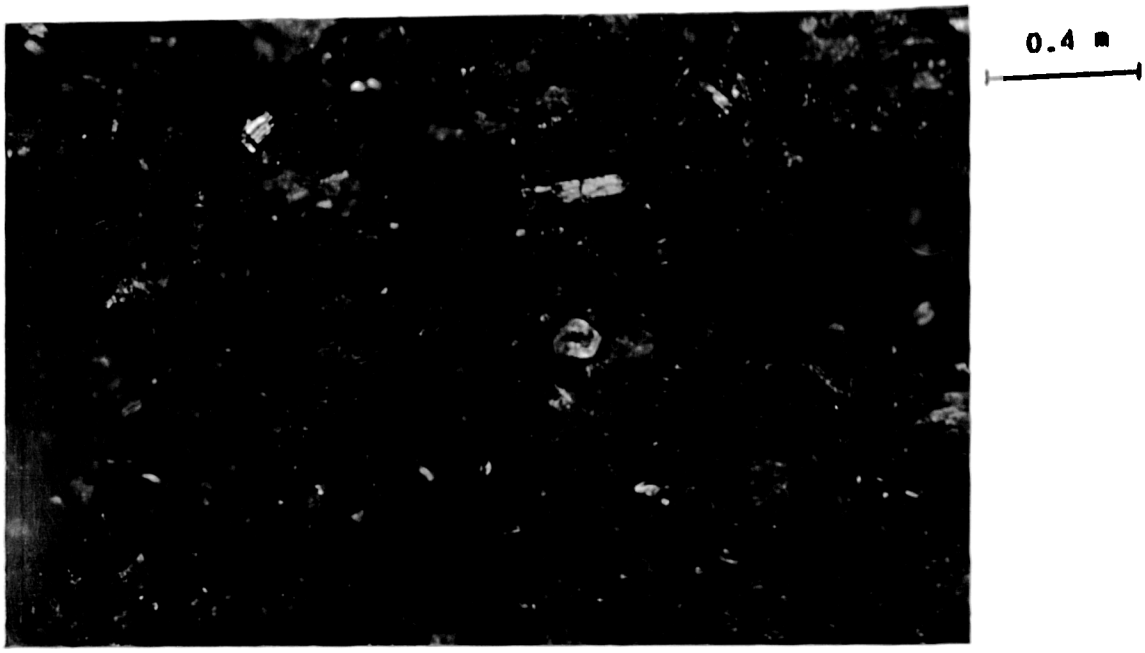

FIG. 101a (After 20 min.)

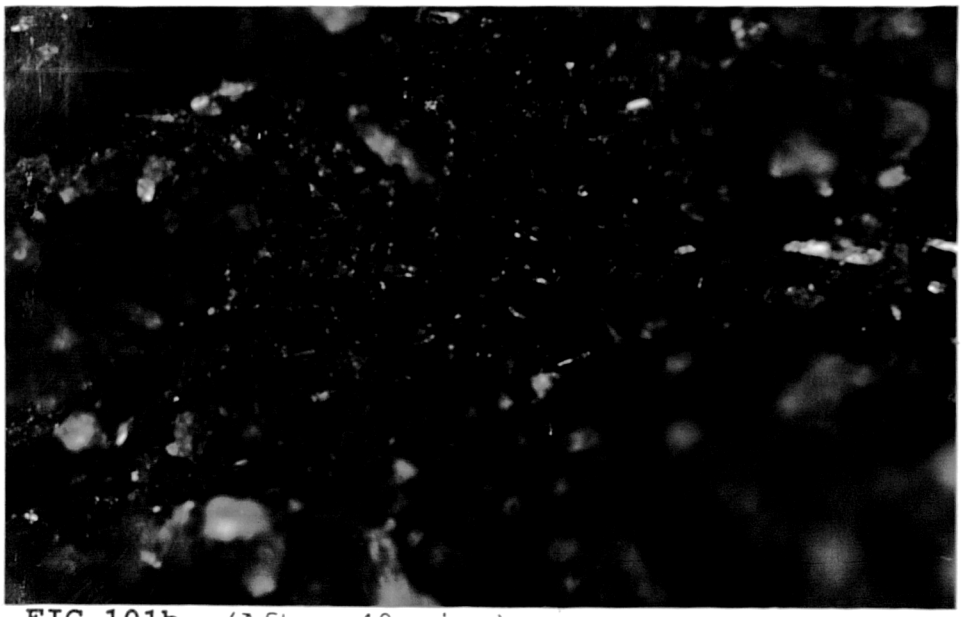

FIG.101b (After 40 min.)

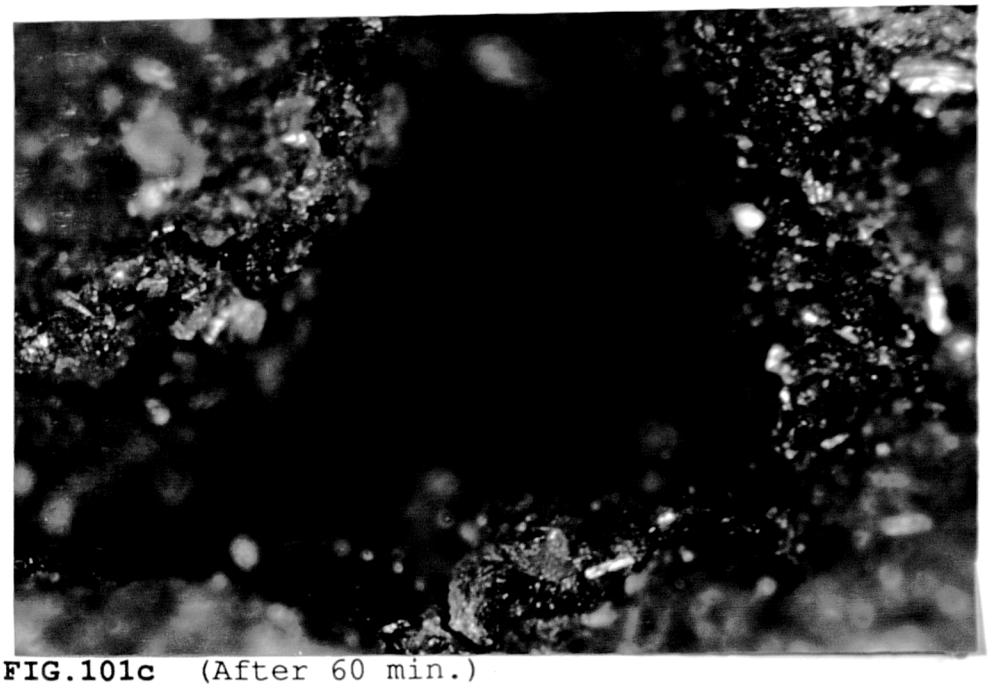

FIG.101c (After 60 min.)

OPTICAL MICROGRAPHS OF DAMAGE PROGRESSION IN EPOXY RESIN

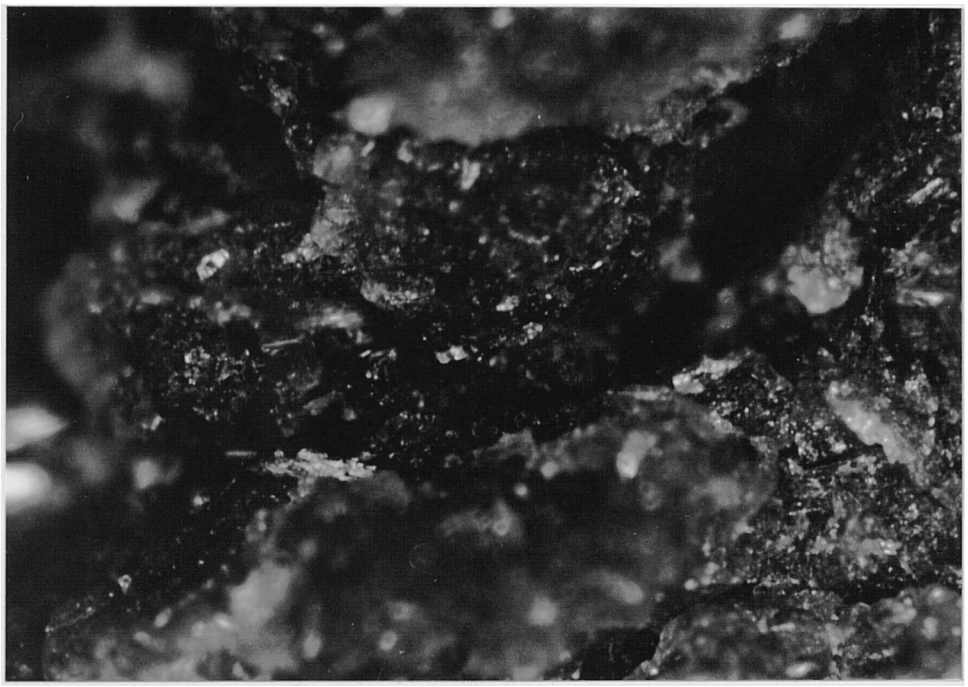

FIG.102a OPTICAL MICROGRAPH OF PERPENDICULAR CRACK IN EPOXY RESIN

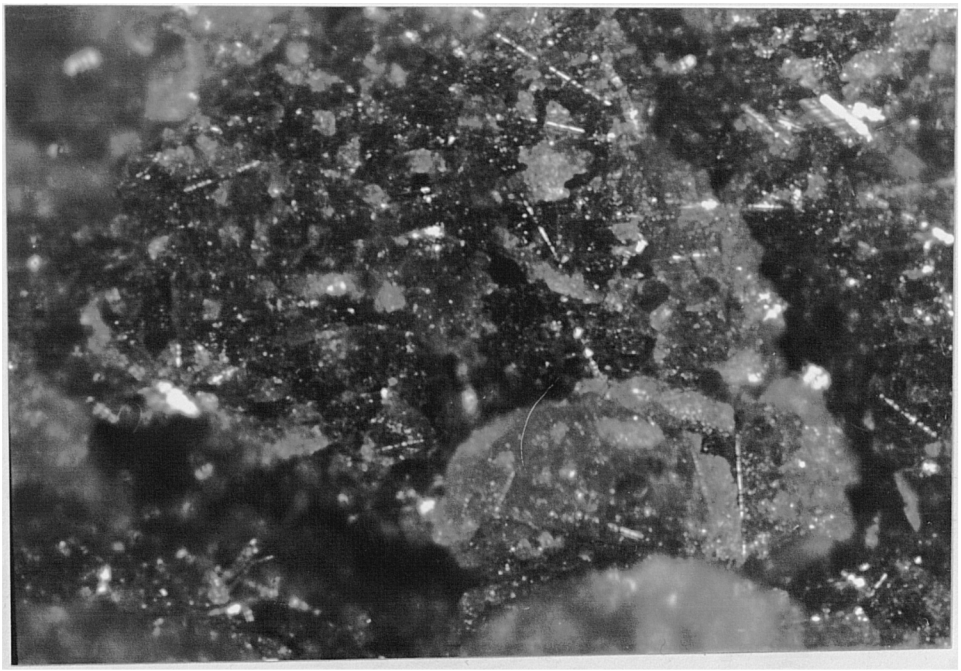

FIG.102b OPTICAL MICROGRAPH OF GRAIN DISINTEGRATION IN EPOXY RESIN

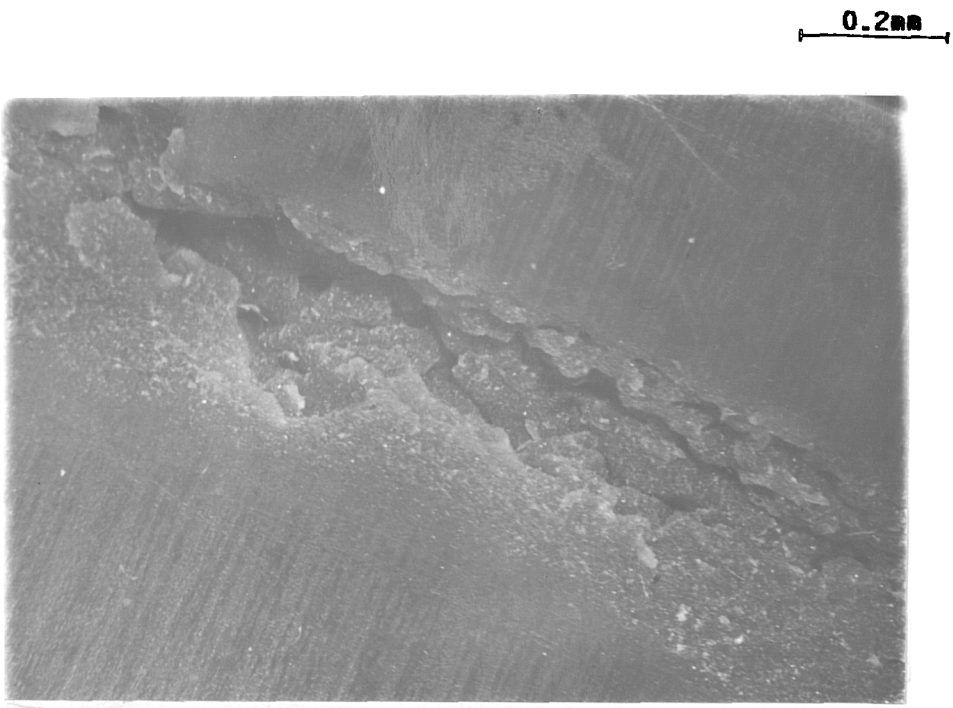

FIG.102c MICROSCOPIC VIEW OF GROSS DAMAGE ON ONE ERODED AREA IN EPOXY RESIN

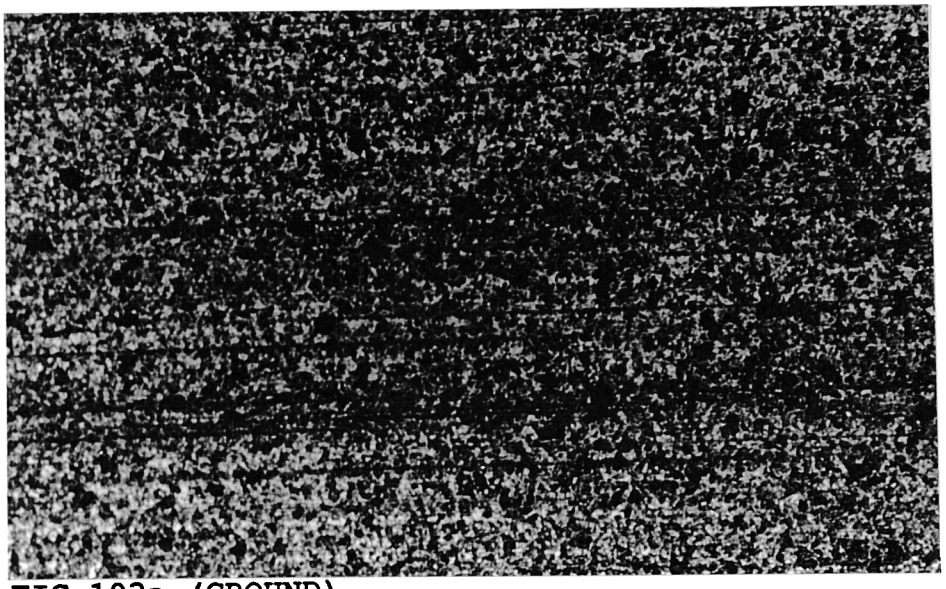

FIG.103a (GROUND)

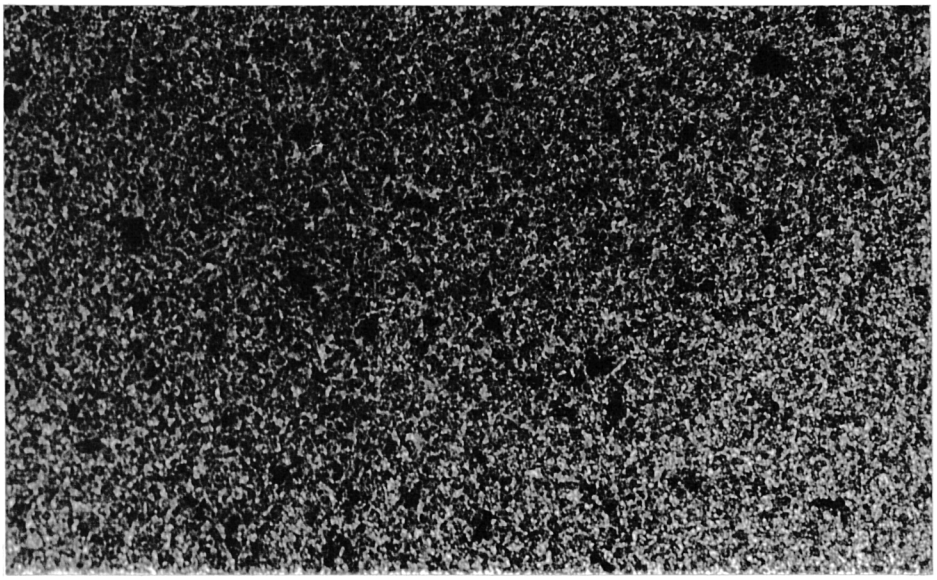

FIG.103b (LAPPED)

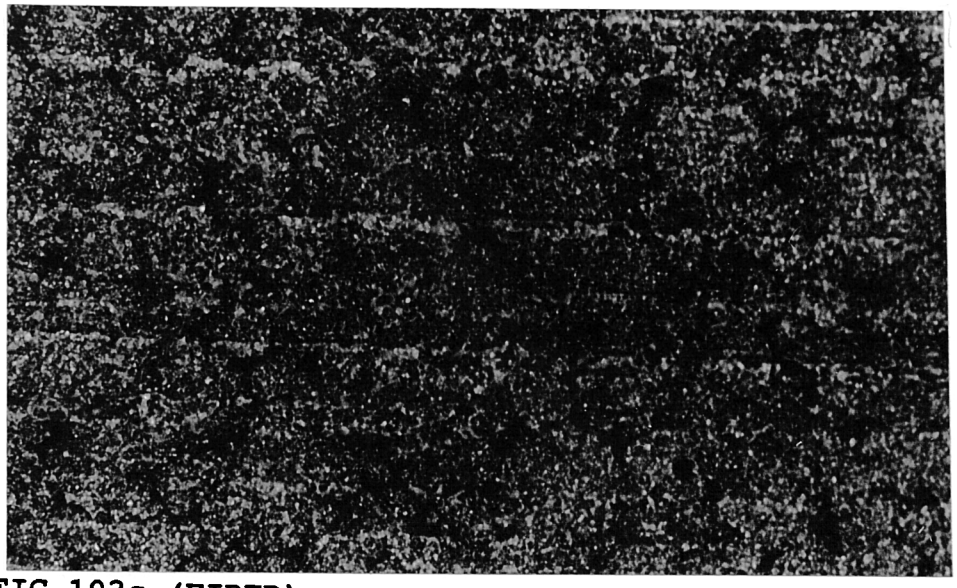

FIG.103c (FIRED)

OPTICAL MICROGRAPH OF THE THREE SURFACE FINISH CONDITIONS OF SILICON CARBIDE

OPTICAL MICROGRAPH OF INITIAL PITTING IN SILICON CARBIDE

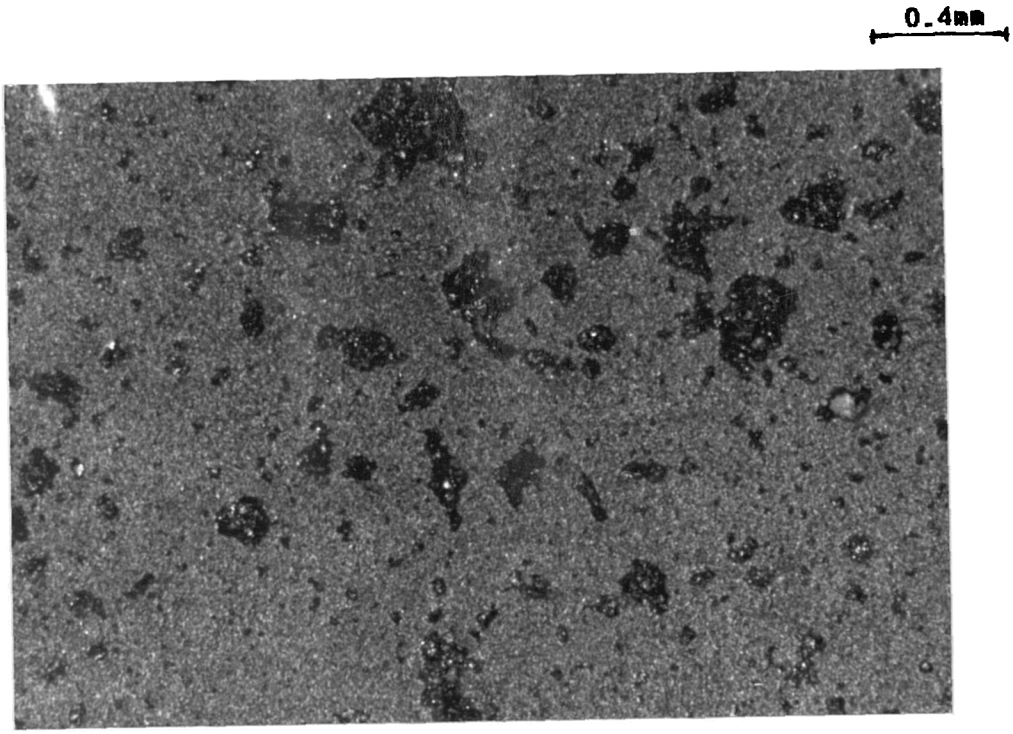

FIG.104a (20 min.)

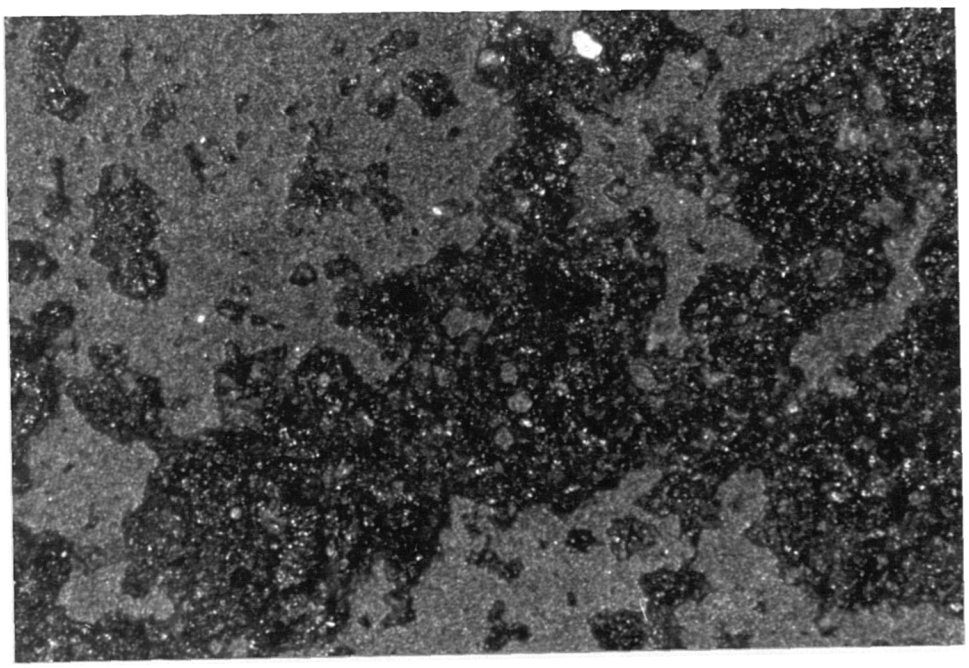

FIG.104b (40 min.)

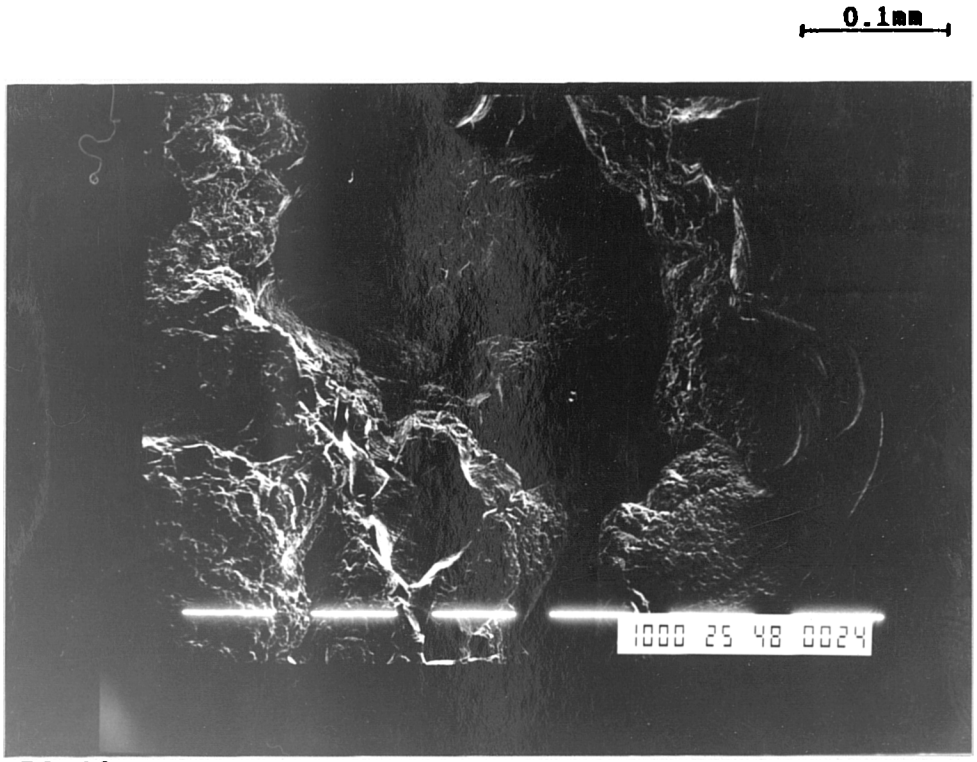

FIG.104c SCANNING ELECTRON MICROGRAPH OF A PIT IN FIG.104b

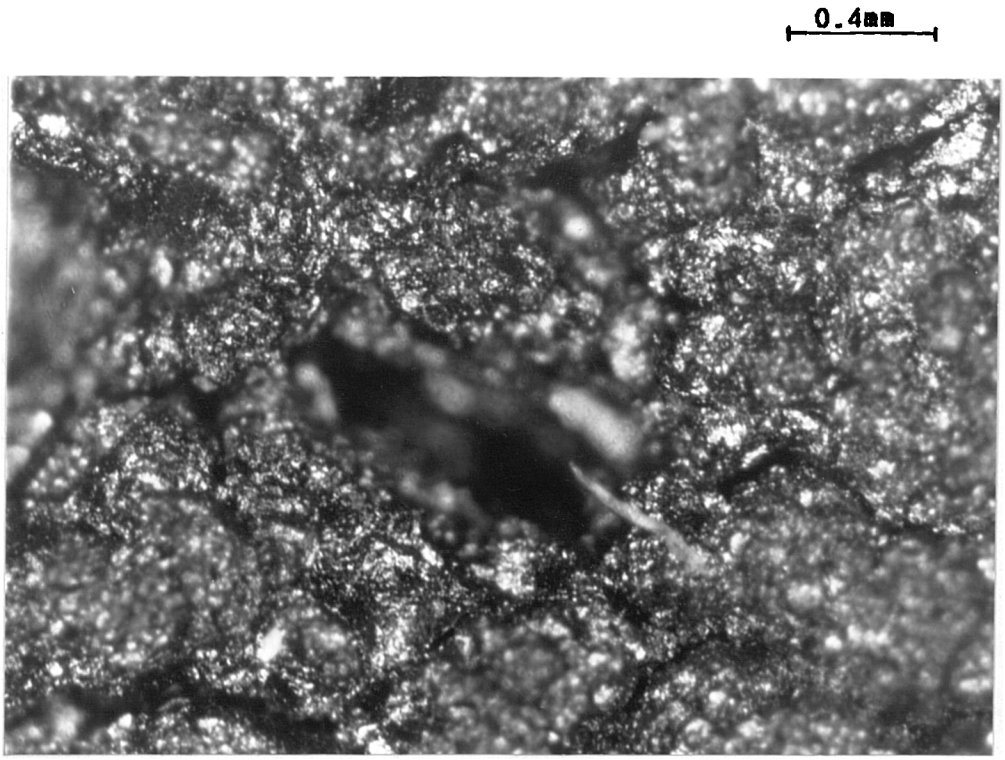

FIG.104d OPTICAL MICROGRAPH OF MATERIAL REMOVAL BY MICRO-CRACKS INTERSECTION IN SILICON CARBIDE

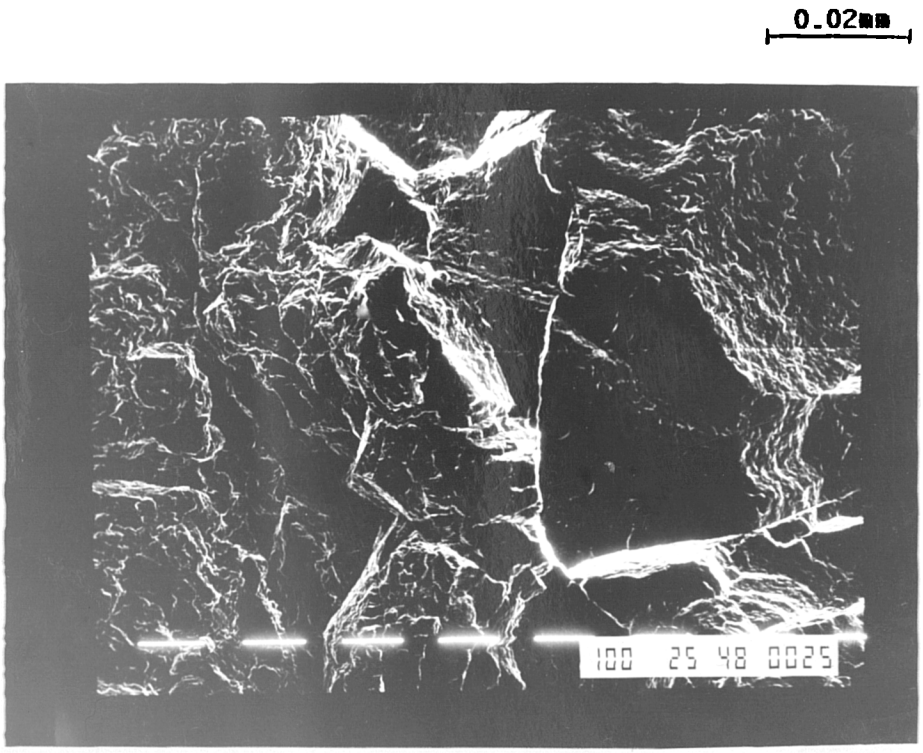

FIG.104e SCANNING ELECTRON MICROGRAPH OF THE PIT IN IN FIG.104d

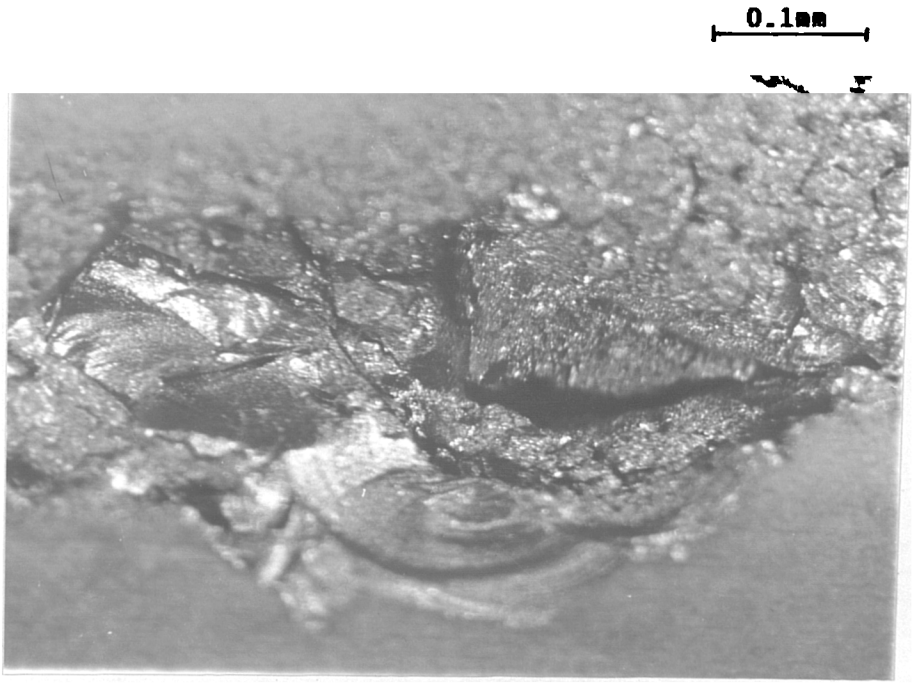

FIG.105a OPTICAL MICROGRAPH OF GROSS DAMAGE ON ONE ERODED AREA SHOWING EFFECT OF CHIPPING

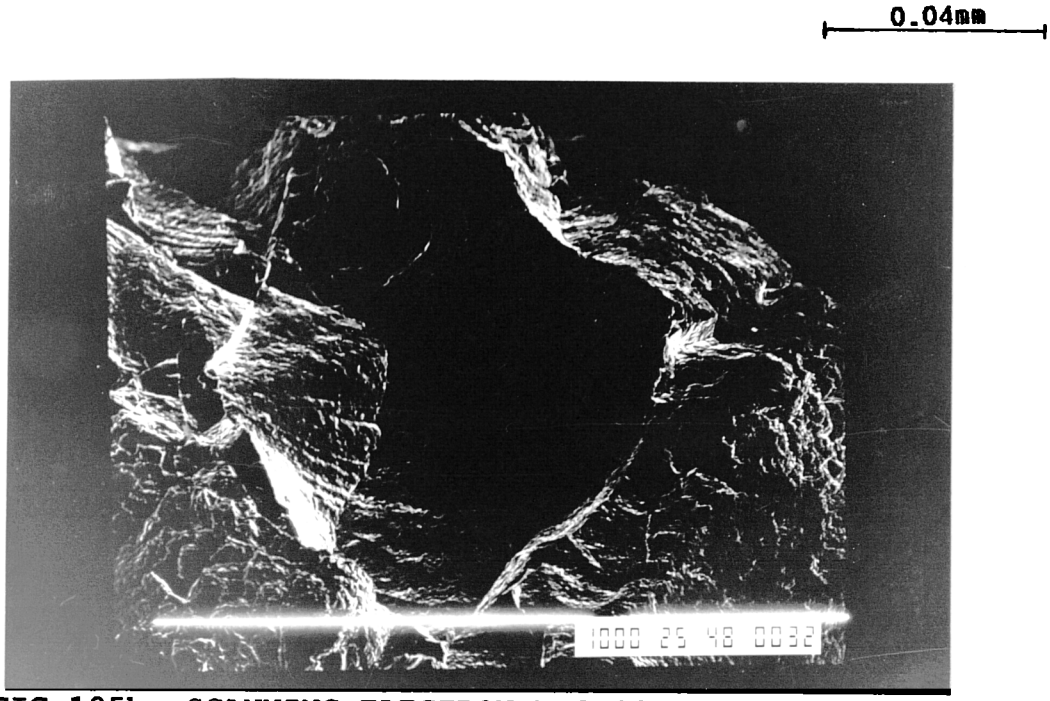

FIG.105b SCANNING ELECTRON MICROGRAPH OF DAMAGE INSIDE CENTRAL REGION IN FIG.105A

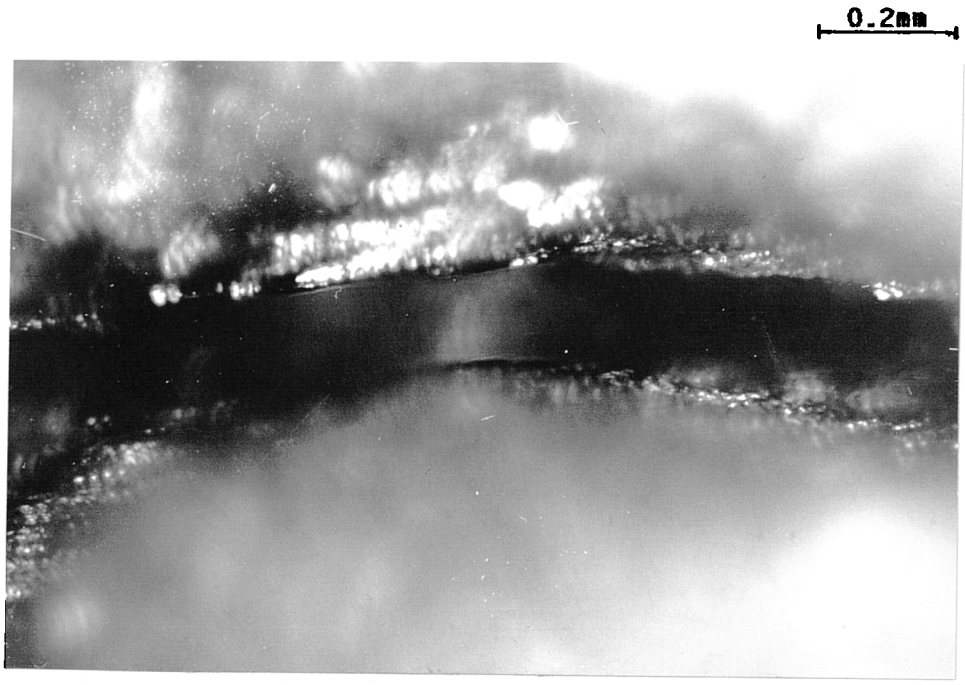

FIG.105c OPTICAL MICROGRAPH OF LOCALIZED CRACK IN CENTRAL EROSION ZONE IN SILICON CARBIDE

FIG.105d OPTICAL MICROGRAPH OF TOPOGRAPHY OF CHIPPED SURFACE OF SILICON CARBIDE

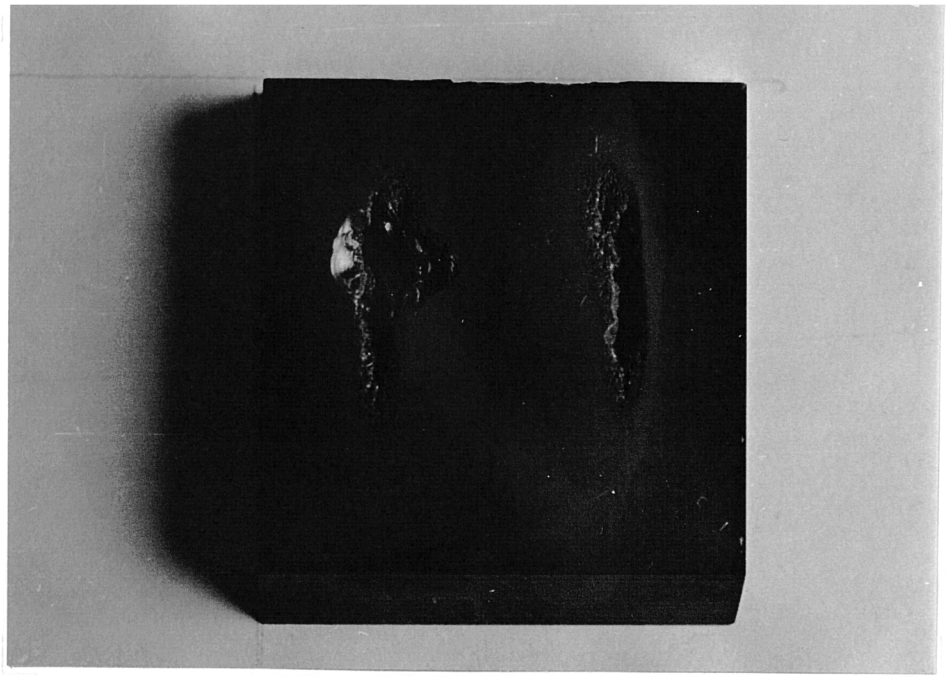

FIG.105e MACROSCOPIC VIEW OF GROSS DAMAGE IN SILICON CARBIDE (300 min.)

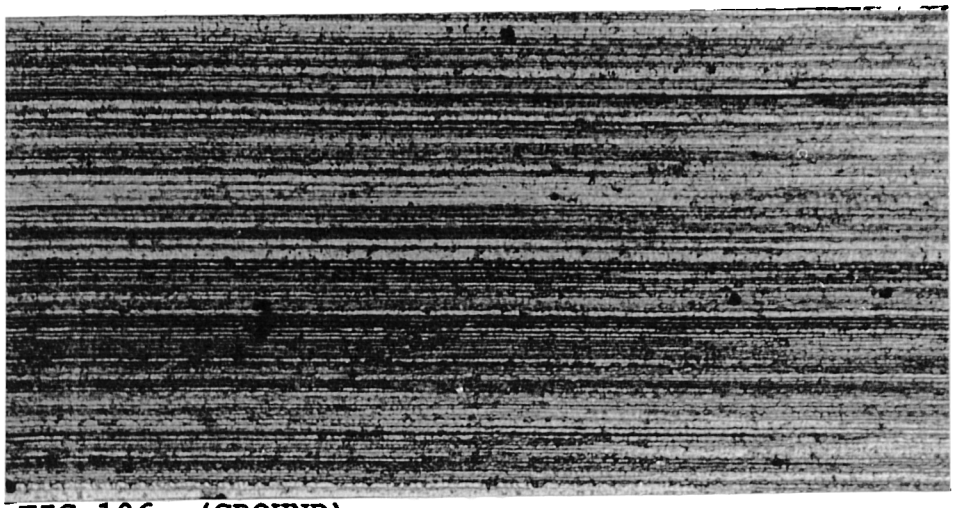

FIG.106a (GROUND)

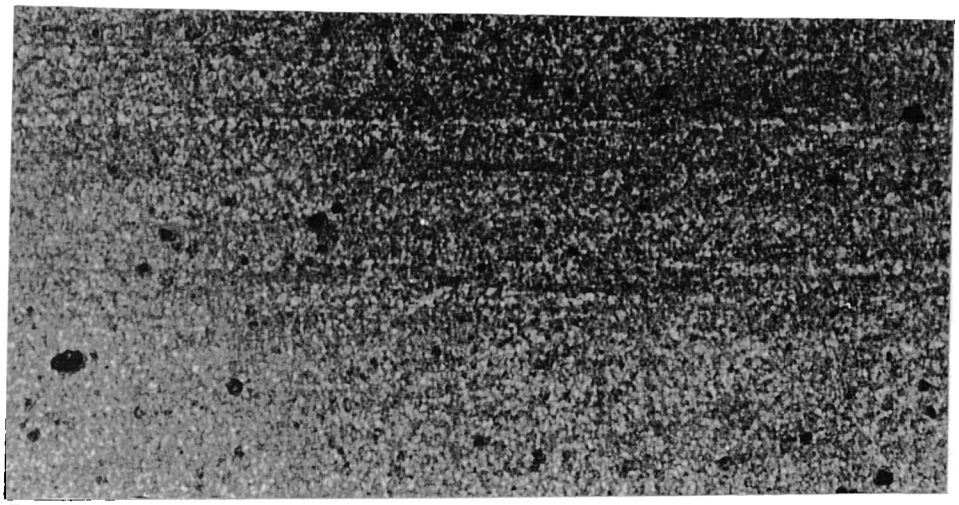

FIG.106b (LAPPED)

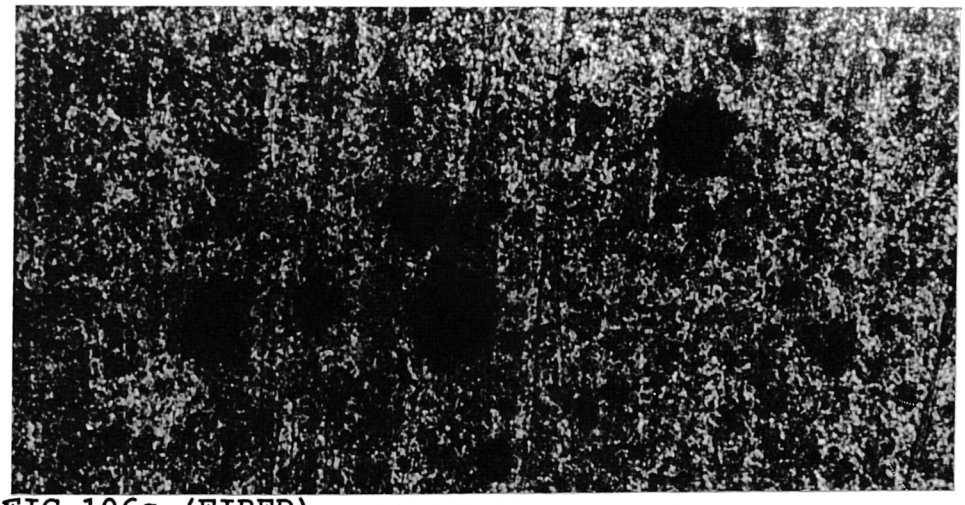

FIG.106c (FIRED)

OPTICAL MICROGRAPH OF THE THREE SURFACE FINISH CONDITIONS OF SILICON NITRIDE

FIG.107a SURFACE OF SILICON NITRIDE PRIOR TO TESTING

FIG.107b EXPOSED FOR 50 min. (OPTICAL MICROSCOPE)

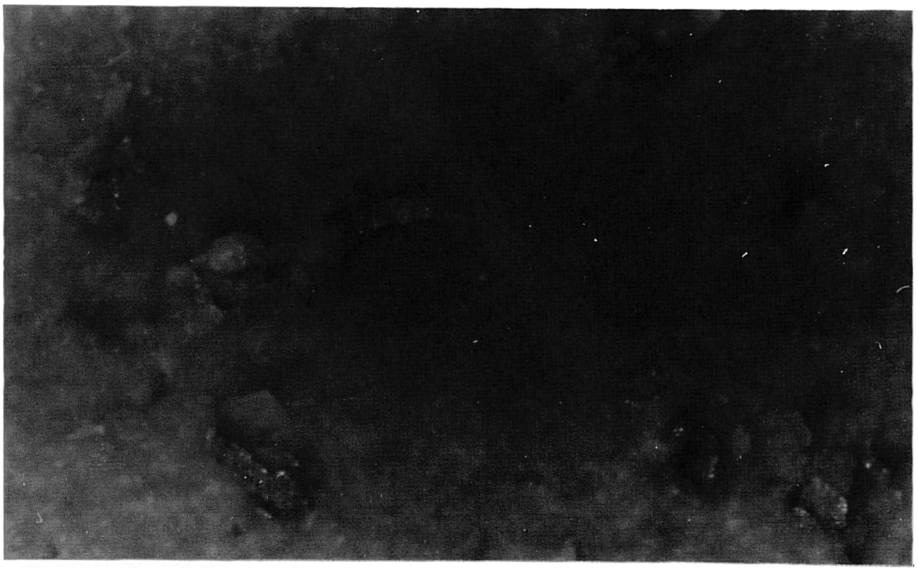

FIG.107c EXPOSED FOR 70 min. (OPTICAL MICROSCOPE)

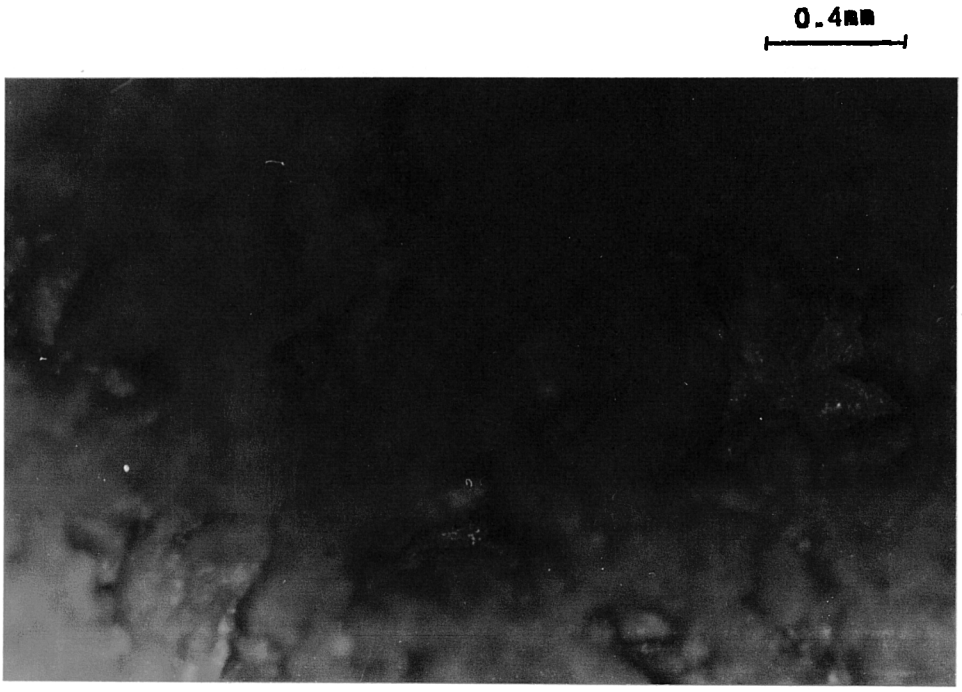

FIG.107d EXPOSED FOR 90 min. (OPTICAL MICROSCOPE)

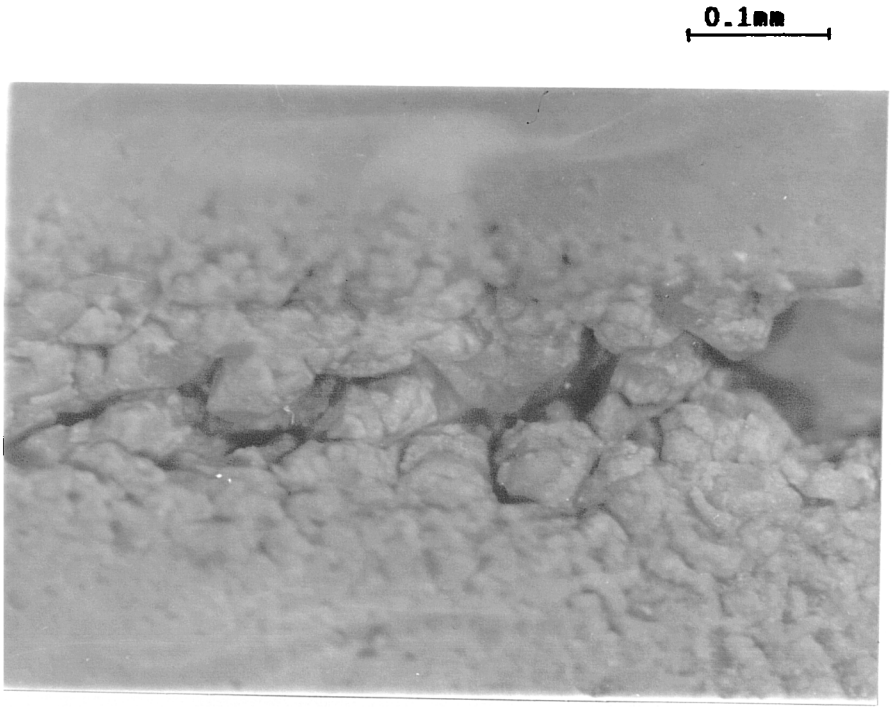

FIG.107e MACROSCOPIC VIEW OF GROSS DAMAGE ON ONE ERODED AREA IN SILICON NITRIDE (320 min.)

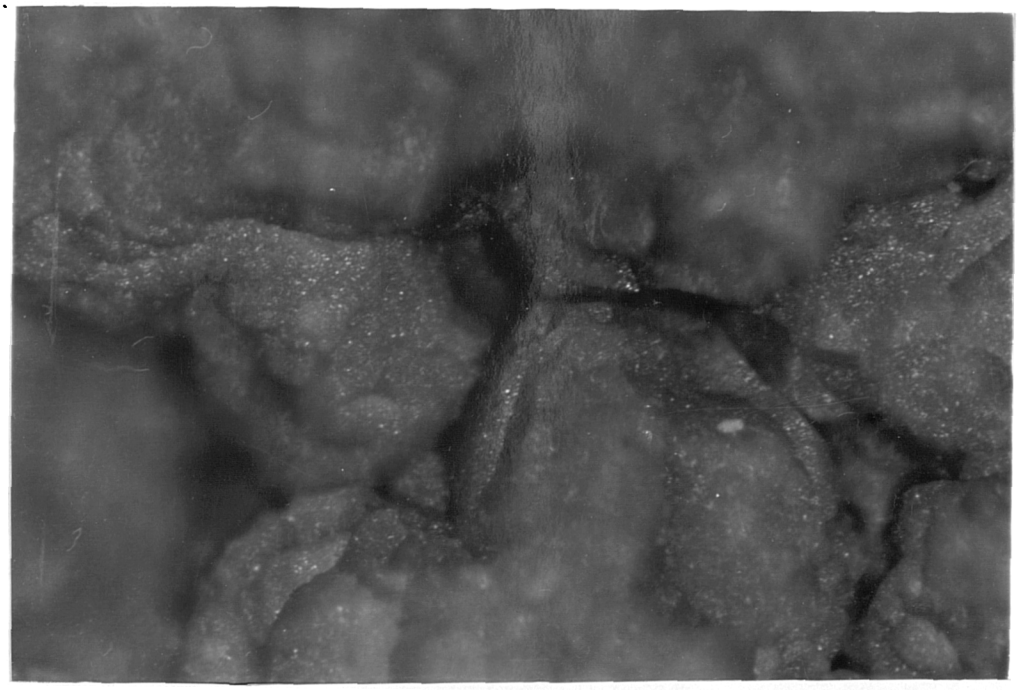

FIG107g

0.4mm

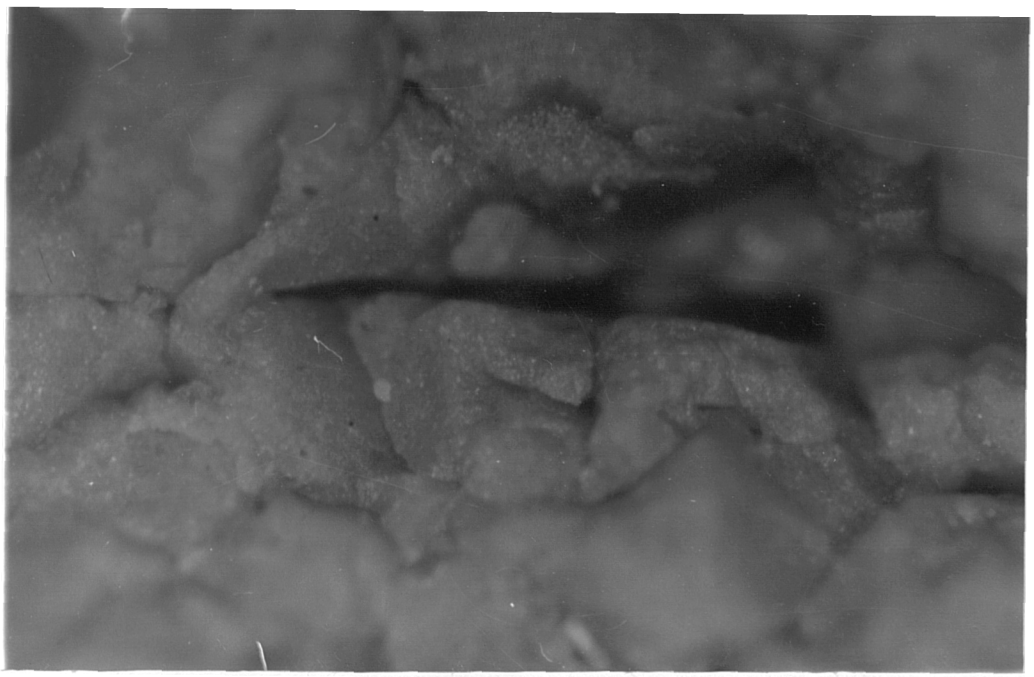

FIG.107f

OPTICAL MICROGRAPHS OF INTERGRANULAR FRACTURE
IN SILICON NITRIDE

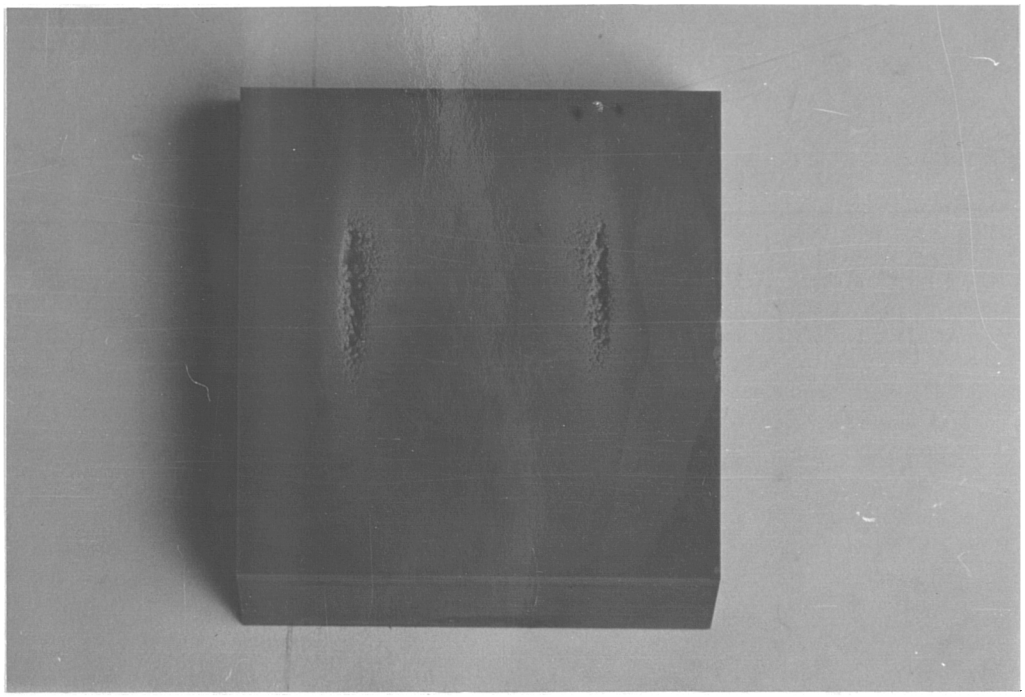

FIG.107h MACROSCOPIC VIEW OF GROSS DAMAGE ON SILICON NITRIDE

FIG.108 OPTICAL MICROGRAPH OF SURFACE OF GRP SHOWING PORES DISPOSITION PRIOR TESTING

0.2mm

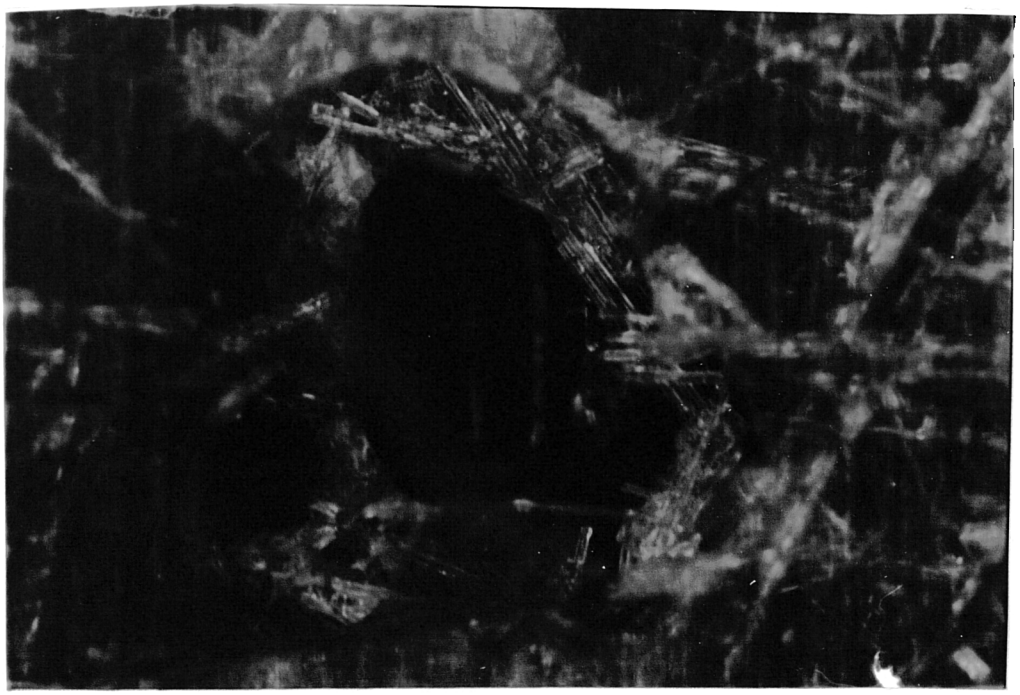

FIG.108a OPTICAL MICROGRAPH OF INITIAL DAMAGE IN GRP (10 min.)

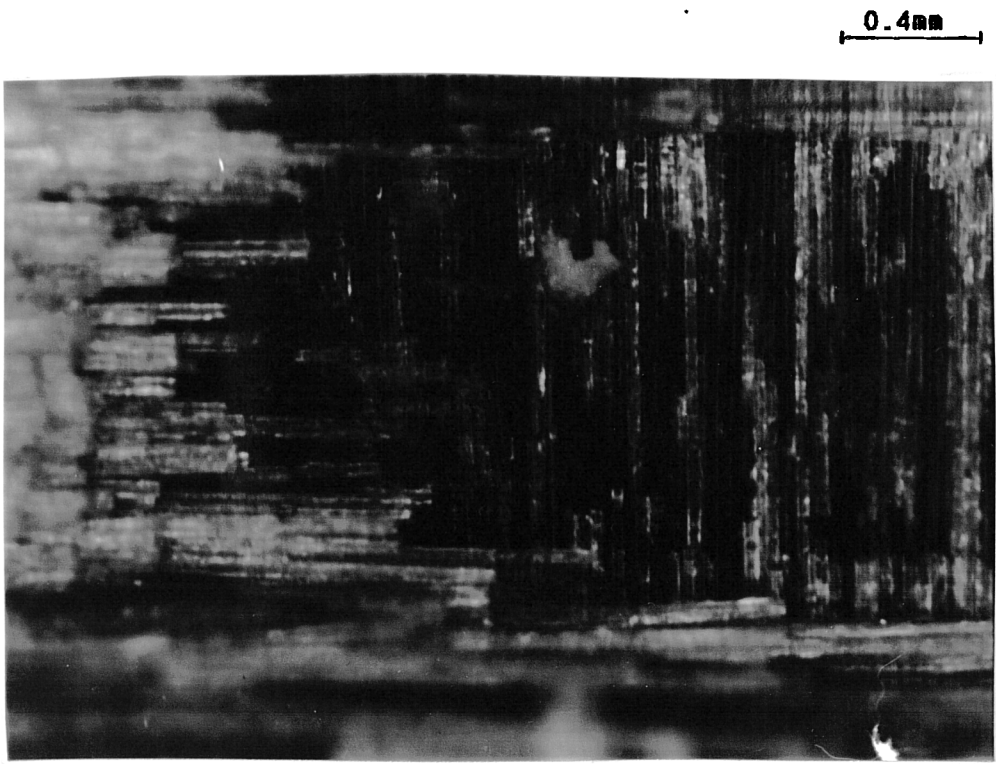

FIG.108b OPTICAL MICROGRAPH OF GRP SHOWING SKELETON NATURE OF FIBRE DEVIOD OF RESIN (30 min.)

FIG.108c OPTICAL MICROGRAPH OF GRP SHOWING EFFECT OF DELAMINATION AND LAYER BY LAYER EROSION

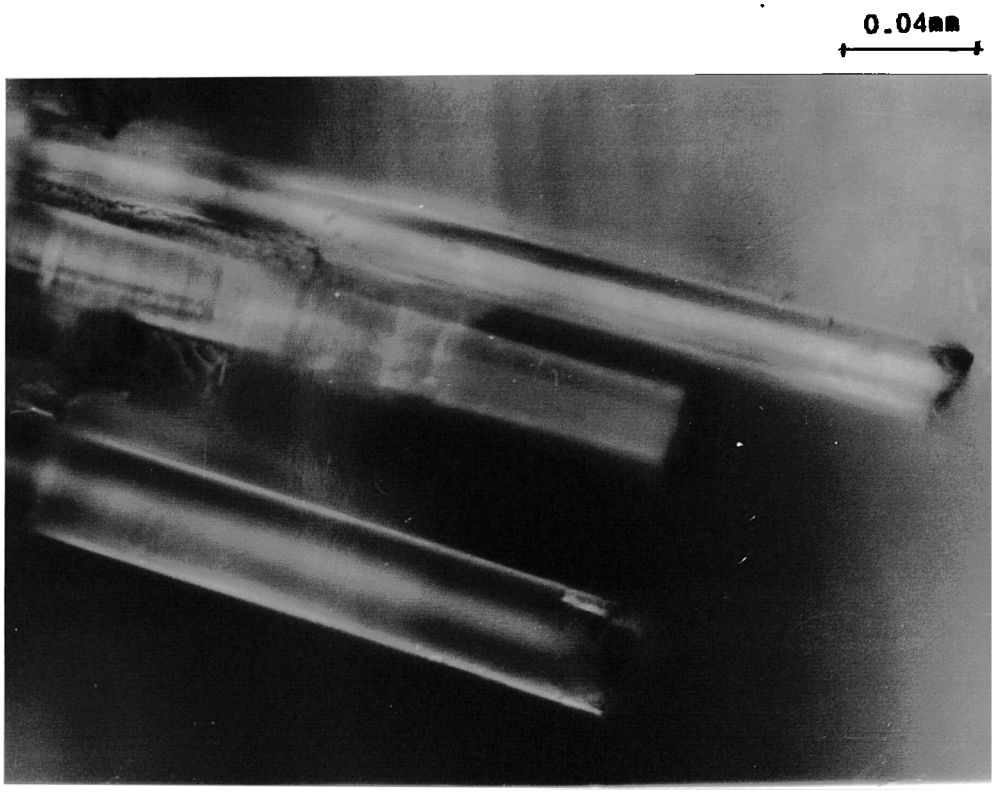

FIG.108d OPTICAL MICROGRAPH SHOWING THREE FRCATURED FIBRES

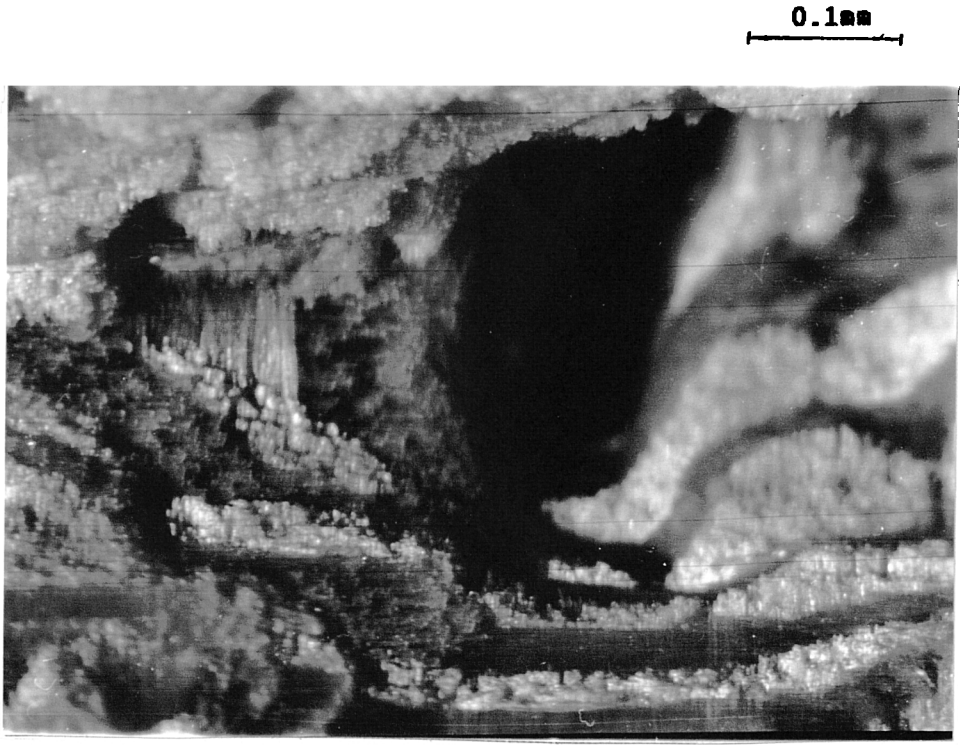

OF

FIG.108e MACROSCOPIC VIEW OF DAMAGED SURFACE GRP SHOWING TUNNELING EFFECT

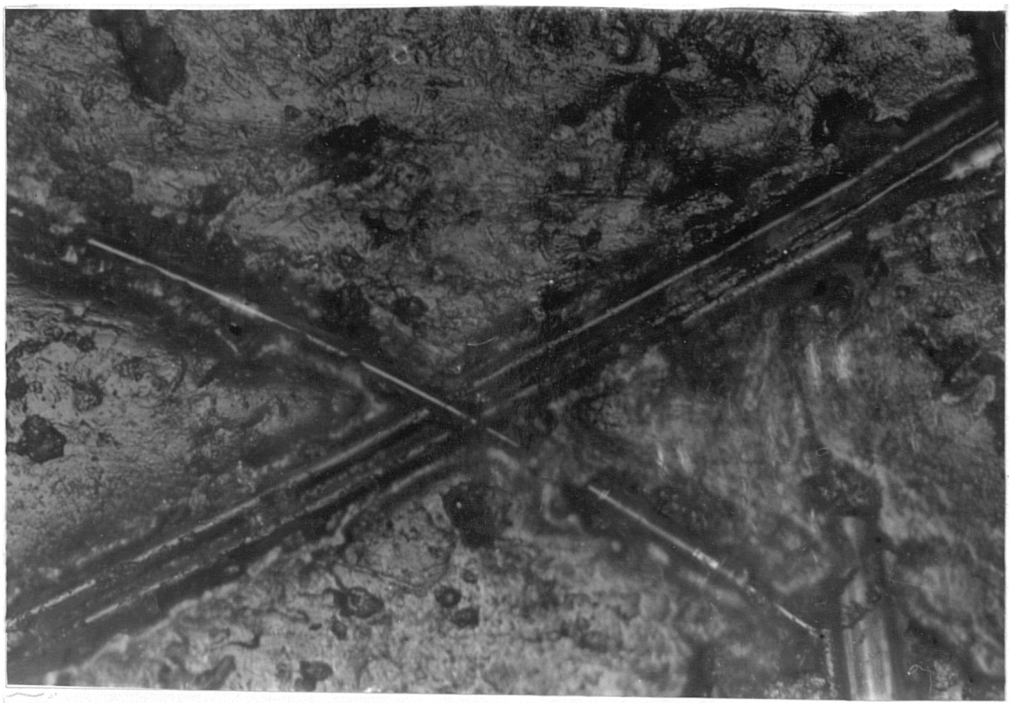

FIG.109 OPTICAL MICROGRAPH OF FYBROC SURFACE PRIOR TO TESTING

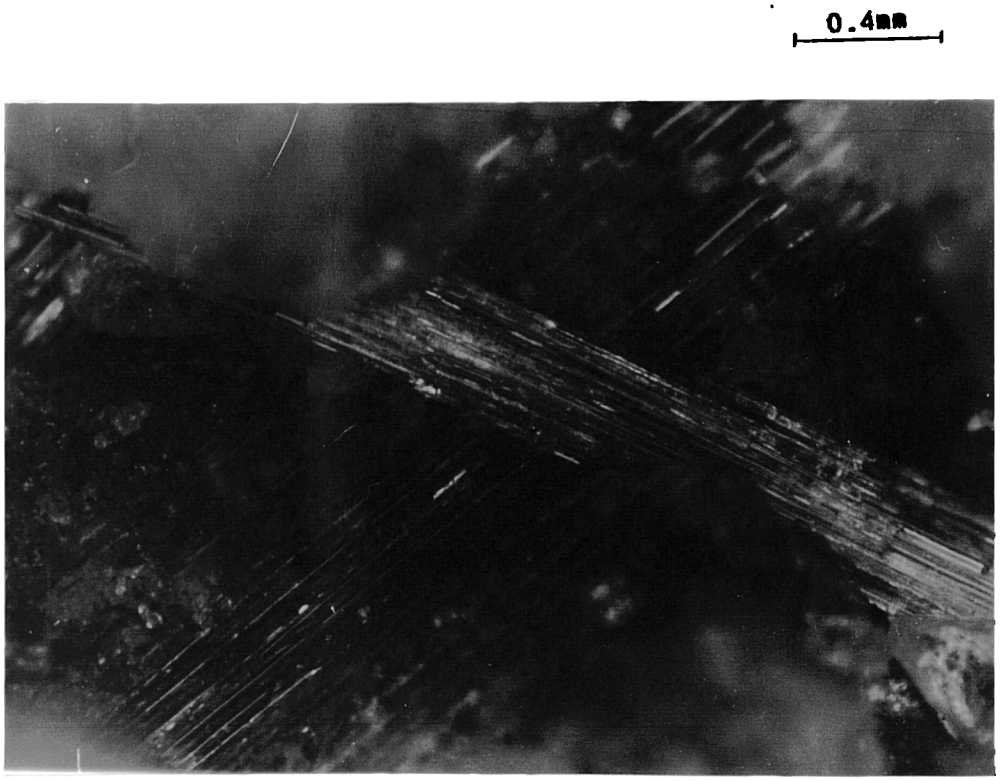

FIG.110a (20 min.)

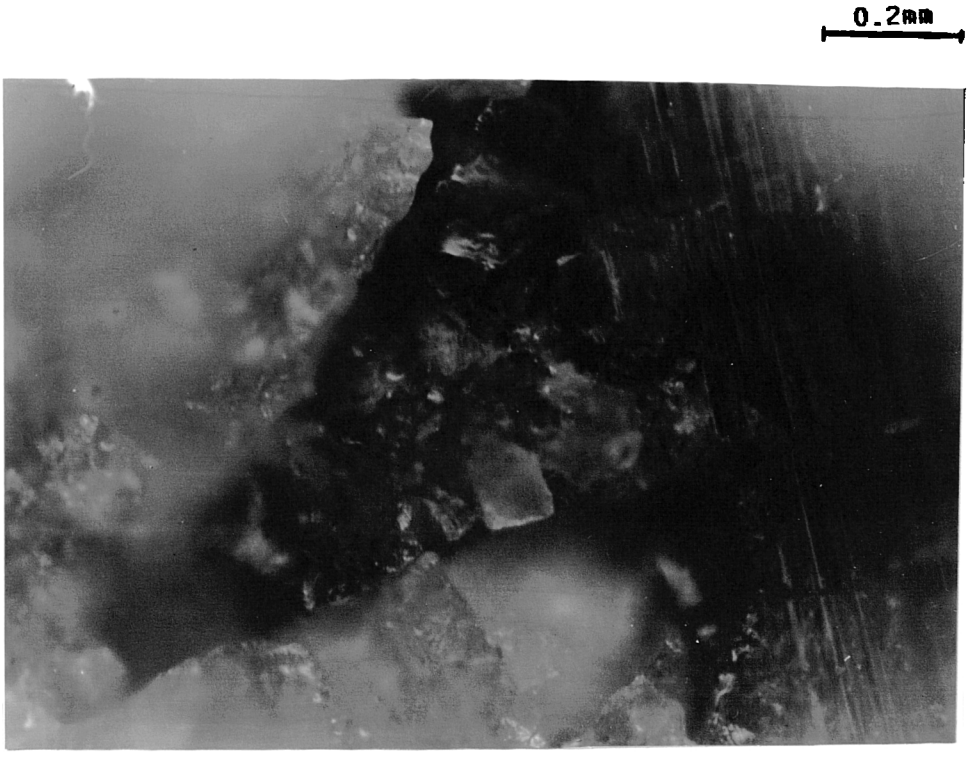

FIG.110b (40 min.)

OPTICAL MICROGRAPH OF INITIAL DAMAGE IN FYBROC EXPOSING FIBRES

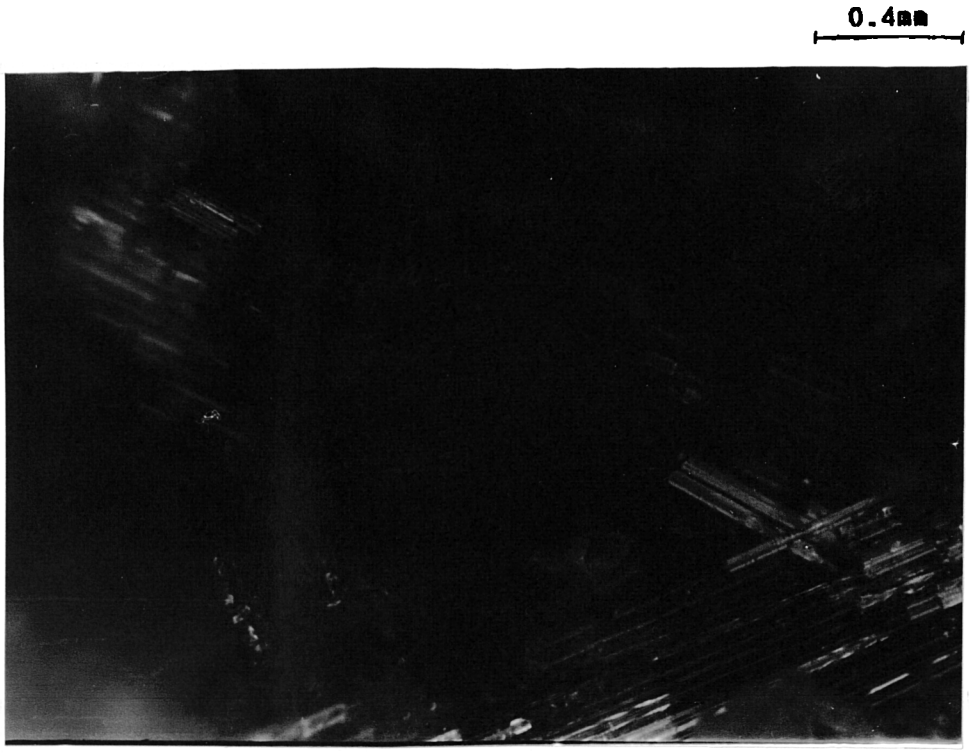

FIG.110c OPTICAL MICROGRAPH OF BROKEN STRAND OF FIBRES IN FYBROC (60 min.)

FIG.110d MACROSCOPIC VIEW OF GROSS DAMAGE IN FYBROC

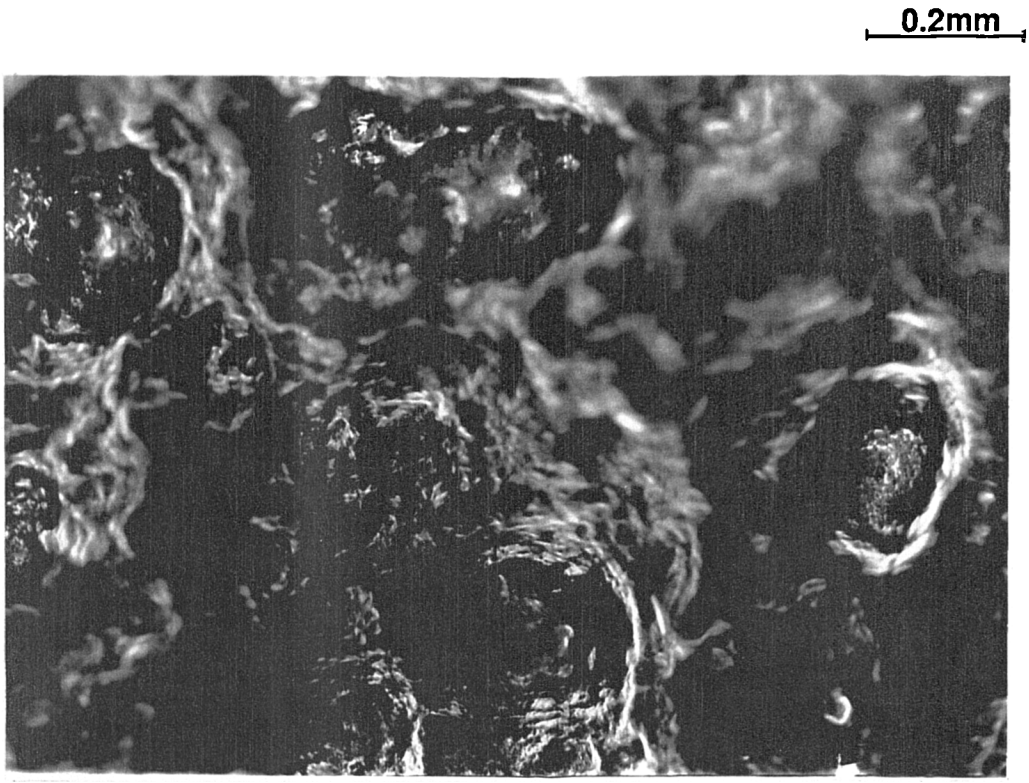

FIG.111a (20 min.)

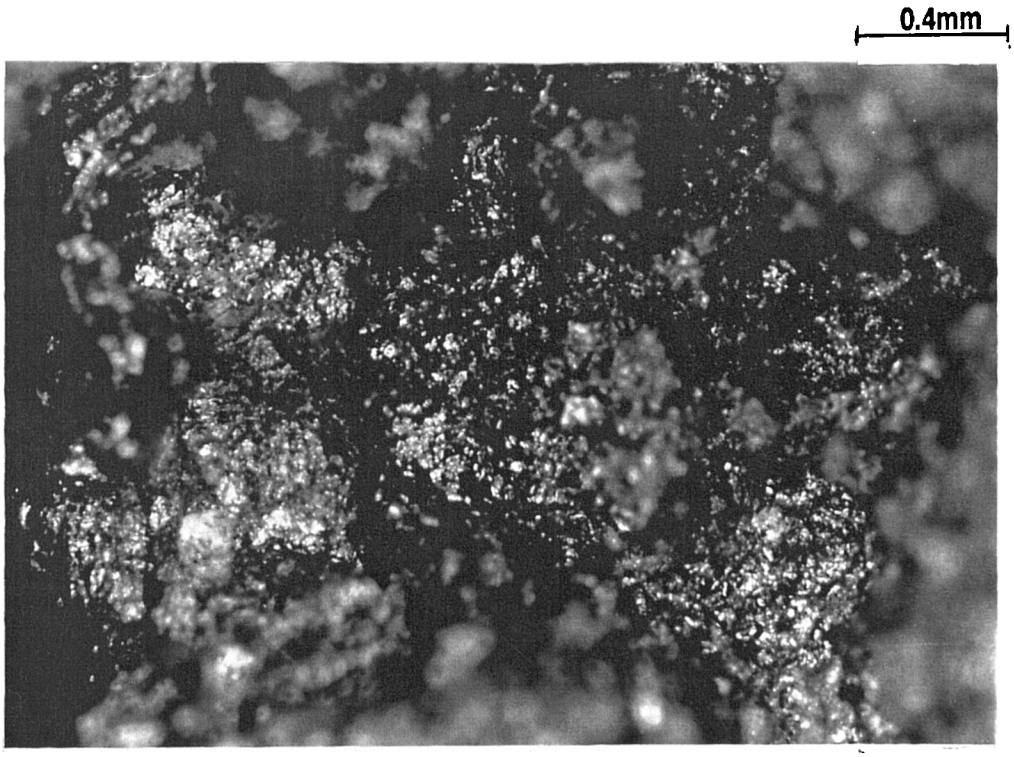

FIG.111b (40 min.)

OPTICAL MICROGRAPH OF INITIAL PITTING IN ALUMINIUM ALLOY (PA2)

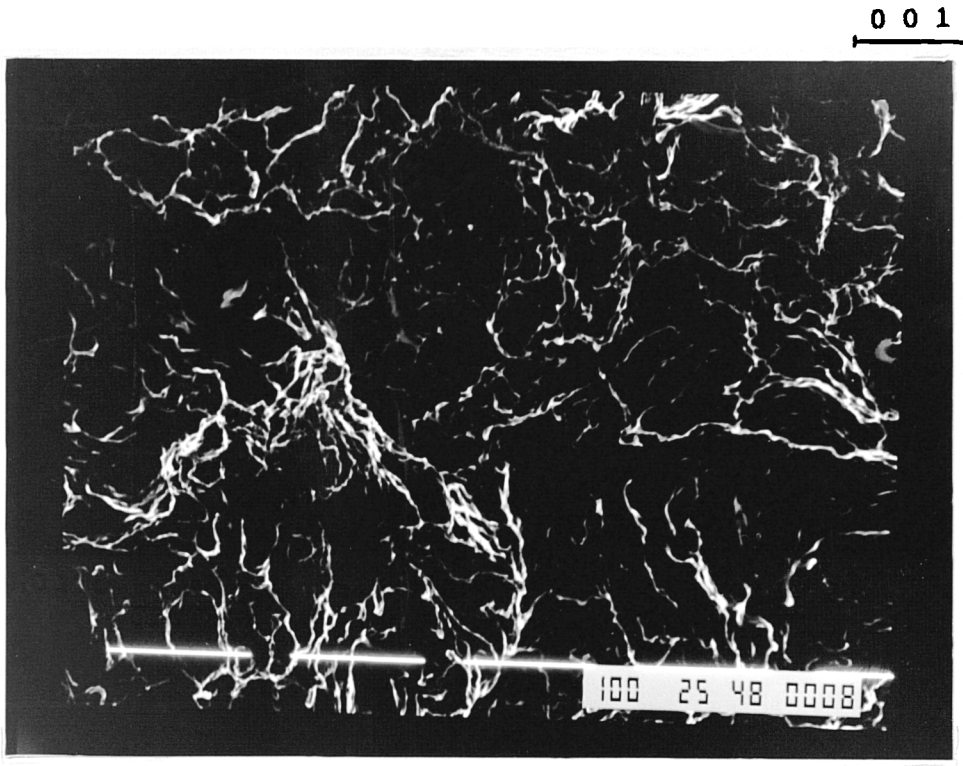

FIG.111c SCANNING ELECTRON MICROGRAPH OF DAMAGE IN CENTRAL ZONE AFTER TEST COMPLETION (160 min.)

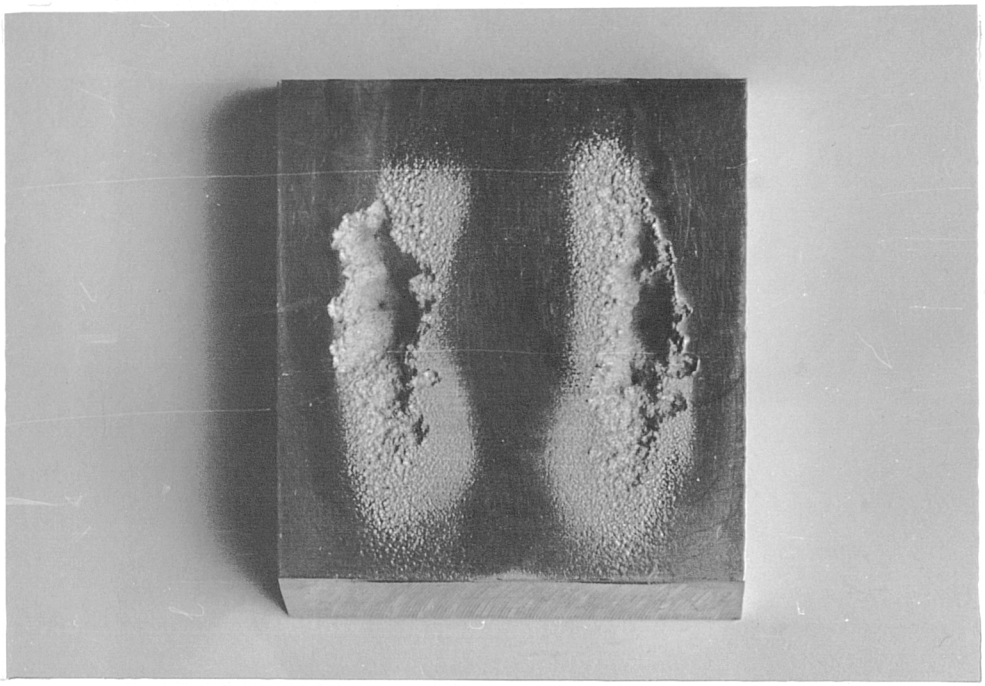

FIG.111d MACROSCOPIC VIEW OF GROSS DAMAGE IN ALUMINIUM (160 min.)

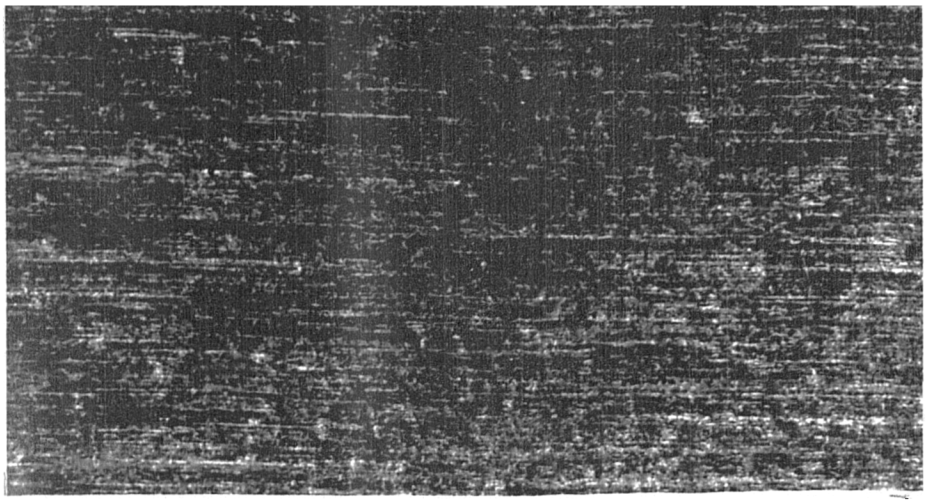

FIG.112a BEFORE TESTING

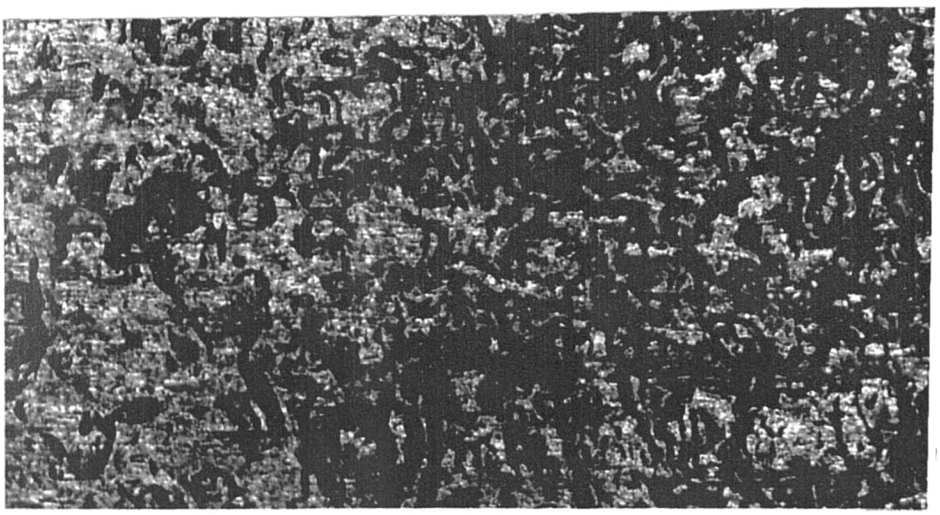

FIG.112b 25 min.

FIG.112c 50 min.

OPTICAL MICROGRAPH OF DAMAGE PROGRESSION IN CUPRO-NICKEL

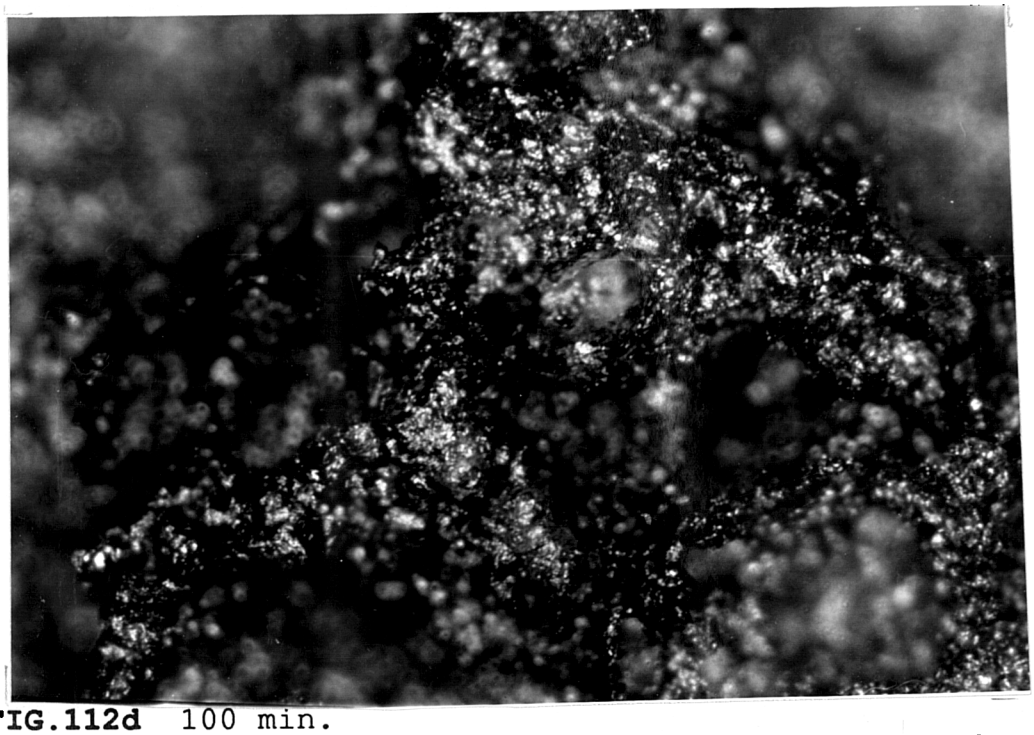

FIG.112d 100 min.

0.4mm

0.004mm

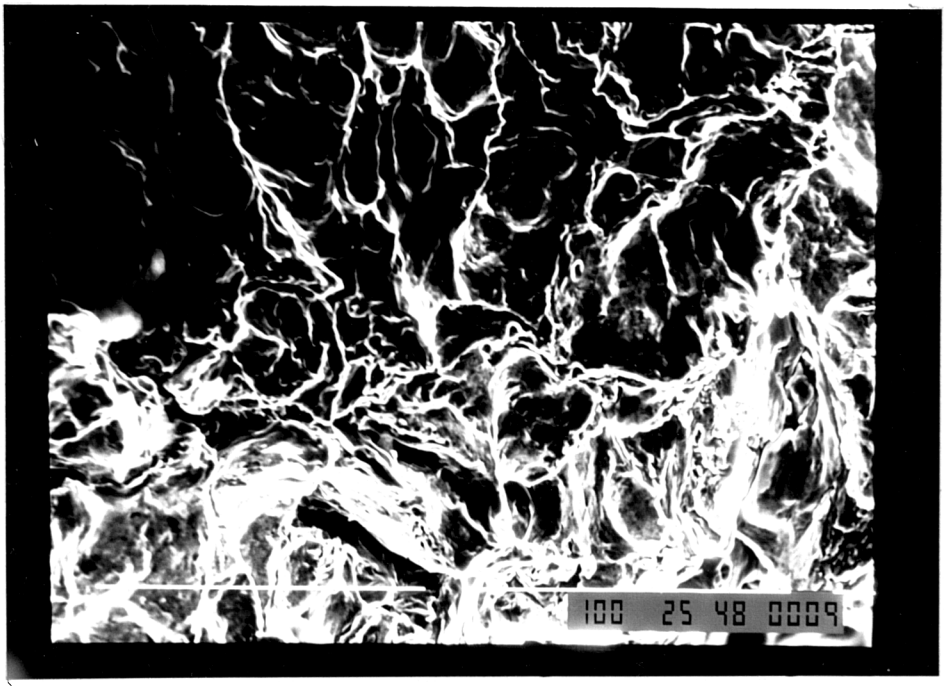

FIG.112e S.E.M TAKEM FROM CENTRAL ZONE IN CUPRO-NICKEL

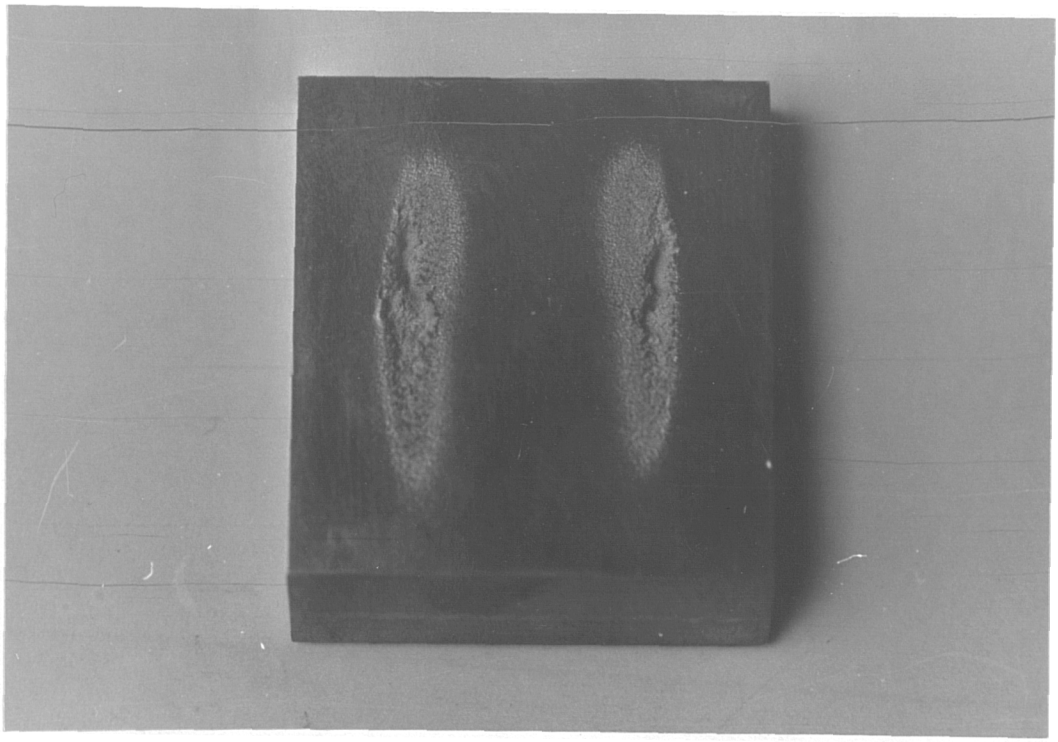

FIG.112f MACROSCOPIC VIEW OF GROSS DAMAGE IN CUPRO-NICKEL (300 min.)

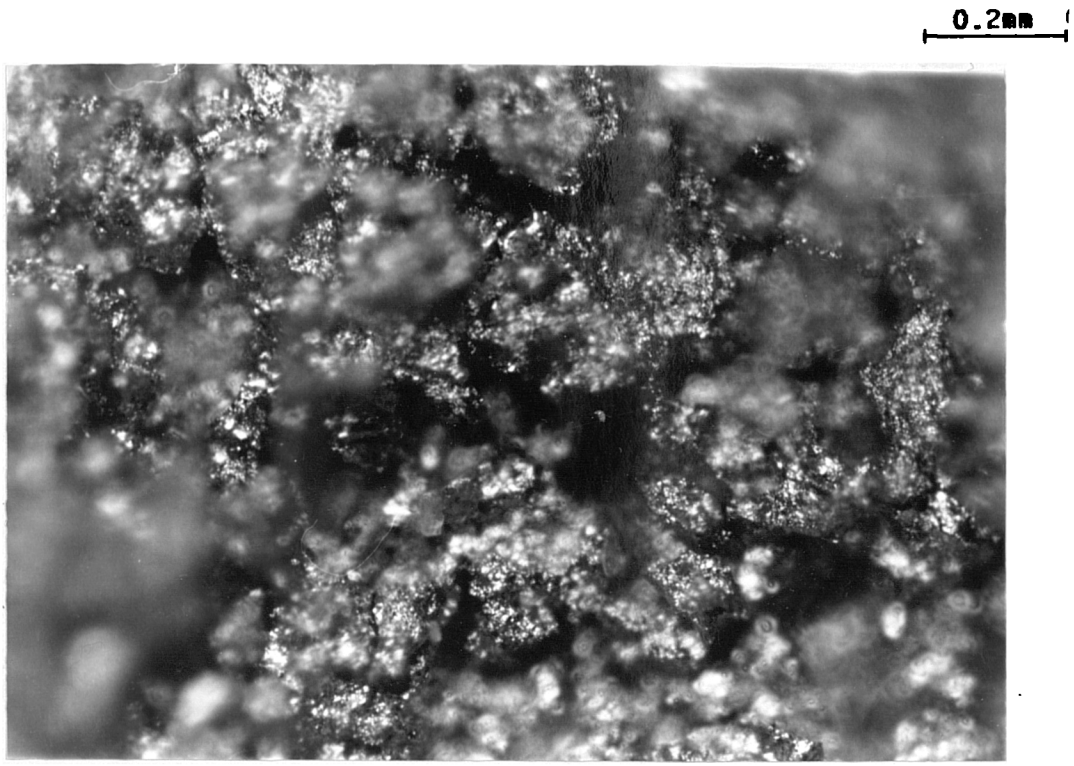

FIG.113a OPTICAL MICROGRAPH OF DAMAGE IN CENTRAL ZONE OF SINGLE PHASE BRASS (225 min.)

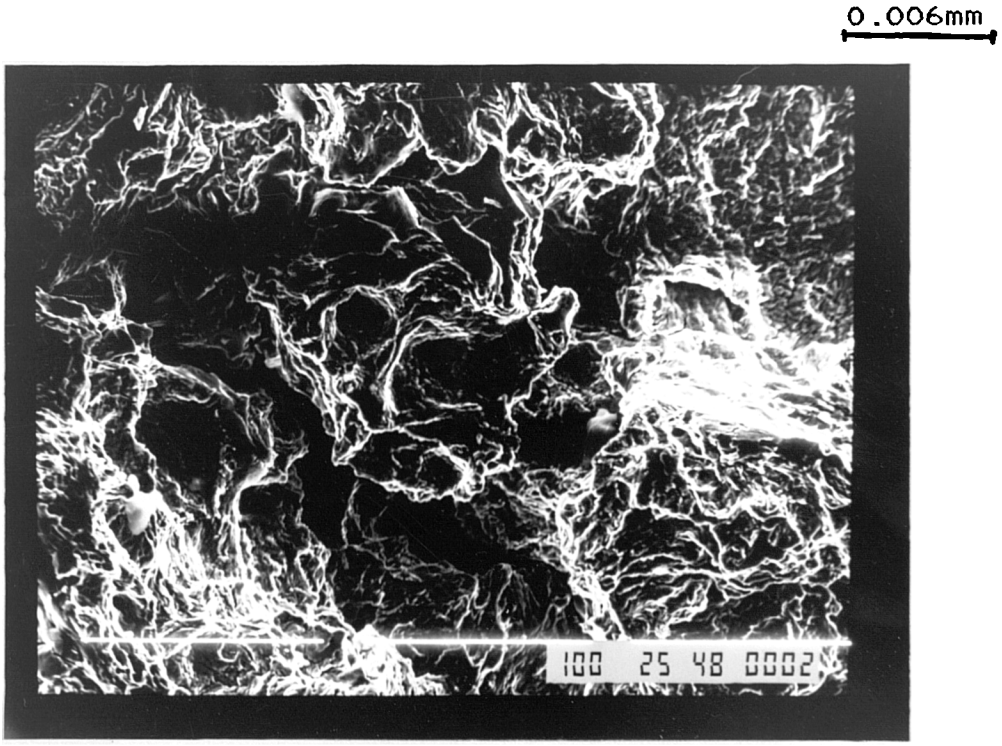

FIG. 113b S.E.M OF DAMAGE IN CENTRAL ZONE SINGLE PHASE BRASS

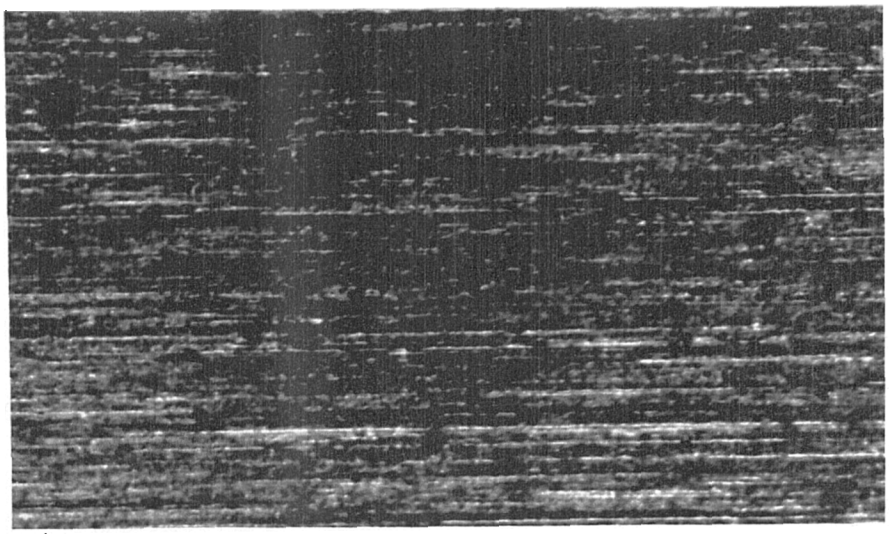

FIG.114a OPTICAL MICROGRAPH OF SURFACE PROIR TO TESTING ARMCO IRON

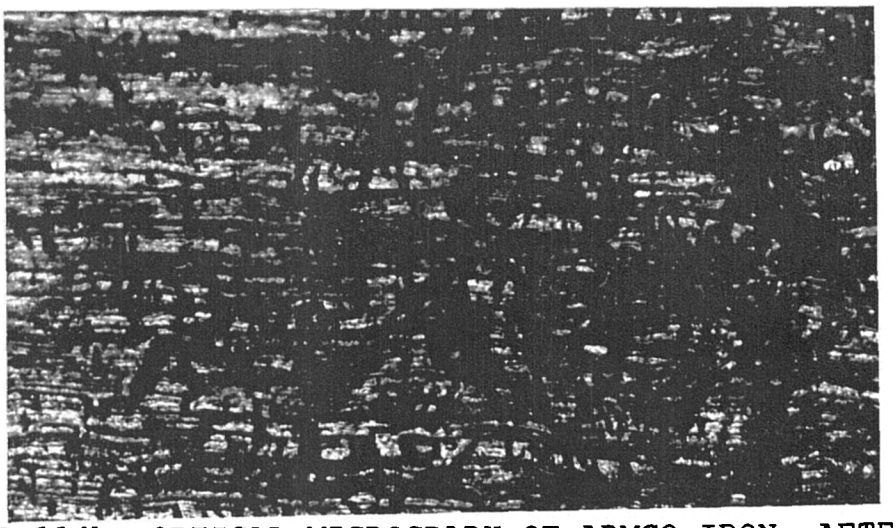

FIG.114b OPTICAL MICROGRAPH OF ARMCO IRON AFTER 30 min.

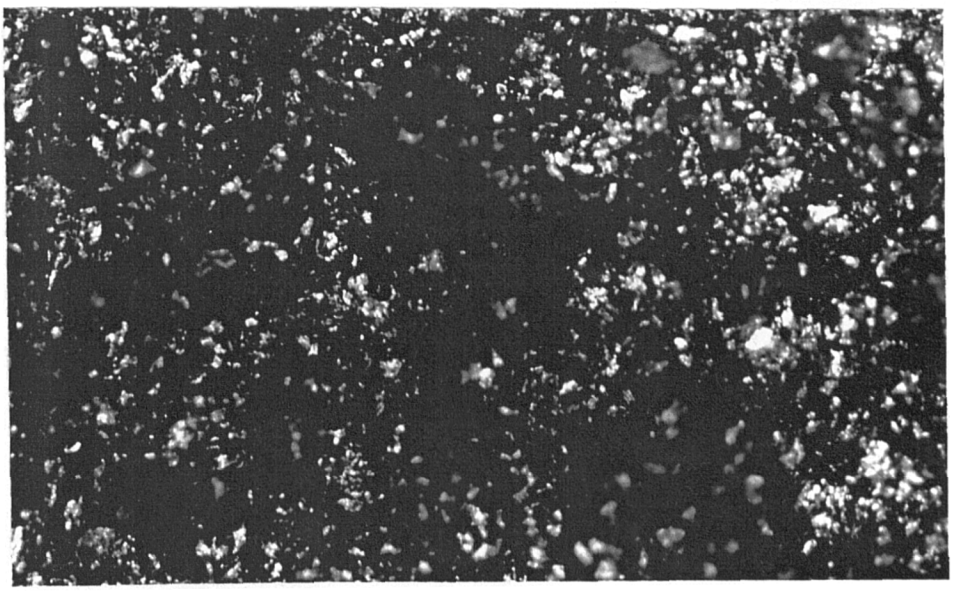

FIG.114c OPTICAL MICROGRAPH OF ARMCO IRON AFTER 60 min.

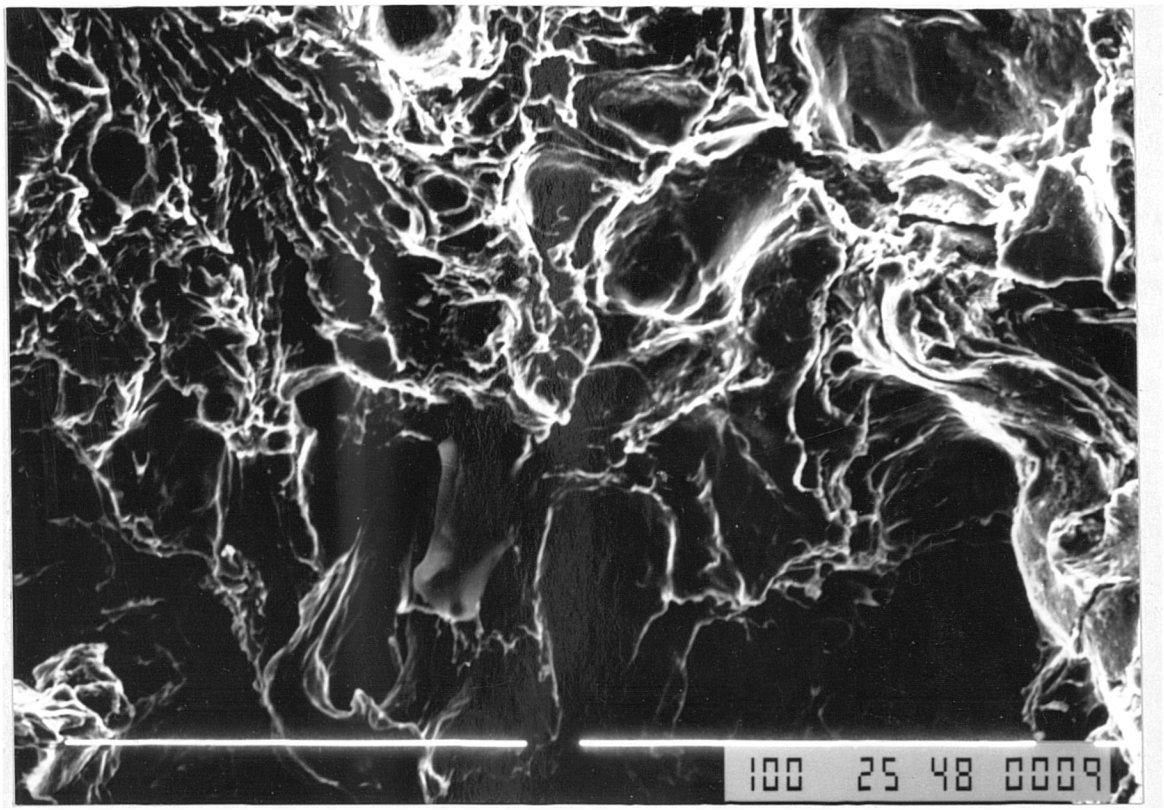

FIG.114d S.E.M OF DAMAGE IN CENTRAL ZONE OF ARMCO IRON (550 min.)

0.004mm

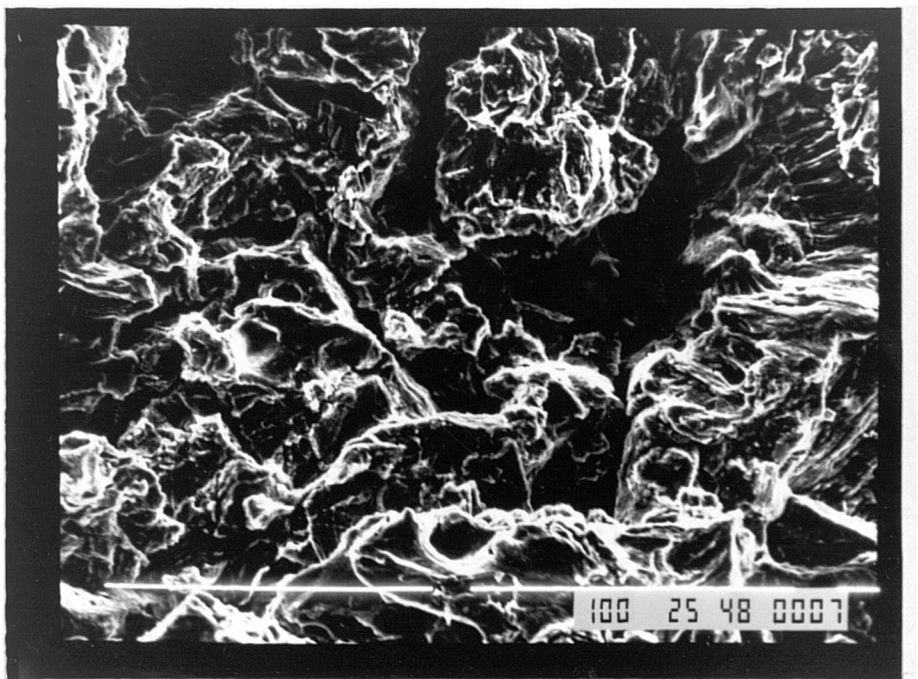

FIG.114e S.E.M OF DAMAGE IN CENTRAL ZONE OF ARMCO IRON (550 min.)

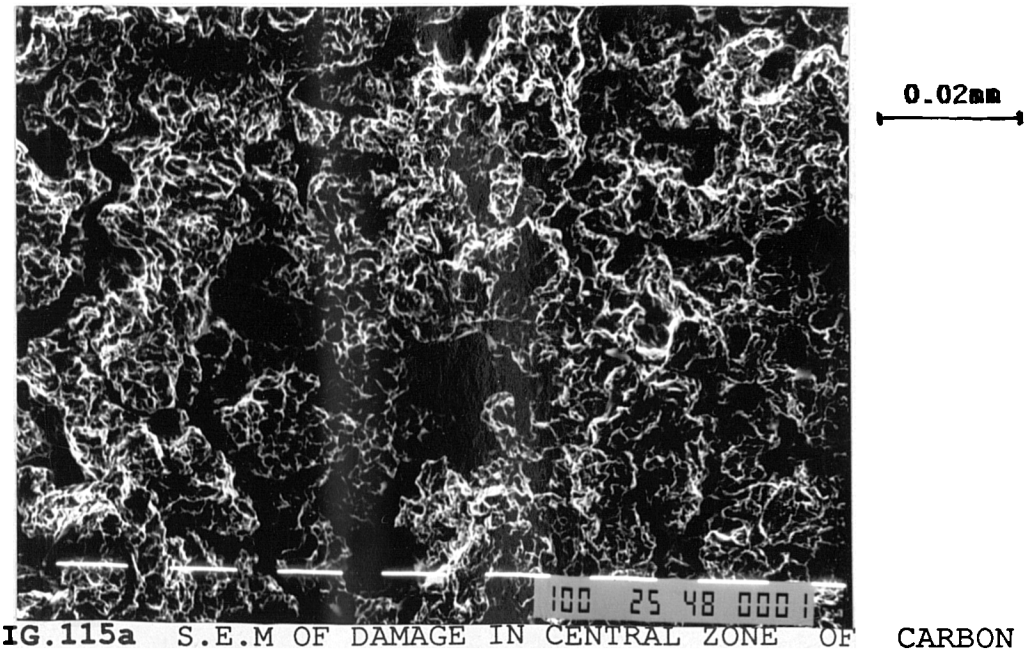

FIG.115a S.E.M OF DAMAGE IN CENTRAL ZONE OF CARBON STEEL HYPER-QUENCHED (600 min)

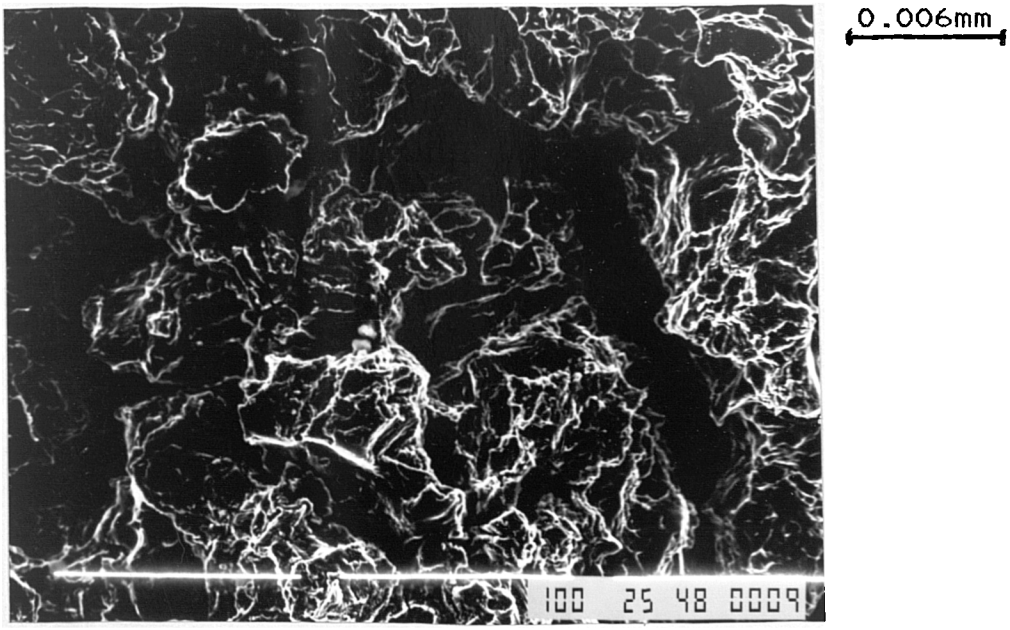

FIG.115b S.E.M OF DAMAGE IN CENTRAL ZONE OF CARBON STEEL HYPER-QUENCHED (600 min.)

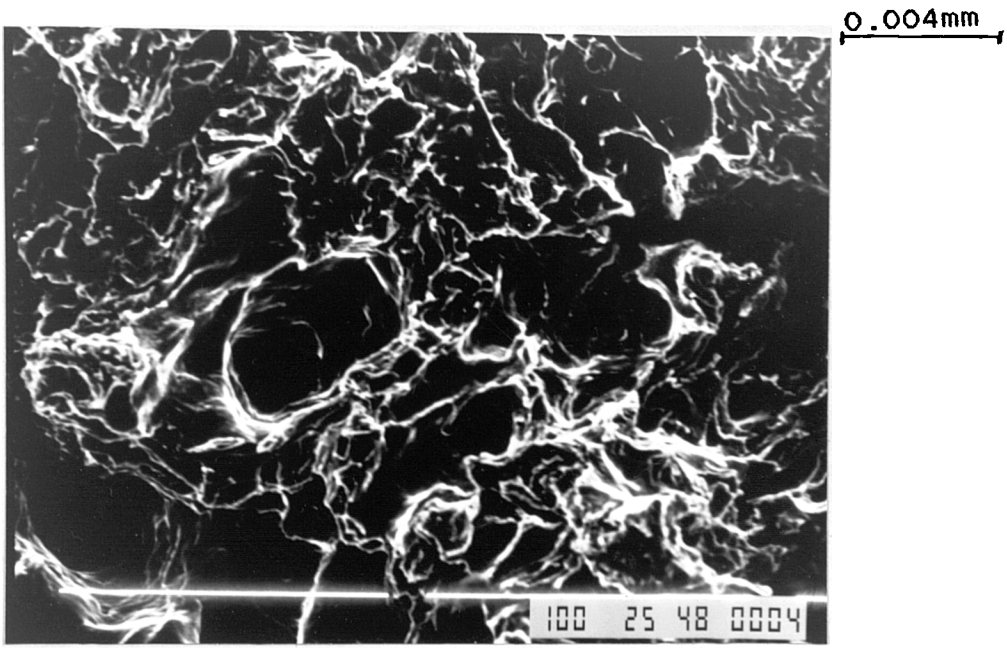

FIG.115c S.E.M OF DAMAGE IN CENTRAL ZONE OF CARBON STEEL AISI1020 (420 min.)

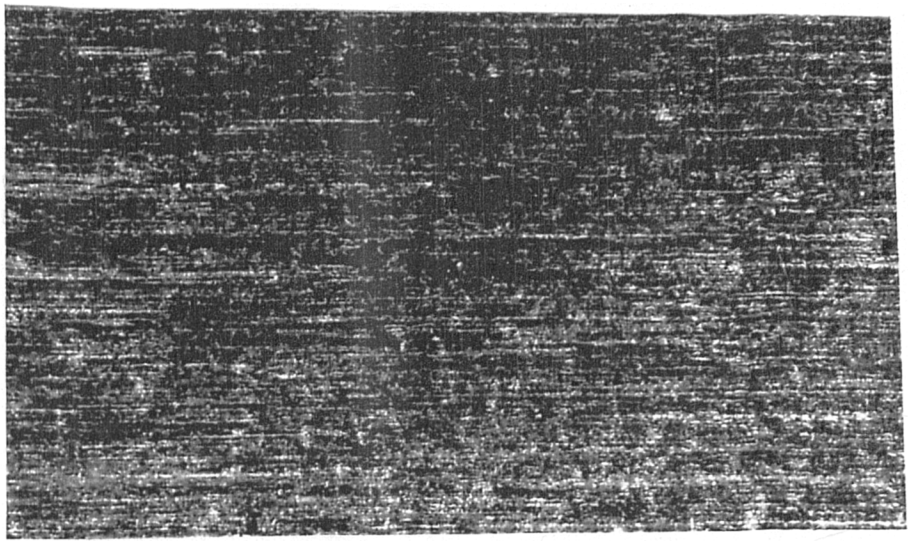

FIG.116a PLAIN SURFACE OF STAINLESS STEEL

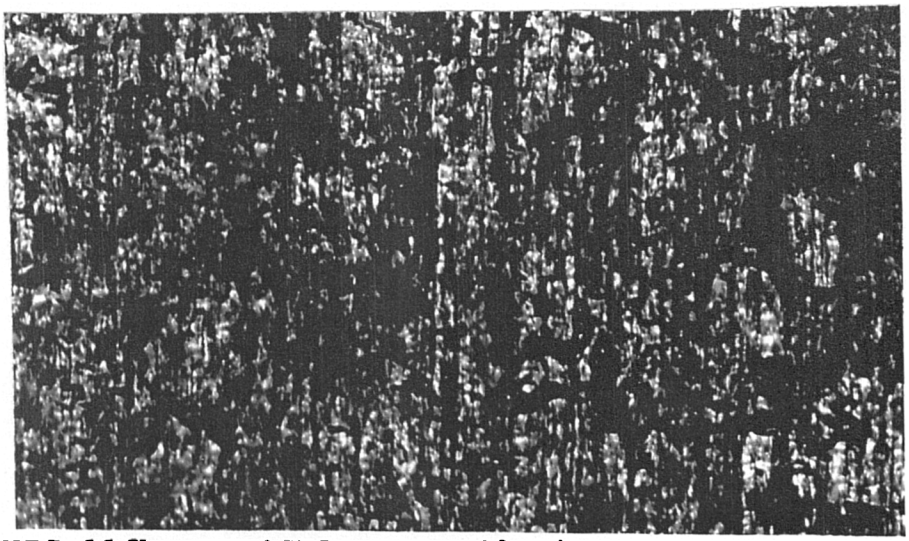

FIG.116b EXPOSED FOR 40 min.

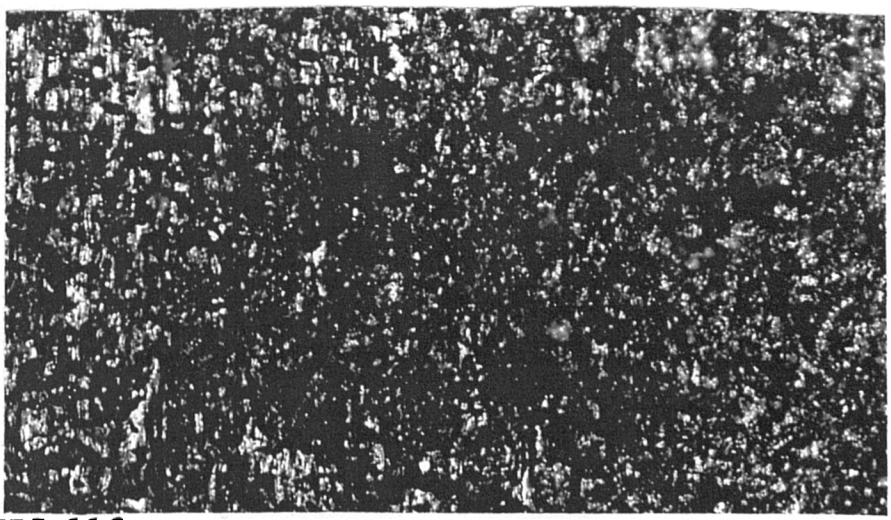

FIG.116c EXPOSED FOR 120 min.

OPTICAL MICROGRAPH OF DAMAGE PROGRESSION IN STAINLESS STEEL (acid resistance)

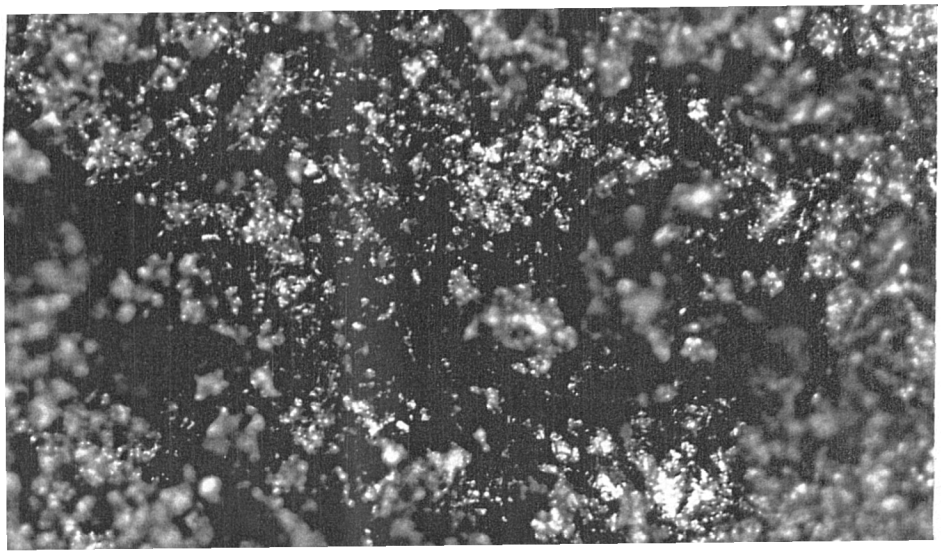

FIG.116d EXPOSED FOR 220 min

0.4mm

FIG.116e EXPOSED FOR 320 min

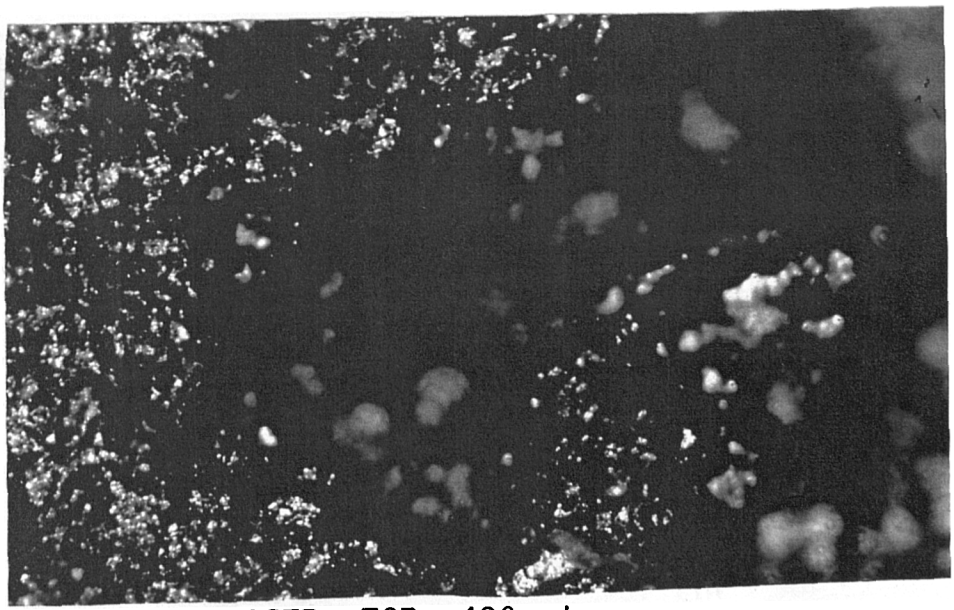

FIG.116f EXPOSED FOR 420 min.

OPTICAL MICROGRAPH OF DAMAGE PROGRESSION IN STAINLESS STEEL (acid resistance)

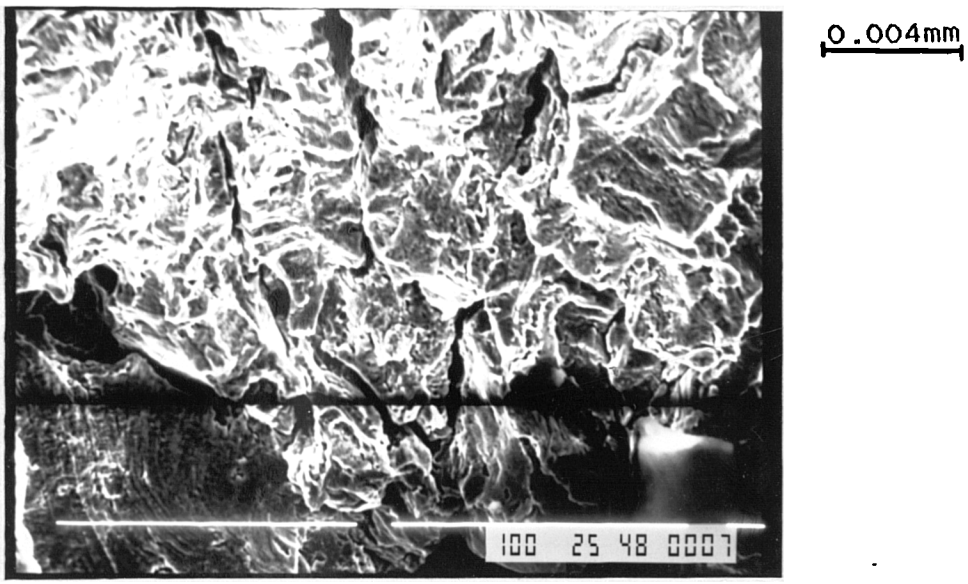

FIG.116g **S.E.M** TAKEN FROM CENTRAL ZONE AFTER COMPLETION OF TEST (620 min.)

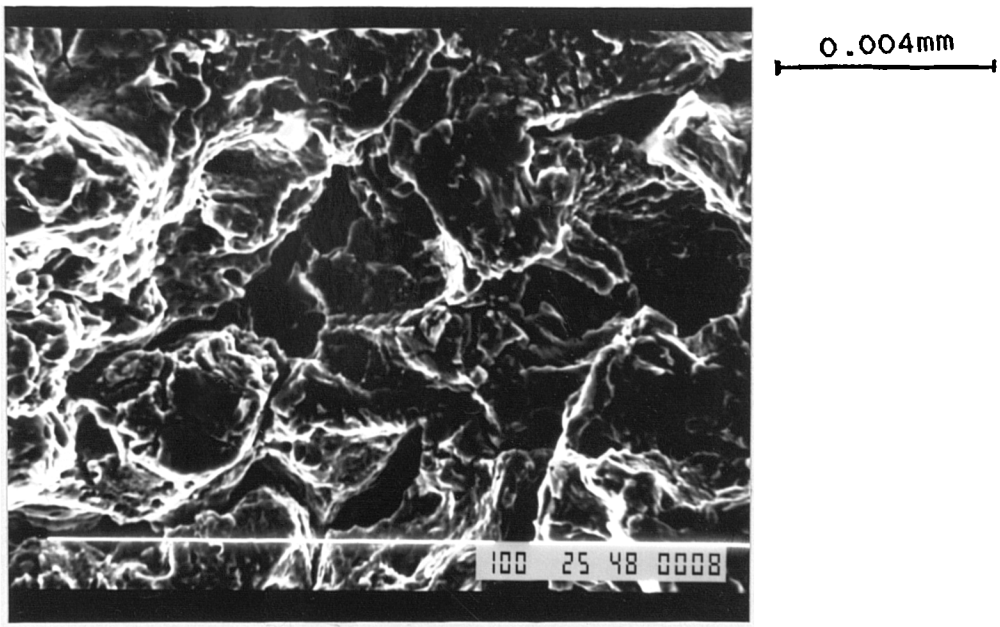

FIG.116h **S.E.M** TAKEN FROM CENTRAL ZONE AFTER COMPLETION OF TEST (620 min.)

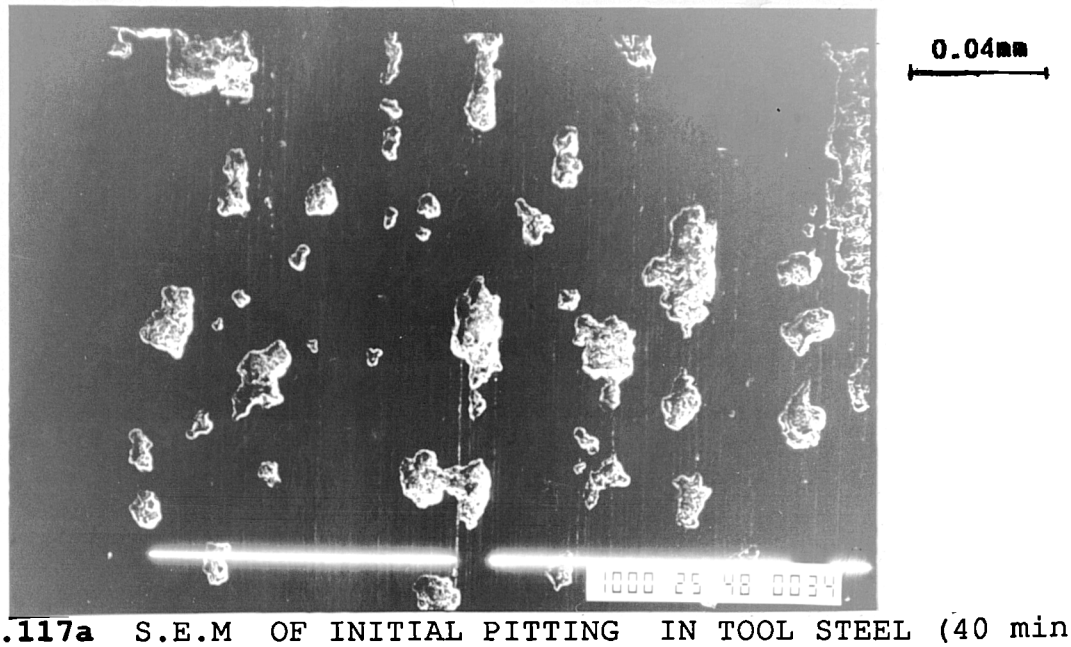

FIG.117a S.E.M OF INITIAL PITTING IN TOOL STEEL (40 min.)

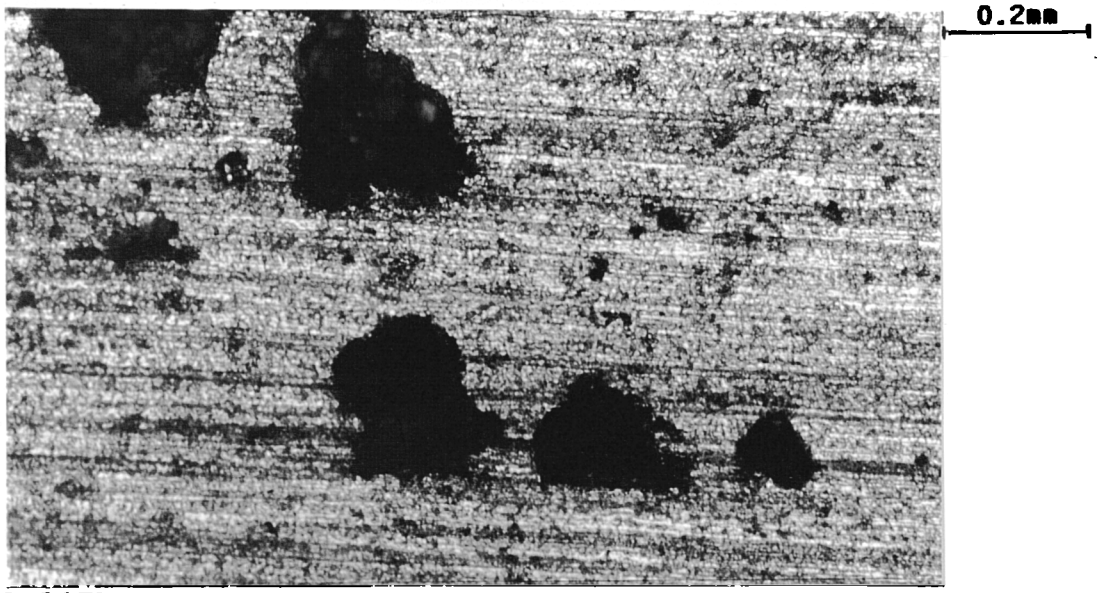

FIG.117b OPTICAL MICROGRAPH OF PITTING IN TOOL STEEL(40min)

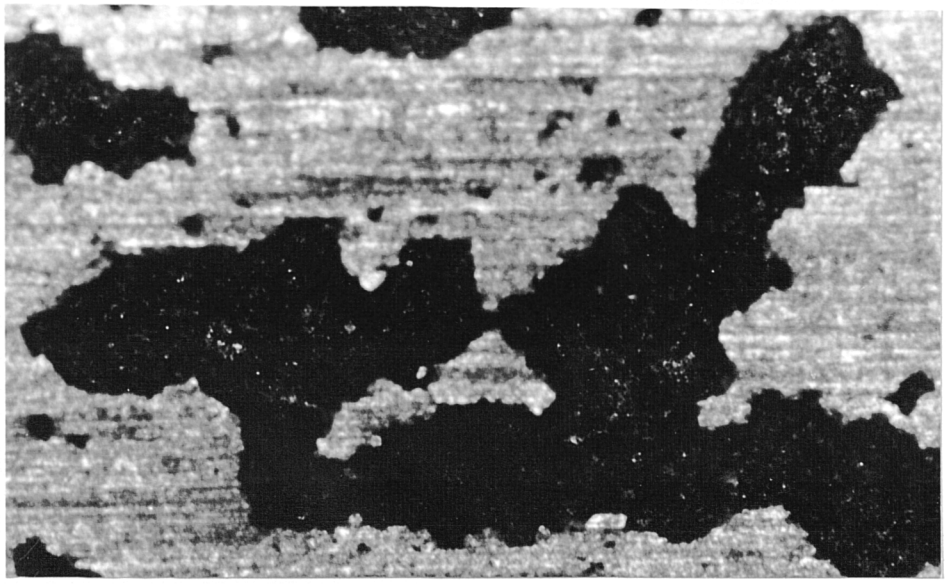

FIG.117c OPTICAL MICROGRAPH OF PITTING IN TOOL STEEL(60min)

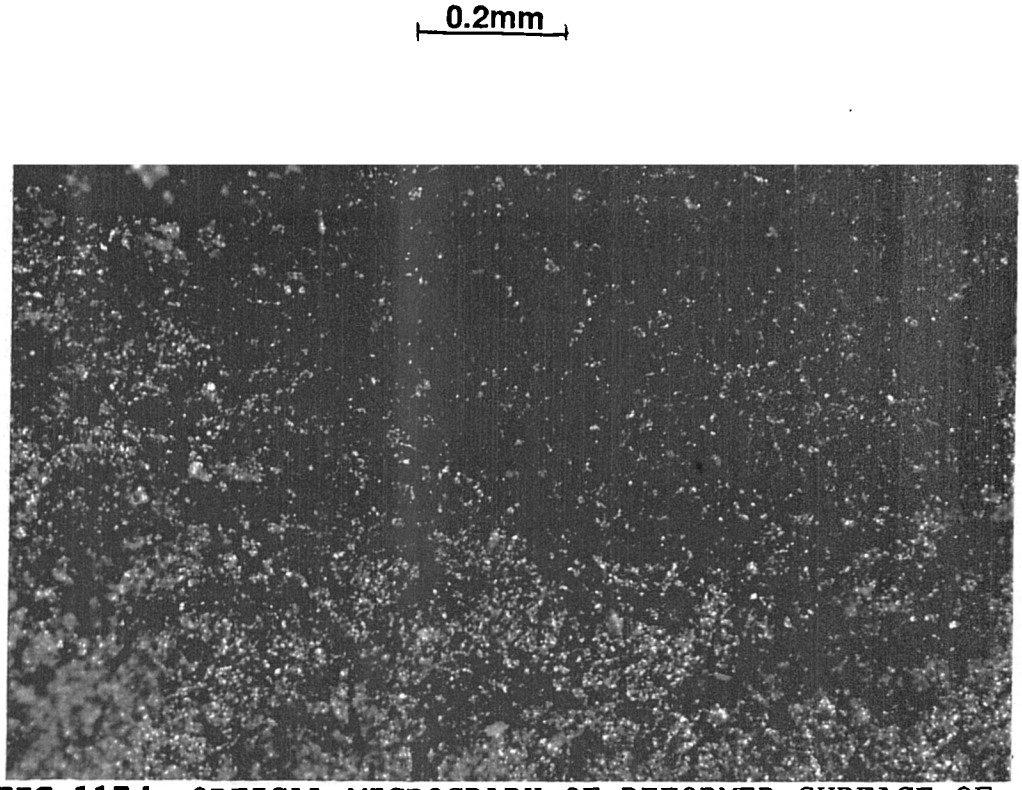

FIG.117d OPTICAL MICROGRAPH OF DEFORMED SURFACE OF TOOL STEEL (120 min)

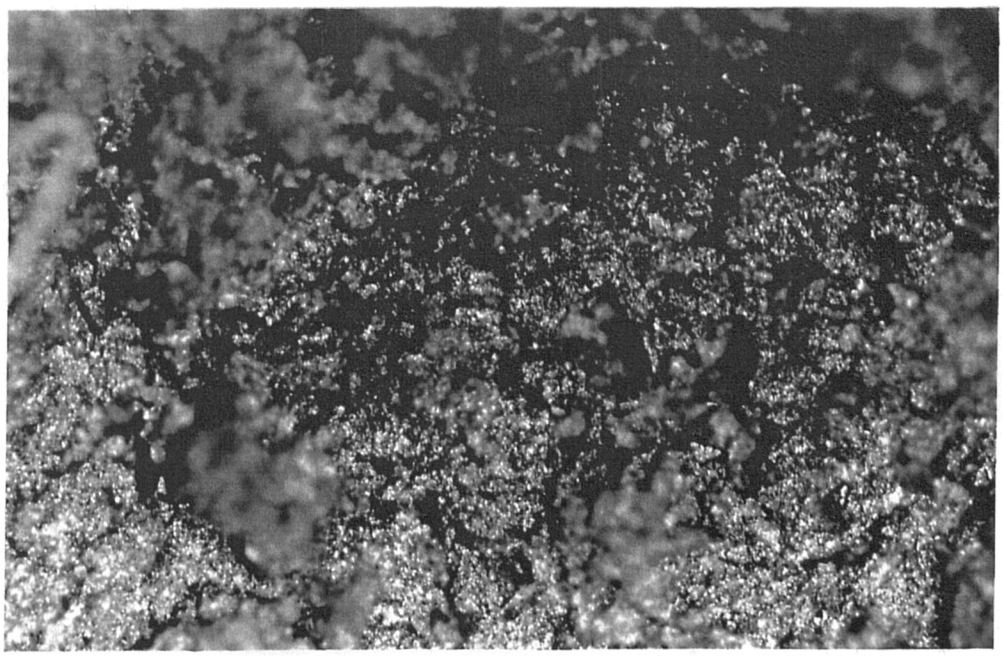

FIG.117e OPTICAL MICROGRAPH OF DAMAGE IN CENTRAL ZONE IN TOOL STEEL (380.min.)

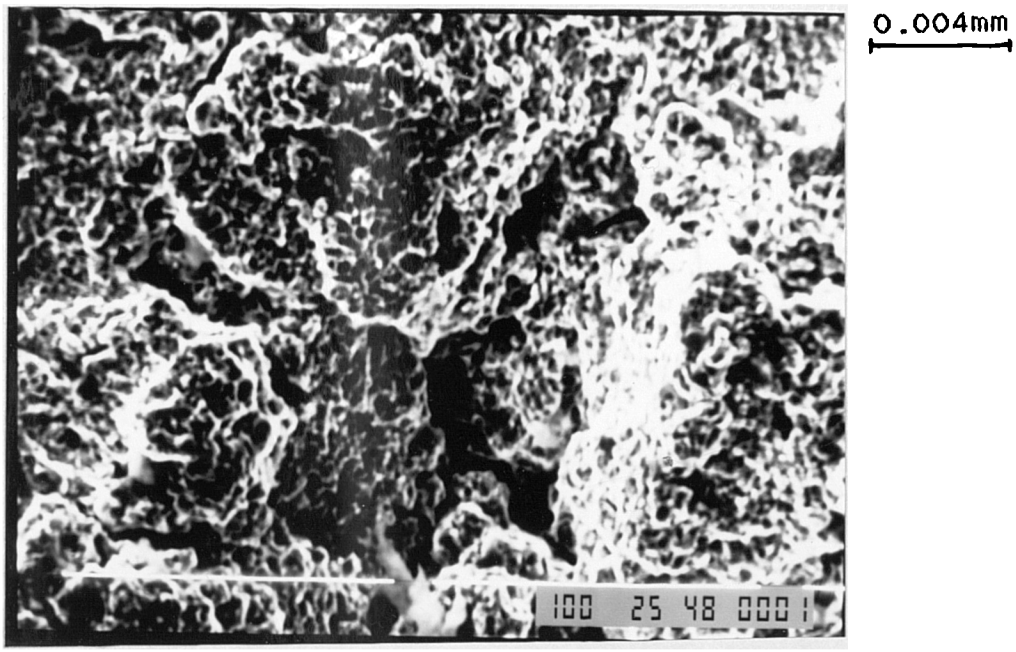

FIG.117f S.E.M OF DAMAGE IN CENTRAL ZONE AFTER TEST COMPLETION (500 min.)

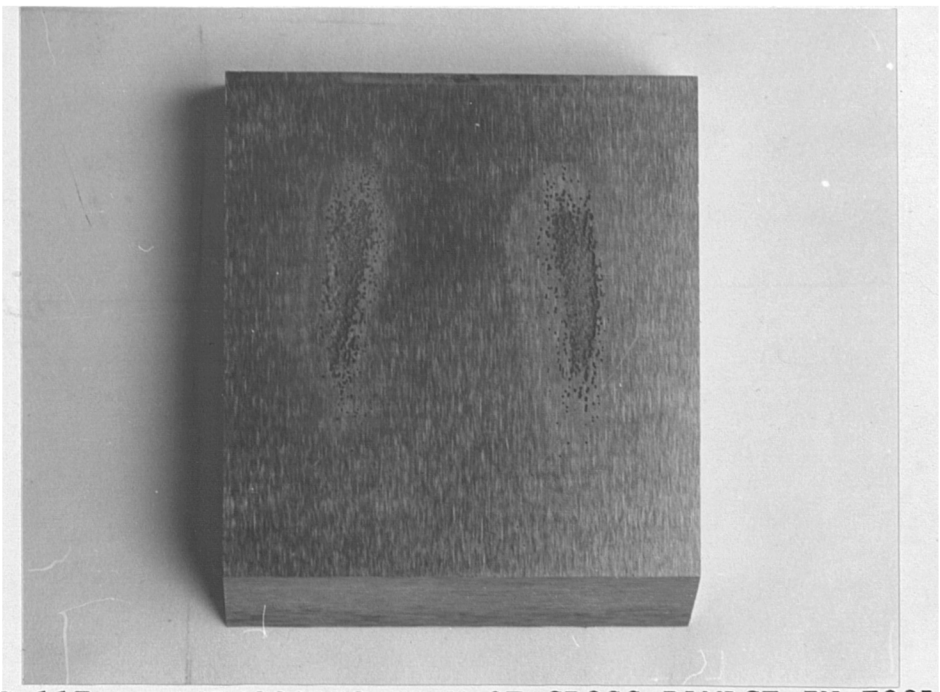

FIG.117g MACROSCOPIC VIEW OF GROSS DAMAGE IN TOOL STEEL

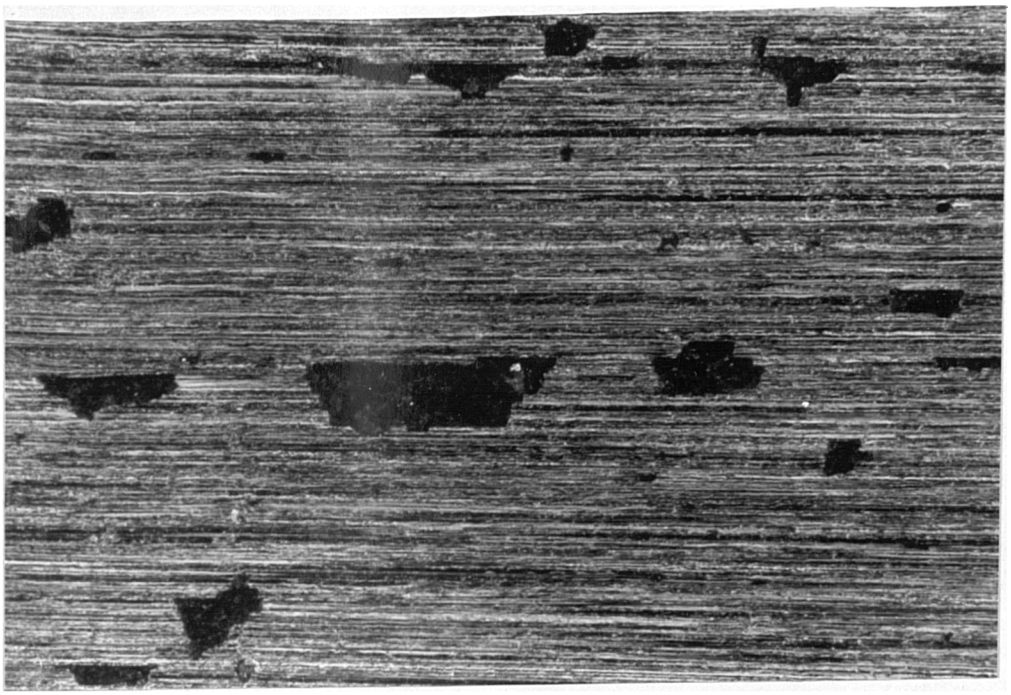

FIG.118a OPTICAL MICROGRAPH OF INITIAL PITTING IN NITRIDED STEEL (40 min)

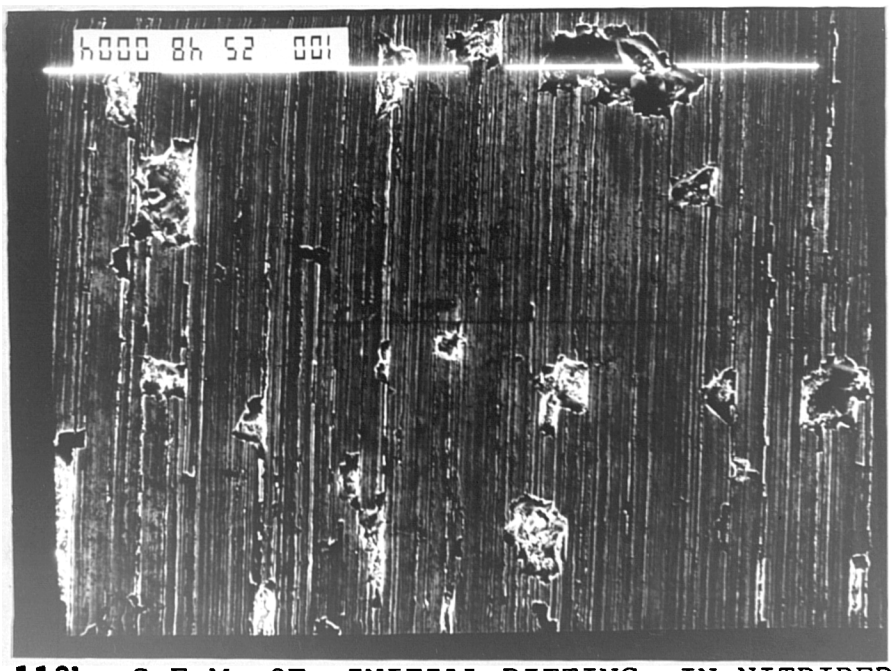

FIG.118b S.E.M OF INITIAL PITTING IN NITRIDED STEEL

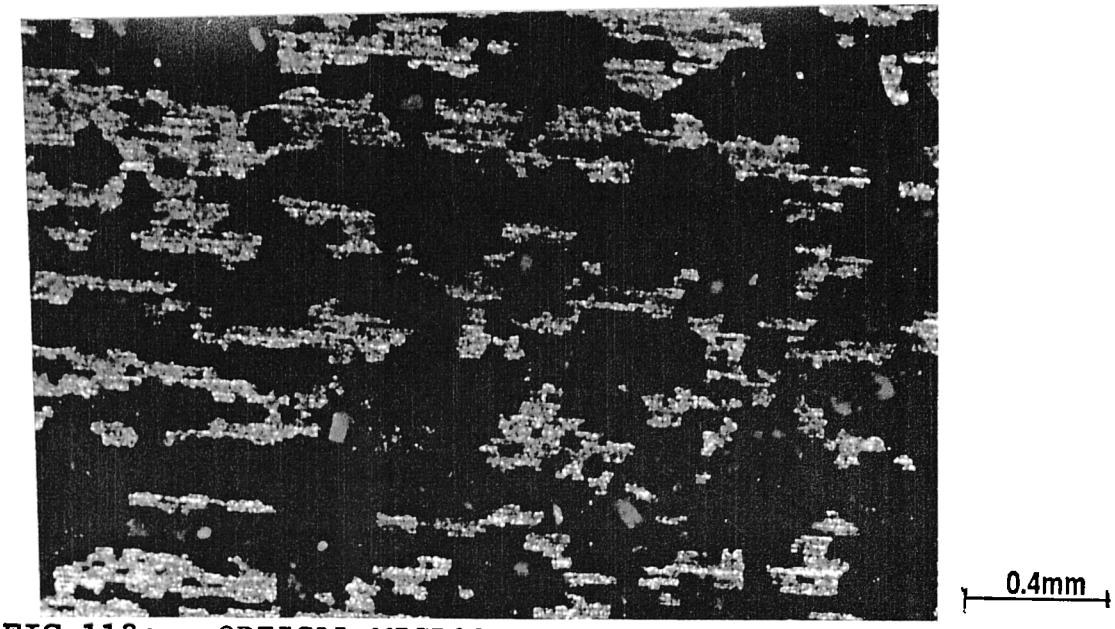

FIG.118c OPTICAL MICROGRAPH OF INCREASED PITTING IN NITRIDED STEEL (80 min)

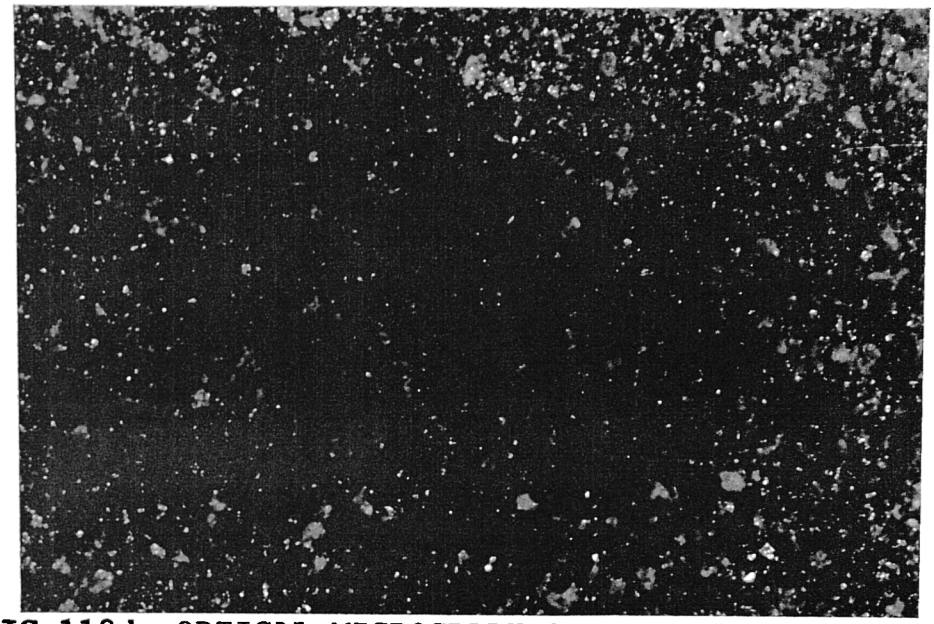

FIG.118d OPTICAL MICROGRAPH OF HIGHLY DEFORMED SURFACE OF NITRIDED STEEL (100 min)

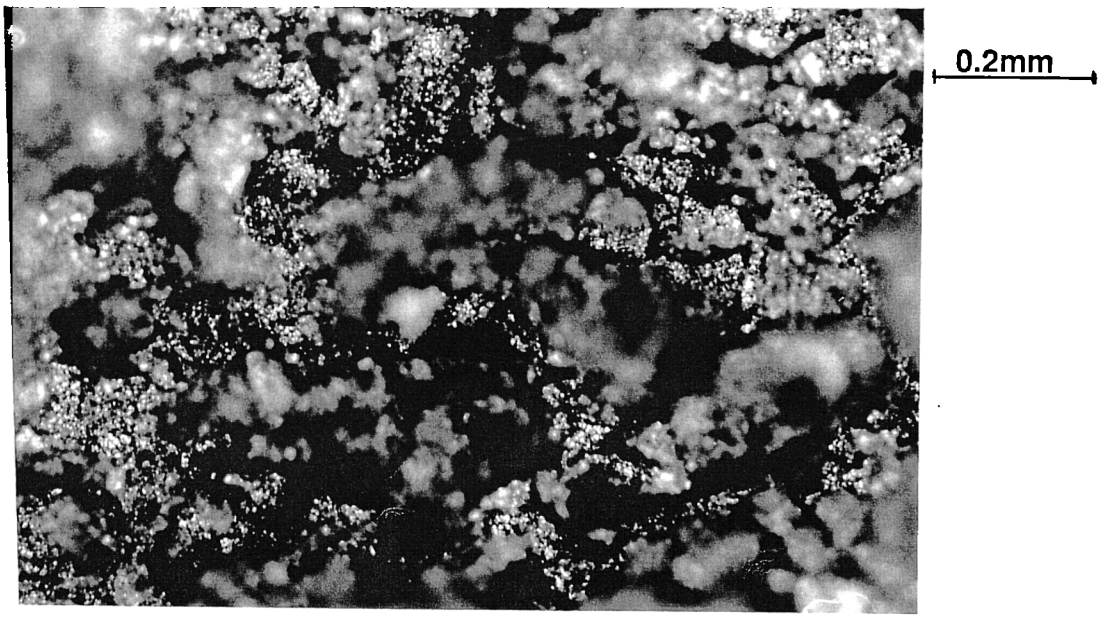

FIG.118e OPTICAL MICROGRAPH OF DAMAGED SURFACE OF NITRIDED STEEL (300 min)

FIG.118f OPTICAL MICROGRAPH OF A SPALLED SURFACE TOPOGRAPHY IN NITRIDED STEEL

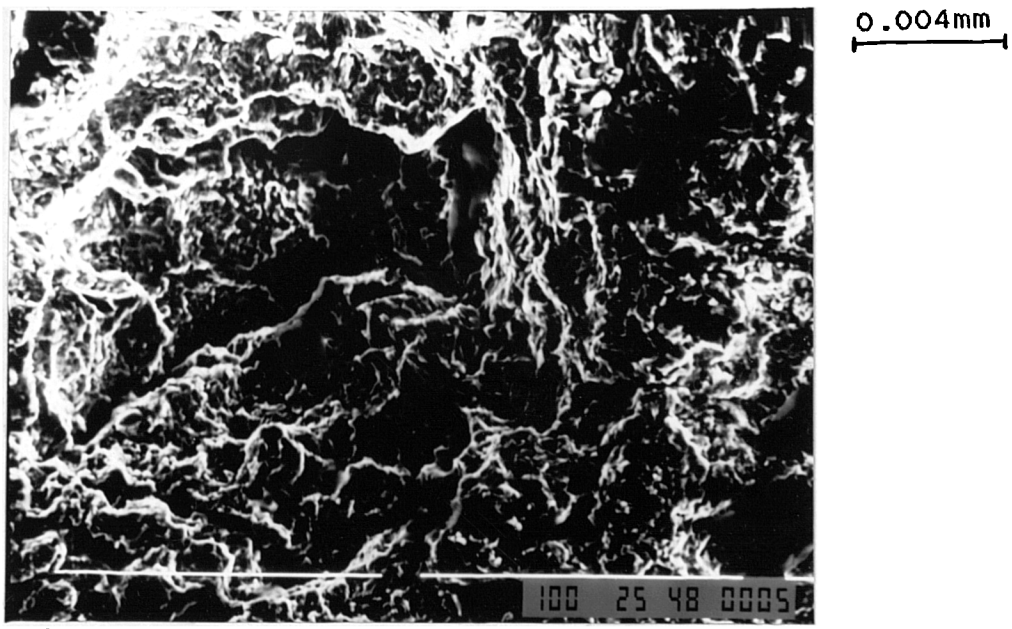

FIG.118g S.E.M OF DAMAGE IN CENTRAL ZONE AFTER COMPLETION OF TEST (420 min)

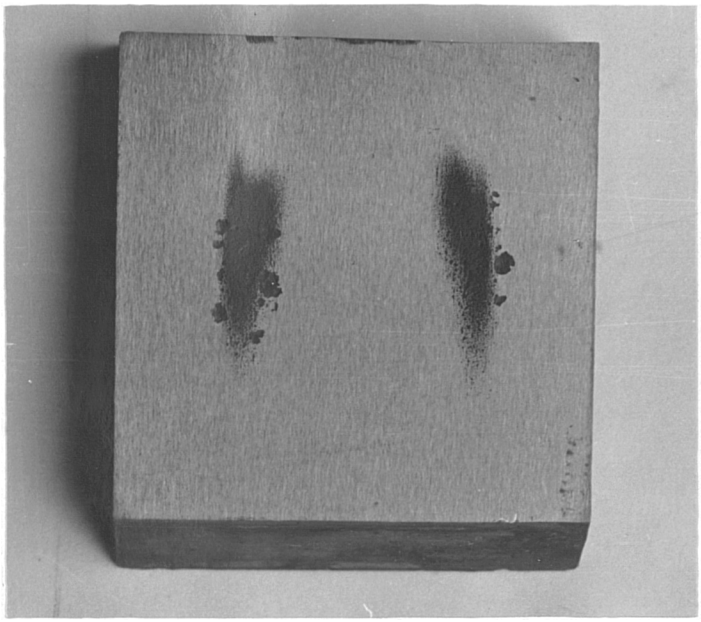

FIG.118h MACROSCOPIC VIEW OF GROSS DAMAGE IN NITRIDED STEEL

MECHANICAL PROPERTY OF EPOXY RESIN

TABLE 7:

PROPERTY	BLACK Q	BROWN G	BROWN MG
DENSITY (KG/M^3)	1800	1800	1800
TENSILE STRENGHT(MPa)	90-115	800-100	75-90
YEILD STRENGTH (MPa)	58.2	52.5	46.3
ELONGATION %	0.9-1.1	0.8-13.5	0.95-1.05
ELASTIC MODULUS (GPa)	8.8-11.2	10-13.5	9.0-10
COMPRESSIVE STRENGHT(MPa)	-	180-200	180-200
FRACTURE TOUGHNESS ($MN/m^{3/2}$)	2.2-3.2	2.5-3.5	1.7-2.4
ULTIMATE RESILIENCE($MNmm^{-3}$)	0.53	0.34	0.35
STRAIN ENERGY ($MNmm^{-3}$)	0.8	0.64	0.64

EPOXY RESIN AS MACHINED

TABLE 8:

No	MATERIAL DESIGNATION	VELOCITY (m/s)	NIP (min)	VLR (mm^3/hr)	Hv	μHv
1	ER BLACK Q	45	0.0	31.4 2.4	54	88
2	ER BROWN G	45	16.6	47.7 4.0	43	72
3	ER BLACK Q	40	2.17	18.1 1.0	54	88
4	ER BROWN G	40	0.26	16.1 1.2	43	72
5	ER BROWN MG	40	17	18.6 1.6	38	72

EPOXY RESIN AS CAST

TABLE 9:

No	MATERIAL DESIGNATION	VELOCITY (m/s)	NIP (min)	VLR (mm^3/hr)	Hv	μHv
1	ER BLACK Q	45	10.0	25.9 2.4	54	88
2	ER BROWN G	45	30.0	26.6 2.0	43	72
3	ER BLACK Q	40	92.3	5.5 0.28	54	88
4	ER BROWN G	40	140.7	8.0 0.66	43	72
5	ER BROWN MG	40	109.5	9.6 0.35	38	72

VELOCITY EXPONENT FOR EPOXY RESIN

TABLE 10:

	MATERIAL DESIGNATION	CONDITION	VLR_1 (mm^3/hr)	VLR_2 (mm^3/hr)	Vel_1 (m/s)	Vel_1 (m/s)	n
1	ER BLACK Q	MACHINED	31.4	18.1	45	40	5
2	ER BLACK.Q	AS CAST	25.9	5.55	45	40	1
3	ER BROWN G	MACHINED	47.7	16.1	45	40	9
4	ER BROWN G	AS CAST	26.6	8.0	45	40	1

NONINAL MECHANICAL PROPERTIES OF CERAMICS

TABLE 11:

PROPERTY	SILICON NITRIDE	SILICON CARBIDE
DENSITY (KG/M^3)	3200	3100
HARDNESS (Hv)	1400	1900
ELASTIC MODULUS (GPa)	310	410
FLEXURAL STRENGTH (MPa)	690	460
FRACTURE TOUGHNESS ($MN/m^{3/2}$)	4.9	3.9
COEFF. OF THERMAL EXPANSION ($*10^{-6}$/ C)	3.5	4.5

SURFACE ROUGHNESS PARAMETER

TABLE 12a:

SUFACE FINISH	CENTRAL LINE AVERAGE (Ra) (m)
FIREED OR SINTERED	0.8
GROUND	0.54
LAPPED	0.12

VELOCITY EXPONENT

TABLE 12b:

SURFACE CONDITION	SILICON CARBIDE	SILICON NITRIDE
LAPPED	22	23
GROUND	24	19
FIRED	20	-

SILIC0N CARBIDE

TABLE 13:

SURFACE CONDITION	VELOCITY (m/s)	NIP (min)	VLR (mm^3/hr)	Hv	μ Hv
LAPPED	40	76	0.61 0.04	1900	4115
GROUND	40	70	0.42 0.03	1900	4631
FIRED	40	107	1.28 0.12	1900	4099
LAPPED	45	40	8.97 0.5	1900	4115
GROUND	45	73	7.29 0.52	1900	4631
FIRED	45	42	13.68 0.52	1900	4099

SILIC0N NITRIDE

TABLE 14:

SURFACE CONDITION	VELOCITY (m/s)	NIP (min)	VLR (mm^3/hr)	Hv	μHv
LAPPED	40	186	0.122 0.01	1400	2967
GROUND	40	185	0.116 0.01	1400	3219
GROUND(HIP)	40	141	0.125 0.0	1700	2967
LAPPED	45	133	1.98 0.19	1400	2967
GROUND	45	135	1.2 0.04	1400	3219
FIRED	45	138	1.38 0.08	1400	2876
FIRED	45	158	1.06 0.103	1700	2876

COMPARISON BETWEEN SILICON CAEBIDE AND SILICON NITRIDE

TABLBE 15:

VELOCITY	MATERIAL	GROUND		LAPPED		FIRED	
		VLR (mm^3/hr)	NIP (min)	VLR (mm^3/hr	NIP (min)	VLR (mm^3/hr)	NIP (min)
40m/s	SiN_4	0.12	185	0.12	186	--	--
	SiC	0.42	70	0.62	76	1.28	107
45m/s	SiN_4	3.8	135	6.4	133	4.4	138
	SiC	22.6	73	27.8	40	42.4	42

COMOSITE

TABLE 16:

No	MATERIAL DESIGNATION	VELOCITY (m/s)	NIP (min)	VLR (mm^3/hr)	Hv	μHv
1	GRP1	30	58.0	13.7 0.58	34	56
2	GRP2	35	10.2	25.1 0.6	34	56
3	GRP3	40	4.0	87.39 10.9	34	56
4	GRP4	45	0.0	128.3 11.7	34	56
5	FYBROC1	35	12.4	19.0 1.2	27	52
6	FYBROC2	40	0.0	52.3 5.7	27	52

METAL ALLOYS

TABLE 17:

No	MATERIAL DESIGNATION	VELOCITY (m/s)	NIP (min)	VLR (mm^3/hr)	Hv	μHv
1	ALUMINIUM SIC	45	3	211	40	72
2	AL. ALLOY HE9	45	4.3	25.5	75	135
3	AL. ALLOY HE10	45	7.17	10.0	90	162
4	AL. ALLOY HE15	45	6.8	5.22	140	252
5	AL. ALLOY PA2	45	7.0	90.5	65	123
6	ARMCO IRON	45	230	1.5	132	308
7	BRASS (M63)	45	72	8.3	117	228
8	CAST STAINLESS	45	44	0.65	210	460
9	CARBON $STEEL_1$	45	117	4.38	145	373
10	CARBON $STEEL_2$	45	332	1.5	176	392
11	CUPRO-NICKEL	45	44	9.84	110	276
12	NITRALLOY (S106)	45	209	1.14	630	874
13	NITRIDED STEEL	45	99	0.232	980	1811
14	STAINLESS STEEL	45	376	0.65	335	515
15	TOOL STEEL	45	142	0.46	758	1574
16	TOOL STEEL (M4)	45	317	0.65	970	1802

1 carbon steel AISI1020
2 carbon steel HYPER QUENCHED

RESULT FOR VARIOUS MATERIALS

TABLE 18:

No	MATERIAL DESIGNATION	VELOCITY (m/s)	NIP (min)	VLR (mm^3/hr)	Hv	μHv
1	GRP	45	0.0	128.4 1	34	56
2	AL. ALLOY (PA2)	45	7.0	90.5 5.6	65	123
3	ER BROWN.G	45	16.6	47.7 4.0	43	72
4	ER BROWN.Q	45	0.0	31.4 2.4	540	88
5	CUPO-NICKEL	45	44	9.84 0.21	110	276
6	BRASS (M63)	45	72	8.3 0.23	117	228
7	SILICON CARBIDE	45	73	7.29. 0.52	1900	4631
8	CARBON $STEEL_1$	45	117	4.38 0.17	145	373
9	ARMCO IRON	45	230	1.5 0.3	132	308
10	CARBON $STEEL_2$	45	332	1.5 0.06	176	392
11	SILICON NITRIDE	45	135	1.2 0.04	1400	3219
12	NITRALLOY (S106)	45	209	1.14 0.56	630	874
13	STAINLESS STEEL	45	376	0.65 0.03	335	515
14	CAST STAINLESS-	45	44	0.65 0.04	210	460
15	TOOL STEEL(M4)	45	317	0.65 0.04	970	1802
16	TOOL STEEL	45	142	0.46 0.03	758	1574
17	NITRIDED STEEL	45	99	0.232 0.0	980	1811

6.0 DISCUSSION

In spite of the fact that cavitation induced erosion has been researched rather frequently in the past, the proper selection of engineering materials for hydraulic equipment exposed to cavitation is still exceedingly difficult in many instances.

It has been generally recognised that the main obstacles to a more rational approach were the absence of truly comparative data on the erosion resistance of an adequate number of materials, which may be given consideration in the course of manufacture and maintenance of hydraulic machinery. And also the lack of definite information regarding characteristics of surface finishing operations which might influence the resistance of materials, as well as the nature of their failure when exposed to cavitation attacks.

In this purely experimental research work, some of the above problems have been addressed. In particular the resistance afforded by various surface finishes in bulk plastics and ceramics. In addition to the above non-metals, cavitation induced erosion tests were also performed on glass reinforced plastics and a range of commercial metal alloys. The results obtained are discussed in this chapter.

6.1 PLASTIC

The results for both Novalac and Bisphenol epoxy resin systems in both machined and as cast conditions are summarised in table 8 and 9 respectively. The effect of time on erosion on the various samples are given in plots of cumulative volume loss against time. These are shown graphically in figures 27 to 36.

For the novalac epoxy resin system in both cast and machined conditions, it is seen as shown in figure 27 and figure 28 that, plots of volume loss against time at high cavitation intensity (i.e 45m/s) were essentially very linear i.e no acceleration period is observed. This characteristic rendered the regression analysis to incorporate all the data points from the test. As seen from the plots, it also had the effect of producing the same value for both absolute and nominal incubation periods.

It is seen from these plots that material removal was instantaneous as soon as cavitation was in play i.e, at this intensity the material did not offer much of a resistance to the cavitation forces, hence no significant incubation period. At reduced intensity i.e at 40m/s, the linearity of the plot with the machined sample is maintained. However the as cast sample showed a marked change between the absolute incubation period and the nominal incubation period. This implies that the as cast sample provided some resistance before the onset of material

removal. The plots for the above two conditions, i.e as cast and machined are shown in figure 29 and 30 respectively.

It is seen from the above two test conditions that, the magnitude of the erosion rate decreases as the velocity decreases, i.e with increase velocity the erosion resistance decreases. This was not surprising as many studies on the effect of velocity on erosion rate , with metal alloys have shown a very high dependency. The general power law for most metal alloys has an average exponent of 6. Grant (1984) testing perspex found the exponent to be 9. Using equation 19 for the two velocities employed, the average exponent for the novalac epoxy resin system is 9.7 .

Comparing the performance of both as cast and machined surfaces, it is clearly seen on the comparison graph in figure 37 that at high cavitation intensity, the as cast sample performed slightly better than the machined one. Quantitatively, the VLR of the machined sample is 1.2 times greater than that of the as cast sample. The NIP for the as cast sample is greater by a factor of ten. At lower cavitation intensity, the difference in performance is even greater as seen in figure 38. The VLR of the machined surface is 3.3 times greater than that of the as cast surface. The NIP of the as cast surface is 43 times greater.

The characteristic curve of erosion rate against time for this sample in both conditions are shown in figure 47. The

"ascast" sample exhibits acceleration and steady state periods, while the machined sample exhibits peak erosion rate and deceleration period. A polymonial of the sixth degree was observed to best fit the data points, with the machined sample data having a 100% residual about mean explained and a standard deviation of 10.0059 mm^3/hr. The corresponding values for the as cast sample were 95% and 10.029 mm^3/hr. Both curves almost conform to patterns reported by Heymann (1967) for metallic materials.

Figure 31 and 32 show the plots of cumulative volume loss against time for the Bisphenol epoxy resin system at high cavitation intensity for both machined and as cast samples respectively. The plots in the above figures are very linear. Similar to the Novalac samples, their nominal incubation period also coincides with their absolute values. This is often an indication of low resistance to the given cavitating conditions. At low cavitation intensity i.e at 40m/s, the individual graphs for both surface conditions are given in figure 33 and 34. With the as cast sample in figure 33, the curve exhibits an acceleration period and hence a nominal incubation period which is different from the absolute value. The regression line here as mentioned in section 5.2 in chapter 5 under result analysis, is analysed up to the last data point in the acceleration region that provides minimum error in the 95% confidence limit. The plot for the machined sample as shown in figure 34 is similar in

all respects to that at high cavitation intensity i.e linear from onset of mass loss.

Performance wise, the nominal incubation period for both as cast and machined surfaces at high cavitation intensity was not that different i.e 30 and 17 minutes respectively .The volume loss rate for the machined sample is 2 times greater than that of the as cast sample. The comparison graph in figure 39 clearly illustrate the performance differences qualitatively for the two surface conditions. At lower cavitation intensity i.e 40 m/s, the performance difference is greater as shown in the comparison graph in figure 40. Quantitatively, the erosion rate for the machined sample is twice that of the as cast sample. The as cast sample nominal incubation period is 140 times greater than that of the machined sample.

The characteristic curve of erosion rate against time for this sample in both conditions are shown in figure 48 and 49. The as cast sample exhibit acceleration and steady state period, while the machined sample exhibit peak erosion rate and deceleration period.

Figure 41 and 42 shows the performance differences between the two epoxy resin systems employed i.e novalac and bisphenol. The plot in figure 41 shows an overall better performance for the machined novalac epoxy resin system in terms of volume loss rate. However, it is seen from the graph that, during the initial stages of material

removal i.e first 70 minutes, the bisphenol epoxy resin system had less material removed. Quantitatively, the volume loss rate for the bisphenol epoxy resin system is 1.5 times greater than that of the novalac system at high cavitation intensity. From figure 41, it is seen that both systems have comparable nominal incubation period. The comparison graph shown in figure 42 illustrates how closely matched their performances were in the as cast condition. The VLR values for both the novalac and the bisphenol system were 25.9 and 26.6 mm^3 /hr respectively, a percentage difference of 2.6. i.e same within the 95% confidence limit. Their nominal incubation periods as seen also from the comparison plot in figure 42, are also very comparable.

For tests done at low cavitation intensity i.e, 40m/s, there was not that much difference between the performances of the two epoxy resin systems as illustrated in the comparison graphs in figure 43 and 44 . In the as cast condition (Fig 43), the VLR of the bisphenol system was 1.4 times greater than that of the novalac system . However, the novalac system had a shorter nominal incubation period of 93 minutes compared with 141 minutes for the bisphenol system. In the machined condition as shown in the comparison graph in figure 44, their performances were almost identical.

Generally, there was no discernable trend as to which performed better when the two resins i.e, novalac and

bisphenol are compared. However, when performance is evaluated solely on their VLR values, the novalac resin seems to have the edge. This is borne out from the fact that, out of the four tests done at both high and low cavitation intensities, the novalac resin performed better in three of them.

The Bisphenol epoxy resin system was also tested in another format in which the abrasive particulate filler were removed from the formulation. With these samples, tests were done only at low cavitation intensity i.e 40m/s. The results obtained at this condition were not that significantly different from samples containing the abrasive particulate filler as shown in the comparison graph in figure 45 and 46. The result for the individual samples in the as cast and machined conditions are shown in figure 35 and 36 respectively . From the above result, it seems the introduction of abrasive fillers does nott influence the erosion behaviour.

In general, it has been observed that for the two epoxy resin systems investigated, the as cast surface always performed better. However, the extent of this performance tends to diminish when the intensity of cavitation is increased as illustrated in the comparison graphs in figure 37-40. From observation studies done on the mechanism of material removal during the erosion process, no apparent difference was observed either between the two surface

conditions or between the two epoxy resin systems employed. The dominant difference on the surface topography prior to testing between the as cast and the machined surface, was the smooth surface of the as cast samples, and the rough machined markings on the machined surfaces. From the graphical results of volume loss against time, it is very evident that in all the plots, the as cast samples have the, tendency of exhibiting a greater resistance during the initial stages of the erosion process, i.e during the first four runs (lasting approximately 100 minutes) at low cavitation intensity and during the first or second run (lasting approximately 20 minutes) at high cavitation intensity. The machined samples on the other hand tend to produced a very linear plot right from the onset of material loss. From the above results, it is evident that the characteristic smooth surface of the as cast sample offer some protection or resistance against crack initiation and hence cavitation induced erosion during the incubation period and the initial stages of material removal. This sort of protection has been observed in other work, in particular in the field of corrosion erosion. It is believed that the machined surface characteristic tool markings act as stress concentration and thus aid the material removal process when exposed to cavitation.

As other investigators have observed including Chatten and Thiruvengadam (1967) and Rao.P.V,(1988) epoxy resins in general tend to have a low resistance at high cavitation intensity i.e, at

high velocity. This is generally due to the resin particles in the deforming epoxy which, despite their viscoelastic nature and high resilience, dissipate the bulk strain energy produced by cavitation and at the same time the strain energy builds up to the point at which shear yielding or tensile fracture occurs. The epoxy resin is, however, resistant to erosion at low velocities owing to the low impact stresses compared with their stress endurance limit.

Very little study has been done on the behaviour of epoxy resin subjected to induced cavitation erosion in a through flow system where cavitation is hydrodynamically simulated. Rao.V.P,(1988) has tested bulk epoxy resin in a rotating disc, and made detailed observations of the material removal process. Using scanning electron microscope, he observed that brittle failure as a result of crack propagation and interaction was the dominant mode of fracture. He also observed four unusual types of fracture which he termed as follows; i) Layered fracture, ii)Channel-like fracture, iii)Micro layer fracture and delamination, iv) Flake-like fracture. Channel-like and flake-like fracture were observed with the epoxy resins tested in this project. Although his plot of cumulative volume loss against time were similar to those presented here, his erosion rate values at a velocity of 37.3m/s were greater by a factor of 10 to what was obtained in this project at a comparable velocity. This discrepancy undoubtedly would be attributed

to the difference in testing device.

6.2 CERAMIC

Fracture of ceramics typically starts with a flaw at, or near, the surface, and hence the properties of the surface have a major influence in determining the strength of the material. In many applications the component must be made to very close tolerances which, owing to the variability associated with sintering, can only be achieved by diamond machining. Stock removal and the surface finish are influenced greatly by the production parameters i.e depth of cut, wheel balancing and dressing, and the vibrational frequency of the grinding machine. (Allor and Baker 1983. Willmann.G 1985). But from a materials perspective it is the final condition of the surface that is important, and here the action of the diamond grits have three effects; i) they create the surface roughness, ii) they introduce subsurface damage, iii) leave the surface in a state of residual stress.

6.2.1 SILICON CARBIDE

The summarised result for this specimen in all three conditions i.e, as ground, as lapped, and as fired are given in table 14. The macro-hardness values of the specimens in their various surface configurations are shown in the result

table in column 6. Here it is seen that the Vickers hardness value is the same for all surface configurations. The micro-hardness values shown in the last column seem to differ slightly with each surface finish. Although not specifically examined in detail, the general feature here was that, the sintered or as fired specimen have their micro-hardness value increased by the grinding process.

The observed damage progression or material removal process for this sample during cavitation induced erosion was given in the previous chapter (section 5.4). Damage with this sample was characteristically brittle in nature. Although there were some characteristic features relating to the various surface finishes i.e, surface roughness, (Table 12), grinding marks and surface pores, variation in the overall observed erosion damage sequence was practically non-existent.

Both micro-crack and macro-crack propagation and intersection were responsible for material removal. Most of the fractured surfaces showed features of transgranular failure as depicted in the photomicrographs of section 5.4 in chapter 5. Another failure mode which was typical with this sample was chipping. In most instances it would occur in remote region from the impact area. This phenomenon of fracture occurring at remote regions from the area of impact are well documented in rain erosion, liquid impact and in solid particles impact of hard brittle materials. Some workers have

attributed this feature to the reflection and interference of the original stress waves in the free surface of the solid (Brunton 1979).

The plots of volume loss against time for this sample are shown in figures 50-55. The general profile is as expected for a brittle material. At high cavitation intensity irrespective of surface finish, the plots are linear from the onset of mass loss (figures 50-52) with the exception of the ground specimen. Comparing the three surface finishes at 45m/s, it is evident from the result in table 14 that, the ground sample performed best, closely followed by the lapped sample, with the fired sample coming last in the ranking. The VLR of the as lapped and fired samples are 1.2 and 1.9 times greater than the ground sample respectively. The nominal incubation period for both as lapped and fired samples are not significantly different. However, compared with the ground, sample they are smaller by a factor of 0.56. Comparison plot showing their relative performances is shown in figure 56.

For test done at low cavitation intensity, i.e 40 m/s, a similar performance order to that found at 45 m/s was observed. Thus, in terms of VLR, the ground sample was best, followed by the as lapped then as fired. The cumulative volume loss against time graphs for the above samples are shown in Figures 53-55. The VLR for the fired sample is 3 times greater

than that of the ground sample and 2 times that of the lapped sample. Comparison plot of the three surface finishes are shown in figure 57.

Plots of cumulative erosion rate versus time for the three surface conditions are shown in figure 71-73. It is seen that they all tend to be of the same shape, exhibiting incubation period, acceleration period and steady state period. It was observed here that a polynomial of the third order (i.e degree 3) tend to produced the best fitting curve with a 98% of residuals about mean explained . The above characteristic curves conform to the pattern reported by Hobbs (1967) and Plesset and Devine (1966).

6.2.2 SILICON NITRIDE

The summarised results for silicon nitride is given in table 15 for test at both high and low cavitation intensities. Also in the above table are values of macro and micro-hardness for the various surface finishes. The hot isostatic packing (HIP) sample had a larger macro-hardness value . However, the micro-hardness value did not differ very much amongst the various surface finishes as shown in column 7 in table 2.

The erosion characteristics of this material has been elucidated in the previous chapter. It was observed that, the various surface topography ascribed by the finishing processes did

not have any marked effect as far as material removal was concerned. For all three surface conditions tested, numerous impact by the cavitation jets were required before any perceptible damage occurred. Thus extensive plastic deformation was evident prior to material removal.

Though brittle fracture was noted to be main mode of failure during the erosion process, initial pits formation however were akin to those observed in metal alloys . This was very evident in pits formed during the incubation period and the initial stages of material removal. The clouding effect of the cavitation zone with tiny little depressions which led eventually to pit formation is a phenomenon common with ductile metal alloys. This was very much evident here. The pits were observed to possess rims similar to those found in metal alloys. The aforementioned ductile process however, became less dominant as exposure time increases. It was observed that as material removal progresses, the failure mode in the central cavitation zone predominantly became brittle. As the optical micrograph in figure 107f depicts, grain boundaries are clearly visible together with signs of intergranular fracture.

The plots of cumulative volume loss against time for silicon nitride in all three surface conditions are given in figures 58-63. For tests done at 45 m/s, it is readily seen in figures 58-60 that there wasn't that much difference between them. Comparatively however, the as ground sample seems to have performed best. It

VLR value is smaller by a factor of 0.8 and 0.6 compared with the as fired and the as lapped samples respectively. In a similarly way to their VLR values, their NIP values did not differ very much. They were 133, 135 and 138 minutes for as lapped, as ground and as fired samples respectively.

At low cavitation intensity, only two surface finishes were tested. These were as ground and as lapped. The as fired sample unfortunately got broken. For these two samples, their comparative performance were almost identical. The differences between their VLR and NIP values were 5% and 0.5% respectively. This is clearly shown in the comparison graph shown in Fig.(61). The graphs for the individual samples shown in Fig.(62) and Fig.(63).

Comparing the performances of the ground sample "hot pressed" and the " hot isostatic packing" (HIP) it is seen that, at high cavitation intensity the HIP sample seems to have a slight edge as shown in the comparison graph figure 64 . The VLR for the HIP and hot pressed are 1.06 and 1.2 mm^3 /hr. respectively. Their NIP values are 158 minutes for the HIP sample and 135 minutes for the hot pressed sample. At low cavitation intensity the hot pressed sample performed better as shown in the comparison graph in figure 65. Generally the performance differences at both high and low cavitation intensities for the two ground samples were not significantly different, although one would have expected

the HIP sample with its more superior dense structure, i.e, less porous, to have performed significantly better. From the above result the production process of hot press and hot isostatic packing does not seem to influence the erosion behaviour significantly .

6.2.3 COMPARISON BETWEEN SILICON CARBIDE AND SILICON NITRIDE

Table 15 summarises the performance between silicon carbide and silicon nitride. And Fig.66-70 show graphically the performance differences between the various surface finishes. At low cavitation intensity , the VLR for silicon carbide in the as ground condition is 3.6 times larger than silicon nitride. In the as lapped condition it is 5 times greater. At this low velocity, the NIP for silicon nitride in both the ground and lapped condition is 2.5 times greater than silicon carbide. Figure 66 and 67 illustrate the above performance graphically.

At high cavitation intensity i.e at 45 m/s the performance of silicon nitride is even better, as illustrated graphically in Figures 68-70. In the ground condition the VLR and NIP values for silicon nitride were 3.8 mm^3 /hr and 135 minutes respectively. The corresponding values for silicon carbide were 122.6 mm^3 /hr and 73 minutes respectively. In terms of the VLR

values, silicon carbide erosion rate is 6 times greater than that of silicon nitride and its nominal incubation period is smaller by a factor of 1.8 . In the lapped condition, the VLR of silicon nitride was 6.4 mm^3 /hr and the NIP was 133 minutes. The corresponding value for silicon carbide were 27.8 mm^3 /hr and 40 minutes respectively. With this surface condition, the erosion rate for silicon carbide was 4.3 times greater than that of silicon nitride and it NIP was smaller by a factor of 3.3. Maximun performance difference between the two silicon base ceramics was encountered with the as fired samples. Here the volume loss rate of silicon carbide was 10 times greater than that of silicon nitride and it nominal incubation period was smaller by a factor of 3.3 .

The above performances could easily have been predicted qualitatively from the failure mode observed during testing. The brittle nature of failure exhibited by silicon carbide samples, was quite conducive to high rate of material removal or erosion rate. The characteristic lateral cracking with eventual chipping of material common with silicon carbide was very much absent with silicon nitride. Silicon nitride with its high strength, comparable low macro and micro hardness values, moderately low modulus of elasticity, and high fracture toughness, proved to be better in resisting cavitation attack.

Comparing in general the performances between the

various surface finishes, it is seen that in both silicon nitride and silicon carbide samples, the as ground samples performed best in both high and low cavitation intensities. When one looks at the micro-hardness values in the result tables (Table 9&10), it is seen that, the ground samples have the highest value, then followed by the lapped samples, with the as fired or sintered samples having the lowest. It then follows from the above observation that, the fired or sintered specimens had their surface hardness increased by the grinding process. Tomlinson (1990) investigating the effect of grinding, lapping and various surface treatment on the strength of silicon nitride also found that the strength of the sintered specimen was increased as a result of grinding. Thus, the better performance of the ground samples could generally be attributed to extensive plastic deformation in their surfaces as a result of the abrasive finishing process.

The lapped sample was the next surface finish in the performance ranking. It is seen from the micro-hardness measurements that values for the lapped surfaces are slightly lower than that of the ground samples. This would indicate that, the lapping process which is normally performed after grinding, tends to reduce the micro hardness of the work hardened ground surface. Other investigators including Allor and Baker (1983) have found the strength of silicon nitride to be slightly reduced after lapping. Tomlinson (1990) on the other hand

observed the reverse with the same material. There is no apparent explanation for the above anomalies. From the surface roughness parameter in table 10, it is seen that the centre line average values show no discernible trend with respect to erosion rate of the various surface finishes.

Using the two test velocities i.e, 40 and 45 m/s the velocity exponent for both silicon carbide and silicon nitride were computed using equation 19. These are shown in table 12b. An average of 22.38 and 21.75 were obtained for both silicon carbide and silicon nitride respectively, for the three surface conditions. These values seem relatively high compared with other classes of materials. However, it should be noted that for a more accurate result more than two data points will be required.

6.3 COMPOSITE

The composite materials tested in this program were glass reinforced plastic (GRP), and Fybroc (vinyl ester with glass reinforcement). Their general formation is given in Table 5. Here, it is seen that they both utilised glass as the reinforcing element. The structure and fibre orientation of the above composites are however different.

From observational studies on material removal mechanism with the composites, it was observed that the general surface damage was essentially similar to that observed with bulk epoxy resins, but with damage concentrated at the discontinuities characteristic of composites i.e. voids, fibre intersections with the surface, and cracks associated with the fibre. Compressive failure was also noted, it was related to stress concentrations arising from differential strain between the matrix and fibre. The damage included fractures, debonding, and matrix failure, each on a fine microscopic scale. Delamination was another mode of failure prevalent with the GRP samples.Gorham and Field (1976) ascribed the above phenomenon to the action of shear stresses set up by bending, by compression of the soft matrix between the hard layers, and by stress wave propagation through the fibres. They associated tensile stresses contributing to delamination with the divergence of the main compression waves as it moved in to

the composite and with its reflection at discontinuities and at the free surface.

The summarised result of the above composite materials are given in table 16. The plots of cumulative volume loss against time from where these results were obtained are shown in figures 77-80 for the GRP samples, and in figure 83-84 for the Fybroc samples. Figure 77 shows the plot obtained at 45 m/s with the GRP specimen. It is seen that, there is a rapid increase in material removal rate during the first 60 minutes, after which there is a slight fall off in the rate. This feature was also observed for test done at 40 m/s as shown in figure 78. With further reduction in cavitation intensity i.e, at 35 m/s the curve obtained was linear throughout the test duration as shown in figure 79. A further reduction in cavitation intensity ,i.e 30 m/s, the plot shown in figure 80 was obtained. Here the characteristic plot of volume loss against time exhibiting a nominal incubation period is evident. For tests at high cavitation intensities, i.e 45 and 40 m/s where two slopes were encountered, the regression analysis to obtain the VLR value were done with data corresponding to the higher slope as shown in the plots . Generally it is seen that with the GRP samples, the characteristic plot of cumulative volume loss against time tend to have a concave profile at high cavitation intensity, which then tend to be linear at intermediate intensity. At low cavitation intensity, the profile tends to be convex.

The above feature could be attributed to the damage sustained on the specimen surface from onset of volume loss to completion of test. For it was observed that, at high cavitation intensity, i.e, at 45 and 40 m/s, the composite did not offer much of a resistance to the cavitation forces. As early as the first run, it was observed that, mass loss had occurred right down to the third ply. With a further three more runs the cavitation zone was fully established. Erosion damage had penetrated right down to the penultimate ply in a total of eight, in a sort of tunnelling mode. Subsequent runs did not significantly alter the damaged profile on the specimen, indicating very little mass loss. The already heavily pitted surface, together with liquid trapped in the tunnel like crater, tend to cushion subsequent micro jets and hence produced the reduction in damage rate. At intermediate velocity (35m/s) where the slope was linear throughout the test duration, the composite did offer some resistance to the reduced cavitation attack. Here it was observed during testing that, almost equal amount of material was removed after each run till completion and that the damage was limited to the third ply . Here the damaged surface had little or no effect on subsequent runs since it was not heavily pitted. Using the four velocities employed with the GRP samples i.e 45, 40, 35, and 30m/s, the variation of erosion rate against velocity was ascertained. The plot of erosion rate versus velocity is shown

in figure 85 The use of log scales resulted in the data lying on a straight line and using least square regression on the data yields the relationship for GRP

$$VLR \alpha U^{6.14} \qquad 21$$

The 95% confidence limits on the above index in the VLR equation is $\pm$ 29.4% . The above exponent for GRP which is a lot more accurate is slightly less than the average of 9.3 found for bulk epoxy resins. Hence the above equation could be used to make judicious extrapolations if required.

Some workers have proposed that VLR varies with $(U-U_o)^n$ suggesting that there is a threshold velocity, U_o below which no damage occurs. Grant (1984) used such an equation with a wide range of values for U_o but he found the simple power law in equation 21 to give the highest correlation coefficients. Using an identical rig he found the exponent for both perspex and aluminium to be 9.0 and 6.92 respectively.

Figure 82 shows a typical plot of erosion rate against time for GRP tested at both 40 and 45 m/s respectively. Here it is seen that at high cavitation intensity, the erosion rate rises rapidly to a maximum and then drops. At low intensity the peak exhibited at higher velocity is completely absent. Here erosion rate rises to a maximum and persists at this value for some

time. The above thus emphasize the fact that, test condition or cavitation intensity should be stipulated when mentioning erosion rate characteristic curves.

The Fybroc samples were tested at velocities of 40 and 35 m/s respectively. Both plots as shown in figure 83 and 84 are very linear throughout the test duration. Figure 85 shows the characteristic plot of erosion rate against time for the fybroc sample. It is seen to be very similar in all respects to that of the GRP sample at a comparable velocity. Both exhibit a peak erosion rate and deceleration.

From the result in table 16 it is seen that at a comparable velocity of 40 m/s the Fybroc sample performed better than the GRP sample, i.e the VLR of the GRP is greater by a factor of 1.67. At a reduced throat velocity of 35 m/s, the ranking did not change, however the performance difference with regard to the VLR values is reduced to a factor of 1.32. The performance difference at the above two velocities are shown in the comparison graphs in figure 86 and 87. As seen also from the table 16, the NIP values for both GRP and Fybroc for the two test conditions are very similar.

Although very little was found in the literature as regards to testing of composite for cavitation erosion resistance, some work have been done on erosion by liquid drops (Schmitt 1974). Here it has been observed that the beneficial effect of strengthening brittle materials by

reinforcement, results in improved subsonic (subsonic flight in a rainy environmemt) erosion resistance, because the presence of the fibre reduces chunking out and breakage in to small pieces by providing a discontinuous path for shock transmission through the material.

For a given glass fibre volume concentration, the two-dimensional laminate construction would provide better reinforcement than the random chopped glass fibre because it provides a more continuous network to reduce the shock transmission. However, the result as mentioned above was completely the opposite. The random chopped fibre of Fybroc performed slightly better than the laminated GRP . Another effect which might have influence the result was the fact that the GRP samples had visible pores on their surfaces which ultimately led to a high void content, although this was not specifically investigated. The void content of a composite can significantly influence its erosion behavior because the high void content composite possesses lower strength properties. Schmitt (1974) found that the morphology of the bulk resin appears to strongly influence the erosion behaviour. Although not specifically investigated, this might give some evidence of the erosion resistance or performance of the two composites examined since both the GRP and Fybroc samples employed epoxy resin and vinyl ester respectively as matrices.

6.4 METAL ALLOYS

Their general test conditions and nominal compositions are given in Table 6a and 6b. As reflected in the above tables, there was no systematic approach in selecting the materials since they were accrued from a number of independent industrial firms and research institutions with varying objectives.

With some of the alloys, damage progression studies were made as mentioned earlier in the previous chapter. These studies were done at high cavitation intensity for the simple reason of the time scale involved.

For the non -ferrous alloys i.e, cupro-nickel and single phase brass, the process of initial damage and subsequent material removal were very similar. With increased cavitation attack the reflectivity of the surface gradually reduces indicating an increase of pit size and number. The formation of pits does not appear to be associated with the grain boundaries or other structural or metallurgical features except for marks from the sample's preparation. Generally, it was observed that material removal was by a ductile mode, i.e ductile tearing. Final damaged surface of the above samples using the scanning electron microscope revealed a dimpled fracture surface, resulting

from microvoid growth and coalescence. Rao et al (1982) observed similar features while testing with a rotating disc device.

The cavitation damage data plotted as a function of time for both cupro-nickel and the single phase brass are shown in Figure 90 and 93 respectively. The plot for cupro-nickel in Figure 90 shows that the material removal rate was almost constant throughout the duration of the test. The single phase brass on the other hand depicts the characteristic S-shape curve, an indication that it was more resistant compared with the cupro-nickel during the early stages of erosion.

Figure 90A is a dublication or repeated test for cupro-nickel. Here the data analysed in figure 90 is compared with data from another specimen under identical testing condition. It is clearly seen from the comparative graph that the degree of repeatability was quite high. Quantitatively the percentage difference between the two VLR values was less then 7% . Similar to figure 90a, figure 93a also shows the high degree of repeatability for the test in this caes with the aluminum alloy specimen.

With the recrystalised annealed aluminium sample, damage was characteristically ductile as expected. Very early damage observed consisted of isolated depressions at the centre of which are deeper, faceted pits (fig.111a). Hansson and Morch (1977) have also observed these features, and they attributed it to the jet impact of individual bubbles collapsing close to the

surface. As the time of exposure is increased, the density of these pits increases until they overlap, and the surface topography then resembles that shown in figure 115b. After some time, the deformation is almost exclusively by crater formation. Material loss during this stage occurs by necking of the rims of the craters.

The plot of volume loss against time for this specimen is shown in Figure 89. In the above plot, it is very evident that the shape of the curve does not quite match the characteristic S-shape. It is seen that, there is an initial surge in volume loss which produces a higher slope during the first 100 minutes, and immediately after this period, the slope reduces. This feature was also very evident with the GRP samples tested at both 40 and 45 m/s.The governing mechanism for this initial material removal is still unclear , perhaps it involves the removal of initial soft spot, inclusions or other imperfections on the material surface. However, a plausible explanation for the reduced slope could be attributed to the fact that, the hydrodynamic effect over the deeply damaged surface caused during the initial stages, significantly diminished the intensity of subsequent cavitation forces, hence the lower slope. Plesset and Devine (1966) have shown photographically that there is a reduction in bubble cloud intensity as a consequence of hydrodynamic effects over deeply damage surface. The VLR value as shown in Figure 89 has been obtained using regression analysis

with the data in the higher slope region of the graph . Figure 89B shows a duplication test plot for the above specimen.

With Armco iron, it was observed that two different modes of failure occur. Iron exhibits a high degree of deformation predominantly by twinning, which is also a characteristic of high strain rates. The first detectable material loss occurs by a ductile mechanism similar to those produced in cupro-nickel and brass. This loss is initiated at grain boundaries, and results in the severe surface distortion as shown in figure 114c. The secondary mode of material removal which results in a greater rate of erosion, is the formation of flat bottom pits by cleavage mechanism. These usually initiate at grain boundaries and propagate rapidly across the grain. Erdmann-Jesnitzer et al. (1974) also observed both brittle and ductile mode of failure in Armco iron. Other workers have found out that in mild steel, the ferrite phase is preferentially eroded (Schulmeister,1965; Wade and Preece,1978) and is little influenced by the presence of carbide unless the phases are in a very fine dispersed form.

The plot of volume loss versus time for armco iron is shown in figure 91. It is clearly seen in this plot that armco iron under went a substantial amount of cold working during the initial stages of cavitation. This is borne out in its nominal incubation period as seen in figure 91 above.

For the two carbon steels tested in the program,

there was not much difference in the observed material removal process during the initial stages of erosion. However, as shown in the final damage photomicrographs in Figure 115a and b, the quenched sample (45) exhibits both ductile tearing and intergranular fracture on different sites on the damage surface . The annealed sample (AISI1020) exhibits ductile tearing (fig.115c). The heat treatment performed on the former would probably account for this discrepancy. Generally, the material removal processes in the above carbon steels were very similar to those observed in Armco iron. This has been attributed to the fact that, carbide in the low carbon steels tested was not finely dispersed (Schulmeister 1965,; Wade and Preece 1978). Although not specifically investigated other workers have found that in plain carbon steels similar to the ones employed here, the proeutectoid ferrite eroded first, followed by the eutectoid ferrite.(Herbert 1965) The plot of volume loss against time for the above two carbon steel specimens are shown in Figures 88 and 94. They both exhibit typical erosion curves in that clearly defined absolute and nominal incubation period with a very linear steady state region are evident.

Observation during damage progression for the acid resistant stainless steel showed damage similar to those of carbon steel but to a lesser degree. There was a substantially prolonged period before any perceptible plastic deformation was

observed on the surface. This was not too surprising since the austenitic matrix has a high propensity to strain hardening. Scanning electron micrographs taken inside the damaged region revealed a dual mode of fracture, i.e, both ductile and brittle failure. The ductile failure was akin to ductile rupture and the brittle failure was intergranular in nature.

The plot of volume loss against time for the above specimen is shown in Figure 95. A typical feature of this class of material is it susceptibility to work harden . This is very much in evidence in the extended nominal incubation period as seen in the figure above. The steady state period that immediately follows, shows a constant removal rate.

The tool steel sample in which observations were made of material removal process was the CPM10V i.e, manufactured from crucible particle metallurgy and air hardened. Unlike carbon and stainless steels, the initial damage for tool steel, were very shallow and non-circular in shape. The pits were totally void of the characteristic raised rims found in iron and low carbon steel. This was obviously an indication of brittle failure. It was observed that, subsequent material removal came about as a result of macro cracks interaction as they propagate from the edges of the pits and coalesce.

The plot of volume loss versus time for tool steel is shown in Figure 98. From the above figure, two distinct slopes are

evident. Initial mass loss which appeared to result from macro cracks interaction was obviously responsible for the first smaller slope. As seen in the above figure this lasted for just under 200 minutes. There after, an increase in the slope occurs. This was essentially constant throughout the remainder of the test. As seen in the figure, values for VLR and NIP were computed using this higher slope region.

Surface treatment would seem to be a logical solution to afford protection from cavitation induced erosion. This is borne out by the fact that, cavitation induced damage occurs predominantly in the surface layers of metals and alloys. Thus any chemical, mechanical or heat treatment process aimed at increasing the hardness of the surface should enhance erosion resistance.

Nitrided steel which utilised nitralloy steel as the base metal, was employed in this project. It was observed during the damage progression sequence that, pits occuring during the initial stages of damage were in all respects similar to those observed in tool steel. They were very shallow and irregular in shape as shown in Figure 118a. Here also initial mass loss was associated with macro-crack propagation and subsequent intersection from the edges of the pits. The micro- cracks and the shallow pits would then coalesce on further exposure to cover the entire cavitation zone. After this stage it was observed that, subsequent pits

formed on this highly deformed surface, turn to be relatively more penetrative in depth compared with those formed during the initial stages of material removal. A plausible explanation for the above feature would be that, during the initial stages of cavitation attack, the very brittle skin of the hard nitrided surface failed in a predominantly brittle mode hence the shallow pits. Once the entire cavitation zone was completely damaged, i.e the hard skin was removed, the softer ductile layer was exposed. And the response to the cavitation attack here was very much ductile in nature hence the deeper pits.

Spalling was also a very special feature common with the nitrided steel. Very often after each run it was observed that, fractures or material removal had occurred in regions remote from the impact area. These were randomly distributed and of various shapes and sizes. Apart from the obvious increase in mass loss, spalling produced a wavy effect on the erosion curve as shown in Figure 96. If comparison is made with the result obtained for the test done at low cavitation intensity (i.e 40 m/s) where spalling was totally absent, the result could hardly be more contrasted as Figure 97 demonstrates. It is clearly seen in this plot that, from the end of the incubation period to completion of test, the slope is essentially constant.

Table 17 lists the results for all the metal alloys tested in this project. In the above table the VLR, NIP, Hv and Hv

values of the tested samples are given, thus enabling easy comparison to be made.

In the above table entry number 1 to 5 gives the result obtained for the aluminium alloy samples tested in the project. Considering the results for test done at 45 m/s i.e, at high cavitation intensity, it is clearly seen that, the solution treated aged alloys (HE30, HE15, HE9) have superior erosion resistance compared with the 99.9% pure SIC and the annealed PA2. The average VLR of the SIC and PA2 samples were 15 and 9 times greater respectively when compared with the aged hardened samples. The better performance of the aged samples is due primarily to the fine precipitates of Mg_2Si which strengthened the alloy by increasing resistance to slip. Thus aluminium alloys which are amenable to precipitation hardening heat treatment are better in resisting cavitation. One should however, be very careful with the heat treatment process. Thompson et al (1989) investigating the effect of precipitation hardening with 6061 aluminium found that, the mechanical properties of yield strength, tensile strength and elongation vary very much with heat treatment. For a given temperature at a comparatively low soaking time, the fcc structure of aluminium is strengthened by extremely fine precipitates which tends to increase resistance to slip. When the soaking time is increased at the same temperature, the precipitates coalesce into much coarser particles, which then becomes

slip sites leading to reduced strength. They observed almost 100% changes in erosion rate as a result of changes in age-hardening. Thus in studies of cavitation erosion using aluminium alloys, it seems vital to use metallurgical controlled materials to insure reproducibility of results.

Entries number 7 and 11 represent the single copper based alloys. Here it is seen that the single phase brass performed better than the 90/10 cupro-nickel of comparable hardness. The VLR for the former is 7.98 mm^3 /hr and for the latter is 9.34 mm^3 /hr. The nominal incubation period were 71.7 and 35.8 minutes for brass and cupro-nickel respectively. The above results tend to confirm the hypothesis first proposed by Woodford and Beattie (1971) that a planner slip mode resulting from a low stacking fault energy is beneficial for erosion resistance. Dakshinamoorthy (1975) testing the above two alloys in a vibrating device also observed a similar performance.

Results for carbon steels tested are given in entry 9 and 10 in the above table. The standard AISI1020 and carbon steel hyper-quenched were employed. Performance wise the VLR for the hyper-quenched sample is 1.35 mm^3/hr while that of AISI1020 is 4.5 mm^3 /hr. Their nominal incubation periods were 331 and 134 minutes for hyper-quenched and annealed carbon steel respectively. From their nominal

composition in Table 6b, it is seen that the above two metal alloys have very similar chemical composition. Thus the improved erosion characteristics of the hyper-quenched steel will obviously be attributed to heat treatment.

When the performance of nitralloy and nitrided steel are evaluated, the effect of nitriding becomes very evident. Nitralloy is the base metal in which the nitriding process was performed. From the result in Table 17 the VLR for nitrided steel at high cavitation intensity is 0.232 mm^3/hr while that of nitralloy is 1.14 mm^3/hr. Thus the nitralloy VLR value is greater by a factor of 5. The nominal incubation period for both nitrided steel and nitralloy were 99 and 209 minutes respectively. Here though the nominal incubation period for nitrided steel is twice less than the base metal nitralloy. Similar performances were observed also at reduced cavitation intensity (40m/s), i.e, the VLR for nitralloy is 7 times greater than nitrided steel and it nominal incubation period is larger by a factor of 1.7. The general inference here is that, nitriding overwhelmingly tends to reduce the overall material removal rate, but has little if not a detrimental effect on the incubation period. Mousson (1937) found that the effect of nitriding could be detrimental. More recently Protheroe (1977) found that nitriding did improved the life of parts exposed to cavitation in hydraulic pump valves . The above discrepancies with Mousson's results is probably due to improvement in nitriding

techniques over the intervening years.

Entries number 15 and 16 in the above Table 17 gives the result for both tool steels, i.e, CPM10V and M4. Unlike the standard M4 grade CPM10V is manufactured by a crucible particle metallurgy process. This produces a material with a simple microstructure which is characterised by spherical uniformly distributed carbides in a medium alloy steel matrix. The VLR of the CPM10V and M4 were 0.46 and 0.65 mm^3/hr respectively. Their nominal incubation periods were 147 minutes for CPM10V and 317 minutes for M4. Apart from the slightly improved nominal incubation period of the M4 grade, the performance difference between the two was not significant.

In Figure 99, the cavitation data of cumulative volume loss with corresponding cumulative time from the best performing samples in each class of material i.e, ceramic, plastic, composite and a selected number of metal alloys are shown for graphical comparison. It is seen from the above plot that, the GRP sample was the least resistant and nitrided steel was the most resistant. It is also seen that the resistance of silicon nitride is comparable with that of cast stainless steel. Epoxy resin is seen to have performed better than aluminium, and more interestingly than the reinforced GRP version. Representation in a tabulated form of the above materials is shown in Table 18. Here their VLR values

are listed in an ascending order for easy comparison.

For all the engineeering materials tested in this research project, it is very evident that their erosion resistances or erosion rates are strongly influenced by their mechanical properties. However, attempt to correlate the above two parameters have not been very successful. Mousson (1937) testing over 266 different alloys concluded that there is some consistent trend of increased erosion resistant with inceased hardness. This assertion was verified with the vast amount of data accrued in this project. (See Appendix 6.1)

Using the important independent parameters in cavitation erosion which are fluid velocity, fluid density, system pressure above saturated vapour pressure, length scale and some suitable paramater characterising the material property in this case hardness, together with the dependent parameters, either VLR and NIP and employing dimensional analysis, it was observed that, VLR and hardness (Hv) were inversely correlated generally for materials with Hv below 500. This broadly corresponded to the non-ferrous metals, steels, plastics, and the composites. Above this value of hardness lies another group which are not so well correlated. These were the ceramics and the hardened steels(Appendix 6.1 fig7). The power law obtained for the former group was

$$VLR = 1.314 * 10^{5} (Hv)^{-2.26} \text{ mm/hr.}$$

The 95% confidence limit on the index was 0.36. This formula could be

used to give judicious guide to performance for most materials.

The corresponding variation between NIP and Hv showed no decernable trend as seen in figure 8 in Appendix 6.1. The general poor correlation for NIP was atrributed to the inherent error in estimating the intercept in the regression analysis

Generally it has been observed that in all three classes of materials examined the characteristic "S" shape curve of volume loss versus time though evident, tend to differ slightly with individual materials. In the extreme case both GRP and alumunium alloy (PA2) at high cavitation intensity exhibited no acceleration region. They showed relatively short steady state period with extended deceleration regions. As seen also in Table 18 it does not necessarily follows that materials with relatively low cavitation erosion rate will have high nominal incubation periods, both parameters should be examined separately if need be.

APPENDIX 6.1

Cavitation erosion of engineering materials

P A LUSH, BSc, PhD, CEng, FRAeS and A E EWUNKEM, BSc, MSc
Department of Mechanical Engineering and Aeronautics, City University, London

SYNOPSIS Over the past few years in the Centre a number of engineering materials have been tested for cavitation erosion under nominally identical conditions of hydro-dynamically induced cavitation. The total number of materials tested has been about 30 and the purpose of this paper is to compare and contrast the results obtained. The study emulates the work of Mousson in the 1930's who subjected some 200 materials to hydrodynamic cavitation under standard conditions, and measured volume loss over a 16 hour period. In the present work we give steady state volume loss rate (VLR) and nominal incubation period (NIP) The cavitation is produced by a 60° wedge inducer placed in a venturi-type channel 30mm x 15mm in cross-section. The specimen which measures 30mm x 30mm x 6mm thick is flush mounted just downstream of the inducer. Tests are done at constant throat velocities of either 45 m/s or 40 m/s at a cavitation number corresponding to maximum erosion or noise intensity. The materials tested range from cast iron, steels and aluminium alloys to epoxy resins and silicon carbides and nitrides. Comparisons between such a wide range of materials are not easy but it has been found that correlations based on hardness (HV) are useful; this also agrees with Mousson's results which have been analysed and are presented for comparison.

1. INTRODUCTION

Although good design can reduce the severity of cavitation, frequently the risk of erosion is accepted and the damage minimised by using erosion resistant materials. The choice of a suitable material is usually made on the basis of some comparative test carried out under the same conditions as a control material, whose cavitation erosion resistance in service is known. In order to reduce the test time, the test will be accelerated by using more severe cavitation conditions.

The accelerated erosion testing has commonly been done using a vibratory testing apparatus, which has the great virtues of convenience and speed of operation. However such tests may produce anomalies because the cavitation is not hydrodynamically induced and because the cavitation intensity is much more severe than service conditions. An alternative to the vibratory test is the hydrodynamically induced cavitation produced in a venturi-type channel, usually placed in a recirculating flow loop. The cavitation intensity is increased to bring testing times down to acceptable levels by using a wedge-shaped or cylindrical inducer and by employing a fairly high (throat) velocity in the region of 30 to 50 m/s.

The rate of erosion measured in this way is unlikely to be equivalent to the erosion rate encountered in service and so comparative testing is necessary. There is a need for a consistent set of comparative test data encompassing a range of engineering materials to assist in the choice of a suitable material in the early stages of a design.

The only consistent set of erosion data to the author's knowledge for engineering materials, carried out under hydrodynamically induced cavitation, was produced by Mousson[1] in the 1930's. He subjected some 200 materials to cavitation attack under standard conditions and measured volume loss in a 16 hour period. Although very comprehensive, the results are unsatisfactory because they take no account of incubation period and cannot be used to obtain the steady state erosion rate. Measurement of these is the minimum amount of information required. The actual erosion characteristics are more complicated in general since there exists a period of accelerating erosion rate between the incubation period and steady state erosion rate and also a period of declining erosion rate at high exposure times. The acceleration period can be accounted for approximately by using the nominal incubation period (NIP) and steady state volume loss rate (VLR). These are defined respectively by the intercept on the time-axis and the slope of a linear regression line for the variation of the cumulative volume loss with time.

This information has been obtained over the past few years at City University for about 30 materials under nominally identical conditions of hydrodynamically induced cavitation. In fact the cavitation number has been maintained constant and throat velocity varied to suit the type of material to be tested. Nevertheless the bulk of the tests have been done at either 45 m/s or 40 m/s. This data is presented in tabular form for ease of comparison. It is possible to use dimensional analysis to correct the data to a common base so that all data can be compared together; the results of this are presented graphically and also compared with some of Mousson's data.

2. THEORETICAL CONSIDERATION

In general the important independent parameters in cavitation erosion are fluid velocity, U, fluid density, ρ, system pressure above saturated vapour pressure, length scale, ℓ, and some suitable parameters characterising the material properties such as hardness, H, or possibly fracture toughness. The dependent parameters are chosen to be nominal incubation period (NIP) and steady state volume loss rate (VLR). Although weight or mass loss is actually measured, neither gravitational nor inertial effects are reckoned to be important and the amount of material removed is properly described by its volume.

After carrying out the dimensional analysis, the following relations are deduced

$$\frac{(VLR)}{\ell^2 U} = f\left(\frac{H}{\rho U^2} , \sigma \right) \qquad (1)$$

$$\frac{(NIP)U}{\ell} = g\left(\frac{H}{\rho U^2} , \sigma \right) \qquad (2)$$

where σ is the cavitation number of the flow. Strictly, a further parameter should be introduced involving the number of nuclei or bubbles per unit fluid volume, n, leading to the additional non-dimensional group, $n\ell^3$; however since the length scale is not changed, it will not be considered further. Also since the tests were all done at maximum erosion or noise intensity, which happens to correspond to a constant cavitation number, this also can be omitted from equations (1) and (2). These relations have been used to correct the data to a common fluid velocity, viz. 40 m/s as follows

$$\left.\begin{aligned} VLR^{*} &= (VLR)\frac{40}{U} \\ NIP^{*} &= (NIP)\frac{U}{40} \\ HV^{*} &= HV\left(\frac{40}{U}\right)^2 \end{aligned}\right\} \qquad (3)$$

where HV is Vickers hardness and the starred parameters are the equivalent values at a fluid velocity of 40 m/s.

These reduced variables allow data for VLR and NIP at different velocities to be plotted against the same correlating parameter, i.e. reduced hardness, HV^{*}. Any correlation as a power law will give both the velocity index and the index for HV.

3. METHOD OF TEST

3.1 The test loop

The test sample was placed in the purpose-built cavitation erosion recirculating flow rig filled with tap water (see fig.1). The test loop consisted essentially of a 22kW Worthington Simpson 2DDM4 Monobloc 2-stage pump connected between high and low pressure vessels. The working section was contained in a pipe also connected between these two vessels. Flow was controlled by means of a bypass valve inserted in a second pipe connected in parallel. The pressure vessels were sealed and the rig was pressurised via a flexible diaphragm using a compressed air cylinder and pressure regulator. Independent control of pressure and flow rate enabled operation of the rig at fixed values of cavitation number and fluid velocity.

The loop was cooled by bypassing a small quantity of flow through a shell and tube heat exchanger. The secondary coolant flow was circulated to a fan-assisted heat exchanger located outside the building. When operating continuously it was found that a working fluid temperature of approximately 40°C could be maintained. A further small diameter bypass was provided to allow continuous filtering of the water in the test loop.

The pipework in the rig including the leg containing the working section was 50mm (2") diameter. The working section consisted of a parallel-sided channel 30mm x 15mm in cross section and 300mm long (see fig.2). It was provided with a smooth round-to-rectangular contraction upstream and a gradually tapering diffuser downstream. A cruciform anti-swirl device was inserted in the pipe upstream of the working section.

Static pressure in the working section was measured using a wall pressure tapping just downstream of the contraction and the flow rate was determined by measuring the differential pressure across the contraction. The pressures were measured using a Platon type P25LA absolute pressure transducer and type P25LD differential pressure transducer. Temperature in the rig was determined using two thermocouples, one acting as cold junction. Air content was checked periodically using a Van Slyke apparatus and was always found to be close to saturation.

3.2 The test section

Cavitation is induced by placing a 60° triangular wedge of side 15mm in the working section with one edge facing upstream (see fig.2). The wedge produces a blockage of nominally 50%, but actually somewhat more than this owing to the presence of a vena contracta. Cavitation is produced downstream of each trailing edge and the flow closely resembles that produced by a circular cylinder, in that there is discrete vortex shedding giving an oscillatory flow at about 600Hz for a velocity of 45m/s. However the advantage of using a wedge instead of a cylinder is that no erosion is produced on the inducer itself and it is free of Reynolds Number effects. At a cavitation number corresponding to maximum erosion rate and incidentally also maximum noise level, the zone of most intense cavitation is around 30mm long. Consequently the test specimen, which is flush mounted, measures 30mm x 30mm on the exposed face and it is held in place by a 30° chamfer at the trailing edge and by being overlapped about 1mm by the inducer at the leading edge. The overall dimensions of the specimen are approximately 33.5mm x 30mm x 6mm thick (see Fig 3).

3.3 Cavitation condition

Tests are done at a constant cavitation number corresponding to maximum erosion rate at a given fluid velocity. This ensures that the erosion always takes place in the same region on the specimen. In order to compensate for the large blockage produced by the inducer, fluid velocity and cavitation number are defined in terms of throat conditions. The amount of blockage is determined from the conditions at choking and this enables throat velocity, U_T, and cavitation number, σ_T to be determined as follows

$$U_T = U_o\sqrt{1 + \sigma_{o_{ch}}} \qquad (4)$$

$$\sigma_T = \frac{\sigma_o - \sigma_{o_{ch}}}{1 + \sigma_{o_{ch}}} \qquad (5)$$

where subscript o corresponds to flow conditions upstream of the inducer and $\sigma_{o_{ch}}$ is cavitation number at choking. It is presumed that the blockage does not change substantially with either cavitation number or velocity. The throat cavitation number corresponding to maximum erosion rate is found to be 0.09.

The choking cavitation number is checked before each run and this allows compensation for small variations caused by removing and remounting the specimen for weighing. In effect the rig is always run at a fixed margin above choking. The intensity of the cavitation is varied by changing the throat velocity. Typically this is chosen to be either 45m/s or 40m/s depending on the likely erosion resistance of the test material. For weak materials velocities down to 30m/s can be chosen. For direct comparisons, the same throat velocity should be chosen but data may be compared indirectly using the normalising scheme outlined in section 2.

In order to assist in maintaining a constant cavitation number during a run, the cavitation noise is monitored using an acoustic emissions transducer (Dunegan type Micro-30) simply mounted on the tunnel wall and connected directly to an oscilloscope and true RMS meter (Hewlett Packard type). The rig can easily be fine controlled to keep the noise at maximum.

3.4 Test procedure

Before the start of each run, the rig is operated in a choked condition to determine the blockage. The specimen is in no danger of eroding during this process because the cavity collapses well downstream. The rig is then set as quickly as possible to conditions determined by solving equations (4) and (5) for $\sigma_T = 0.09$ and the requisite throat velocity. A simple program is run on a dedicated PC for this purpose. The test rig is usually run for a duration of 10 to 30 minutes at a time. The specimen is removed, dried and weighed before remounting in the rig.

Weights are determined using a Mettler type AE160 balance which weighs up to 160gms to the nearest 0.1mg. The heaviest samples tested weighed about 50gms. Some difficulty was experienced with certain plastics, such as PMMA and GRP, which absorbed water; however the most satisfactory procedure was found to be to use a lengthy period of pre-soaking in order to stabilise the weight.

The cumulative mass and hence volume loss is determined as a function of time for a period between one and ten hours depending on the erosion resistance of the test material.

4. CORRELATION OF DATA

Cumulative volume loss data as a function of time have been been analysed in a standard way to determine NIP and VLR. Typical examples for epoxy resin, silicon carbide and carbon steel are shown in figs. 4, 5 and 6. The data points are analysed using linear regression and NIP and VLR are determined from intercept and slope respectively. The 95% confidence limits for the slope are also determined. This process is straightforward when there is an obvious linear or steady state portion; however if there is a substantial acceleration or even deceleration period, it is not appropriate to include all the data points. In order to deal with this in an objective way, the linear regression analysis is run repeatedly with fewer data points until the 95% confidence limits reach a minimum value. This condition is taken to define the slope and intercept of the best fit line and hence determine the VLR and NIP. For some less erosion resistant materials the incubation period is apparently negative; in these cases NIP is taken to be zero.

This process has been applied to all the data and the results are shown in the table. The materials are listed alphabetically and the VLR and NIP values for throat velocities of both 40m/s and 45m/s are shown alongside for easy comparison at different cavitation intensities. Some materials are identical but have different surface treatments; where this is the case it is indicated in the table. The Vickers hardness values are also given for information. Where repeat runs have been done, the average value of NIP and VLR are given.

Some data has been obtained at velocities other than 40m/s and 45m/s. In order to compare all the data, the normalising scheme described in section 2 has been used to correct the values of NIP and VLR to a throat velocity of 40m/s. The results are shown in figs. 7 and 8 using the reduced value of Vickers hardness as the correlating parameter. In these figures, repeat measurements have been shown separately. A reasonable correlation of VLR is observed for most materials, except for the very hard brittle materials, such as Nitralloy and silicon carbides and nitrides. The correlation for NIP is less good even excluding the hard brittle materials.

5. DISCUSSION OF RESULTS

It is not our purpose in this paper to discuss in minute detail the differences between the various materials and surface treatments. However several highlights will be noted and some general conclusions drawn.

It can be seen by inspecting the table that the rank order is different for each column. For instance, on the basis of minimum value of VLR, the most erosion resistant material is nitrided steel at 40m/s and nitrided steel and cast stainless steel at 45m/s. However on the basis of maximum NIP, these are replaced by Nitralloy at 40m/s and chromium nickel steel at 45m/s. The least erosion resistant material, according to the maximum VLR, is GRP at 40m/s and pure aluminium at 45m/s. On the basis of minimum NIP i.e. zero, these are cast iron and vinyl ester at 40m/s and epoxy resin and GRP at 45m/s. Although there are gaps in the table, it can be used to find the relative performance of any material tested with respect to NIP or VLR.

More general behaviour can be seen using the normalised variables in figs. 7 and 8 where VLR^* and NIP^* are correlated with respect to hardness (HV^*). It is apparent that VLR^* and HV^* are inversely correlated for materials generally below HV^* of about 200-400. This broadly corresponds to steels, non-ferrous metals, plastics and epoxies. Above this value of hardness lies another group which are not well correlated; this comprises ceramics and hardened steels. It is possible that they may be individually correlated with hardness but not collectively.

The power law for the former group is given by

$$VLR^* = 1.314 \times 10^5 (HV^*)^{-2.26} \ mm^3/h \qquad (6).$$

The 95% confidence limits on the index are ±0.36. This formula can be used to give a reasonable guide to *performance for most* materials except ceramics and hardened steels. The implicit velocity dependence of VLR in (6) is $U^{5.53}$, which is close to the commonly quoted and accepted value of 6. Comparisons with Mousson's data are very favourable. In a precious publication[2], Mousson's results for volume loss over a 16 hour period for stainless steels (omitting Austenitic steels) and brasses, bronzes and non- ferrous alloys were correlated using Brinell hardness. It was found that

$$VLR = 3.786 \times 10^6 (HB)^{-2.74} mm^3/h \qquad (7)$$

and the 95% confidence limits on the index were ±0.35. This result is remarkably close to that determined for the present data. The index is very similar but the erosion rate for the Mousson data is approximately three times larger for hardness in the range 30-300; however this is not surprising considering the difference in test apparatus.

The idea of correlating erosion rate with hardness is not new but these results vindicate the usefulness of the idea and moreover the normalising scheme allows the velocity index to be incorporated at the same time. So equation (6) and by association (7) can be used to predict erosion rate at different velocities.

The pattern for NIP is not as clear (fig.8). There are again the same two broad groups one above and the other below HV^* of about 200-400. Neither group is particularly well correlated but the group below a hardness of 200 shows an increasing NIP with hardness, as expected. If aluminium alloys are excluded, the trend is more apparent but the data is still not well correlated. The group with the larger hardness is, if anything, inversely correlated with hardness.

The generally poor correlation for NIP may be simply due to the greater inherent error in estimating the intercept. A better quantity may be the time to remove a certain volume of material, say $1mm^3$, which will be nearer the mean values of the volume loss versus time data and hence subject to smaller error.

For the very hard group of materials it is apparent that hardness is not a good correlating parameter; it is possible that a parameter, such as fracture toughness, may be more suitable but this has not been explored.

6. CONCLUSIONS

Comparative erosion data has been presented, which should be useful for design in many situations where cavitation attack is likely to be a problem. The normalising scheme given has been shown to be a useful way of correlating erosion data and gives information on erosion performance with both fluid velocity and material hardness. The power law deduced can be used tentatively to scale VLR for different fluid velocities and also for different material hardnesses.

REFERENCES

1. MOUSSON J.M. Pitting resistance of metals under cavitating conditions. Trans. A.S.M.E. 59, 399-408, 1937

2. LUSH P.A. Materials for minimum cavitation. C.M.E., October 1987

AKNOWLEDGEMENTS

The authors are grateful to the following past research students and assistants at City University, who carried out some of the work reported here: T.P. Butler, M.McD. Grant and S.M.A. Selim.

The authors are also grateful to the following organisations for financial support and assistance in supplying materials: B.P. Research; Dowty Fuel Systems; Institute of Fluid Flow Machinery, Polish Academy of Sciences; P.P.I. Ltd; Worthington Simpson; and Admiralty Research Establishment (now Defence Research Agency), Holton Heath.

TABLE 1: CAVITATION EROSION DATA

No	MATERIAL	VELOCITY 40 m/s		VELOCITY 45 m/s		
		VLR (mm /hr.)	N I P (min.)	VLR (mm /hr.)	N I P (min.)	Hv
1	Aluminium SIC	21.1	79.2	211	3	40
2	Al. alloy HE9	9.37	12	25.5	4.27	75
3	Al. alloy HE30	3.18	1.41	10	7.17	90
4	Al. alloy HE15	3.19	1.3	5.22	6.8	140
5	Al. alloy PA2			120.8	11	65
6	BrassSingle PhaseM63			7.96	71.7	117
7	Cupro-Nickel 90/10	3.47	105	9.34	35.8	110
	Epoxy Resin					
8	Black Q, Machined	18.1	2.17	31.4	0	54
9	Brown G, Machined	16.1	0.26	47.7	16.6	43
10	Brown MG,Machined	18.6	17			38
11	Black Q, As Cast	5.55	92.9	25.9	10	54
12	Brown G As Cast	8	140.7	26.6	29.5	43
13	Brown MG, As Cast	9.61	109.5			38
14	G R P	100.4	6	139.2	0	34
15	Armco Iron E04			1.7	230	132
	Cast Iron BS 1452					
16	Machined	3.99	48.8			130
17	As Cast	3.95	0			162
18	Nitralloy S106	0.37	330	1.14	209	630
19	PMMA	20.8	45.6			25
	Silicon Carbide					
20	Lapped	0.613	76	7.02	50	1900
21	Ground	0.419	70	7.29	73	1900
22	As Fired	1.28	107	13.68	42	1900
23	Lapped (improved)			10.58	35	1900
24	Ground (improved)			10.81	74	1900
	Silicon Nitride					
25	Lapped	0.122	186	1.98	133	1400
26	Ground	0.116	185	1.2	135	1400
27	As Fired			1.38	138	1400
28	Post HIP *	0.125	141	1.06	158	1700
29	Carbon Steel 45			1.35	331	176
30	Carbon Steel AISI 1020	0.39	205	4.5	134	145
31	CrNi Steel 1H18NAT			0.765	335	198
32	Nitrided Steel BS. S134	0.048	195	0.232	99	980
	Stainless Steel 316C16					
33	Machined			0.232	122	210
34	As Cast			0.65	44.2	205
35	Tool Steel CPM10V	0.087	122	0.46	147	758
36	Tool Steel M4			0.65	317	970
37	Tool Steel M4 + Ti C			0.82	122	940
38	Vinyl Ester	52.3	0			27
*	Hot Isostatic Packing					

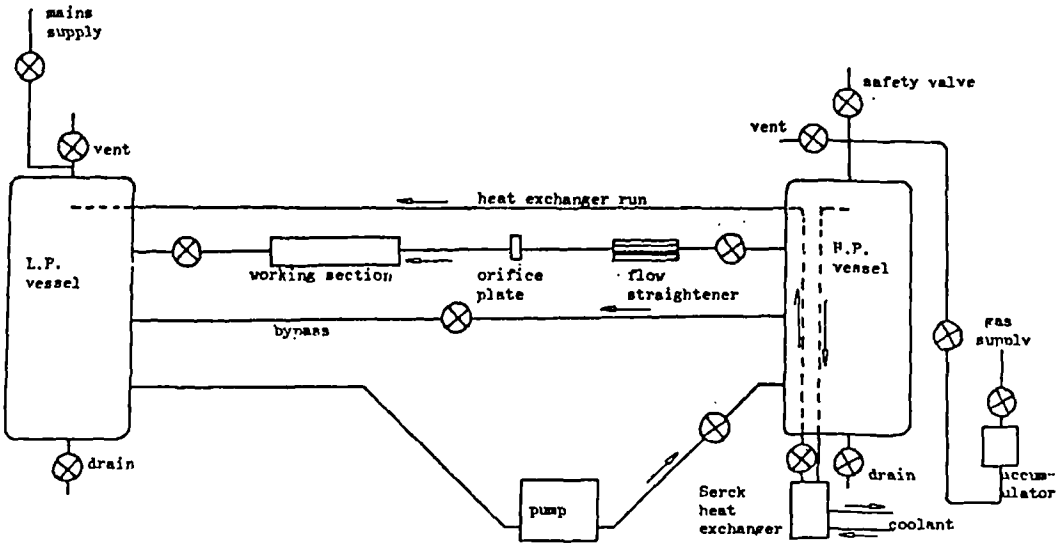

Fig.1 CAVITATION EROSION TEST FACILITY

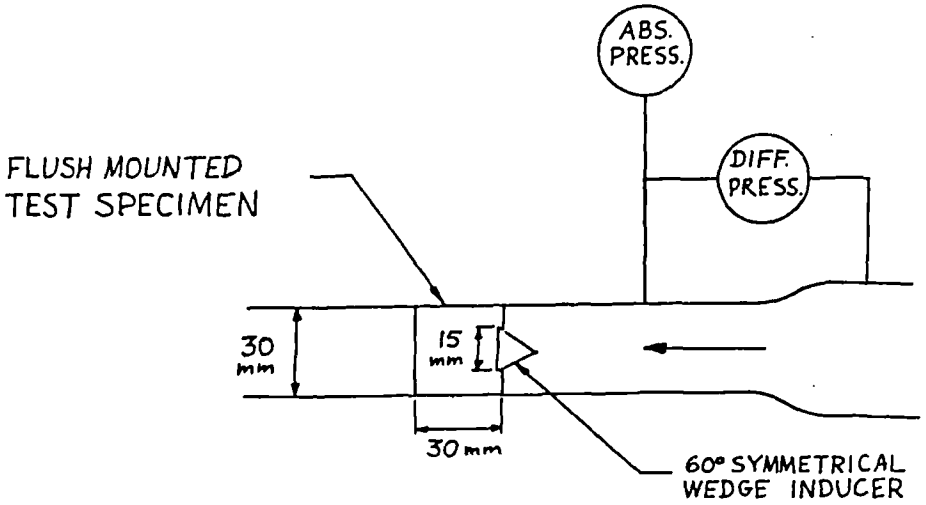

Fig.2 DETAIL OF WORKING SECTION

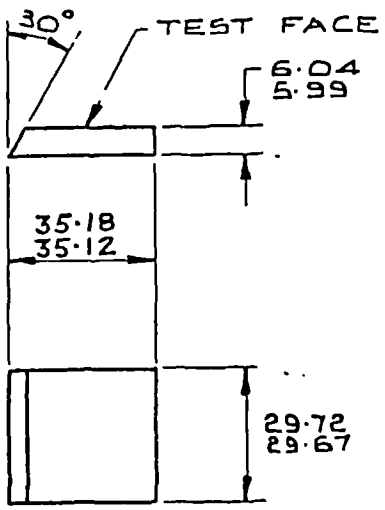

Fig.3 CAVITATION EROSION TEST SPECIMEN

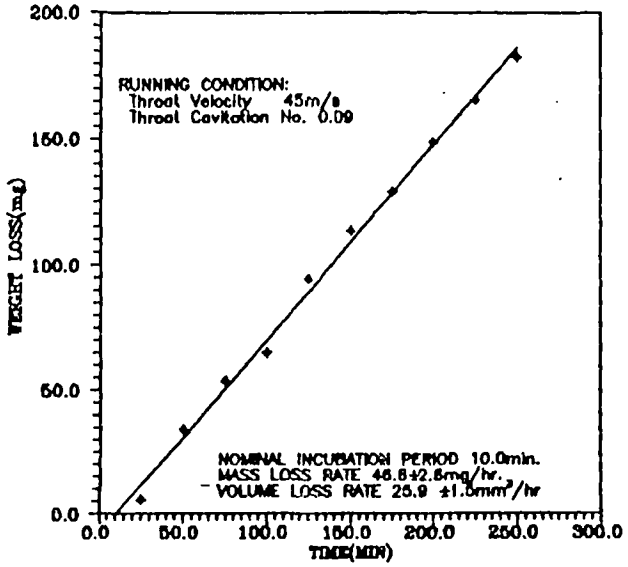

Fig.4 TYPICAL GRAPH OF CUMULATIVE WEIGHT LOSS AGAINST TIME FOR EPOXY RESIN

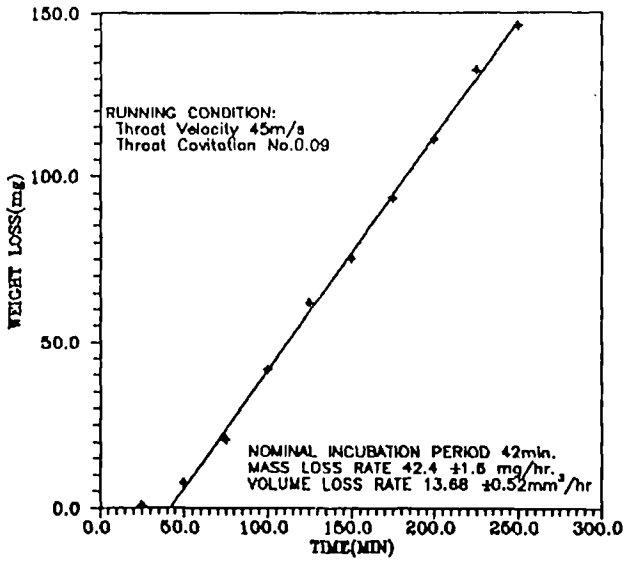

Fig.5 TYPICAL GRAPH OF CUMULATIVE WEIGHT LOSS AGAINST TIME FOR SILICON CARBIDE (AS FIRED)

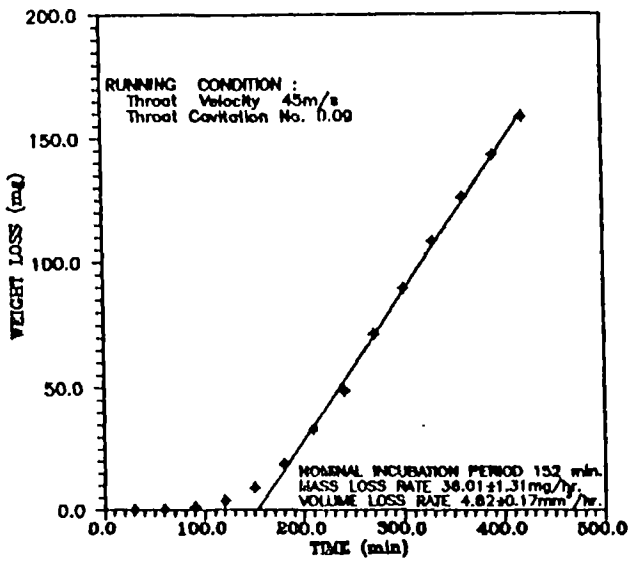

Fig6. TYPICAL GRAPH OF CUMULATIVE WEIGHT LOSS AGAINST TIME FOR CARBON STEEL

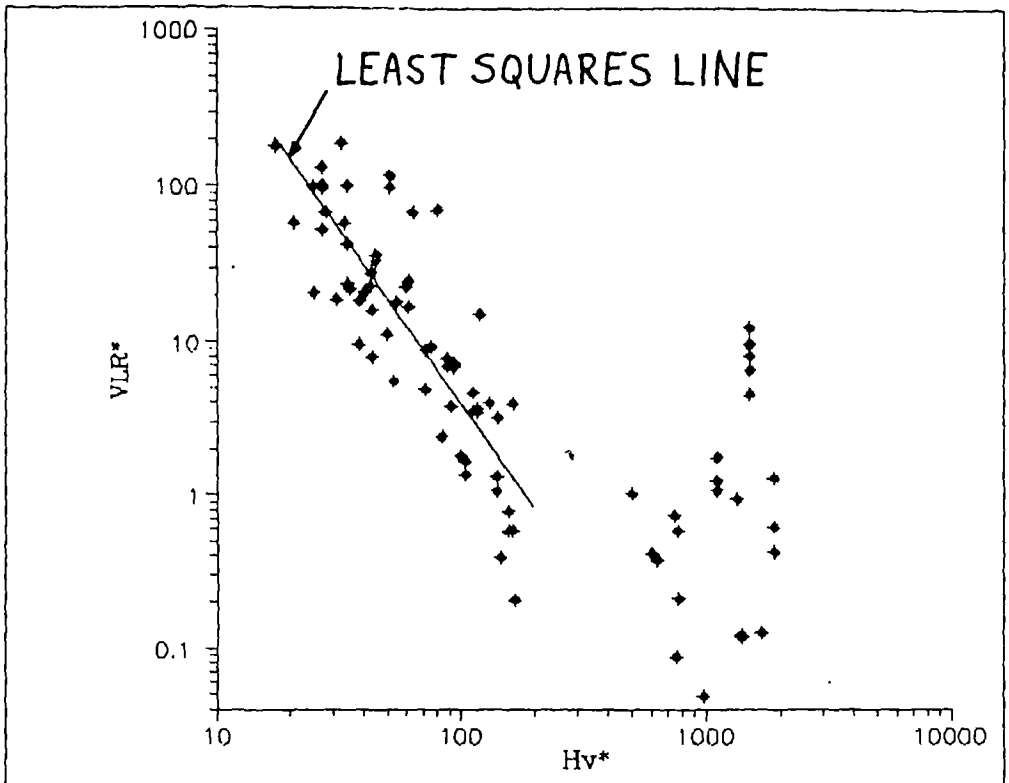

Fig 7 Variation of VLR against Hv using normalised variables for all materials tested

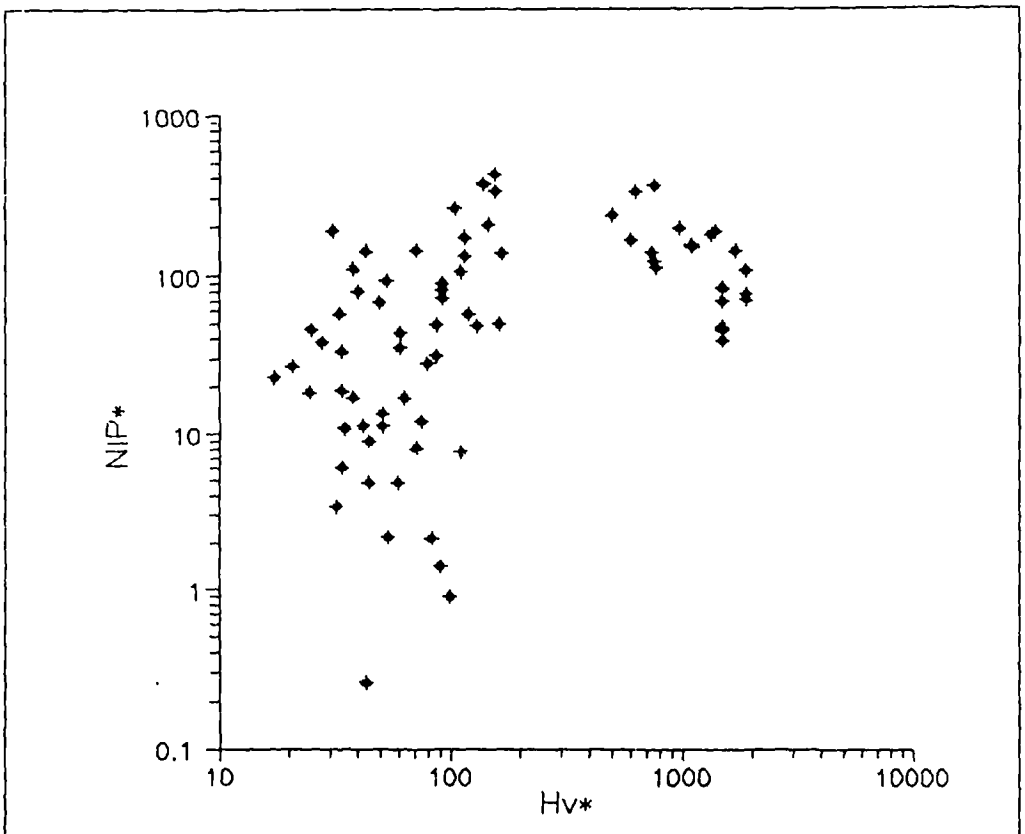

Fig 8 Variation of NIP against Hv using normalised variables for all materials tested

7.0 CONCLUSIONS AND RECOMMENDATIONS FOR FUTURE WORK

In this experimental research project, a number of engineering materials have been tested for their cavitation erosion resistance in a venturi testing device. Four classes of materials were employed. These were plastic, composite, ceramic and metal alloys.

The plastic tested was epoxy resin, and this came in two formulations i.e, the novalac and the bisphenol system . Production of the above plastics came via two manufacturing processes, these were in as cast and machined conditions.

Tests to evaluate the influence of the manufacturing process on hydrodynamically induced cavitation erosion conclusively showed the "as cast" sample to be better in resisting cavitation in both resin formulations. Comparison of the two epoxy resin systems tested did not show any significant difference, although on the basis of their VLR values alone, the novalac tends to have a slightly better performance. With the bisphenol epoxy resin system, the addition of abrasive particulate filler did not alter the overall erosion resistance.

Observational studies on the material removal process revealed that, brittle failure as a result of crack propagation

and interaction was the dominant mode of fracture with the epoxy resin samples.

It is recommended that, further investigations be carried out on the nature of the "as cast" surface. The characteristic skin formed on the surface of the "as cast" samples, was observed to be the principal influence on its erosion performance. It is proposed that, further studies be done with detailed analysis of the structure of the cast surface film. The morphology of the bulk resins appears to strongly influence their erosion behaviour. Although not specifically investigated there is some indication that, the degree of crystallinity or amorphousness of the bulk polymer may control it erosion resistance. Studies with appropriate control over the degree of crystallinity is recommended for further work.

The Ceramic materials tested in this project were silicon carbide and silicon nitride. These were tested under three surface conditions i.e, ground, lapped and as fired or sintered . Thus with the ceramic materials, the objective was twofold. Firstly to ascertain the performances of the three surface finishes and secondly to establish which of the silicon base ceramics would resist cavitation induced erosion better.

Generally it has been found that, grinding and lapping finishing operations improve the cavitation erosion resistance of both silicon carbide and silicon nitride .

Of the three surface finishes employed, the results obtained showed that the ground sample performed best. It was followed closely by the as lapped sample with the fired sample coming last in the ranking. The above performance order was common to both silicon carbide and silicon nitride. Comparison between the two silicon base ceramics i.e, silicon carbide and silicon nitride overwhelmingly showed the latter to be better in resisting cavitation induced erosion in all the three surface finishes employed.

From observational studies of material removal it was ascertained that, failure as a result of induced cavitation erosion in silicon carbide was predominantly brittle in nature. Both optical and scanning electron micrographs do revealed evidence of transgranular fracture. Chipping was also observed to be prominent in the erosion process.

Silicon nitride on the other hand exhibited a dual mode of failure. Initial deformation and pitting were very similar to those observed in iron and low carbon steels. Plastic deformation was very much evident prior to initial material removal. "Necking" of the ridges formed by adjacent pits was responsible for material removal in the early stages. At advanced stages of the erosion process brittle mode of failure tend to dominate in silicon nitride.

From the above results, it is evident that the surface

finishing operations have a significant influence on the erosion behaviour of the bulk silicon base ceramics employed. However it as recognised that finishing operations performed on ceramics usually leave the surface in a state of residual stress. They also introduce both surface and subsurface flaws i.e, micro cracks. Their effects on the results obtained in this work is not very apparent. It is recommended that further work be carried out to investigate the effect of residual stress, micro cracks, flexural strength, and fracture toughness to cavitation erosion resistance.

Of the two composite materials tested, "Fybroc" with a vinyl ester matrix and randomly oriented chopped glass fibres performed better than GRP with an angle-ply laminate construction of glass fibre in an epoxy resin matrix. The above two composites utilised thermosetting resins as the matrix, a common practice with aerospace structure where they are noted for their strength properties. It is recommended that the effects of random chopped-fibre reinforcement versus conventional 2-D reinforcement in a thermoplastic resin be investigated. Further work also should be carried out on the effect the orientation of the reinforcing element has on the erosion behaviour. It is also suggested that, fibre concentration be varied to ascertain its effect with erosion behaviour.

The erosion characteristics of a number of engineering

metal alloys have also been investigated. It was ascertained from observational studies that initial damage were in the form of microscopic craters. With longer exposure time damage becomes more wide spread with a deepening of previously formed shallow pits. Material lost in the early stages were by ductile fracture of asperities and of ridges between erosion pits.

A comprehensive list of cavitation data has been accrued as a result of this project, facilitating easy comparison of relative erosion resistance. The comparative erosion data obtained will be useful for design in many situations were cavitation attack is likely to be a problem, and also enhance the existing cavitation data base.

REFERENCES

ALLOR, R.L. and BAKER,R.R (1983)
Amer. Soc. Mech. Eng., 83-GT-203. ,

ANDERSON,C.A. and BRATTON, R.J. (1979)
"In the Science of Ceramic and Surface Finishing II" ,Ed. B.J.Hockey, and R.W. Rice. Nat. Bur. Stds SP562, Washington, DC, pp. 477. ,

Backstrom, T.E (1967)
Tech. Rep. No. Ch. E-72, Chemical Engineering Branch, U.S. Bureau of Reclamation, Denver, Colorado.

CHATTEN, C.K. and THIRUVENGADAM, A. (1967)
"Testin of Polymers"
Eds, J.V. Schmidz and W.E. Brown. Vol. III, pp.245 ,
Willey, New York.

DAKSHINAMOORTHY, S. (1975)
M.S. Thesis, Dept. of Material Science, State university New York at Stony Brook.

DOUGLAS,F.J., GASIOREK, J.M. and SWAFFIELD, J.A. (1979)
"Fluid Mechanics". Pitman, London.

EISENBERG,P., PREISER, H.S. and THIRUVENGADAM,A. (1965)
Trans. Soc. Naval Archit. Mar. Eng. 73, 241.

ERDMANN, J.F. and LOUIS, H. (1974)
"Studies on Cavitation Damages "
Ed. A. Thiruvengadam, Erosion, Wear and Interfaces with ,Corrosion. ASTM. STP 567, pp.171-195.

ERDMANN-JESNITZER,F., LOUIS, H. and Matsuruma, M. (1977a)
Arch. Eisenhuttenwes. 48, 179.

FURNESS, R.A. (1974)
"Studies of the Mechanics of Fixed Cavities in Two-Dimemsional Convergent-Divergent Nozzle". I.Mech. Conf. on Cavitation. Edinburgh, Paper C160/74.

GORHAM, D.A. and FEILD, J.E. (1976)
Jnl. Phys. D Appl Phys. 9. pp.1529.

GRANT, M.McD (1982b)
"Correlation of Cavitation noise and Erosion".
City University, M.E.D Rep. No.142. ,

GRANT, M.McD (1984)
"Prediction of Cavitation Erosion Rates". PhD. Thesis
City University, London. ,

HAKULINEN, M. (1985)
Jnl. of Mater. Sci., 20, pp. 1049.

HAMMITT, F.G. (1963)
"Observation of Cavitation Damage in a Flow System". Trans. ,
ASME Jnl. Basic Eng. D, 85, 3, pp.347-359.

HAMMITT F.G. (1965)
"Initial Phases of Damage to test Specimens in a Cavitating
Venturi". Trans. ASME Jnl. Basic Eng. D 87,2 pp.453-464.

HAMMITT, F.G. and GARCIA, R. (1967)
"Cavitation Damage and Correlation with Material and Fluid
Properties". Trans. ASME, Jnl. Basic Eng. 89, 4, pp.753-763.

HAMMITT, F.G. (1980)
"Cavitation and Multiphase Flow Phenomena". McGraw-Hill,
New York.

HANSSON, I. and MORCH, K.A. (1977)
SCAND. J. Metall. 6, 10.

HERBERT, W. (1965)
Proc. Int. Conf. Rain Eros , 1st. pp.114.

HEYMAN, F.J. (1967)
"Erosion by Cavitation or Impingment". ASME. STP 408,
pp. 70.

HOBBS, J.M. (1962)
N.E.L. Rep. No. 69, National Engineering Laboratory, East ,
Kilbride, UK.

HOBBS, J.M., (1967)
"Erosion by Cavitation or Impingement" ASTM . STP 408 ,
pp. 159.

HOLL,J.W. and WOOD, G.M. (1964)
Symp. Cavitation Res. Facilities. Tech. ASME, New York.

HUTTON, S.P and AL-MESHHEDANI, W.A. (1992)
"The Effect of Air Injection upon Cavitation Erosion"
Proc. I.Mech.E. on Cavitation, Cambridge, UK.

KER, S.L, and RSENBERG, K. (1958)
ASME, 80, pp.1308.

KNAPP, R.T. (1955)
"Recent investigations of the Mechanics of Cavitation and Cavitation Damage". ASME, Jnl. Basic Eng. 77, pp.1045-1054.

KNAPP, R.T. (1956)
Proc. NPL Symp. on Cavitation, Hydrodynamics, Paper 19.

KNAPP, R.T. (1957)
"Investigation of the Mechanics of Cavitation and , Cavitation Damage". Final Report.

KNAPP,R.T., DAILY, J.W. and HAMMITT, F.G. (1970)
"Cavitation". McGraw-Hill, New York. ,

LAIRD, A. and HOBBS (1971)
National Engineering Lab., No. 496. East Kilbride, UK.

LICHTMAN, J.Z. and WEINGRAM, E.R (1964)
Symp. Cavitation Res. Facilities Tech. ,
Ed. J.W. HOLL and G.M. WOOD, ASME, pp.185. New York.

LUSH, P.A. and SKIP , S.R. (1986)
"High speed cine observations of Cavitating flow in a Duct". Int. Jnl. of Heat Flow. ,

LUSH, P.A. (1987)
"Materials for minimum Cavitation"
C.M.E.

MORCH, K.A. (1979)
"Cavitation Erosion", Appearing in Treatise on Materials Science and Technology, Vol. 16, Erosion. Academic Press, London

MOUSSON, J.M. (1937)
"Pitting Resistance of Metals Under Experimental conditions". ASME. 59, pp.399-408.

NAUDE, C.F. and ELLIS, A.T. (1961)
"On The Mechanism of Cavitation Damage by Non Hemispherical , Cavities Collapsing in Contact with a Solid Boundary".ASME , Jnl. Basic Eng. 83, pp.648-656.

PLESSET, M.S. and DEVINE, R.E. (1966)
Trans. ASME. Ser. D 88, 691.

PLESSET, M.S. and CHAPMAN, R.B. (1971)
"Collapse of an Initial Sperical Vapour Cavity in the Neighbourhood of a Solid Boundary". Jnl. Fliud Mechs, 47, , pp. 283-290.

PREECE, C.M. (1979)
"Cavitation Erosion", Appearing in Treatise on Materials Science and Technology, Vol. 16 Erosion . Academic Press.

PROTHEROE, B. (1977)
Private Communication, South Africa Chamber of Mines.

RAO, B.S.C., RAO,N.S.L. and SEETHARAMIAH, K. (1970)
"Cavitation Erosion Studies with Venturi and Rotating Disk in Water" ASME Jnl. Basic Eng. 92, 3.

RAO, V.P., RAO, L.N.S. RAO, S.B.C. (1980)
"Erosion and Cavity Characteristics in a Rotating component". Jnl. of Testing and Evaluation . Vol.8 No. 3 , pp. 127-142.

RAO, P.V. and YOUNG, S.G. (1983)
"A Comprehensive Analysis of Cavitation and Liquid Impingement Erosion Data". Proc. of Mech. E. Conf. on Cavitation, Edinburgh.

RAO, P.V. (1988)
"Evaluation of Epoxy Resin in Flow Cavitation Erosion" , Wear, 122, pp.77-95.

RASMUSSEN, R.E.H. (1955)
"Some Experiments on Cavitation in Water mix with Air". Proc. Symp. on Cavitation in Hydrodynamics. NPL, , Teddington pp.20.

RAYLEIGH, L. (1917)
"On The Pressure Developed in a Liquid During The Collapse of a sperical cavity". Phil. Mag., 34 pp.94-98 ,

RICHMAN, R.H. and McNAUGHTON,W.P. (1990)
"Correlation of Cavitation Erosion behaviour with Mechanical Properties of metals". Wear, 140, pp.63-82.

SCHMITT, G.F., Jr. (1974)
"Material Paramaters that Govern the Erosion behaviour of Polymeric Composites in Subsonic Rain Enviroments" ASME, Composite Materials; Testing and Design, 3rd. , Conf. pp.303-323.

SCHULMEISTER, R. (1965)
Proc. Int. Conf. Rain Eros. 2nd. ,
Ed. A.A. Fyall. Royal Aircraft Establishment, Farnborough, UK.

SELIM, S.M.A. (1977)
"Measurement of Air Content in a Cavitation Tunnel Using The Van-Slyke Apparatus".University of Southamton, Rep. No.Me/77/26.

SELIM, S.M.A. and HUTTON, S.P. (1983)
"In Classification of Cavity Mechanics and Erosion". 2nd Int Conf. on Cavitation, Edinburgh.

SHALNEV, K.K. (1955)
"Experimental Study of the Intensity of Erosion due to Cavitation". Cavitation in Hydrodynamics, NPL, Teddington , England 22, 37, pp.1-22.

THIRUVENGADAM, A. and WARING, S. (1964)
Tech. Rep. No. 233-5. Hydronautics Inc. Laurel, Maryland.

THIRUVENGADAM,A. and PREISER,H.S. (1964)
Jnl. of Ship Res. 8, 39.

THIRUVENGADAM, A. (1971)
Tech. Rep. No. 233-5, Hydronautics Inc. Laurel, Maryland.

THOMPSON, L.D., PEDERSEN, A.M. and HOYT, J.W. (1989)
"Cavitation Eroaion in 6061; Effect of Precipitation , Hardening". Cavitation and Multiphase flow Forum. ,

TICHLER, J.W., VAN Den Elsen, J.S and De GEE, A.W.J. (1970)
Trans. ASME Ser. 92, 220.

TOMLINSON, W.J. and NEWTON, R.C (1990)
Ceramic International, 16, pp. 253-257.

WADE, E.H.R. and PREECE, C.M. (1978)
Metall. Trans. Ser. A 8A, 915.

WILLMANN, G. (1985)
Ceramic Industries Journal, 15.

WOOD, G.M., KNUDSEN, L.K. and HAMMITT, F.G. (1967)
"Cavitation Damage Studies with Rotating Disk in Water".
ASME Jnl. of Basic Eng., 89, pp. 98-110.

WOODFORD, D.A. and BEATTIE, H.J. (1971)
Metall. Trans. 3, pp. 1137. ,

ZHOU, K.S. and HERMAN, H. (1982)
"Cavitation Erosion of Titanium and Ti6al-4V; Effects of Nitriding". Wear 80, pp.101-113.

ZHOU, Y.K. and HAMMITT, F.G. (1983)
"Vidratory Cavitation Erosion in Aqueous Solution"
Wear 87, pp.163-171.

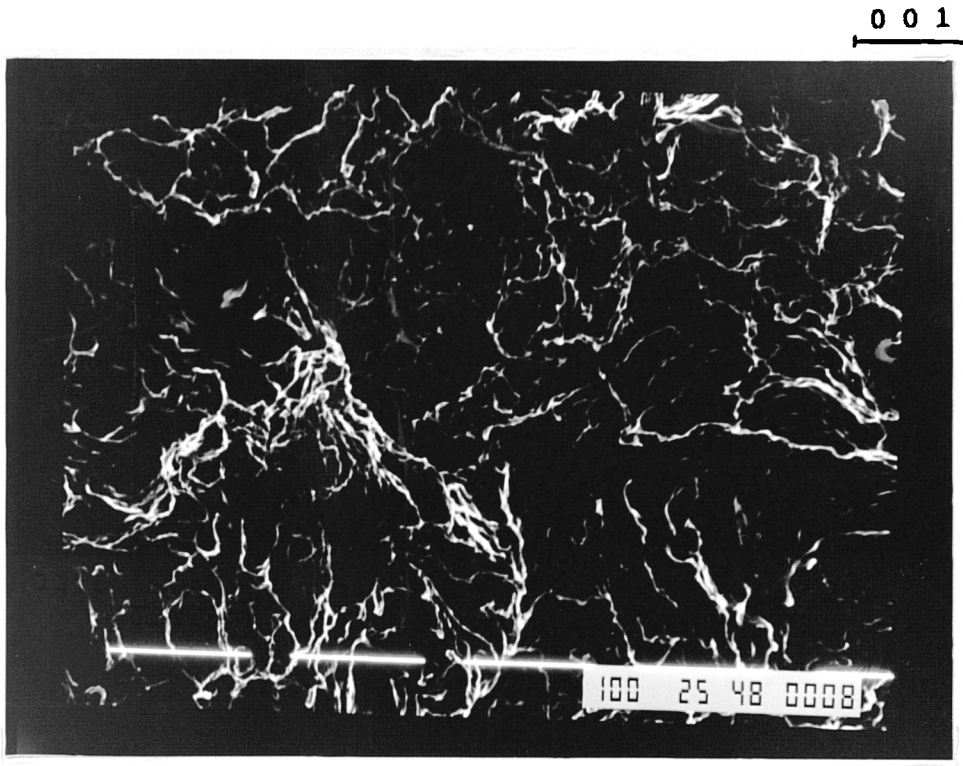

FIG.111c SCANNING ELECTRON MICROGRAPH OF DAMAGE IN CENTRAL ZONE AFTER TEST COMPLETION (160 min.)

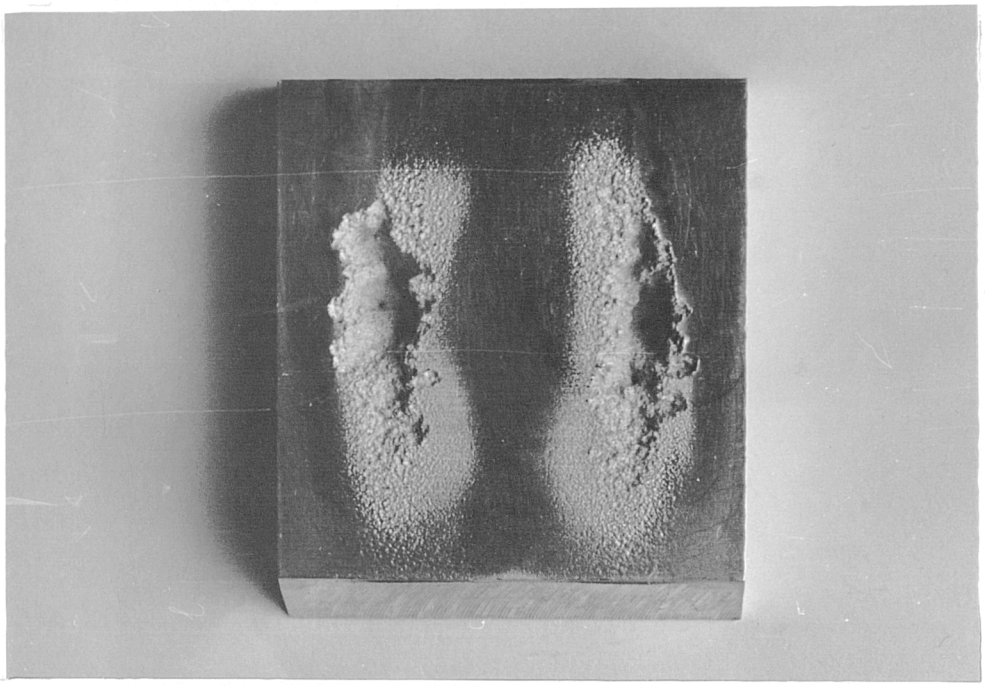

FIG.111d MACROSCOPIC VIEW OF GROSS DAMAGE IN ALUMINIUM (160 min.)